

LNG/Fuel cascades and flammable cloud formation

Marco Macchi

Thesis submitted for the Degree of Doctor of
Philosophy of Kingston University London

Faculty of Science, Engineering and Computing
Kingston University London
April 2018

To my fiancée Marta

Acknowledgements

I would like to express my sincere gratitude to my supervisory team, Prof. Jennifer Wen, Dr Konstantin Volkov, Dr Yongmann Chung and Dr Ali Heidari for the continuous support during my PhD. Their help and knowledge have been fundamental in order to produce the work presented in this thesis.

I would also like to thank the European Commission for allowing me to take on such an important research project and for supporting me and Kingston University during these 4 years.

My sincere thanks also go to all my colleagues in the SafeLNG project for the helpful discussions on the topic and the pleasant time spent together.

I thank my family for their continuous support even far from home, and for helping me during the difficult relocation to the UK.

Last but not the least, I would like to thank my fiancée Marta, for helping me with any difficulty and supporting all my choices. Without her, none of this work would have been possible.

*All truths are easy to understand once they
are discovered; the point is to discover them.*

Galileo Galilei

Contents

1	Introduction	3
1.1	Background and Motivation	3
1.2	Aim of the current work	5
1.3	Liquefied Natural Gas	5
1.3.1	Floating Liquefied Natural Gas	6
1.3.2	Hazards and Risks	7
1.3.3	Transportation	8
1.4	Research Topics of the SafeLNG Project	9
1.4.1	LNG/Fuel Cascades and Flammable Cloud Formation	10
1.4.2	LNG Spill and Dispersion in the atmosphere	10
1.4.3	LNG Rollover	10
1.4.4	LNG Flashing Jets	11
1.4.5	LNG Pool Fires	11
1.4.6	DDT in non-uniform LNG vapour mixtures	11
1.5	Physics of the process	12
1.6	Chapter summary	16
2	Literature Review	17
2.1	Previous work on fuel cascades	17
2.1.1	Tank design and effect on liquid discharge	20
2.1.2	Investigation of tank section	21
2.1.3	Effect of liquid properties on the spray structure	23
2.1.4	Effect of obstacles in the vapour accumulation	23
2.1.5	CFD analysis	25
2.1.6	Splashing of droplets	26
2.2	Previous work on droplet impact onto solid surfaces	27
2.2.1	Splashing-deposition limit	29

2.2.2	Dry and wet impact	29
2.2.3	Temperature of the wall	30
2.2.4	Numerical simulations of droplet impact	31
2.3	Previous work on LNG modelling	32
2.4	Chapter summary	33
3	Computational methodology and governing equations	34
3.1	Conservation Principles	35
3.1.1	Material Derivative	35
3.1.2	Continuity Equation	36
3.1.3	Momentum Equation	36
3.1.4	Energy Equation	38
3.1.5	Conservation of Scalar Quantities	38
3.1.6	Summary of the Conservation Equations	39
3.2	Simplified forms of the equations	39
3.2.1	Incompressible Flow	40
3.2.2	Inviscid Flow	40
3.3	Simulation of Multiphase Flows	41
3.3.1	The Eulerian-Eulerian Approach	43
3.3.2	The Lagrangian-Eulerian Approach	44
3.3.3	Lagrangian formulation in OpenFOAM	46
3.4	Turbulence Modelling	51
3.4.1	RANS Models	52
3.4.2	LES Models	55
3.4.3	DNS Models	58
3.5	Numerical Methods for Fluid Dynamics	58
3.5.1	Mathematical Model	59
3.5.2	Discretisation Method	59
3.5.3	Computational Grid	60
3.5.4	Finite Approximations	62
3.5.5	Solution Method	62
3.5.6	Convergence Criteria	62
3.6	Convergence, Consistency and Stability	62
3.7	Discretisation approaches	63
3.7.1	Finite Difference Method	63
3.7.2	Finite Volume Method	63

3.7.3	Finite Element Method	64
3.8	The Finite Volume Method	64
3.8.1	Flux Integration	66
3.8.2	Source Term Integration	68
3.8.3	Boundary Conditions	69
3.9	Resolving the System of Algebraic Equations	69
3.9.1	Direct methods	70
3.9.2	Iterative methods	71
3.9.3	Under-Relaxation	73
3.10	Pressure-Velocity coupling	73
3.10.1	The pressure equation	74
3.10.2	The SIMPLE algorithm	74
3.10.3	The PISO algorithm	75
3.10.4	The PIMPLE algorithm	76
3.11	Chapter summary	76
4	Cascade Solver Development	77
4.1	Interaction of parcels with solid surfaces	77
4.2	Buoyancy effects	78
4.3	Development of the cascadeFoam solver	81
4.3.1	Liquid Film Region	81
4.3.2	Enhanced Buoyancy	83
4.3.3	Comparison of the two solvers	84
4.4	Solver Validation	84
4.4.1	Experimental Setup	85
4.4.2	Computational Model used by HSL	86
4.4.3	Computational Model	86
4.4.4	Droplet Setup	89
4.4.5	Meshing	90
4.4.6	Simulation without splashing	92
4.4.7	Simulation with splashing	95
4.4.8	Large Eddy simulation setup	101
4.4.9	Mesh size	102
4.4.10	Results	103
4.5	Chapter summary	104

5	Splashing Model Development	106
5.1	Numerical analysis of the process	106
5.1.1	Volume of Fluid method	107
5.1.2	Level Set method	109
5.1.3	Coupled LS-VOF methods	109
5.2	Contact angle	110
5.3	Physics of the process and model formulation	112
5.3.1	Transition Criteria	113
5.3.2	Post-impingement characteristics	114
5.4	Description of interFoam solver	117
5.5	Validation of the solver for inertia-dominated flows	118
5.5.1	Water droplet impact on flat surface	118
5.5.2	Crown Evolution of Droplet Impact	120
5.5.3	Conservation of mass	121
5.5.4	Effect of liquid properties on splashing	121
5.6	Splashing of Droplets	122
5.6.1	Model Development	126
5.6.2	Development of the Correlations	128
5.7	Implementation of the new model in the lagrangian solver	136
5.8	Validation against experiments	139
5.9	Chapter summary	140
6	Implementation of LNG	142
6.1	Liquid Library for Lagrangian solvers	143
6.1.1	NSRDS Functions	145
6.2	Properties of Liquid Methane	146
6.2.1	Calculation of the coefficient for vapour pressure	148
6.3	Simulation of liquid spill in an LNG plant	149
6.3.1	Geometry setup	150
6.3.2	Turbulence modelling	150
6.3.3	Mesh sensitivity analysis	150
6.3.4	Evaporation of droplets	152
6.3.5	LFL and cloud contour	154
6.3.6	Spray Pattern	158
6.4	LNG dispersion in a plant and Explosion	161
6.4.1	Results	163

6.5 Chapter summary	166
7 Conclusions	167

List of Figures

- 1.1 Buncefield Cloud 4
- 1.2 An LNG terminal facility (source: www.thenews.com.pk) 6
- 1.3 LNG Transportation Process 9
- 1.4 All the scenario addressed in the SafeLNG project 12
- 1.5 Schematic picture of a jet spray 13
- 1.6 Definition of flammability limits 15

- 2.1 Video frames of the site showing the cloud formation 18
- 2.2 5 stages modelled 19
- 2.3 Types of tank and release scenarios 21
- 2.4 Model 1 (left) and Model 2 (right) 22
- 2.5 Spray structure of water (left) and petrol (right). Observations
made 14m below the plane of release 24
- 2.6 Average vapour concentration and temperature within the bund . 25
- 2.7 Contours of the vapour concentration at the LFL. The surfaces are
coloured by their height from the ground 26
- 2.8 Difference between dry and wet splashing 27

- 3.1 Definition of a Control Volume 35
- 3.2 Drag Coefficient for a sphere as a function of Reynolds number for
rough and smooth surface 48
- 3.3 Deformation of a droplet undergoing a bag-breakup 51
- 3.4 Filtering operation 56
- 3.5 Structured Grid around a semi-cylinder 60
- 3.6 Unstructured Grid around a cylinder 61
- 3.7 Hybrid Grid used to model the boundary layer 61
- 3.8 General shape of a control volume 64
- 3.9 Notation for a 2D Control Volume 67

4.1 Schematic of the different impact regimes	78
4.2 Methane (main component of LNG) density at atmospheric pressure compared to the air one	80
4.3 Splashing of droplets onto the liquid region	82
4.4 Liquid Region	82
4.5 Experimental setup for the solver validation	85
4.6 Geometry given in the HSL report	87
4.7 OpenFOAM Geometry	87
4.8 Cumulative Distribution and Probability Density Functions of the setup	91
4.9 Mesh zoom obtained with the <i>blockMesh</i> utility	91
4.10 Parcels of Hexane droplets injected in the domain coloured by temperature	92
4.11 Comparison of the cascade shape between Experiments and CFD (droplets are coloured according to their temperature)	93
4.12 Side view fo the spray pattern	94
4.13 Front view fo the spray pattern	94
4.14 Maximum diameter of the droplets with height	95
4.15 Average velocity of the droplets with height	95
4.16 Domain showing the zones where the comparison was made	96
4.17 Temperature predictions in the bulk of the cascade (Point A)	97
4.18 Temperature predictions far from the cascade (Point B)	98
4.19 Velocity predictions on the line 0.15m from ground	98
4.20 Comparison of the predicted droplet splashing with the experimental observation	99
4.21 Temperature predictions on the line 0.15m from ground	99
4.22 Hexane mass fraction predictions on the line 0.15m from ground	100
4.23 Contour plot of Hexane mass fraction in a slice	100
4.24 Contour plot of Temperature in a slice	101
4.25 Contour plot of Turbulent Kinetic Energy in a slice	101
4.26 Contour plot of the predicted fuel concentration at 0.5 LFL	102
4.27 Concentration of hexane on a symmetry plane through the domain	104
5.1 Definition of the phase fraction	107
5.2 Local refinement used in OpenFOAM	108
5.3 Results obtained with the coupled solver	110

5.4	Definition of contact angle	111
5.5	Impinging and Ejecting droplet main parameters	114
5.6	Qualitative comparison between CFD and experiment	119
5.7	Droplet diameter evolution with time	120
5.8	Crown evolution with time	121
5.9	Droplet mass evolution with time	122
5.10	Comparison between simulations (left) and experiments (right) for velocities of 2.17 m/s (a) and 4.22 m/s (b) and non-dimensional film thicknesses of 1. Diameter of droplet is always 2mm.	123
5.11	Comparison between simulations (left) and experiments (right) for velocities of 2.17 m/s (a) and 4.22 m/s (b) and non-dimensional film thicknesses of 0.1. Diameter of droplet is always 2mm.	124
5.12	Mass splash ratio for the validation testcases	124
5.13	Splash angle for the validation testcases	125
5.14	Mesh detail on the droplet and underlying film	127
5.15	Initial Condition for the simulation	128
5.16	Droplet absorbed in the film (left, test 33)and droplet splashed (right, test 49)	128
5.17	Splash Regimes for $H = 0.5mm$	133
5.18	Splash Regimes for $H = 1mm$	133
5.19	Splash Regimes for $H = 2mm$	134
5.20	Correlation for the splashing angle	135
5.21	Correlation for the mass splash ratio	136
5.22	Droplets splashing at $t=0.053$ s using the Bai and Gosman model (left) and the new model (right)	138
5.23	Droplets splashing at $t=0.067$ s using the Bai and Gosman model (left) and the new model (right)	138
5.24	Droplets splashing at $t=0.1$ s using the Bai and Gosman model (left) and the new model (right)	138
5.25	Temperature predictions in the bulk of the cascade (Point A)	139
5.26	Temperature predictions far from the cascade (Point B)	140
6.1	Composition of LNG	142
6.2	Domain used for the CFD calculations (D=70m, A=50m, L=300m, H=100m)	150
6.3	Mesh showed on the symmetry plane	151

6.4	Temperature profile on line 1	152
6.5	Velocity profile on line 1	153
6.6	Temperature profile on line 2	153
6.7	Velocity profile on line 2	154
6.8	Cascade Evolution	154
6.9	Droplets evaporation mass flow rate	155
6.10	Contours showing the cloud and the LFL at 5s	155
6.11	Contours showing the cloud and the LFL at 10s	156
6.12	Contours showing the cloud and the LFL at 15s	156
6.13	Contours showing the cloud and the LFL at 20s	156
6.14	Contours showing the cloud and the LFL at 25s	157
6.15	Contours showing the cloud and the LFL at 30s	157
6.16	Contours showing the cloud and the LFL at 35s	157
6.17	Contours showing the cloud and the LFL at 40s	158
6.18	Human presence close to the tank	158
6.19	Front view of the spray	159
6.20	Side view of the spray	159
6.21	Average diameter of the droplets	160
6.22	Maximum diameter of the droplets	161
6.23	Average velocity magnitude of the droplets	161
6.24	Geometry used for the CFD calculation (tank diameter is 70m, height is 50m, plant base area is A=150m, B=80m and domain size is 450x450x100m)	162
6.25	Mesh obtained by <i>snappyHexMesh</i>	163
6.26	Contours showing the LFL for the 12 kg/s case	164
6.27	Contours showing the LFL for the 36 kg/s case	165

List of Tables

1.1	Flammable limits for different substances	16
4.1	Differences between standard solver and <i>cascadeFoam</i>	84
4.2	Properties of Hexane	89
4.3	Turbulence quantities calculated for different locations	103
5.1	Properties for the different liquids analysed	122
5.2	Results for Bai and Gosman validation	125
5.3	Setup quantities range for the simulations	127
5.4	Simulation Setup	129
5.4	Simulation Setup	130
5.4	Simulation Setup	131
5.5	Coefficients of the linear interpolation	137
6.1	Properties of Methane (CH_4)	146
6.2	Properties of Methane to be considered constant with temperature	147
6.3	Grid level and number of computational cells used	151
6.4	Definition of line 1 and 2 for the mesh sensitivity results	152

Nomenclature

A	Area [m^2]
\mathbf{a}	Acceleration [m/s^2]
Bo	Bond Number
C_D	Drag Coefficient
c_p	Specific Heat Capacity at Constant Pressure [$J/(kg \cdot K)$]
D	Drag Force [N]
d	Droplet Diameter [m]
E	Energy [J]
e	Specific Internal Energy [J/kg]
F	Force [N]
\mathbf{f}	Volume Force [N/m^3]
\mathbf{g}	Gravitational Acceleration [m/s^2]
h	Specific Enthalpy [J/kg]
H^*	Dimensionless Film Thickness
h_{fg}	Latent Heat of Formation [J/kg]
\mathbf{J}	Flux
k	Thermal Conductivity [$W/(m \cdot K)$]
k	Turbulent Kinetic Energy [J/kg]

l_m	Turbulence Length Scale [m]
La	Laplace Number
m	Mass [kg]
N_s	Number of Secondary Droplets
Nu	Nusselt Number
Oh	Ohnesorge Number
p	Pressure [N/m^2]
Pr	Prandtl Number
r_m	Splashing Mass Ratio
Re	Reynolds Number
S	Lagrangian Source Term
T	Temperature [K]
t	Time [s]
\mathbf{u}	Velocity [m/s]
We	Weber Number
α	Contact Angle [$^\circ$]
β	Thermal Expansion Coefficient [$1/K$]
Δt	Time Step [s]
Δx	Grid Spacing [m]
δ_{ij}	Kronecker Delta
ε	Turbulence Dissipation Rate [$J/(kg \cdot s)$]
λ	Second Coefficient of Viscosity [$N \cdot s/m^2$]
μ	Dynamic Viscosity [$Pa \cdot s$]

ν	Kinematic Viscosity [m^2/s]
ω	Specific Turbulent Dissipation Rate [s^{-1}]
Φ	Dissipation Function
φ	Velocity Potential [m^2/s]
ρ	Density [kg/m^3]
σ	Surface Tension [N/m]
τ	Stress Tensor [N/m^2]
θ	Droplet Impact Angle [$^\circ$]

Glossary

BC	Boundary Condition
CDF	Cumulative Distribution Function
CFD	Computational Fluid Dynamics
CSF	Continuum Surface Model
CV	Control Volume
DDT	Deflagration to Detonation
DNS	Direct Numerical Simulation
FD	Finite Difference
FE	Finite Element
FLNG	Floating Liquefied Natural Gas
FV	Finite Volume
HSE	Health and Safety Executive
HSL	Health and Safety Laboratory
LE	Lagrangian Eulerian
LEL	Lower Explosive Limit
LES	Large Eddy Simulation
LFL	Lower Flammability Limit
LNG	Liquefied Natural Gas
LS	Level Set
PDE	Partial Differential Equation
PDF	Probability Density Function
PISO	Pressure Implicit with Splitting of Operator
RANS	Reynolds-averaged Navier-Stokes
SIMPLE	Semi Implicit Method for Pressure Linked Equations
TLS	Turbulent Length Scale
UEL	Upper Explosive Limit
UFL	Upper Flammability Limit
VOF	Volume of Fluid

Abstract

The aim of the current work is to reproduce spills of fuel from storage tanks in order to better understand and replicate the effects of this phenomenon which can cause several damages. The vapour production that occurs when there is a failure in a storage tank could cause an explosion if there is any source of heat such as an electrical power failure.

The vast increase in computational resources that we experienced in the last years has given the Computational Fluid Dynamics (CFD) community growing resources to simulate difficult flow problems that were impossible to solve 20 years ago.

In order to solve the multiphase flow which represents the spilling of fuel from a storage tank a Lagrangian-Eulerian approach is adopted, as with most of the work done in the literature. The importance of splashing of droplets on flat surfaces has also led to the development of an adapted splashing model based on existing correlations. This was done by the use of a volume-of-fluid (VOF) methodology to characterise splashing.

Comparison of experimental results with the ones obtained by numerical simulation show good agreement (less than 10% error) and confirm that CFD could be an advantageous tool in the prediction of this type of flow.

Moreover, the computational simulations give an overview of what is happening and more specifically physical quantities in each point of the computational domain, while the experimental facilities are restricted to some points and the presence of some tools invade the flow.

The main findings of this work are related to the splashing of liquid droplets into solid surfaces and the differences between cascades of hydrocarbons that have a boiling point above normal ambient temperatures and liquids such as Liquefied Natural Gas (LNG) that are boiling when they come in contact with the atmosphere. The splashing of liquid droplets in the current application was found to be significantly different respect to most of the work discussed in the

literature. Because of the large size of the droplets simulated, the parameters of interest such as splashing threshold, angle and mass splash ratio were found to be out of the previous ranges predicted by other authors. These parameters were then put back into the splashing model which showed improved results, giving a higher accuracy regarding vapour produced.

Liquid cascades of Liquefied Natural Gas were found to be significantly different than gasoline ones, with most of the liquid being vapourised before hitting the ground. This is due mostly to the boiling of the liquid and also on the different layout of the storage tanks, these being much larger in an LNG plant than in a typical fuel plant.

The models formulated in the current application can be used for the prediction of the flammable cloud in a spill scenario in a plant, where the vapour can reach high concentration and the risk of an explosion is not remote. The physical models mentioned above were implemented within the framework of the open-source tool OpenFOAM by modifying and/or adding new models in the code.

Chapter 1

Introduction

1.1 Background and Motivation

Cascades of liquid flow can be observed every day, such as the flow coming out from the tap of a kitchen sink, waterfalls, the rain and plenty of other phenomena. The multiphase nature of these flows makes it hard for numerical modellers to reproduce accurately the physics of such phenomenon and this is a challenge for the Computational Fluid Dynamics (CFD) community.

Multiphase flows are complex to model and there are different approaches based on the characteristics of the problem, where priority is given to one aspect or another.

In the primary framework of liquid cascades, the ones resulting from Liquefied Natural Gas (LNG) or fuel tanks overflowing or rupture of elevated pipes create a source of flammable vapour cloud, although other processes can lead to a similar vapour formation such as aircraft impacts [1]. There is a lack of adequate models treating the underlying physics of this phenomenon and the SafeLNG project ¹ aims to bridge this knowledge gap. It involved developing robust and accurate models for the instabilities and aerodynamic breakup in the cascade which contributes to the formation of the cloud, air entrainment and liquid impingement on deflector plates. The predictions of the developed models were validated with some proprietary liquid fuel cascade experimental data.

One of the examples of the catastrophic consequences that a tank spill can produce is the well-known Buncefield fire [2], a conflagration that occurred on

¹SafeLNG is an Innovative Doctoral Programme (IDP) funded by the Marie Curie Action of the 7th Framework Programme of the European Union on the Numerical characterization and simulation of the complex physics underpinning the Safe Handling of Liquefied Natural Gas

the 11th of October 2005 at the Hertfordshire Oil Storage Terminal which caused important damages but fortunately no fatalities. The explosion (the black cloud shown in Figure 1.1 was visible from the satellite) was caused by a tank that over-filled, which created a significant flammable cloud eventually ignited by an electrical power failure. This catastrophic event caused substantial economic losses and also increased awareness of the safety of fuel plants and the consequences of a safety failure, especially in the UK.

Image removed
for copyright
reasons

Figure 1.1: Buncefield Cloud [3]

Another example of the catastrophic consequences of an explosion is the fire that occurred the 23rd of October 2009 at the Caribbean Petroleum Corporation oil refinery and oil depot in Bayamón, Puerto Rico (this event is best known as Cataño oil refinery fire [4]). The fire lasted for two days and was extinguished the 25th of October. Fortunately, no fatalities occurred, but three people were injured. The size of the fire was enormous and 11 tanks containing gasoline, jet fuel and diesel were completely destroyed.

Because of the complex physics involved in such scenario, the CFD model has to address a large number of problems, including the multiphase nature of the flow, turbulence, splashing of droplets on the ground and on other surfaces, and obviously all of these need to be coupled in one solution, which is challenging from the modeller point of view.

1.2 Aim of the current work

The aim of the current work is the development of a tool able to reproduce spills of fuel from storage tanks. The complex physics involved means that the computational model will need to address a number of problems and accurately describe the multiphase nature of the flow, turbulence, and the interaction between the liquid and solid surfaces. The models available in the literature are limited to different types of applications and limited work to this specific problem can be found. The main goals of this work are to develop an accurate model to simulate fuel and LNG cascades as well as the development of a tailored model for liquid droplets wall interaction.

1.3 Liquefied Natural Gas

LNG is natural gas that has been converted into liquid form for ease of transport and storage. It is primarily made of methane (CH_4), which contributes to more than 90% of its composition, and its boiling point is -162°C . Before it is liquefied, LNG is purified in order to remove the higher-boiling hydrocarbons and the impurities, and in this way the percentage of methane becomes around 95% or more. LNG is clear, colourless and essentially odourless and it is neither corrosive nor toxic. The main advantage of this product is that it occupies a very small fraction of the volume occupied at its gaseous state and it is therefore more economical to transport across large distances, and makes it storable in large quantities. In the liquid state LNG is neither flammable nor explosive, but if it vaporises and mixes with air in the proper proportions (the flammable range for methane which is the main component of LNG is about 5 - 15% [5]) and is then ignited, it burns.

The interest in LNG safety is growing, because even though it has quite a good record in terms of safety [6], accidents still occur and they can be catastrophic. Moreover, the usage of LNG is increasing by approximately 5% every year [7]. This means that from the 2016 demand of 258 million tonnes per annum [8] it could go as high as 430 million tonnes per annum in 2025. In 1964, when the LNG was traded for the first year, only 80,000 tonnes of LNG were shipped. This is mainly because global economies are choosing LNG over other resources because it is a relatively cleaner and flexible source of power generation. For example China LNG consumption has increased dramatically recently. On the other hand, economies that have been using LNG for a large period, such as

Japan and North Korea, are quite stationary as other resources find their slice in the energy market.

Image removed
for copyright
reasons

Figure 1.2: An LNG terminal facility (source: www.thenews.com.pk)

1.3.1 Floating Liquefied Natural Gas

A large number of natural gas resources are located offshore, and therefore the extraction of resources is challenging and problematic with the current technology. For this reason, starting from the 90s, some oil companies began developing facilities that could extract natural gas offshore and convert it to its liquid form to then ship it to the mainland. These take the name of Floating Liquefied Natural Gas (FLNG), and they produce, liquefy and store natural gas at sea. Although there is no FLNG ship in production, a large number of oil companies are developing FLNG facilities to face the increase in LNG demand using offshore resources.

Although it may seem an easy process, the construction of FLNG facilities is challenging and uses extremely advanced technology. The two significant challenges are the considerable size of the facility (Shell has produced Prelude FLNG, which is 488m long [9]), and the fact that all the elements present in a conventional LNG facility must be present in a moving object, on a much more confined space. This is obviously a major problem regarding safety, as the FLNG needs to comply with the same safety level of a land facility. Another major problem

is the movement of the sea, which can damage the storage tanks due to sloshing.

At the same time, the construction of FLNG facilities has a good impact on the environment and economy. First, it has a much smaller footprint if compared to a conventional land-based plant, and also it eliminates the need for long pipelines on land.

1.3.2 Hazards and Risks

As most hydrocarbons, there are some hazards related to LNG, the main ones being:

- **Rapid Phase Transition:** when LNG comes in contact with water, it could vaporize violently, due to the heat absorbed from the water, causing what is known as a physical explosion, or cold explosion. Because of the small fraction occupied by LNG, the expansion is very fast and strong, and can cause damages to the equipment.
- **Asphyxiation:** when the LNG vaporise, it starts occupying a fraction of the air. Due to this behaviour, the concentration of oxygen in the air starts decreasing. If the concentration in the air is less than 6 volume %, a human can die due to asphyxiation (this corresponds to a concentration of gas about 71 volume %). The normal concentration of oxygen in the air is about 21 volume %. If the concentration is reduced to less than 15 volume % the breathing is impaired and vomiting occurs when it is less than 10 % (corresponding to values of 28 and 52 volume % of LNG in the air).
- **Roll over in storage tanks:** The hydrostatic pressure of LNG exerts a force in a tank, so the LNG at the bottom of the tank is at a pressure and equilibrium temperature higher than the one on the top, and due to the buoyancy effects it can rise to the top of the tank. What happens is that a small fraction of LNG would rapidly vaporize, and since the LNG vapour liquid ratio is about 600:1, a huge volume of gas would be formed and could lead to a failure of the roof or wall of the tank.
- **Pool and Jet fires:** If a leak occurs in a pipe or storage tank, the liquid formed on the ground surface or the high pressurised spray could be at risk of ignition and if a fire does occur, the consequences can be catastrophic and hard to control. In the case of liquid formed onto the ground surface the

phenomenon takes the name of pool fire, while if the source of combustion is a high pressurised jet this is called jet fire.

- Explosion: if a vapour cloud is formed as a consequence of a spill and is ignited, this could be a risk of explosion if there is a dense presence of obstacles (such as trees or close buildings). Again the consequences of such phenomenon are severe and practically impossible to control.

1.3.3 Transportation

The process that brings natural gas from the extract point to the user depends on the specific geographic location, but it usually takes on average around 12 days. The main steps involved in the process are the following:

- The gas is extracted from the reserve
- The gas is cleaned from impurities and water while being carried through pipes and vessels
- The gas is liquefied being cooled to -162°C and its volume is reduced by 600 times, turning to LNG
- LNG is stored in tanks
- LNG is pumped into vessel tanks to be carried overseas by carriers
- LNG is pumped into onshore storage tanks close to its final destination
- LNG is warmed back and returns to the gaseous state
- Natural gas is distributed to the user via pipeline

During the processes involved in the handling of natural gas, a number of possible scenarios can occur that can lead to catastrophic consequences. Therefore safety measures have to be implemented in order to avoid any damage to the facility or worse human casualties.

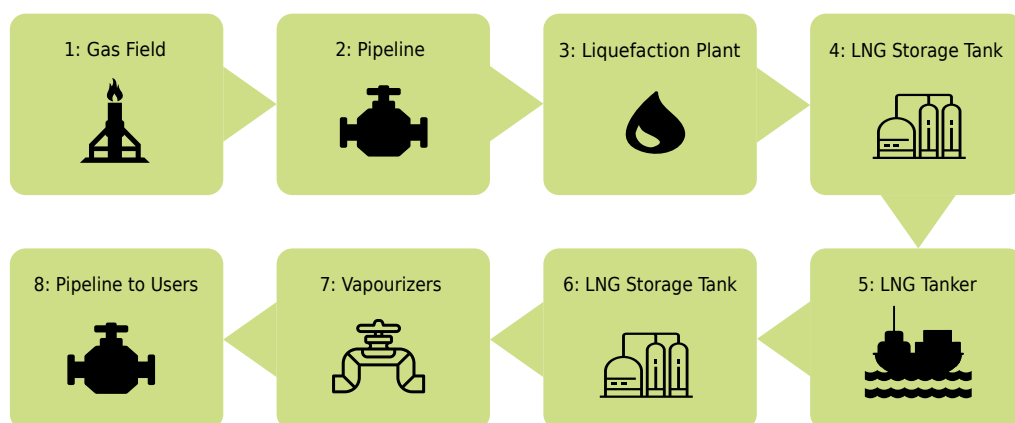


Figure 1.3: LNG Transportation Process

1.4 Research Topics of the SafeLNG Project

The current work was sponsored by the European Commission under a project called SafeLNG, which aims to develop strong computational models that can predict the consequences of a risk scenario. The project is an innovative doctoral programme funded by the Marie Curie Action. The research topics are 6 and are related to the following:

- To gain insight of the complex physics in LNG/fuel cascades and flammable cloud formation, and develop predictive tools;
- To characterize different LNG release scenarios and develop robust source term models;
- To develop a robust model for accurate prediction of rollover;
- To develop and validate Large Eddy Simulation (LES) based predictive tools for LNG flashing jet;
- To develop and validate LES based predictive tools for large LNG pool fires;
- To validate and improve models for explosions in non-uniform LNG vapour mixtures.

In order to better understand the possible hazards that can arise during the handling of Natural Gas from the extract point to the user, all the topics are discussed more in details.

1.4.1 LNG/Fuel Cascades and Flammable Cloud Formation

This is the scenario analysed in the current work, and will be discussed much more in details in the following chapters. To give an overview of the process, in storage tanks there is a possibility that some sensors fail or break, in this case there is an overfilling of the tank which leads to a liquid cascade on the side of the tank and consequently vapour formation of a flammable cloud. This is precisely what happened in Buncefield and the consequences were catastrophic. For this reason, some industrial plants have bounds surrounding storage tanks to avoid that the cloud formed by evaporating liquid spreads around.

1.4.2 LNG Spill and Dispersion in the atmosphere

The failure of an LNG ship could result in a massive release of LNG and pool formation onto water surfaces, and consequently dispersion of Natural Gas into the atmosphere because of a high rate of vaporisation of LNG due to its cryogenic nature. Modelling of such scenario is essential and a large number of authors have investigated dispersion of natural gas in the atmosphere, using both commercial and open source software.

1.4.3 LNG Rollover

Rollover is a process during which a rapid release of vapour in a storage tank takes place due to stratification of LNG. It is one of the most delicate topics because of a number of accidents recorded in the LNG industry (the most catastrophic one occurred in La Spezia, Italy, in 1971). The main reason why rollover happens is the presence of two layers of different density present in a tank [10]. This could be caused by different things such as temperature difference inside the tank, and when a difference in density occurs, such as the liquid at the top of the tank becoming heavier than the one at the bottom, rollover takes place. The main consequences of this are the increase in boil off rate by an order of magnitude, the growth of over pressurisation of the tank and the lift of the relief valve in the tank. There are some measures present in industrial plant and transport ships to avoid rollover, and CFD can be used to understand the risks and improve the safety of LNG plants.

1.4.4 LNG Flashing Jets

Pipes that carry LNG have a very high pressure, and therefore in the case of a spill there would be a flashing jet which vaporises very rapidly, highly difficult to model computationally.

The fast dynamics of the problem makes it difficult to model because cavitation can occur within the spill and consequent rapid atomization of the liquid [11, 12, 13], which complicates the modelling even furthermore. Such problems are usually approached using hybrid combinations of computational models, to model appropriately both regions of the domain (the zone where cavitation occurs and the zone after the high atomization of the liquid).

1.4.5 LNG Pool Fires

If there is a pool of flammable gas, being fuel or LNG, and a source of heat in the nearby region, this liquid region can start burning, and these fires are usually extraordinarily violent and difficult to control [14]. The modelling of such fires is delicate and the need to use an appropriate turbulent model is fundamental as well as modelling the radiation model, since the soot formed by such fires is at the same temperature as the gas, strongly emitting thermal radiation which can damage the surrounding structures and be lethal to the human.

1.4.6 DDT in non-uniform LNG vapour mixtures

Fires in industrial plants can occur and are usually controlled by the action of trained personnel, but the presence of artificial or natural obstacles can accelerate the burning speed of a flame leading to a point where its speed exceeds a certain value and the flow becomes supersonic (one of the physical processes that could occur is called Deflagration to Detonation (DDT) transition), leading to a huge pressure jump and destroying the plant facilities (clearly evident in the Buncefield accident), not mentioning casualties if anyone is present on site. The modelling of such phenomenon is delicate and the mesh size in order to capture the microscopic scales of the process has to be enormous (the cell length has to be in the order of microns). The time step is also extremely small because of the combustion process which is taking place, leading to simulation times which sometimes exceed months. Being the flow usually fully turbulent, there is a need to model turbulence. LES simulations are usually used, because RANS cannot

give a detailed map of the pressure in each point of the domain, fundamental when designing containment surfaces. A large number of authors in the literature use a 2D approach to model DDT, mostly because a 3D approach is computationally very expensive.

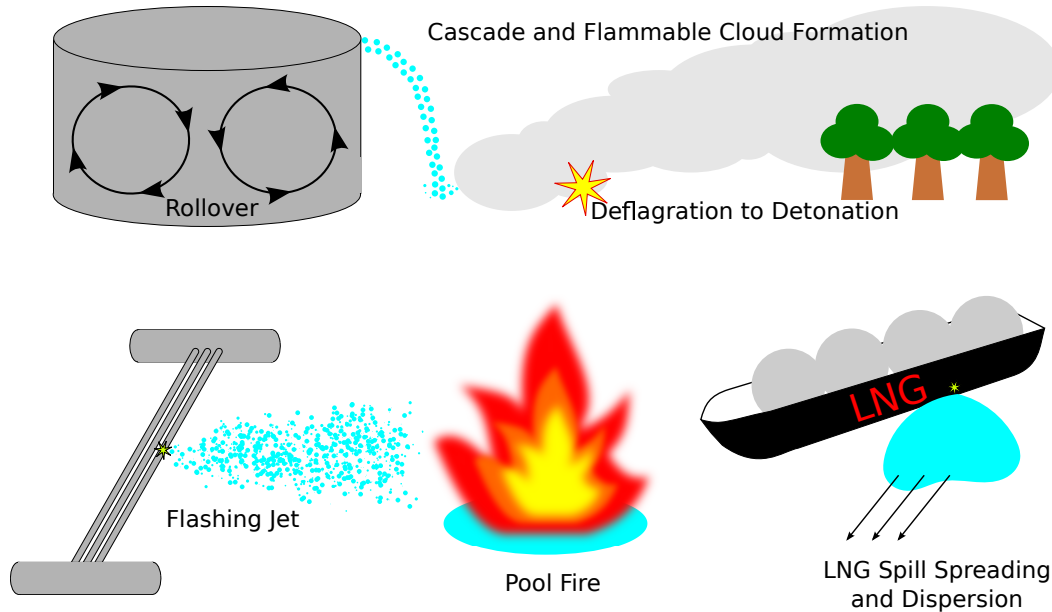


Figure 1.4: All the scenario addressed in the SafeLNG project

This study focuses on liquid cascades (pictured in Figure 1.4) of flammable liquid such as gasoline or LNG. The main risk of a liquid cascade of a hydrocarbon is that there is a high evaporation rate due to the presence of a large number of droplets which will eventually form a flammable cloud that if ignited can lead to catastrophic consequences.

1.5 Physics of the process

The physics of liquid sprays is highly complicated and their modelling is challenging from both an experimental and computational point of view.

Figure 1.5 shows a generic spray. The initial liquid discharged through an orifice starts deforming due to external pressure and hydrodynamic instabilities, and ligaments will detach from the bulk of the liquid. These ligaments are unstable and will later form droplets of quite a large diameter. This initial process is called primary breakup, or also atomization, and it is difficult to model because the timescales related to the process are small and the mechanism depends widely

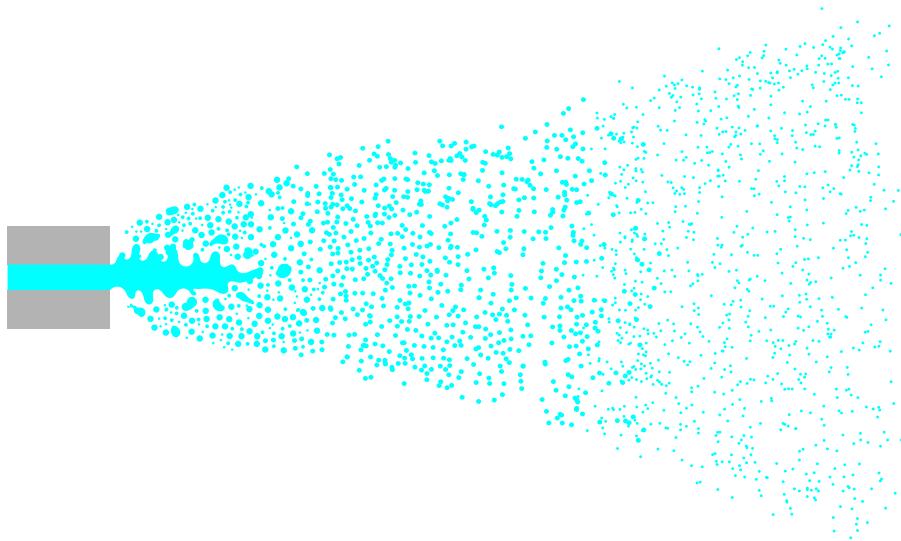


Figure 1.5: Schematic picture of a jet spray

on the orifice size, pressure at which the liquid is discharged and material used.

Once the droplets have become spherical, the forces acting around them due aerodynamics cause the droplets to deform, and if the shape they assume during the deformation is unstable, breakup will take place, shattering the bigger droplets in smaller ones [15]. This process is defined as secondary breakup and several models exist in the literature to account for it [16]. Depending on the Weber number ($We = \rho u^2 d / \sigma$, where d is the droplet diameter, ρ is the fluid density, u is the droplet velocity and σ its surface tension) of the droplet, a different kind of breakup will take place.

Another force acting on liquids in contact with gases is the capillary pressure. This is defined as the pressure difference across the interface between two immiscible fluids. This is a result of forces such as surface tension and interfacial tension acting on the fluids. In a wide range of applications the capillary pressure is of high importance, but in the current work it will be neglected mainly because the liquid phase, made primarily by droplets, is at a pressure equal or similar to the one of the surrounding air, therefore the capillary pressure can be neglected.

The importance of gravity acting on the droplets is best represented by the Morton and Eotvos numbers. These numbers are usually very important in the simulation of rising bubbles in liquids and their shape, but in the current application they will not be considered, mainly because the problems examined are driven by inertia and surface tension.

In order to model a spray completely, two main approaches are ideally used,

depending on the region modelled. In the area close to the nozzle, where the bulk of the liquid is present, a Eulerian formulation is advantageous, in order to model properly all the hydrodynamic instabilities due to surface tension and inertia. In the region far from the nozzle, where the droplets have ideally broken up to a stable condition and spherical shape, a Lagrangian approach is more suitable and computationally achievable. Due to growing computational resources, in the past years some researchers [17, 18] have developed hybrid solvers capable to handle both Eulerian and Lagrangian formulations in the same application, where the Eulerian model is used in the close region to the nozzle, while when the droplets have reached a diameter small enough for the cell size the solver switches to a Lagrangian formulation.

In industrial applications, spray can occur widely and their structure and droplet diameter distribution varies case-by-case. For example, in the beauty industry, the nozzle is built in such a way to have the finest droplet distribution possible, so to maximise the vapourisation. This is achieved by controlling the primary atomization using a specific pressure and nozzle diameter. In the current work, atomization and droplet breakup is not attained by the willing of the user, but the liquid release through some kind of orifice in a storage tank is such that the atomization process takes place and the bulk of liquid forms a large number of droplets in the very early stage of the cascade. This is also eased by the fact that hydrocarbons have a low surface tension if compared to water and other liquids, therefore it is easier for the ligaments to break up. Due to the large size of the domain to be analysed, it would be too costly in terms of computational resources to use a Eulerian approach to model the cascade, even only in the spill region in order to model the primary atomization. For this reason, and also using the results available in the literature, a known profile for the droplets diameter is used and a fully Lagrangian approach will be used in the following chapters.

It is worth mentioning that although the two phenomena have few things in common, sprays from pressure nozzles and fuel cascades have some fundamental differences. Although for both cases droplets are formed from the breakup of liquid due to hydrodynamic instabilities, in the case of a fuel cascade droplets accelerate constantly until reaching an asymptotic velocity or hitting the ground. The size of the droplets and the spill size is also such that liquid formed onto the ground or any solid surface evaporates slowly therefore creating a large pool where droplets interact with a relatively thick liquid region if compared to more conventional sprays where the liquid region is very limited and evaporates much

faster. This means that the interaction between liquid particles and walls can lead to different outcomes in the two applications, and that models cannot be exported from one to another easily.

Specific limits



Figure 1.6: Definition of flammability limits

In the presence of a flammable substance such as methane, there are some important numbers that define the limits for which the mixture of air can be ignited or not. These numbers are the Lower Flammability Limit (LFL), Upper Flammability Limit (UFL), Lower Explosive Limit (LEL) and Upper Explosive Limit (UEL) (Figure 1.6 illustrates the concept of flammability limits).

The definition of such numbers is that a flammable mixture will ignite only if the concentration of the substance is between the LFL and UFL for the given temperature and pressure, which means that if the concentration is lower than the LFL or higher than the UFL the mixture cannot ignite. These values are in most cases equivalent to the LEL and UEL and the terms are most of the time used interchangeably.

These values are usually defined in terms of volume percentage and usually the LFL is the most important one since it is improbable for a mixture to reach the UFL, especially in an open domain such as an LNG/fuel plant where there is enough air change to dilute the mixture. The flammable limits for the most important hydrocarbons and hazardous substances are shown in Table 1.1.

Table 1.1: Flammable limits for different substances

Substance	LFL	UFL
Methane	4.4	16.4
Benzene	1.35	6.65
n-Butane	1.86	8.41
Decane	0.8	5.4
Diesel Fuel	1.35	6.65
Ethane	3	12.4
Gasoline	1.4	7.6
Hexane	1.1	7.5
Hydrogen	4	75

1.6 Chapter summary

The information given in this chapter regarding liquid spills from storage tanks have demonstrated that although the likelihood of such an event is profoundly low, the consequences could be catastrophic by considering previous accidents that happened in the past 20 years. The physics of such process is such that computational models are complicated to derive. There is also a lack of models available to reproduce the effects of splashing in fuel liquid cascades, mainly because the main formulations were adopted in a scenario where droplet sizes and velocities are smaller than the ones experienced in a tank spill. Liquid spills of Liquefied Natural Gas also lack of models, primarily because of the excellent safety record of such industry. The present work will be focused on these two aspects of the problem, deriving appropriate physical models and highlighting the findings and the differences with what is present in the literature.

Chapter 2

Literature Review

2.1 Previous work on fuel cascades

Although a large number of researchers have worked in the study of sprays [19, 20, 21, 22], there is not much work done concerning the modelling of fuel cascades and almost no data are available for LNG. This is because the physics of such phenomena is complex and the LNG industry has a quite good safety record [23], being the reason for such poor research. Nonetheless, the possibility of an accident in an LNG facility is real, and the consequences could be catastrophic. Therefore the safety can be improved understanding the factors that affect vapour production in the case of a spill. Research has been carried out using integral models [24], but their applicability is limited and local quantities cannot be easily estimated.

Prior to the Buncefield accident, there had not been any serious study related to the safety of fuel tanks, and the understanding of how flammable vapour clouds could be formed was very limited. It was common opinion that a spill from a fuel storage tank would lead to the formation of a liquid pool that would evaporate very slowly [25], therefore not likely to form any sort of fire. The night of the accident, the release of fuel from the opening vents of the roof of the storage tank led to a cascade of gasoline droplets which produced a flammable cloud at a very high rate (Figure 2.1 shows two frames of the site at the beginning of the discharge and after 11 minutes and 40 seconds, the cloud is clear). HSL reported [25] that it took 25 minutes for the vapour to fill an area of 500m by 400m from 2m to 4m high. As reported from sensors around the plant, wind intensity was very low, therefore the cloud spread mainly because of the slope of the ground. The

explosion that took place was strong and fortunately there was not any casualty, but the damage on the plant accounted for around \$1.5 billion [25].

Image removed for copyright reasons

Figure 2.1: Video frames of the site showing the cloud formation [3]

Other incidents followed Buncefield around the world, the main ones taking place in Jaipur (India) [26], San Juan (Puerto Rico) [27] and the Amuay Refinery (Venezuela) [28].

It was therefore clear after the Buncefield accident that tank spills can indeed produce a significant amount of vapour, no matter what the evaporation rate of the pool is, and Computational Fluid Dynamics can surely be a strong item for this purpose.

Following Buncefield accidents, Health and Safety Executive (a public body of the United Kingdom) was appointed to investigate and understand what caused the massive explosion. One of the main issues related to this is also how the industry reacts and what kind of new rules and regulations have to be issued in order to raise the safety of industrial plants. The sponsored programme investigated the formation of flammable clouds due to tank spills using both experiments and computational models. Even though these reports do not take into consideration for LNG tank spills, they are essential for the validation of the tool that would eventually be used to analyse a risk scenario in an LNG plant, due to the lack of work done regarding LNG spills.

The technical problem investigated by HSL [29] was divided into several stages that required different types of analysis:

1. Initial liquid discharge
2. Liquid fragmentation
3. Developed cascade flow

4. Impact zone
5. Splash evaporation and/or fall out zone
6. Near field dispersion
7. Bund interactions
8. Long range dispersion

The attention in the current work will be focused in the first five stages (a diagram showing them is depicted in Figure 2.2), as the last three are out of the scope of the present research.

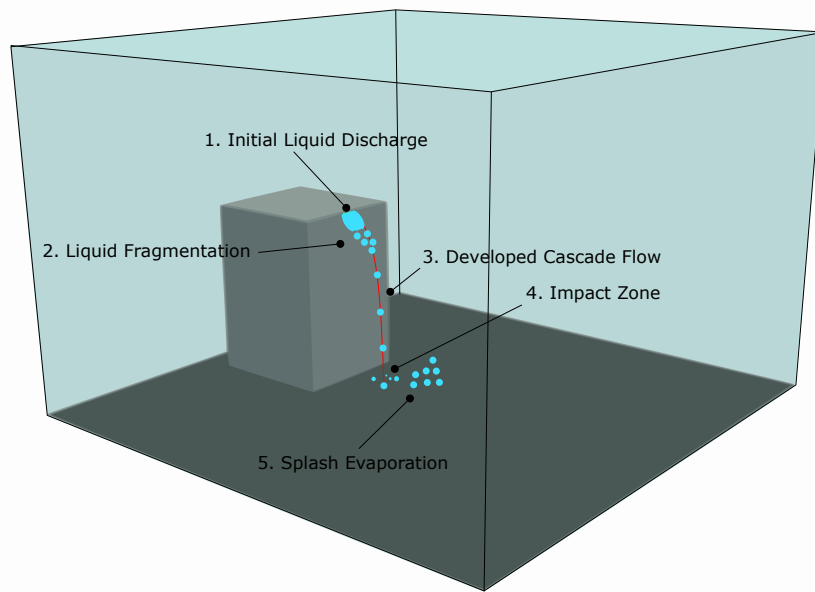


Figure 2.2: 5 stages modelled

The initial liquid discharge depends on the design of the tank, the layout of the top of it, and how much is the mass flow rate. However, most industrial tanks present a similar layout, therefore the liquid will overtop the deflection plate and fall as a free cascade, while the rest of the flow, if there is any, will fall down on the tank walls and may eventually hit a wind girder, a part of the tank designed to make the structure stronger and able to stand strong wind currents. After the liquid starts flowing from the top of the tank, liquid fragmentation will take place, due to the Plateau-Rayleigh instability, leading to the formation of a considerable amount of droplets. Photographs and high-speed videos of hexane and decane cascades under a range of conditions have shown that the bulk of mass is concentrated in droplets with diameters of around 2mm [30] but there is also a range of smaller size droplets. Droplets of a few hundred microns tend to

vaporise completely. The developed cascade flow will be the one modelled by the Lagrangian solver, and once the cascade comes in contact with the ground there will be an impact zone, which is probably the most challenging region in terms of CFD modelling, because of the lack of models available for such a big scale problem. The last stage of the problem is to model the splash evaporation and fall out zone.

As discussed already, the last three stages of the analysis are not part of the scope of this research, but the results obtained from the first stages such as the velocity field and composition of the vapour flow driven by the falling liquid spray can be used in a later stage as an input for large-scale dispersion modelling.

2.1.1 Tank design and effect on liquid discharge

In order to correctly simulate the liquid discharge of fuel from a storage tank, a study on the tank design and possible pattern of liquid cascade has to be undertaken. Although most storage tanks share a number of characteristics, the structure at the top can change depending on the country, supplier and human choice.

If we consider only how the liquid is discharged, we can differentiate the tanks only on their external structure, neglecting the internal design. In the UK there are three main classes of tanks used to store hydrocarbons [31]:

- Fixed roof tanks with vents (FRV)
- Fixed roof tanks with pressure/vacuum valves (FRPVV)
- Floating deck tanks with no fixed roof (FD)

In the first type of tanks (FRV), the liquid will hit the deflector plate and run down the tank walls, but if the flow is sufficiently high part of the liquid flow will overtop the deflector plate forming a liquid cascade, which is what happened in Buncefield.

The dynamics of a liquid discharge in the second type of tanks (FRPVV) is such that a crack will form on the pressure valves because it is not designed to contain a high liquid discharge. The overtopping flow in this type of tank is likely to be well structured with high density.

The last type of tank (FD) will be likely releasing the liquid in the whole perimeter hitting the wind girder and falling free down to the ground. Figure 2.3 shows the types of tank and their possible release scenario.

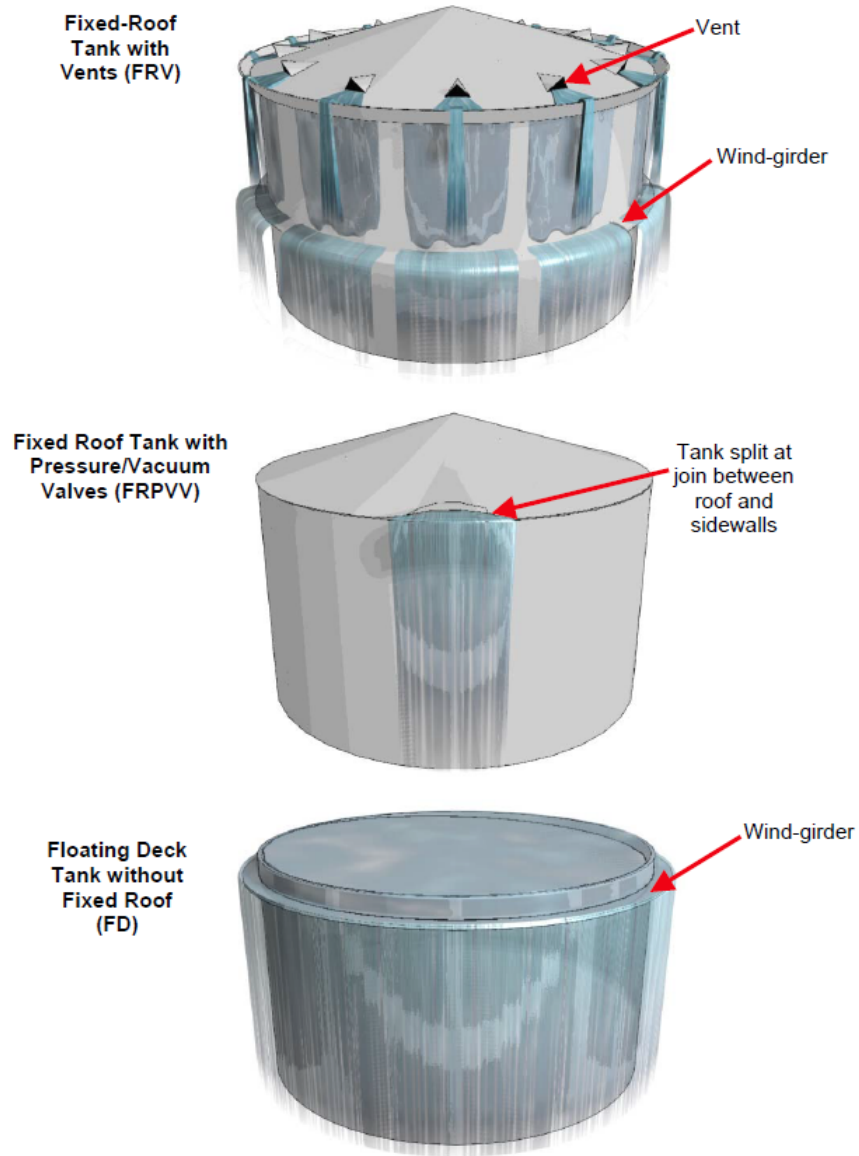


Figure 2.3: Types of tank and release scenarios [31]

In the present work (and in the research conducted by HSE), the second type of tank will be investigated, because of the availability of experimental results, but the models developed can be applicable to all the three types of tank.

2.1.2 Investigation of tank section

In the first stages of the research carried out by HSE, the dynamics of the fall of liquid from a tank was investigated from an experimental point of view [30]. Even though the set up represented only a small section of a tank, the findings are

useful for future use and give a better understanding of the dynamics of cascades.

Image removed
for copyright
reasons

Figure 2.4: Model 1 (left) and Model 2 (right) [30]

Figure 2.4 shows the two sections of a full tank that have been modelled. The main findings from the investigation are:

- The width of the flow overtopping the deflector plate increases with the increase of the flow rate
- Depending on the volume of liquid released the amount of overtopping flow changes together with the flow that runs onto the tank walls
- The main effect of the wind girder was to deflect the wall flow and also dispersing the overtopping flow
- Experiments with water showed that the droplet size of the cascade is variable, but usually greater than 5 mm above the wind-girder, while their size is reduced to few millimetres below it
- Petrol sprays tend to have a droplet spectrum much smaller than the one achieved with water. This is due to the difference in surface tension and dynamic viscosity (smaller in petrol)
- Surprisingly, the rate of vapour production is insensitive to the droplet size

- Results obtained from preliminary CFD simulations show that the value of hydrocarbon vapour concentration achieved in the bulk of the cascade is around 70%

2.1.3 Effect of liquid properties on the spray structure

The liquids that pose a threat to the safety of an LNG/fuel plant are mostly hydrocarbons, which have a well-defined set of physical properties if compared to a more familiar liquid such as water. In the event of a spill, the structure formed by the liquid highly depends on such properties, and different liquids can show different behaviour, therefore it is fundamental to understand the different dynamics. The parameter that controls the breakup of a droplet that is moving through air with a certain velocity is the Weber number, defined as the ratio between inertial and surface tension forces. It is clear that different liquid can give a wide range of Weber numbers if there is a substantial difference in terms of surface tension. HSE [30] has run some experiments comparing the cascade structure for water and petrol. The different droplet distribution is shown in Figure 2.5.

The main observations that can be made are that the spray produced by water releases is usually composed by larger droplets and more variable in diameter, while on the other hand sprays produced by petrol (and hydrocarbons in general) are more uniform in terms of droplets distribution and the droplet diameter is significantly smaller. They also reported that the sound made by the petrol cascade was softer than the one produced by water.

The fact that different liquids show different spray structures can also be understood by analysing the empirical formula of Brodkey [32].

2.1.4 Effect of obstacles in the vapour accumulation

An essential aspect in the formation of a flammable cloud in a fuel or LNG plant is the presence of obstacles surrounding the liquid spill, which can be neighbour tank, pipes or most importantly bund walls. Bund walls are solid surfaces built around a tank for the purpose of containing flammable liquid or gas coming out from the tank. This problem was investigated by HSL [29] by the use of CFD. In the report, the spreading of a flammable cloud around a circular tank was simulated using different bund configurations (the bund height was fixed for all

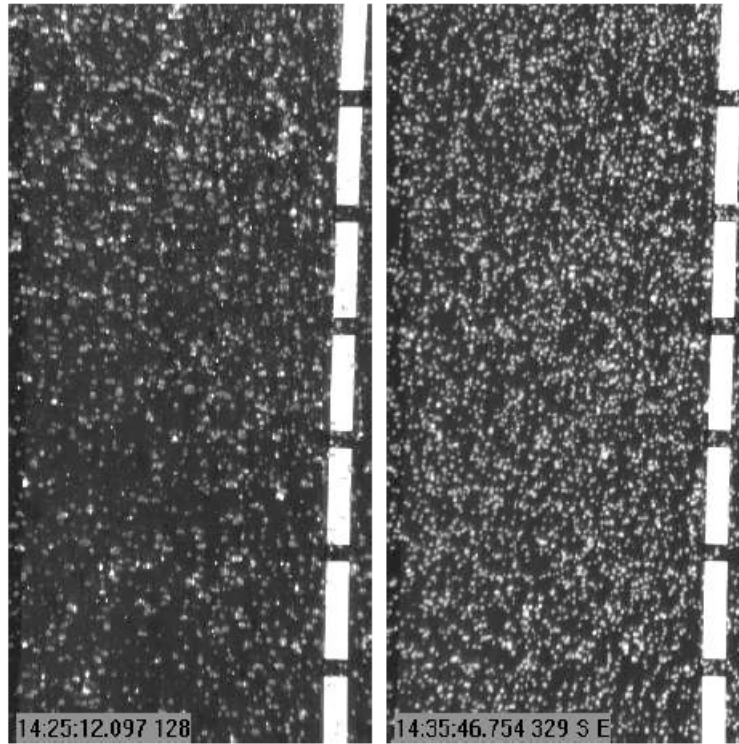


Figure 2.5: Spray structure of water (left) and petrol (right). Observations made 14m below the plane of release [30]

the simulations at 2 m), monitoring the vapour concentration within and outside the bund as well as the liquid temperature.

Results showed that in terms of liquid temperature the effect was minimal for different bund configurations, and the same can be said regarding the vapour temperature inside the cascade region.

The results for the configurations with the bund were analysed in terms of vapour concentration and temperature inside the bund region.

Figure 2.6 clearly shows that for cases E,F,G the effect of the different bund design was minimal, while case D shows that concentration was higher than all the other cases and temperature lower, mainly because the small distance of the bund respect to the tank did not allow the vapour to dilute enough.

Figure 2.7 shows the contour of vapour concentration at the LFL coloured by its height, with a maximum equivalent to the height of the bund. The increase of the bund distance results in a decrease of the cloud height outside the banded region. For case D, the cloud is highly irregular outside the bunds.

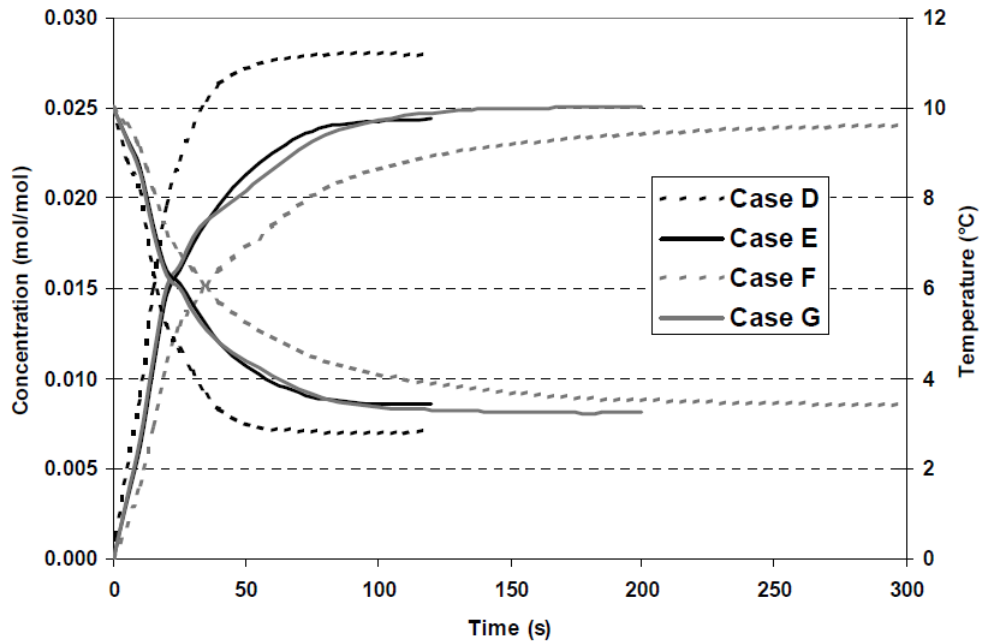


Figure 2.6: Average vapour concentration and temperature within the bund [29]

2.1.5 CFD analysis

As a part of the investigation of the Buncefield accident, HSE has also approached the problem by using CFD analysis, because even though modelling is challenging, the results obtained can give a more detailed view of the driving factors and how to improve the safety of fuel plants. A large number of simulations were run in order to first validate the model against the experiments and then to show the effect of bunds and close obstacles on the vapour dispersion [33]. The software used in their calculation was ANSYS CFX, a general purpose commercial software which had the limitation of fixed physical modelling from the ones available already in the package. As mentioned earlier, in the case of fuel cascades the large number of droplets and big size of the domain to analyse limits the use of Eulerian approaches, therefore a Lagrangian method is the most advantageous option available, and it was the one adopted by HSL. The main limitation of their work is the fact that they did not adopt a full splashing model, and used a dummy one to simulate the impact of liquid droplets onto flat surfaces. In the current work, on the other hand, a full splashing model was implemented, which includes the capability of simulating a liquid 2D region that represents the pool formed by the liquid droplets impacting onto the ground.

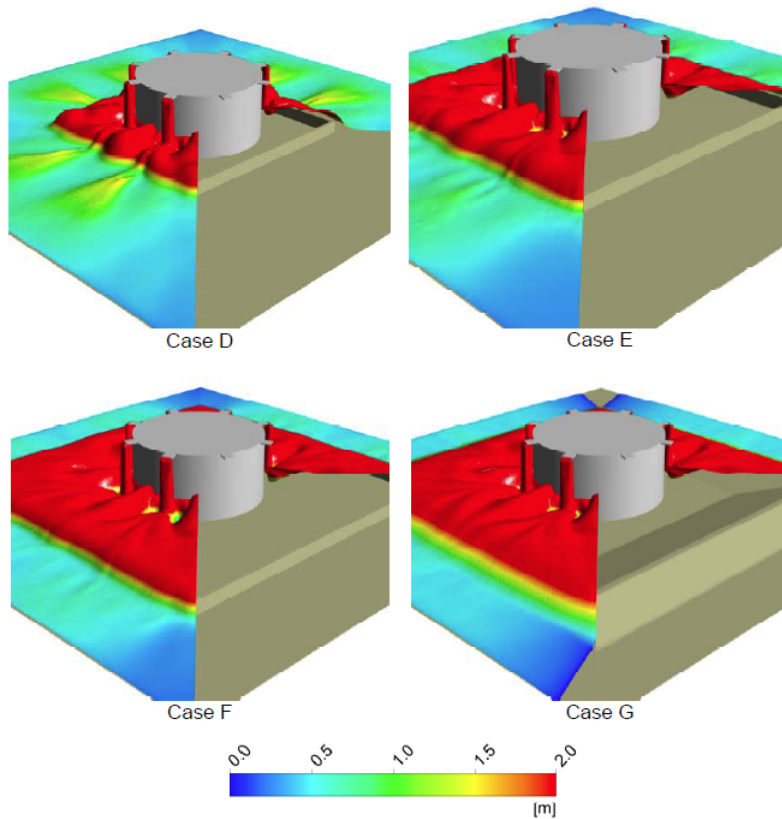


Figure 2.7: Contours of the vapour concentration at the LFL. The surfaces are coloured by their height from the ground [29]

2.1.6 Splashing of droplets

Among the findings from the CFD calculations, one of the most important is the effect of impinging droplets on the ground. The limitation of applicability of the models available in the software was the reason why they modelled the splashing region with a secondary inlet of particles representing the splashed droplets.

Several studies have been done in the past 50 years regarding droplet impact on solid surfaces [34, 35, 36, 37, 38, 39, 40] which varies from the coating industry to internal combustion engine applications. The recent development of high-speed cameras which can now shoot at millions of frames per seconds has speeded up the process and given us a more detailed analysis of the whole process. Also, in parallel, there has been a huge development in computational facilities which has allowed accurate and detailed numerical simulations as well [41].

Among all the parameters that influence the outcome of the splashing process, the condition of the impact surface is one of the most important, and the

2.2. PREVIOUS WORK ON DROPLET IMPACT ONTO SOLID SURFACES

phenomenon can assume different outcomes if the droplet hits a dry surface or a pre-formed liquid film. Even though dry impacts are significant in some applications, in most sprays after an initial transitory phase a liquid film is formed, therefore, the droplets will hit a wet surface (the difference between the two types of splashing is shown in Figure 2.8).

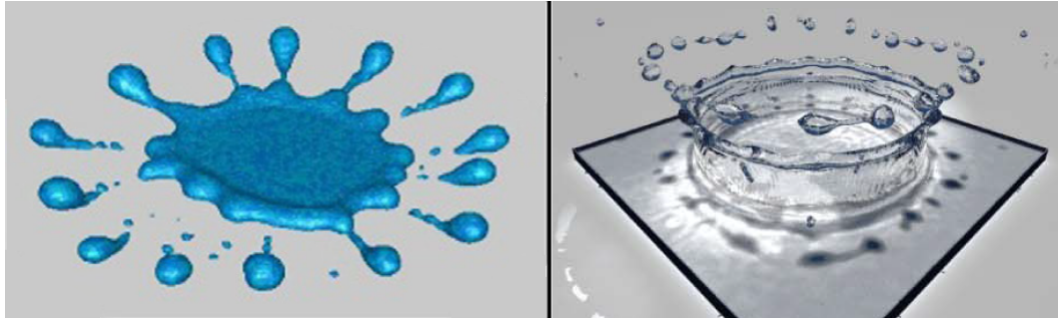


Figure 2.8: Difference between dry and wet splashing [42, 43]

The main difference observed is that for dry impact the droplet starts spreading on the solid surface, and the thickness of the lamella (this is how the shape assumed by the droplet is called) decreases up to a certain point where the surface tension is not able to keep the liquid together anymore, and consequently some satellite droplets start detaching. After the droplet has reached its maximum extension, the satellite droplets will continue to move outwards while the centre of the liquid will begin receding towards the middle. Although this is the most common splashing outcome for dry impact, other types may be observed. For example, as the impact velocity increases, a more and more violent disruption takes place and eventually no liquid is present in the centre of splashing anymore. Also, the process is profoundly influenced by the solid surface properties such as the roughness, where an increase in this value facilitates the splashing process.

2.2 Previous work on droplet impact onto solid surfaces

In the modelling of liquid cascades using a Lagrangian approach, one of the most delicate things to model is the splashing of droplets once they come in contact with solid surfaces.

2.2. PREVIOUS WORK ON DROPLET IMPACT ONTO SOLID SURFACES

Investigation of droplet impact onto solid surfaces is more than 100 years old. One of the first researchers to investigate this phenomenon was A. M. Worthington in 1876, who investigated the behaviour of droplet impact [44]. However, after his studies, authors did not find the topic attractive for research purposes until 50 years later where the phenomenon was analysed in more details. The reasons that led the researchers to investigate droplet impact were mainly two: the development of technological tools to examine the process and also the interest in a variety of applications were the topic had great importance.

In the early second half of the 20th century, the main contribution was made by the use of experimental apparatus, because the computational tools available at the time were utterly insufficient to give a detailed analysis of the process. The use of high-speed cameras was fundamental in understanding the splashing process, and quantitative analysis of the process can be found in Engel [45], Savić & Boulton [46], Levin & Hobbs [47] and Stow & Stainer [48]. The results obtained showed that a droplet impinging on a flat surface produces ligaments as described by Worthington [44]. Although the findings from such papers are interesting, Stow & Hadfield [49] were the first one to describe the structure of the substrate on which the droplet was impacting in details, with the exception of Stow & Stainer [48], which also pointed out that a high polished target reduces dramatically the possibility of a splashing event. Within their work, a significant finding was also that if the surface roughness is negligible compared to the thickness of the film liquid formed onto the surface, the critical velocity above which splashing occurs shows a precise range of definition.

If at the beginning of the splashing process the outcome of splashing seemed completely unpredictable, with the advance of technology a number of researchers started to understand that the outcome parameters were primarily driven by the input parameters, and showed a trend that fits in a number of correlations. The most famous correlations for splashing are those obtained by Bai & Gosman [50, 51], Kalantari & Tropea [52], Stanton & Rutland [53]. These correlations have been obtained considering for a single droplet impact on a flat surface because multiple droplet splashing analysis is challenging to perform as well as studying the effect of the surface geometry. It is worth mentioning, however, that a single droplet impact will behave differently than a group of droplet splashing within a very close region, mainly because the effect of neighbour splashing droplets is to affect the gas flow surrounding the droplet and because splashing crown are mostly non-symmetrical, due to previous impinging droplets, whereas in a

single droplet analysis the resulting flow will be completely symmetrical on a flat surface.

Although the splashing correlations fit well with the experimental data under specific circumstances [54], the chaotic behaviour of splashing limits the applicability of such models if the input parameters are changed to lay outside the values chosen by the authors. For this reason, the applicability of each splashing model is recommended only in a specific range of values, while outside there is no guarantee that the model will behave correctly.

2.2.1 Splashing-deposition limit

When a droplet impacts onto a solid surface, the outcomes can be several depending on the physical properties of the droplets and its velocity. The most critical transition regime is the one between deposition and splashing. A large number of correlations is available which define a critical Weber number above which splashing occurs, as a function of the Laplace or Ohnesorge number ($La = d\rho\sigma/\mu^2$, $Oh = La^{-1/2}$).

While for the dry impact the literature is consistent with the definition of the critical Weber number, in the presence of a thin liquid a number of correlations can be found [55]. For example, in the Bai and Gosman model [50], the critical condition for wet splashing is independent of the film thickness, mainly because the model was developed under the assumption that the liquid film is very thin and evaporates quickly. Cossali et al. [56], have on the other hand produced a correlation for the critical Weber number which takes into account the non-dimensional film thickness (δ), but it is only valid for values of $\delta < 1$. A correlation that considers for different regimes of the film thickness can be found in the model developed by Kalantari [57].

2.2.2 Dry and wet impact

As mentioned earlier, the properties of the surface on which the droplet impacts could change the outcome of the process entirely. The main effect of surface roughness is to trigger splashing at lower velocities. If a large number of droplets impact on a surface, it is likely that a layer of liquid will form on the surface, and this can affect the outcome of the next incoming droplets. In this case, the effect of the surface roughness is essential only when the liquid layer is 'thin'

if compared to the surface roughness. On the other hand, when the thickness increases, the effect of the solid surface properties are negligible.

The difference between dry and wet impact is not only in the structure of the surface but also in the dynamics of splashing. While on a dry surface the splashing is observed through the formation of ligaments on the droplet surface as the latter spreads onto the surface, with the presence of an existing film it is usually observed the formation of a 'crown', which expands in a radial direction until it becomes unstable, and ligaments are formed with consequent formation of satellite droplets.

Although dry impact can be observe in la large number of applications, this is usually limited in time because eventually a thin liquid film will be formed [58, 59, 60, 61, 62]. Some authors have also investigated the effect of a deep liquid pool, in which bouncing can be experienced [63].

Cossali et al. [64], carried out a series of experiments in which single water droplets impacted onto a pre-existing film. Among their findings, they showed that the crown evolution follows a law which is independent of the droplet velocity and film thickness while being affected by the Weber number. Also, in terms of secondary droplets formed, it was demonstrated that for high impact velocity the secondary droplets size increases with time, while for smaller velocities the droplet size is almost constant with time. On the other hand, the film thickness showed no significant effect in defining the secondary droplet diameter.

2.2.3 Temperature of the wall

While most of the experiments regarding droplet impact were carried out under an isothermal condition, the growing interest in boiling liquids has drawn the attention on droplet impact for hot surfaces [39, 65, 37, 66].

The effect of high temperature on the wall is well documented in Fujimoto et al. [67], where experiments of a single droplet impinging onto a hot metal surface were analysed.

The parameter that plays a vital role in such regimes is the Leidenfrost temperature, which is the temperature above which a gas layer would be formed between a liquid droplet and a solid surface. This is of extremely importance for LNG spills not only from a splashing point of view, but also for the vapourisation rate when a spill occurs in water or solid ground, because the low temperature of LNG in contact with a relatively 'hot' surface creates a layer of gas which lowers

the heat exchange between solid and liquid, therefore decreasing the vapourisation rate.

2.2.4 Numerical simulations of droplet impact

The growing computational resources available, as well as strong mathematical formulation capable of simulating free surface flows, led a number of authors to investigate droplet impact using numerical simulations.

The modelling presents a large number of challenges above which the most important is the correct solution of the interface movement. The liquid-vapour interface is a theoretically zero thickness region, and in most approaches, this is spread along several computational cells, but there is also a number of authors who implemented a zero thickness interface by using moving meshes, which obviously presents some limitations for large movements of the interface. For this reason, static meshes are currently the most widely used along with adaptive mesh refinement in the region where small droplets could be formed and high resolution is needed.

Another problem is the large mesh to be used. In the splashing event, a droplet with a diameter in the order of millimetres will produce a large number of splashed droplets with much smaller diameter, some of which in the order of microns, especially in the early stages of a wet splashing (the so-called prompt splashing). In such situation, the numerical simulation will need to capture every single droplet. Therefore the mesh needs to be fine enough to correctly capture the interface for such particles, and this would need a considerable amount of computational cells. If we consider that in the study of impinging droplets a set of simulations have to be run in order to understand the effect of input parameters on the outcome, the computational time for such study becomes out of reach, and therefore a compromise between accuracy of the simulations and simulation time has to be agreed. This can also be justified if we consider that in the splashing process the most important quantities are the splashing threshold, angle, mass ratio and other quantities that can be correctly computed without the need to capture all the smaller droplets.

The main approaches used in the literature can be divided into Volume of Fluid (VOF) methods and Level Set (LS) methods. Yokoi [68] have developed a coupled approach using both methods that utilise the advantages of both. The approach has proved to be reliable in a number of applications such as bub-

ble rising [69], droplet impact onto dry and liquid surfaces and multiple droplet splashes.

In the framework of OpenFOAM, the well validate solver *interFoam* which uses a VOF approach has been widely used by a range of authors [70, 71] for different applications in which the interface tracking plays an important role.

Mahulkar et al. [42] have used a commercial software to produce a number of data and correlation for a dry splashing regime using droplets with a diameter of 50 and 100 μm .

2.3 Previous work on LNG modelling

To conclude this literature review chapter, existing work on LNG modelling will be introduced. Liquefied natural gas is a relatively new component of the world energy production. This is one of the reasons why modelling of such fuel is being investigated only recently [72]. The LNG industry has a good safety record, mainly because the technology used to transport has evolved and is highly developed, and secondly the hazards that it can cause are known, and therefore companies make sure that these are prevented.

Still, the hazards that could arise from the transport of LNG can be catastrophic, and the challenges are many in the modelling [73].

One of the topics that attracted the interest of a large number of researchers is the modelling of LNG dispersion in open atmosphere. Since the density of LNG depends highly on temperature, the behaviour observed when there is a large release of LNG resulting from a spill from a storage tank or ship is the dispersion of the vapour cloud close to the ground at the beginning of the spill, when the low temperature of gas makes it heavier than air. The increase in temperature due to mixing with fresh air results in a decrease of the density of the vapour cloud which therefore starts rising in the atmosphere, and in the presence of wind, the atmospheric boundary layer drives the cloud away from the release point.

Gavelli et al. [74] have studied the dispersion of LNG for several applications and type of spills. The software used was FLACS, developed by GexCon and validated against experimental data for a different application. One of the requirements that the US government imposes on the LNG terminal developers is that in the case of an accidental spill the flammable vapour cloud (defined by 1/2 of the LFL) does not extend beyond the property boundary. Typical scenarios they analysed are the ones resulting from pipe ruptures that result in flashing jets

or tank failures that lead to a pool formation and consequent evaporation of natural gas. The physics involved in such scenarios is complex and different models have to be applied depending on the type of spill and dispersion to analyse.

Commercial codes such as Ansys CFX and Fluent have been used to model stratification in LNG storage tank [75].

Another topic of large interest is the simulation of pool fires, where the importance of turbulence has drawn the attention of researchers on Large Eddy Simulation.

2.4 Chapter summary

Existing work related to the simulation of fuel cascade was discussed at the beginning of this chapter. A number of investigations have been carried out by HSL from both an experimental and numerical point of view. The advantages of a numerical formulation are obvious in terms of cost, scenarios that can be analysed and range of data available in each point of the computational domain. The fact whether we can rely on these results depends on the validation against experiments. Experiments on such phenomena are limited to the ones obtained from the investigation that followed Buncefield and the hazards and cost of these somehow restrict the type of problems that we can study. For these reasons the experiments are usually carried out on much simpler cases than the ones that we would experience in a real plant. These can be however used in the validation of CFD codes which accuracy is usually in doubt by the large number of models to be used. Both experimental and numerical results obtained by HSL will be used in the current work in order to obtain a tool capable of simulating various scenarios. The models used include but are not limited to the primary breakup of the initial liquid discharge, droplet distribution, effect of splashing and the liquid film on the total vapour cloud formation. The importance of the splashing model adopted to compute the impact of droplets with solid surfaces was reviewed. This led to the introduction of the state of art on interaction of liquid droplets with solid surfaces and current limits of the existing computational models. At last a brief review of previous work on LNG modelling was discussed, pointing to the fact that very limited work is available on computational method on safety of LNG plants, mainly because it is a relatively new source of energy and also because of its very positive safety record.

Chapter 3

Computational methodology and governing equations

Computational Fluid Dynamics is currently used worldwide to describe a vast variety of processes from the Oil and Gas industry to the semiconductor one. The development that supercomputers have witnessed in the past 10-20 years has allowed researchers and engineers to reproduce flows with such an accuracy that we could not have achieved a few years back.

The base concept behind CFD is to solve the equations of fluid dynamics using a discretisation process [76]. In the current application, the open source software OpenFOAM [77] was used because of the possibility of implementing new models and for its reliability as demonstrated by the broad application in several industries.

In order to explain the computational methodology, the equations that describe the state of a fluid will be defined first.

To define the conservation equations, instead of following a parcel as we do in classical mechanics, it is more convenient to establish a Control Volume (CV) which will be our region of interest [78, 79] (Figure 3.1).

A Control of Volume is defined as a large and finite region of the flow. The conservation principles are applied to the control volume and to the fluid that crosses the control surface. Using this procedure we obtain the conservation equations in the so-called *Integral* form, but we can easily derive the differential form from the integral one.

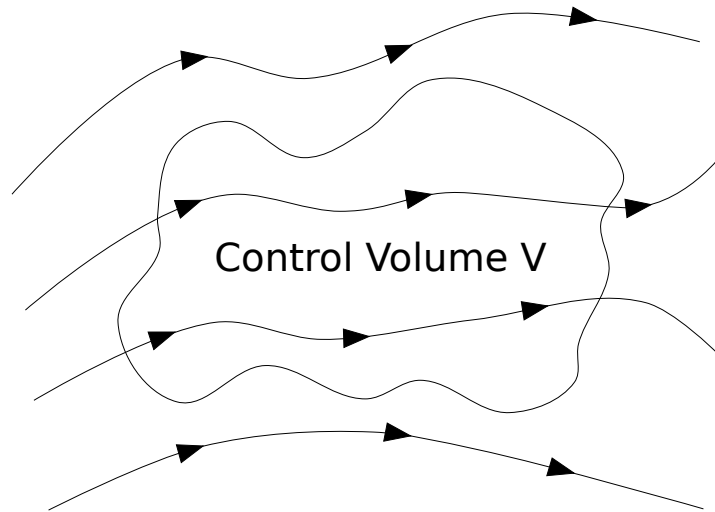


Figure 3.1: Definition of a Control Volume

3.1 Conservation Principles

In order to define the conservation equations a quantity that is widely used in Fluid Dynamics, the so-called Material Derivative, has to be determined first. This will be of particular use in order to simplify the equations and use them in a computational context. The conservation principles that will be derived are the conservation of mass, momentum and energy. These three principles are enough to calculate the state of a fluid, and the equations derived are usually coupled with each other, although some simplifications can be made in some instances, where the number of dependent variables reduces and therefore it is easier to find a solution to the particular mathematical problem.

3.1.1 Material Derivative

The Material Derivative (also known as Substantial Derivative) of a variable is defined as the instantaneous change of the variable itself of a fluid element and it is calculated in the following way:

$$\frac{D\psi}{Dt} = \frac{\partial\psi}{\partial t} + \mathbf{u} \cdot \nabla\psi \quad (3.1)$$

Where ψ can be any tensor field and \mathbf{u} is the velocity field. Focusing on the last equation, we can therefore conclude that the variable change rate in time following a fluid element ($D\psi/Dt$) is equivalent to the local time derivative ($\partial\psi/\partial t$) plus the convective derivative of the same variable ($\mathbf{u} \cdot \nabla\psi$). This means

that the state of a fluid element is changing as the element moves in the domain because the flow could change in time in that point and also because the element is moving to another point where the fluid has different properties.

3.1.2 Continuity Equation

One of the most important principles in fluid dynamics is the conservation of mass. This follows the chemical principle that mass is neither created nor destroyed in any chemical reaction. Following the above, the continuity equation can be defined. If we consider a fluid region, the conservation of mass tells us that the sum of the mass that comes into a closed domain, the mass that leaves the domain and the mass change inside the domain equals to zero. In a differential form, the equation can be written using the material derivative as:

$$\frac{D\rho}{Dt} + \rho \nabla \cdot \mathbf{u} = 0 \quad (3.2)$$

The Continuity Equation could be also written developing the Material Derivative introduced before, and it assumes the following form:

$$\frac{\partial \rho}{\partial t} + \nabla \cdot (\rho \mathbf{u}) = 0 \quad (3.3)$$

If we assume that the flow is incompressible, that is a flow where we can expect that the density is constant both in space and time ($\rho = \text{const}$), the equation becomes much more straightforward:

$$\nabla \cdot \mathbf{u} = 0 \quad (3.4)$$

3.1.3 Momentum Equation

In the study of mechanics of solid objects, Sir Isaac Newton derived in 1686 the second law of motion which correlates the change in momentum of an object to the external force applied to it. In a mathematical for this assumes the following equation:

$$\mathbf{F} = m\mathbf{a} \quad (3.5)$$

The last equation can be used in our application as it can be easily applied to fluids as well. In the case of a fluid, this equations states that the momentum

change of a fluid element varies accordingly to the resultant forces applied to that element. For a fluid element, the forces applied to it include volume forces (such as gravity) and surface forces (i.e. viscous and pressure forces).

If we assume an infinitesimal fluid element and all the forces acting on each surface of the element, we can write Newton's equation for all the three Cartesian axes in the following form:

$$\rho \frac{Du_x}{Dt} = -\frac{\partial p}{\partial x} + \frac{\partial \tau_{xx}}{\partial x} + \frac{\partial \tau_{yx}}{\partial y} + \frac{\partial \tau_{zx}}{\partial z} + \rho f_x \quad \text{x axis} \quad (3.6)$$

$$\rho \frac{Du_y}{Dt} = -\frac{\partial p}{\partial y} + \frac{\partial \tau_{xy}}{\partial x} + \frac{\partial \tau_{yy}}{\partial y} + \frac{\partial \tau_{zy}}{\partial z} + \rho f_y \quad \text{y axis} \quad (3.7)$$

$$\rho \frac{Du_z}{Dt} = -\frac{\partial p}{\partial z} + \frac{\partial \tau_{xz}}{\partial x} + \frac{\partial \tau_{yz}}{\partial y} + \frac{\partial \tau_{zz}}{\partial z} + \rho f_z \quad \text{z axis} \quad (3.8)$$

Where p is the pressure, $\boldsymbol{\tau}$ is the viscous stress tensor and \mathbf{f} are the volume forces. These three scalar equations are usually called *Navier-Stokes equations* because the two scientists discovered them independently during the nineteenth century. The viscous stress tensor components are calculated in the following way:

$$\tau_{ij} = \mu \left(\frac{\partial u_i}{\partial x_j} + \frac{\partial u_j}{\partial x_i} - \frac{2}{3} \delta_{ij} \frac{\partial u_k}{\partial x_k} \right) + \delta_{ij} \lambda \frac{\partial u_k}{\partial x_k} \quad (3.9)$$

where i, j and k assume values of x, y, z , δ_{ij} is the Kronecker delta, μ is the first coefficient of viscosity (usually simply called dynamic viscosity) and λ is the second coefficient of viscosity. The latter is typically assumed to be zero in most cases, but if assumed different from zero the most common approximation is:

$$\lambda = -\frac{2}{3}\mu \quad (3.10)$$

With these assumptions, and developing the material derivative on the left hand side, we obtain the following vectorial form of the Navier-Stokes Equations:

$$\rho \left(\frac{\partial \mathbf{u}}{\partial t} + \mathbf{u} \cdot \nabla \mathbf{u} \right) = -\nabla p + \nabla \cdot (\mu(\nabla \mathbf{u} + \nabla \mathbf{u}^T)) + \nabla \left(-\frac{2}{3}\mu \nabla \cdot \mathbf{u} \right) + \rho \mathbf{g} \quad (3.11)$$

3.1.4 Energy Equation

The main principle behind the energy equation is that energy is conserved, meaning that the energy rate of change in a material particle is equal to the energy received by heat and work to the particle. The equation can be written in the following way:

$$\rho \frac{De}{Dt} + \rho \frac{DK}{Dt} + \nabla \cdot (\mathbf{u}p) = -\nabla \cdot \mathbf{q} + \nabla \cdot (\boldsymbol{\tau} \otimes \mathbf{u}) + \rho\phi \quad (3.12)$$

where e is the specific internal energy, $K = |\mathbf{u}|^2/2$ is the local kinetic energy, \mathbf{q} represents the heat flux, $\boldsymbol{\tau}$ is the mechanical stress tensor and ϕ the heat source from other processes than the ones mentioned. Developing the material derivatives the equation becomes:

$$\frac{\partial \rho e}{\partial t} + \nabla \cdot (\rho \mathbf{u}e) + \frac{\partial \rho K}{\partial t} + \nabla \cdot (\rho \mathbf{u}K) + \nabla \cdot (\mathbf{u}p) = -\nabla \cdot \mathbf{q} + \nabla \cdot (\boldsymbol{\tau} \otimes \mathbf{u}) + \rho\phi \quad (3.13)$$

Sometimes the equation can be expressed in terms of enthalpy, assuming a similar expression to the one presented for the internal energy.

3.1.5 Conservation of Scalar Quantities

In several applications of fluid mechanics, in addition to the standard quantities (ρ, \mathbf{u}, T) , a number of secondary scalar quantities can be present, such as chemical species or for example soot in the presence of a fire. These quantities evolve according to a transport equation (also called convection-diffusion equation for obvious reasons) where the change in time of the scalar is linked to convection and diffusion of the quantity itself and any other source term that could be present.

For a general scalar quantity ϕ it is possible to obtain a conservation equation as the ones derived before.

$$\frac{D\rho\phi}{Dt} + \rho\phi\nabla \cdot \mathbf{u} - \nabla^2(\rho D\phi) = q_\phi \quad (3.14)$$

where D is the diffusion coefficient of the scalar ϕ and q_ϕ is a source terms that represent the transport of ϕ by mechanisms other than convection or diffusion and any sources or sinks of the scalar. Developing the material derivative with its definition the equation becomes:

$$\frac{\partial \rho \phi}{\partial t} + \nabla \cdot (\rho \phi \mathbf{u}) - \nabla^2 (\rho D \phi) = q_\phi \quad (3.15)$$

This equation can be applied for example to species mass fractions in reacting flows where more than one component is present. In this case, the equation is applied to $\phi = Y_n$ quantities (n is the number of species present in the domain). The source term q_ϕ represents the combustion process and mass fraction coming from any lagrangian phase where evaporation takes place.

3.1.6 Summary of the Conservation Equations

We have described in this section all the conservation equations for a generic fluid, expressed using their conservative form, which will be repeated here for a better visualization:

$$\frac{\partial \rho}{\partial t} + \nabla \cdot (\rho \mathbf{u}) = 0 \quad (3.16)$$

$$\frac{\partial \rho \mathbf{u}}{\partial t} + \mathbf{u} \cdot \nabla (\rho \mathbf{u}) = -\nabla p + \nabla \cdot (\mu (\nabla \mathbf{u} + \nabla \mathbf{u}^T)) + \nabla \cdot \left(-\frac{2}{3} \mu \nabla \cdot \mathbf{u} \right) + \rho \mathbf{g} \quad (3.17)$$

$$\frac{\partial \rho e}{\partial t} + \nabla \cdot (\rho \mathbf{u} e) + \frac{\partial \rho K}{\partial t} \nabla \cdot (\rho \mathbf{u} K) + \nabla \cdot (\mathbf{u} p) = -\nabla \cdot \mathbf{q} + \nabla \cdot (\boldsymbol{\tau} \otimes \mathbf{u}) + \rho \phi \quad (3.18)$$

These are partial differential equations for any generic unsteady flow. In practical applications, these equations are usually simplified by assumptions that arise from the type of flow that we are analysing. For example, in the assumption of incompressible flow, the energy equation is decoupled from the momentum and continuity ones.

3.2 Simplified forms of the equations

The conservation principles introduced are a very general description of a flow and their solution is complicated because the equations involved are in general non-linear and coupled with each other. Therefore there is no general solution and the uniqueness of the solution for a specific set of boundary conditions has not been proved yet.

An exact solution exists only for very specific cases (flows in pipes or parallel plates for example), and even though these are important in order to understand some of the basic concepts of fluid dynamics, their relevance is limited in real applications.

In order to solve the complex set of equations, a number of simplifying assumptions can be made, a common practice in all the branches of engineering. With these assumptions, some terms become equal to zero, and still, an analytical solution does not exist for the equations, but their numerical solution is much simpler to obtain. Inevitably, these assumptions introduce an error because the flow analysed is not ideal, but the error introduced is in most cases negligible.

3.2.1 Incompressible Flow

In a wide range of flows observable in nature, the value of density can be assumed constant, for example for flows of liquids and for gasses where the Mach number does not exceed 0.3. These flows are called incompressible, and if we also consider that the flow is isothermal, the conservation equations are simplified as:

$$\nabla \cdot \mathbf{u} = 0 \quad (3.19)$$

$$\frac{\partial \mathbf{u}}{\partial t} + \mathbf{u} \cdot \nabla \mathbf{u} = -\frac{1}{\rho} \nabla p + \nabla \cdot (\nu(\nabla \mathbf{u} + \nabla \mathbf{u}^T)) + \mathbf{g} \quad (3.20)$$

These are still very complex but their numerical solution is easier to obtain if compared to the full equations.

3.2.2 Inviscid Flow

Considering a flow far from any solid surface, the viscosity effects are usually negligible, therefore the stress tensor reduces to $\mathbf{T} = -p\mathbf{I}$ and the Navier-Stokes equations reduce to the Euler equations (this is the reason why inviscid flows are also called Euler flows):

$$\frac{\partial \rho}{\partial t} + \nabla \cdot (\rho \mathbf{u}) = 0 \quad (3.21)$$

$$\rho \left(\frac{\partial \mathbf{u}}{\partial t} + \mathbf{u} \cdot \nabla \mathbf{u} \right) = -\nabla p + \rho \mathbf{g} \quad (3.22)$$

This simplification is widely used in Aeronautical flows far from walls because at high Reynolds number the effect of viscosity is restricted to regions close to solid surfaces. The solution of such flows allows coarse grids close to walls and therefore much faster to be obtained if compared to a viscous solution. However, as said, the lack of any viscosity on walls allows for a slip condition ($\mathbf{u} \neq 0$) which leads to non-physical solutions.

3.3 Simulation of Multiphase Flows

The conservation equations obtained so far are valid for any type of fluid problem, and depending on the complexity of the physics involved these can simplify into forms that are easier to solve numerically. For example, the assumption that a single phase is present throughout the domain is in most cases acceptable, especially in aerospace and external aerodynamics applications. On the other hand, a broad set of industrial problems involve the presence of two or more distinctive phases in the domain, which introduces a more complex phenomenon to solve and the need to use different equations according to the properties of the phases present. A multiphase flow is defined as a flow in which two or more separate fluids with separate phases and physical properties are present, that can be either in independent states (gas or liquid) or the same state. A multiphase flow is therefore defined by one of the following:

- Materials that have different states or phases (gas, liquid or solid)
- Materials that have the same state or phase but have different physical properties (such as density)

The main difficulties encountered in the analysis of multiphase flows are the different physical properties of the phases and the tracking of the interphase between them. Although the term multiphase flow refers to a flow where two or more phases are present, in the current section the solution of two-phase flows will be investigated, because of simplicity and the applicability to the current work, but the formulation can be extended to n-phase flows with some adjustments in the equations.

Although there is a wide variety of numerical approaches for the solution of multiphase flows, the most used methods are the so-called Lagrangian-Eulerian [80] and Eulerian-Eulerian formulation [81]. The terms Lagrangian and Eulerian

refer to how a single phase is solved. In a Lagrangian framework, the phase is modelled using points which usually represent droplets, while the Eulerian framework uses the standard approach of the fluid being represented by a continuum with specific properties. In a Lagrangian-Eulerian (LE) approach, one of the two phases is described using a Lagrangian framework while the other one using a standard Eulerian framework. On the other hand, in a Eulerian-Eulerian approach, both the phases are represented with a standard Eulerian framework.

Whether a problem is more suitable for one approach or the other has to be determined by the physics involved. In most cases, in a multiphase problem, it can be observed that there is a primary and a secondary phase, meaning that one phase occupies a larger volume than the other. Defining the volume fraction of a phase by:

$$\text{Volume Fraction} = \frac{\text{Volume of one phase}}{\text{Total Volume}} \quad (3.23)$$

one primary phase can be determined by calculating this value and also one can obtain some information on the secondary phase as to whether the latter is dilute or dense respect to the primary one (usually dilute regimes are characterised by values of volume fraction in the order of 1-5%, while dense regimes are everything above that value).

As in every engineering application, the two methods mentioned earlier have their advantages and drawbacks respectively. Eulerian formulations have usually higher accuracy and are widely used in free surface flows or in the case of dense phase but need higher computational cost compared to Lagrangian formulations which are generally cheaper and utilised in dilute phases such as spray and coating applications.

A whole study of a liquid cascade formed by an overflowing tank would have to simulate the whole physical process involved, starting from the bulk of fluid formed at the top of the tank, where obviously the liquid phase is dense, to the breakup of such liquid into smaller droplets and the impact of these on the ground, where a more dispersed phase can be observed. This is obviously computationally expensive and difficult to model. A simplification can be made if we consider for the experimental observations of such problem which have shown that the jet spilling from the top of a tank breaks up almost immediately into smaller droplets, meaning that one could skip the modelling of the primary atomization of the jet and directly take into account for the bulk of the flow which is composed

entirely by small droplets. This means that a pure Lagrangian approach could be used because of the nature of the flow, simplifying the problem and opening the opportunity to a much faster simulation.

3.3.1 The Eulerian-Eulerian Approach

If the dispersed phase occupies a large volume in the domain, treating both the dispersed and carrier phase using a Eulerian approach is the most used method in the literature. Among a large number of models available, the two where the attention will be focused here are the free surface flow and the Eulerian two-phase modelling.

The first method mentioned applies to problems where two immiscible fluids are separated by a well-defined interface, such as droplets of liquid immersed in a gas or bubbles moving into a liquid. Two main classes of methods exist among the free surface approaches, the interface tracking and interphase capturing approaches. The interface tracking approach is used in a wide range of applications for the chemical industry. The central concept underlying this method is to identify the interface between the two fluids and moving it according to its velocity field. Obviously, in order to do that, a re-meshing of the domain has to be applied, according to the new position of the interface. This method provides high accuracy regarding tracking the interface, but its main drawback is the applicability to cases where the interface is not moving largely, therefore it cannot simulate any breakup or coalescence of droplets or bubbles. On the other hand, the interface capturing methods are able to simulate these type of flows, because the interface is 'captured' by the solver and no re-meshing is needed (apart from cases where the mesh could be refined in some regions of the domain). The most used capturing methods are the Volume of Fluid (VOF) and Level Set (LS) approaches.

The VOF method was developed by Hirt and Nichols [82] and can easily capture topologies changes of the moving surfaces, such as coalescence or breakup of droplets. It is based on the definition of a function called volume fraction which is solved using a transport equation.

$$\frac{\partial \psi}{\partial t} + \mathbf{u} \cdot \nabla \psi = 0 \quad (3.24)$$

Such method is highly conservative in mass but presents the drawback of smearing the interface, which also has to be reconstructed from the volume frac-

tion field, making the process even more complicated. However, its simplicity and high mass conservation have made it one of the most used methods for a broad set of application.

The other method mentioned for interface capturing approaches is the Level Set method. Based on a one fluid approach as the VOF method, the former relies on the definition of a level set function, which assumes a value of zero on the interface surface and has to satisfy the transport equation mentioned earlier. This method has proved to be more reliable than VOF concerning the accuracy of the interface, but its lack of mass conservation has limited its applicability. Some authors [83, 84] have tried to couple the advantages of both the VOF and LS methods to overcome the limits of both, obtaining satisfactory results.

Free surface approaches cannot be used when the two liquids are well mixed and therefore a two-phase eulerian approach is more suitable. While in the former methods one equation only is solved for both fluids, the latter approach uses two separate equations for the continuity, momentum and energy conservation equations, which contain additional terms to account for the interface between the two fluids.

3.3.2 The Lagrangian-Eulerian Approach

If one of the two phases is highly dispersed in the other one, for example a spray in the region far from the nozzle, the representation of the dispersed phase can be done using a Lagrangian approach, to avoid the use of a large number of computational cells, which is in most cases unachievable. The primary phase is solved using a standard Eulerian approach. The LE approach uses a statistical description of the dispersed phase, and the two phases are coupled using source terms in the conservation equations for the carrier (main) phase. This formulation requires that the particles have to be considerably smaller than the grid size ($d_p \ll \Delta x$), otherwise the effect of the dispersed phase on the carrier phase is too significant to be taken into account in a single grid cell.

One of the critical points in such formulation is the choice of the level of interaction between the two phases [85]. Depending on the application and on the degree of accuracy, there can be significant differences. For example, for solid particles such as dust, there is no source term in the continuity equation for the carrier phase as the mass of the droplets is constant. For this reason, LE approaches can be divided into three groups depending on the level of interaction

between the phases:

- One-Way coupling: the carrier phase affects the dispersed phase, but the latter does not influence the former. This is usually the approach used when the droplets size and their number is not large enough to affect the carrier phase significantly.
- Two-Way coupling: there is mutual coupling between the droplets and the carrier fluid. This is used when there is a significant effect on the carrier from the dispersed phase.
- Four-Way coupling: This is the most complicated approach and includes interactions between different droplets (collision and/or coalescence) in addition to the interactions between droplets and carrier phase.

The choice between the three levels of interaction can profoundly affect the solution and the computational effort increases as the number of interactions considered increases too.

As mentioned before, the Lagrangian approach is mostly used in the solution of dispersed flows, especially for spray applications where the droplet size is in the order of microns [86, 87]. This approach gives us a good compromise between accuracy of the solution and cost. One of the key points of this formulation is the choice of adequate submodels that describe how the two phases interact, and this can practically change the outcome of a simulation completely.

The Lagrangian phase is represented through N_s particles and their physical variables such as position, velocity, radius (which is directly linked to the mass by the density) and any other quantity depending on the needs of the modeller ($\mathbf{X}^{(i)}(t), \mathbf{u}^{(i)}(t), R^{(i)}(t), i = 1, \dots, N_s(t)$). The position of the particles is represented using Lagrangian coordinates, which are completely independent of the grid used in the Eulerian phase. All the quantities mentioned above can change during time (position, velocity, radius) because of the motion of the droplet and because of thermophysical processes such as evaporation.

The Eulerian phase, on the other hand, is solved as usual using the Navier-Stokes Equations but introducing source terms arising from the Lagrangian phase in the Continuity, Momentum and Energy equations.

3.3.3 Lagrangian formulation in OpenFOAM

The Lagrangian-Eulerian approach in OpenFOAM is available for both solid and fluid particles. Even though the two formulations are quite similar, we are going to concentrate mainly on liquid droplets because of the interest in our application.

As in every lagrangian formulation, the representation of the dispersed phase is done using a certain number of parcels, which consist in much reduced number respect to the actual number of droplets present in the domain, this because representing each droplet would be too demanding and we can obtain accurate results even with such approximation. Each parcel contains an amount of particles n_s . The equations that describe the Eulerian phase for a compressible flow are the following:

$$\frac{\partial \rho}{\partial t} + \nabla \cdot (\rho \mathbf{u}) = S_\rho \quad (3.25)$$

$$\rho \frac{\partial \mathbf{u}}{\partial t} + \nabla \cdot (\rho \mathbf{u} \mathbf{u}) = -\nabla p + \nabla (\mu \nabla \mathbf{u} - \frac{2}{3} \mu \nabla \cdot \mathbf{u}) + S_u \quad (3.26)$$

$$\frac{\partial \rho e}{\partial t} + \nabla \cdot (\rho \mathbf{u} e) + \frac{\partial \rho k}{\partial t} + \nabla \cdot (\rho \mathbf{u} k) + \nabla \cdot (\mathbf{u} p) + \alpha_{eff} \nabla^2 e = S_e \quad (3.27)$$

These are the Mass, Momentum and Energy Equation with an additional term in each of them to take into account for the Lagrangian phase (α_{eff} is the thermal diffusivity that takes into account for the laminar and turbulent terms). In the mass conservation equation, the source term is present because due to evaporation of parcels there can be some mass introduced into the carrier phase or subtracted from it due to evaporation and/or condensation. In the momentum equation, the source term represents the influence of the parcels on the velocity field due to drag and lift forces, and other forces that may act on the droplets. At last, we find the source term in the energy equation due to heat transfer and phase change on the parcels that affect the Eulerian phase. These three terms can be different from zero but can also assume a null value if we consider only one-way coupling where the dense phase affects the dispersed one while the latter has negligible or no influence on the Eulerian phase.

The Lagrangian phase is solved by the use of a different set of equations. These take into account the fact that the particles are considered spherical, and that the mass changes due to evaporation/condensation. We can then write the

equations that describe the evolution of the particles:

$$\frac{dm_d}{dt} = \dot{m} \quad (3.28)$$

$$\frac{d\mathbf{X}_d}{dt} = \mathbf{u}_d, \quad (3.29)$$

$$m_d \frac{d\mathbf{u}_d}{dt} = \sum (\mathbf{F}_i + \mathbf{f}_i). \quad (3.30)$$

where the subscript d refers to the parcel. These three equations are solved for each parcel. For this reason, the solution of a given cloud can become really expensive if we increase the number of parcels to be closer to the real solution. The sum over the vectors of the forces acting on the droplet can be simplified if we assume that the primary forces are gravity and aerodynamic drag. Gravity is simple to define while for the drag force we need a bit more detailed analysis. As commonly done in Aerodynamics theory, a drag coefficient C_D can be determined for the parcel, using the following equation:

$$C_D = \frac{F_D}{\frac{\rho_F}{2} |\mathbf{u}_F - \mathbf{u}_d|^2 A_d}, \quad (3.31)$$

with F_D being the aerodynamic drag acting on the parcel, ρ_F the density of the surrounding fluid, u_F and u_d are the velocities of the fluid and the droplet respectively, and $A_d = d_p^2 \pi / 4$ is the cross-section of the spherical droplet.

The mass of the droplet can be expressed as:

$$m_d = \rho_d \frac{1}{6} \pi d^3 \quad (3.32)$$

therefore calculating the drag force from Equation 3.31 and multiplying and dividing by m_d we obtain:

$$F_D = \frac{3}{4} \frac{m_d \rho_F}{\rho_d d} C_D |\mathbf{u}_F - \mathbf{u}_d| (\mathbf{u}_F - \mathbf{u}_d) \quad (3.33)$$

The calculation of the drag force relies on the drag coefficient only because all the other quantities are given.

The drag coefficient is calculated as a function of the Reynolds number (the ratio between inertia and viscous forces):

$$Re = \frac{\rho_F |\mathbf{u}_F - \mathbf{u}_d| d}{\mu_F} \quad (3.34)$$

Results obtained from experiments of flow around a sphere show that the drag coefficient does not have a simple correlation with the Reynolds number and also C_D depends on the surface shape of the sphere, as shown in Figure 3.2. When the sphere surface is not smooth, experimental observations showed that the transition from laminar to turbulent flow occurs at lower Reynolds number respect to a smooth sphere.

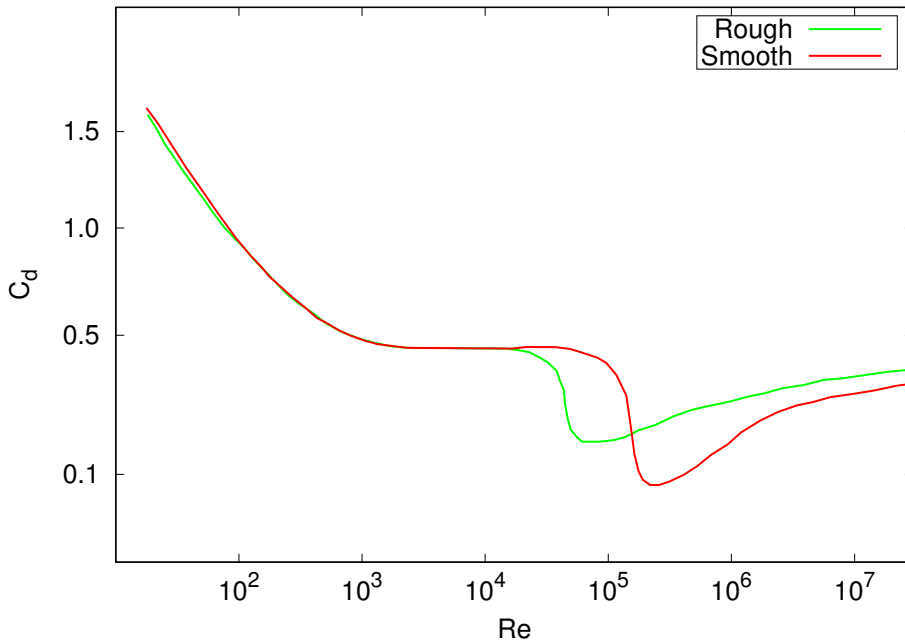


Figure 3.2: Drag Coefficient for a sphere as a function of Reynolds number for rough and smooth surface

Mainly three regimes are observed: the laminar, transitional and turbulent regimes. For each regime, a different correlation is used. For small values of the Reynolds number ($Re < 0.5$), i.e. a laminar regime, the drag coefficient is calculated as:

$$C_D = \frac{24}{Re} \quad (3.35)$$

This is also called Stokes regime because he found an analytical solution for the drag. For the transitional regime ($0.5 < Re < 1000$) several correlations have been proposed, and in OpenFOAM the one obtained by Schiller and Neumann

[88] can be found:

$$C_D = \frac{24}{Re} \left(1 + \frac{1}{6} Re^{2/3}\right) \quad (3.36)$$

At last we find the turbulent regime ($Re > 1000$) which is characterized by an almost constant value of the drag coefficient, which is expressed by:

$$C_D = 0.424 \quad (3.37)$$

For higher values of the Reynolds number ($Re > 10^5$) the drag coefficient has a drop and eventually recovers. These values are usually not experienced in spray applications and therefore not modelled. It was also mentioned that the shape of the sphere could affect the value of the drag coefficient, and usually, for rough spheres, this results in an earlier drop in drag respect to the smooth sphere. This is why golf balls have small holes on the surface because the drag is highly reduced at a typical speed and they can cover longer distances. In the case of a liquid droplet, the surface can be considered smooth and therefore we can use the standard correlations.

For differently shaped droplets (non-spherical) the drag coefficient is more complicated and different assumptions have to be made.

After the calculation of the drag coefficient, the solver has to calculate the drag force and makes use of it in the momentum equation to solve the motion of the droplet. This would be enough to describe the status of a solid droplet where heat transfer does not play an important role, but in the case of a liquid droplet, boiling and evaporation can take place. Therefore we need to introduce two more equations, the energy and mass conservation principles. The first one takes into account for all the types of heat exchange that can affect the temperature of the droplet and calculates the temperature change accordingly, while the second one gives the change in mass of the droplet which can be positive (condensation) or negative (evaporation).

The equation that calculates the change in temperature for the droplet is the following:

$$m_d c_p \frac{dT_d}{dt} = \dot{Q} + h_{fg} \frac{dm_d}{dt} + A_d \sigma \epsilon (T_a^4 - T_d^4) \quad (3.38)$$

where h_{fg} is the specific enthalpy of condensation/vapourisation, σ is the Stefan-Boltzmann constant and ϵ is the emissivity of the droplet surface for the

liquid analysed.

On the left-hand side of this the equation we find the temperature change of the droplet weighted by its mass and heat capacity, while on the right-hand side the three main contributors to the temperature change due to conduction-convection, latent heat and radiation. The first term, the convective heat transfer (\dot{Q}) is usually calculated by using the heat transfer coefficient:

$$\dot{Q} = htc(T_s - T_d)A; \quad A = 4\pi r^2 \text{(Droplet surface area)} \quad (3.39)$$

$$htc = \frac{Nu \cdot \lambda}{d} \quad (3.40)$$

where Nu is the Nusselt number, λ is the thermal conductivity of the liquid droplet, and d is the diameter of the droplet. The value of the Nusselt number is calculated with the correlation obtained by Ranz-Marshall [89]:

$$Nu = 2 + 0.6Re^{1/2}Pr^{1/3} \quad (3.41)$$

where $Pr = c_p\mu/\lambda$ is the Prandtl number, defined as the ratio between momentum and thermal diffusivity ($Pr = \nu/\alpha$).

The second term is the temperature change due to evaporation/condensation, because of latent heat. When a droplet evaporates, there is heat released due to the evaporation process, and this causes a temperature drop for the droplet. The third and last term in the temperature equation is heat exchange due to radiation. This term can assume essential values when a combustion process is taking place, while it is mostly negligible for any other type of application.

One of the assumptions of the models presented here is about the shape of the droplets. All the droplets are considered to be spherical in order to simplify the problem and make some assumptions on parameters such as the aerodynamic drag. This highly depends on the shape of the droplet, and a maximum deformation of the droplet can lead to an increase in drag by a factor of 4 [90], which obviously is not negligible when a single droplet is considered. The change in the shape also depends on the Reynolds number, because an increase in the latter leads to an increase in the shear stress on the droplet surface, therefore modifying its shape. From a breakup point of view, this is somehow linked to the deformation of the droplet, because during the breakup process the droplet experiences a time-dependent deformation until it reaches a value where the surface tension

cannot hold the droplet together anymore, as shown in Figure 3.3. In the current application, the large number of droplets and the relatively low Reynolds numbers involved are such that accounting for the droplet deformation would be too demanding and the results obtained would not show significant differences, for this reason, the droplets are all considered spherical (this assumption comes into the droplet drag and heat transfer), which simplify our approach to the problem.

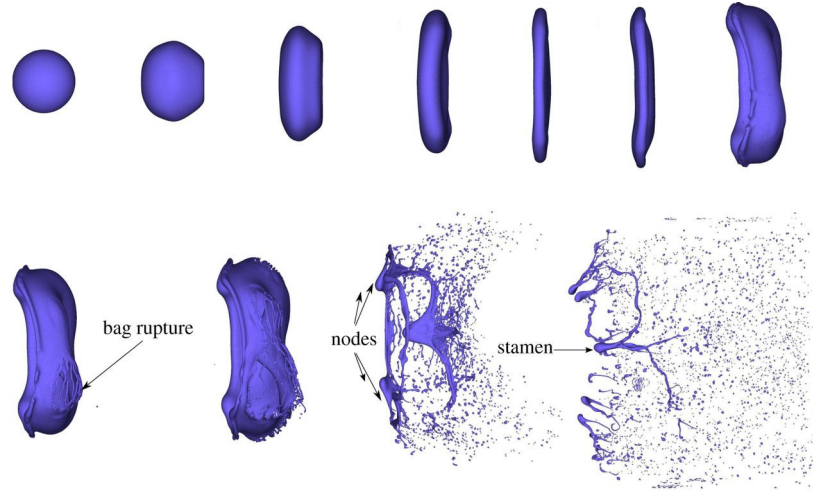


Figure 3.3: Deformation of a droplet undergoing a bag-breakup [91]

3.4 Turbulence Modelling

In the study of fluid flows, one significant distinction can be made based on their nature: laminar and turbulent flows. The term laminar refers to cases that are simpler to model and where the physical quantities have a particular value in space. Also, the streamlines that characterise a laminar flow do not intersect each other at any time, because the flow field is characterized by molecules moving in parallel layers, without interacting with the adjacent layers, from which the term laminar. On the other hand, turbulent flows are characterised by chaotic movement of the fluid, and this makes the modelling of such problems much more complicated and computationally challenging. Turbulence modelling in multiphase flows is even more challenging due to the interaction between the turbulent structures of the primary phase with the secondary one. Therefore it is easy to conclude that laminar flows are easier to solve, but the fact that most flows observable in nature are turbulent somehow limits the number of application for which a laminar approach is suitable.

It is therefore crucial for a computational model to be able to solve the turbulence associated with a specific flow, and as with every other method the accuracy comes with a cost.

In the literature, a large variety of turbulent models can be found, and their applicability depends on the type of problem analysed and on the accuracy that the modeller wants to achieve. In the framework of OpenFOAM, the choice is between three approaches, which are usually the most adopted ones in general, respectively called RANS, LES and DNS. The three methods will be discussed individually in the following paragraphs.

A variety of turbulent models developed by numerous people is available, but the two main categories available in OpenFOAM are the RANS (Reynolds-averaged Navier-Stokes) and LES (Large Eddy Simulation) models. It is worth also mentioning about DNS (Direct Numerical Simulation) methods, which are the most accurate ones, where each scale of the turbulent motion is solved, but these are usually too expensive for most types of applications, especially for large-scale problems.

3.4.1 RANS Models

Reynolds-averaged Navier-Stokes (RANS) methods are probably the most used in industry because they give acceptable results and relatively small computational times. They are by definition the least accurate of the three methods presented here but nonetheless can provide very good results when a specific set of values in the domain are investigated.

The idea behind the RANS models, from which they take their name, is to calculate a time average of the conservation equations in order to obtain a mean value for the physical variables, which is the value that will eventually be obtained from solving the set of equations. The equations obtained by such averaging are very similar to the initial equations that describe the 'full' quantities but present an additional term due to the averaging procedure which is the term that has to be modelled.

The velocity field can be decomposed into its mean and fluctuating components:

$$\mathbf{u}(\mathbf{x}, t) = \bar{\mathbf{u}}(\mathbf{x}) + \mathbf{u}'(\mathbf{x}, t) \quad (3.42)$$

where the term $\bar{\mathbf{u}}(\mathbf{x})$ represents the time averaged velocity field while $\mathbf{u}'(\mathbf{x}, t)$

its fluctuating component. We can apply this decomposition to the continuity and momentum equations. For simplicity equations are shown for incompressible flows only.

$$\nabla \cdot (\bar{\mathbf{u}} + \mathbf{u}') = 0 \quad (3.43)$$

$$\frac{\partial(\bar{\mathbf{u}} + \mathbf{u}')}{\partial t} + (\bar{\mathbf{u}} + \mathbf{u}') \cdot \nabla(\bar{\mathbf{u}} + \mathbf{u}') = -\frac{1}{\rho} \nabla(\bar{p} + p') + \nu \nabla^2(\bar{\mathbf{u}} + \mathbf{u}') \quad (3.44)$$

Averaging the last equation in time, and considering that $\bar{\mathbf{u}}' = 0$, we obtain the averaged form of the continuity and momentum equations:

$$\nabla \cdot \bar{\mathbf{u}} = 0 \quad (3.45)$$

$$\frac{\partial \bar{\mathbf{u}}}{\partial t} + \bar{\mathbf{u}} \cdot \nabla \bar{\mathbf{u}} = -\frac{1}{\rho} \nabla \bar{p} + \nu \nabla^2 \bar{\mathbf{u}} + \overline{\mathbf{u}' \cdot \nabla \mathbf{u}'} \quad (3.46)$$

The continuity equation is the same as the initial one, while the momentum one differs only by the last term in the equation ($\overline{\mathbf{u}' \cdot \nabla \mathbf{u}'}$) which arises from the averaging of non-linear terms. This last term is an added source term that contributes to the momentum of the mean velocity and comes from the transport of fluctuating momentum by turbulence velocity fluctuations. This term obviously introduces a new unknown variable to the problem. Therefore we need to close the equation by using another equation that describes this term. This term is commonly known as the Reynolds stress and can be represented using Einstein's notation as:

$$\tau'_{ij} = \overline{\rho u'_i u'_j} \quad (3.47)$$

A number of solutions for the Reynolds stress have been obtained, but the most commonly used one are the linear eddy viscosity models, where the Reynolds stresses are modelled by a linear constitutive relationship with the mean flow straining field, such as:

$$\tau'_{ij} = -2\mu_t S_{ij} + \frac{2}{3}\rho k \delta_{ij} \quad (3.48)$$

where μ_t represents the turbulent viscosity, k is the mean turbulent kinetic energy and S_{ij} is the strain rate tensor.

Plenty of linear eddy viscosity models exist, but probably the most known is the $k - \varepsilon$ model which gives two additional transport equations for the turbulent kinetic energy (k) and turbulent dissipation (ε) [92]. The equations used in the standard model are the following:

$$\frac{\partial(\rho k)}{\partial t} + \mathbf{u} \cdot \nabla(\rho k) = \nabla \cdot [(\mu + \mu_t)\nabla k] + P_k + P_b - \rho\varepsilon + S_k \quad (3.49)$$

$$\frac{\partial(\rho\varepsilon)}{\partial t} + \mathbf{u} \cdot \nabla(\rho\varepsilon) = \nabla \cdot [(\mu + \mu_t)\nabla\varepsilon] + C_{1\varepsilon}\frac{\varepsilon}{k}(P_k + C_{3\varepsilon}P_b) - C_{2\varepsilon}\rho\frac{\varepsilon^2}{k} + S_\varepsilon \quad (3.50)$$

in which a number of constants have been introduced, as well as the effect of the mean flow in the production of k (P_k) and the impact of buoyancy as well. The $k - \varepsilon$ model has been successfully used in the presence of sizeable adverse pressure gradients such as regions where the flow detaches from a wall. The main drawback of such model is the limit of applicability where the wall effects become significant. For the latter case, another two-equation model has been derived and widely used in the solution of flows where wall effects are predominant, the $k - \omega$ model. This solves an equation for the turbulent kinetic energy as well as one equation for the specific rate of dissipation of kinetic energy (ω).

A successful model has been obtained by combining the $k - \varepsilon$ and $k - \omega$ models, in order to take advantage of both formulations in regions where wall effects are dominant or where these are negligible. This model takes the name of $k - \omega$ SST model and is widely used in industrial problems due to the higher accuracy respect to a standard $k - \varepsilon$ model.

Within the framework of OpenFOAM, a number of RANS turbulence models are available, including the $k - \omega$ SST model, which will be the one used in the current application. The latter model combines both the $k - \varepsilon$ and $k - \omega$ turbulence models using the advantages of both. The equations used are one for the turbulent specific dissipation rate ω and the turbulent kinetic energy k [93]. The equation used for k is:

$$\frac{\partial(\rho k)}{\partial t} + \mathbf{u} \cdot \nabla(\rho k) = \nabla \cdot [(\mu + \mu_t)\nabla k] + \rho g - \frac{2}{3}\rho k(\nabla \cdot \mathbf{u}) - \rho\beta^*\omega k + S_k \quad (3.51)$$

While for ω :

$$\frac{\partial(\rho\omega)}{\partial t} + \mathbf{u} \cdot \nabla(\rho\omega) = \nabla \cdot [(\mu + \mu_t)\nabla\omega] + \frac{\rho\gamma g}{\nu} - \frac{2}{3}\rho\gamma\omega(\nabla \cdot \mathbf{u}) - \rho\beta^*\omega^2 - \rho(F_1 - 1)CD_{k\omega} + S_\omega \quad (3.52)$$

where a lot of constants have been introduced. The values used for these constants vary from application to application, but standard values are available and used in most applications. The main advantage of this model is the ability to capture flow separation and at the same time compute the free streams eddies, which has proven to be of enormous benefit on a large number of industrial applications.

3.4.2 LES Models

The idea behind the LES turbulence models is to model the larger unsteady turbulent motions while the effects of the smaller-scale motions are modelled. This leads to higher computational cost respect to the RANS models, but naturally higher accuracy. LES use in CFD has grown in the past years due mostly to the increase in computational resources, being applied to a large number of applications [94, 95, 96, 97]. In LES the larger-scale motions, which are usually affected by the flow geometry, are solved, while as stated before the smaller-scale motions are modelled, this mainly because these motions have to some extent a universal behaviour and modelling decrease the cost of the solution by orders of magnitude.

The LES models are obtained by four steps:

- The velocity field $\mathbf{u}(\mathbf{x}, t)$ is filtered and results into the sum of a resolved component $\bar{\mathbf{u}}(\mathbf{x}, t)$ and a residual component $\mathbf{u}'(\mathbf{x}, t)$. The resolved component represent the motion of the large eddies.
- The evolution of the velocity field is obtained by filtering the Navier-Stokes equations. This lead to an additional term in the momentum equation that has to be modelled.
- The term arising from the filtering operation in the momentum equation is modelled by an eddy-viscosity model.
- The velocity field is solved using the eddy-viscosity model in the momentum equation to obtain the large-scale motions of the flow.

One of the most delicate operations in LES formulations is, therefore, the filtering, and in the next paragraph, a brief description on the topic will be given.

Filtering

The filtering operation was introduced by Leonard in 1974 [98] and is defined by:

$$\bar{\mathbf{u}}(\mathbf{x}, t) = \int G(\mathbf{r}, \mathbf{x}) \mathbf{u}(\mathbf{x} - \mathbf{r}, t) d\mathbf{r} \quad (3.53)$$

with the integration over the whole fluid domain, and the filter function G satisfying the normalization condition

$$\int G(\mathbf{r}, \mathbf{x}) d\mathbf{r} = 1 \quad (3.54)$$

We can simplify the filter function by assuming that it is homogeneous, independent of \mathbf{x} . The residual field is defined as:

$$\mathbf{u}'(\mathbf{x}, t) \equiv \mathbf{u}(\mathbf{x}, t) - \bar{\mathbf{u}}(\mathbf{x}, t) \quad (3.55)$$

So that the velocity field is obtained as the sum of a filtered quantity plus a residual field. This operation appears to be similar to the Reynolds decomposition obtained for RANS models. However, the latter is a time-averaged decomposition, while the filtering operation operates in space and therefore the filtered velocity is time-dependent.

In order to understand the meaning of the filtering operation, a plot representing the filtering operation in one dimension is shown in Figure 3.4.

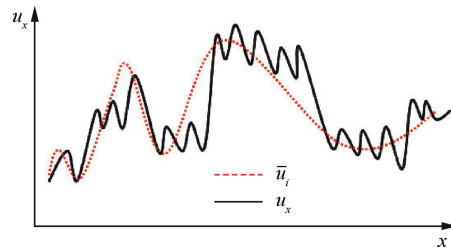


Figure 3.4: Filtering operation

In CFD, the filtering operation usually depends on the volume of the cell used, meaning that instead of an explicit filtering on the single terms of the equations, an implicit filtering is carried out by the computational domain. In this case, the filter assumes the form:

$$G(\mathbf{r}, \mathbf{x}) = \Delta \quad (3.56)$$

where Δ is the cell volume of the computational grid used.

Filtered Conservation Equations

The filtering operation is applied to the conservation equations [99] in order to obtain the evolution of the filtered velocity $\bar{\mathbf{u}}$. The equations will be derived for compressible flows, which are of interest in the current application. The filtered continuity equation is:

$$\frac{\partial \bar{\rho}}{\partial t} + \overline{\nabla \cdot (\rho \mathbf{u})} = \frac{\partial \bar{\rho}}{\partial t} \nabla \cdot (\bar{\rho} \bar{\mathbf{u}}) = 0 \quad (3.57)$$

From this equation, assuming the limit of incompressible flow we obtain the following:

$$\nabla \cdot \bar{\mathbf{u}}' = \nabla \cdot (\mathbf{u} - \bar{\mathbf{u}}) = 0 \quad (3.58)$$

The filtered compressible momentum equation leads to:

$$\frac{\partial(\bar{\rho} \bar{\mathbf{u}})}{\partial t} + \overline{\mathbf{u} \cdot \nabla(\rho \mathbf{u})} = -\nabla \bar{p} + \nabla(\mu \nabla \bar{\mathbf{u}} - \frac{2}{3} \mu \nabla \cdot \bar{\mathbf{u}}) \quad (3.59)$$

This equation is not equivalent to the N-S equation applied to the filtered velocity because of the non-linear advection term appearing on the left hand side. If we define the residual-stress tensor as:

$$\tau_{ij} = \overline{u_i u_j} - \bar{u}_i \bar{u}_j \quad (3.60)$$

we can then derive the N-S to be solved for the filtered velocity field:

$$\frac{\partial(\bar{\rho} \bar{\mathbf{u}})}{\partial t} + \bar{\mathbf{u}} \cdot \nabla(\bar{\rho} \bar{\mathbf{u}}) = -\nabla \bar{p} + \mu \nabla^2 \bar{\mathbf{u}} - \nabla \cdot (\bar{\rho} \boldsymbol{\tau}) \quad (3.61)$$

Equivalently to the RANS equations, the filtered N-S equations need to be closed, meaning that we have to model the residual stress tensor $\boldsymbol{\tau}$. A variety of models exist for the SGS term, the most used ones representing the term $\boldsymbol{\tau}^{dev}$ as a function of the rate of strain of the rate of strain of the large scales. This can be expressed in mathematical terms as:

$$\boldsymbol{\tau}^{dev} = -2\nu_{sgs} \bar{\mathbf{S}} \quad (3.62)$$

with ν_{sgs} being the kinematic eddy viscosity. The most known formulation for the eddy viscosity was obtained by Smagorinsky in 1963 [100] and is represented by the following equation:

$$\nu_{sgs} = (C_s \Delta)^2 |\bar{\mathbf{S}}| \quad (3.63)$$

with $|\bar{\mathbf{S}}| = \sqrt{2\bar{\mathbf{S}}\bar{\mathbf{S}}}$, Δ being the filter width (volume of the cell) and C_s a constant that usually takes a value between 0.1 and 0.2. This model assumes that an equilibrium exists between the energy production in the large scales and dissipation in the small scales, which is not always a correct assumption.

3.4.3 DNS Models

The main concept behind DNS modelling is to solve the Navier-Stokes equation on the fluid domain without the use of any turbulence model. This means that the mesh is fine enough in all the regions of the domain to be able to solve the smallest dissipative scales (Kolgomorov scales). The increasing availability of computational resources has increased the use of DNS simulations in the literature, but these are usually restricted to simple geometries and low Reynolds numbers, therefore not yet universally used. The number of mesh points (N) has to respect the following [92]:

$$N^3 \geq Re^{2.25} \quad (3.64)$$

therefore we can understand the enormous amount of resource needed in order to simulate even a flow with low Reynolds number. DNS simulations are however used in many cases to validate turbulence models because they represent technically the real flow and give much more information respect to experiments, where physical quantities are usually measured in a point.

3.5 Numerical Methods for Fluid Dynamics

As stated in the previous section, there is currently no universal analytical solution for the conservation equations. Therefore one approach used to solve fluid dynamics problems is by Computational Fluid Dynamics (CFD), by solving the equations numerically using modern computers. There are other approaches for the solution of fluid dynamics problems, such as the use of experimental facili-

ties, which have the advantage of representing the real physics, in the limitations given by the apparatus. Experimental analysis provides excellent results in the measurements of flow quantities such as the lift of an object, or the velocity field in a domain. The main problems are the intrusion caused by the measurement tools, and the limitation on the number of quantities and points that can be measured, not to mention the difficulty in reproducing real flows by matching the non-dimensional quantities.

On the other hand, CFD has theoretically no limitations in the representation of a problem, and the quantities given are available in all the mesh cells of the domain, providing a more detailed view of the whole flow field. Still, there are issues related to CFD solutions, such as the mesh sensitivity, stability and convergence of the solutions. In the past years, due to the exponential increase of computational resources, CFD solutions have become much more accurate, and the number of users taking advantage of them has grown massively.

Any method used for a numerical solution needs to go through some base components such as the mathematical model, the discretisation method, the choice of a computational grid, finite approximations of physical quantities, a solution method and eventually a convergence criterion. All these steps will be discussed briefly.

3.5.1 Mathematical Model

The first step for the solution of a CFD problem is the choice of a specific set of equations. The general conservation equations are too complicated, and one needs to make some assumptions in order to simplify them (2D flows, incompressible, isothermal, etc.). This is done because it is unachievable to obtain a set of equations valid for every type of problem, and some simplifications are only valid for a particular kind of flows (for example assuming that the flow around a supersonic aircraft is incompressible would lead to entirely wrong results).

3.5.2 Discretisation Method

The next step to be taken is to choose which type of discretisation to apply to the specific set of equations. This usually means to build a specific set of algebraic equations that represent the original partial differential equations in particular points of the domain. The solution of algebraic equations is easier and obtained by the use of iterative methods. There is a wide range of approaches that lead

to different formulations, but the most used ones are the Finite Difference (FD), Finite Volume (FV) and Finite Element (FE) methods. All three methods lead to the same solution if the mesh is fine enough in all the approaches. The choice of one or the other depends on the type of problem and the developer.

Most of the commercial and open-source software is currently using the Finite Volume Method, because it is highly conservative, and this will be the only one described in details.

3.5.3 Computational Grid

As the CFD process leads to a set of discretised equations, the solution is available in determined points or cells, depending on how the grid was obtained. A wide range of types of grid exists, but the primary classification is: structured or unstructured.

- A structured grid is usually defined by regular connectivity, and each point or cell of the grid can be numbered consecutively, allowing a high space efficiency, better convergence and higher resolution. An example of a 2D structured grid is shown in Figure 3.5.

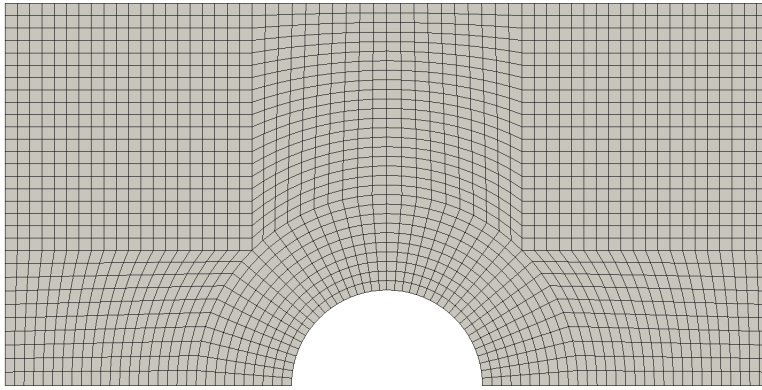


Figure 3.5: Structured Grid around a semi-cylinder

Even though they are advantageous from a solution point of view, structured grids are limited to simple geometries, and due to their nature, a fine spacing in one specific area of interest leads to a waste of resources in other zones where fine spacing is not required, increasing the data size and computational time.

- Unstructured grids are the most flexible because they can fit any arbitrary solution domain boundary. Connectivity is irregular in such grids. Therefore it is not simple to express them as an array of points in a simple way, such as

structured grids, and for this reason, the solution is usually slower if compared to a structured mesh. The most used types of unstructured grids are triangular in 2D domains and tetrahedral in 3D ones, but there is no restriction in the shape of the elements nor the number of neighbours of each cell. An example of an unstructured grid is shown in Figure 3.6.

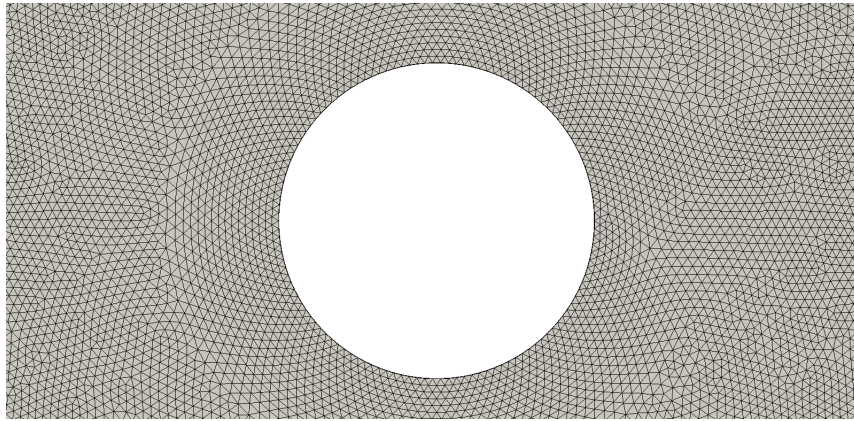


Figure 3.6: Unstructured Grid around a cylinder

- Structured and unstructured grids can be used in the same domain, defining a so called "hybrid" grid. These type of grids are somehow advantageous.

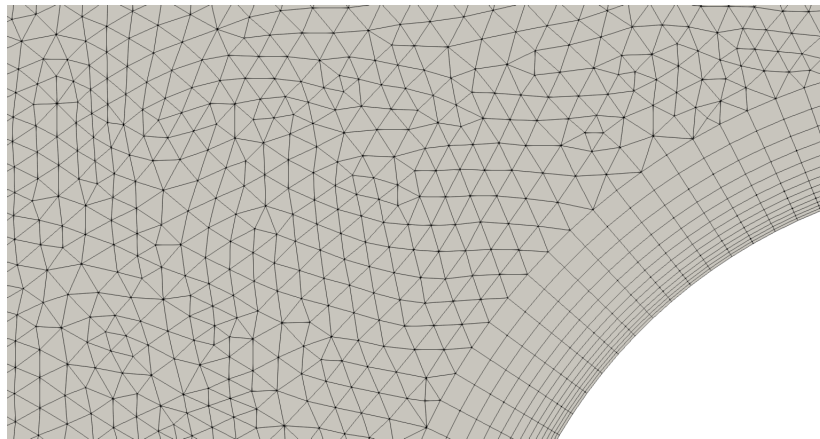


Figure 3.7: Hybrid Grid used to model the boundary layer

To conclude this section on computational grids, it is worth mentioning the meaning and use of staggered grids. While on collocated (also known as non-staggered) grids the variables are all stored in the same location, in staggered grids the scalar variables are stored in the cell centres of the control volume, while vectorial quantities such as velocity are located at the cell faces. This allows to face coupling problems between pressure and velocity. On the other hand, the

main disadvantage of staggered grids is that variables are stored in different places bringing complications in the code. In the current work collocated grids will be used as it is the standard method used in OpenFOAM.

3.5.4 Finite Approximations

After having defined a computational grid, it is necessary to determine how to approximate mathematical quantities in the discretisation process. For example, in the Finite Volume Method, one has to define how to approximate the surface and volume integrals. The choice depends on the user and how approximate they want the solution to be. Higher approximations require more nodes for the calculation of the derivative for example, but they are not always a better choice over lower approximations.

3.5.5 Solution Method

The system to be solved to obtain the physical solution is non-linear and contains a large number of quantities. The solution method depends pretty much case by case but the general rule is that for steady state flows a pseudo-time marching iterative scheme is used, while for unsteady flows each time steps is solved through an iterative process.

3.5.6 Convergence Criteria

The last step in the solution of a CFD problem is the choice of a convergence criterion. Usually, this is made by choice of residual values below which the solution is considered converged to its exact value, or by a number of maximum iterations above which the solver will not go.

3.6 Convergence, Consistency and Stability

Every solution method should follow some rules, in order to obtain the correct physical solution. This is usually achieved by the observation of three properties, the convergence, consistency and stability (the Lax equivalence theorem states that a consistent numerical method for a well-posed linear initial value problem is convergent if and only if it is stable).

- A numerical method is *convergent* if the solution of the discretised equations tends to the exact solution with the grid spacing and time step tending to zero.
- A numerical method is *consistent* if the truncation error (defined as the difference between the discretised equation and the exact one) of a discretised equation tends to zero with the grid spacing and time step tending to zero. The truncation error is usually proportional to the power of the grid spacing and/or time step $\Delta x^n, \Delta t^m$. Consistency is therefore fulfilled if the values of n, m are greater than 0. It can also happen that the truncation error is a function of the ratio between Δx and Δt , and in this case the condition of $n, m > 0$ is not enough, and other approaches have to be used to prove consistency.
- A numerical method is *stable* if an error in the solution is not magnified during the calculation process.

3.7 Discretisation approaches

When an engineering problem where partial differential equations (PDE) have to be solved is approached, one can choose between different approaches, depending on how the domain of interest is discretised and the equations solved.

3.7.1 Finite Difference Method

Historically this was the first method used, and it is easy to implement in very simple geometries. The conservation equations are solved in their differential form on a grid by approximating the derivatives at the nodes of the grid. This is usually achieved by using Taylor's series. This method is typically applied to structured grids. Despite this method is easy and high order approximations are not complicated to implement, the limitation on a simple grid and the lack of conservation regarding physical quantities are the main reasons why it is not widely used.

3.7.2 Finite Volume Method

This is the method most used in the literature [101], and it is the one used in the current work. The main advantages are the enforced conservation and its flexibility to adapt to any type of grid. Main disadvantages are the difficulty in implementing high order schemes and the more complex formulation.

3.7.3 Finite Element Method

This method is relatively similar to the finite volume one, but the main difference is that the equations are weighted on each element before being solved. It is highly adaptive on any type of mesh and is mostly used in structural analysis problems, while its use is limited in CFD applications.

3.8 The Finite Volume Method

The discretisation method for the equations of fluid dynamics has a difficult task because the equations are coupled and non-linear. Although there is a wide range of methods to approach this, as stated in the previous section the Finite Volume Method is the most widely used in commercial codes and by OpenFOAM, the software used in the current work.

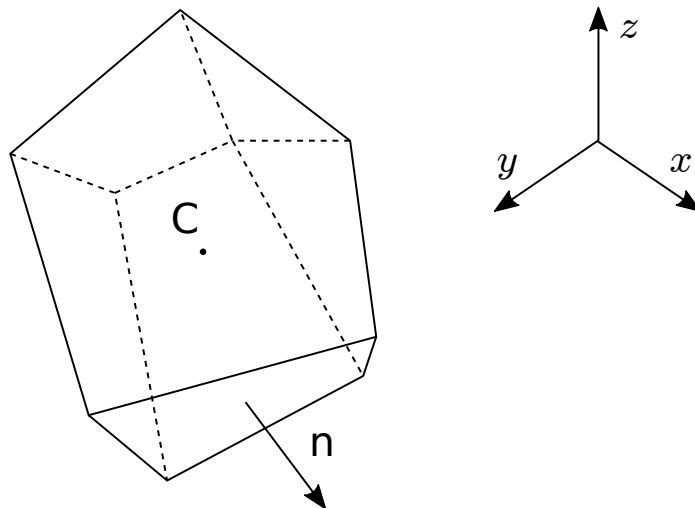


Figure 3.8: General shape of a control volume

The Finite Volume Method, often abbreviated with FVM, is an approach used in Computational Fluid Dynamics to discretize and calculate the solution of a defined flow problem. Its great flexibility as a discretization method and its conservativeness make it the most used method in commercial CFD codes.

The main concept behind this method is to divide the domain into subvolumes (Figure 3.8 shows a general control volume with the cell centre and the normal of one of its faces) where the discretised Navier-Stokes equations are solved. All the equations are then put together into a system and solved simultaneously. Introducing the conservation equation for a given scalar variable ϕ :

$$\frac{\partial(\rho\phi)}{\partial t} + \nabla \cdot (\rho\mathbf{u}\phi) = \nabla \cdot (\Gamma^\phi \nabla \phi) + S^\phi \quad (3.65)$$

Where we can identify the transient term, convective term, diffusion term and source term. If we define a closed volume, we can integrate the previous equation. To simplify the problem, we are going to assume also that the problem is steady state. Therefore the conservation equation becomes:

$$\nabla \cdot (\rho\mathbf{u}\phi) = \nabla \cdot (\Gamma^\phi \nabla \phi) + S^\phi \quad (3.66)$$

The terms $\phi, \Gamma^\phi, S_\phi$ vary with the equation that we are considering and assume the following values:

$$\phi = 1, \Gamma^\phi = 0, S_\phi = 0 \quad \text{for the continuity equation} \quad (3.67)$$

$$\phi = \mathbf{u}, \Gamma^\phi = \mu, S_\phi = -\nabla p \quad \text{for the momentum equation} \quad (3.68)$$

$$\phi = e + K, \Gamma^\phi = \alpha, S_\phi = \nabla \cdot (\vec{u}p) \quad \text{for the energy equation} \quad (3.69)$$

Considering the element defined by its centre C shown in Figure 3.8 we can then integrate:

$$\iiint_{V_C} \nabla \cdot (\rho\mathbf{u}\phi) = \iiint_{V_C} \nabla \cdot (\Gamma^\phi \nabla \phi) + \iiint_{V_C} S^\phi \quad (3.70)$$

This equation is valid for all the single volumes in which the domain is divided, and if we sum up all the integrals for all the volumes in the domain, we obtain a conservation equation for the whole domain, because the surface integrals in neighbour cells cancel out.

Using the divergence theorem, we can transform the volume integrals in surface integrals:

$$\oiint_{\partial V_C} (\rho\mathbf{u}\phi) \cdot d\mathbf{S} = \oiint_{\partial V_C} (\Gamma^\phi \nabla \phi) \cdot d\mathbf{S} + \iiint_{V_C} S^\phi \quad (3.71)$$

3.8.1 Flux Integration

As evidenced in the last equation, the convective and diffusive terms have to be integrated on the volume surfaces, and this is one of the fundamental discretisations in the FVM. If we introduce the convection and diffusion flux terms respectively with $\mathbf{J}^{\phi,C}$ and $\mathbf{J}^{\phi,D}$, the total flux on a certain cell is defined by the sum of the two:

$$\mathbf{J}^{\phi} = \mathbf{J}^{\phi,C} + \mathbf{J}^{\phi,D} \quad (3.72)$$

The surface integrals of the fluxes can be obtained by the sum of the fluxes over the faces of the volume element, leading to:

$$\oint_{\partial V_C} \mathbf{J}^{\phi,C} \cdot d\mathbf{S} = \sum_{faces(V_C)} \left(\iint_{S_i} (\rho \mathbf{u} \phi) \cdot d\mathbf{S} \right) \quad (3.73)$$

$$\oint_{\partial V_C} \mathbf{J}^{\phi,D} \cdot d\mathbf{S} = \sum_{faces(V_C)} \left(\iint_{S_i} (\Gamma^{\phi} \nabla \phi) \cdot d\mathbf{S} \right) \quad (3.74)$$

$$\oint_{\partial V_C} \mathbf{J}^{\phi} \cdot d\mathbf{S} = \sum_{faces(V_C)} \left(\iint_{S_i} \mathbf{J}_f^{\phi} \cdot d\mathbf{S} \right) \quad (3.75)$$

where S_i represents one of the faces of the volume considered. In order to obtain conservation, it is fundamental that the volumes do not overlap with each other.

These equations, instead of integrating the quantities within the volume, calculate the fluxes on the faces of the element, making the Finite Volume Method conservative.

In order to understand how these surface integrals are calculated, only one face of a specific cell will be considered. Figure 3.9 shows a typical layout for a structured 2D grid in order to simplify the problem (3D grids are equivalent and the process is the same). To calculate the surface integral on the cell, it is necessary to know the values of the fluxes along the whole surfaces. This is obviously not feasible in the FV method as the values of the variables are stored only in the cell centres, for this reason, some approximations have to be made. The first approximation is that the surface integrals are approximated by using the variable value only at one point of a cell face. The second is that the cell face values of the quantities are calculated using the cell centre values via an

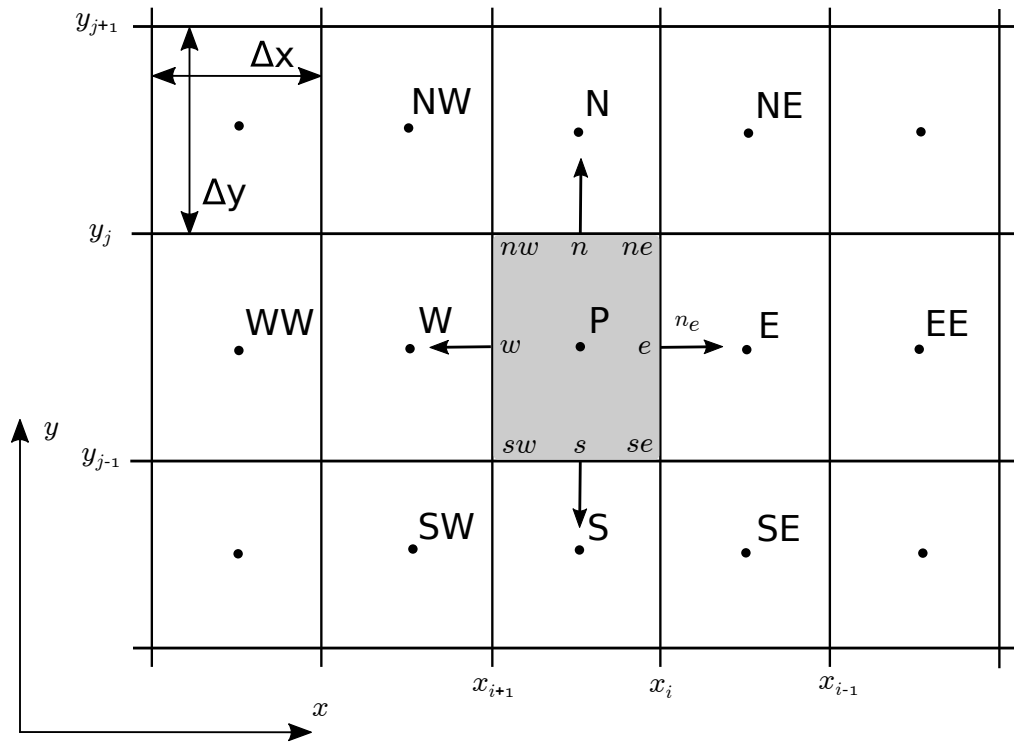


Figure 3.9: Notation for a 2D Control Volume

interpolation process.

The approximation of surface integrals can be done for example using a Gaussian quadrature procedure. This is a numerical tool used to approximate the definite integral of a given function by using known values at specific points of the element.

For example, given a function $f(x)$ (one dimensional just to simplify) known over the interval $[a, b]$, we can use the Gaussian quadrature to calculate its integral over the interval in the following way:

$$\int_a^b f(x)dx = \sum_{i=1}^n \omega_i f(x_i) \tag{3.76}$$

therefore using the function value in the point i and its weighting function ω_i .

The accuracy of the integration process depends on the number of points available and the weighing function. The simplest possible integration is the so-called trapezoidal rule, where only one point on the face is used, and the weighting function is equal to 1. This is second order of accuracy and can be extended to 2D and 3D cases.

For example, considering the face e in Figure 3.9, the surface integral of the

flux \mathbf{J}^ϕ can be obtained as:

$$\iint_{S_e} \mathbf{J}^\phi \cdot d\mathbf{S} = \mathbf{J}_e^\phi \cdot \mathbf{n}_e S_e \quad (3.77)$$

There are also other possibilities to choose from in order to calculate surface integrals, for example the trapezoidal rule, a second order of accuracy integration that uses the values in two points of the surface:

$$\iint_{S_e} \mathbf{J}^\phi \cdot d\mathbf{S} = (\mathbf{J}_{ne}^\phi \cdot \mathbf{n}_e + \mathbf{J}_{se}^\phi \cdot \mathbf{n}_e) \frac{S_e}{2} \quad (3.78)$$

Another possibility is to use a higher order of accuracy interpolations, where the values at more than 2 points are needed, such as the Simpson's rule:

$$\iint_{S_e} \mathbf{J}^\phi \cdot d\mathbf{S} = (\mathbf{J}_{ne}^\phi \cdot \mathbf{n}_e + 4\mathbf{J}_e^\phi \cdot \mathbf{n}_e + \mathbf{J}_{se}^\phi \cdot \mathbf{n}_e) \frac{S_e}{6} \quad (3.79)$$

As mentioned, the value of the variables (and therefore the fluxes) are usually stored in the cell centre (this is valid for most commercial and open-source software), consequently a second interpolation has to take place in order to calculate the values on the cell faces. The above mentioned trapezoidal rule has a second order of accuracy. Therefore one needs to interpolate the surface values with at least the same order of accuracy.

3.8.2 Source Term Integration

In the conservation equations, after having evaluated the surface integrals, there might be some source terms that have to be integrated within the control volumes. Making use again of the Gaussian quadrature integration we can compute the integral in the following way:

$$\iiint_V Q^\phi dV = Q_C^\phi V_C \quad (3.80)$$

where C denotes the cell and the value of Q^ϕ is calculated in the cell centre. Since this value is available, no interpolation is needed as in the surface integration terms. The calculation of volume integrals with the above equation is exact if the solution is constant or varies linearly within the cells. If not, it has an accuracy of second order.

3.8.3 Boundary Conditions

Every computational cell provides an algebraic equation, and if summed up altogether these equations give a system to be solved. Some of the cells in a computational domain are not entirely surrounded by other cells, and these are called boundary cells. Therefore the system requires that the values on such faces have to be specified by the user. These values take the name of boundary condition (B.C.), and they have to be set in such a way as to represent the computational model the closest possible to the real one.

Although there is a wide range of boundary conditions available, they can be all described by two types: the Dirichlet and the Neumann boundary condition. The Dirichlet B.C. specifies the value of a quantity on the boundary, while the Neumann B.C. specifies the gradient of the variable on the boundary. All the other B.C. are a combination of these.

In CFD it is common practice to use standard B.C., but there is no general rule. For example, on solid walls, the value of the relative flow velocity is set to be zero, because particles cannot cross the surface and because the tangential velocity is null because of viscosity, and the pressure gradient is set to be zero, as it can be easily demonstrated using the boundary layer equations. Inlet boundaries are usually defined by a constant value of velocity set according to the flow properties and zero gradient for pressure. The presence of outlets is necessary for the domain so that the conservation of mass can be respected.

3.9 Resolving the System of Algebraic Equations

It was shown earlier that the discretisation process of the conservation equations leads to a system of algebraic equations, which can be linear or non-linear depending on the nature of the problem and the equation discretised. The matrices obtained from such procedure are most of the time sparse, meaning that a large number of elements are zero. This is not always valid, especially when using unstructured grids. For this reason, the solution of fluid dynamics problems using structured grids is faster, because the structure of the matrices is used to accelerate the solution procedure. On the other hand, unstructured grids are more straightforward to make, but the solution of the algebraic system is usually slower, leading to longer computational times.

The general structure of an algebraic system can be expressed as:

$$\mathbf{A}\phi = \mathbf{Q} \tag{3.81}$$

In order to solve such equation two main approaches are used, the direct and iterative method. Direct methods are usually effective when the matrix \mathbf{A} is very sparse while iterative methods (the most used) are effective when the matrix has a general structure, and the number of coefficients is very high.

3.9.1 Direct methods

Direct methods aim to solve the algebraic system with a finite number of operations. In theory, in the absence of rounding errors (which cannot be neglected in computer calculations), the solution obtained with such methods is equal to the exact solution. While this seems of significant advantage, the increase of computational costs for large sparse systems of equations is too demanding and therefore direct methods are rarely used.

The basic method adopted in direct methods [102] is named after the German mathematician Carl Friedrich Gauss. The base concept behind this method is to reduce the large system of equations to smaller ones. During this procedure, only the coefficient matrix \mathbf{A} is modified. Therefore the method can be described without involving the vector of the dependent variable. The general structure of the matrix \mathbf{A} can be expressed as:

$$\mathbf{A} = \begin{pmatrix} a_{11} & a_{12} & \dots & a_{1n} \\ a_{21} & a_{22} & \dots & a_{2n} \\ \vdots & \vdots & \ddots & \vdots \\ a_{n1} & a_{n2} & \dots & a_{nn} \end{pmatrix} \tag{3.82}$$

The concept is to eliminate the coefficient a_{21} , replacing it with a 0. This can be achieved by multiplying the first row by a_{21}/a_{11} and subtracting it from the second row. By using this procedure, all the elements in the second row are modified as well as the vector on the right-hand side of the system \mathbf{Q} . The same process can be used to eliminate the first coefficient of the other rows, just multiplying the first row by a_{n1}/a_{11} and subtracting it from the n^{th} row. This procedure is then applied to the second coefficient of the third row on, and so on. At the end of such operation, one obtains a matrix with the following structure.

$$\mathbf{U} = \begin{pmatrix} a_{11} & a_{12} & \dots & a_{1n} \\ 0 & a_{22} & \dots & a_{2n} \\ \vdots & \vdots & \ddots & \vdots \\ 0 & 0 & \dots & a_{nn} \end{pmatrix} \quad (3.83)$$

This is called in algebra an upper triangular matrix. As mentioned before all the elements of the vector on the right-hand side of the equations are also modified. It is therefore possible solve all the equation starting from the last one:

$$\phi_n = \frac{Q_n}{A_{nn}} \quad (3.84)$$

The next equation contains therefore only one unknown variable ϕ_{n-1} since ϕ_n has been just calculated, hence the unknown variable can be obtained. This procedure can be applied moving upwards and consequently the value of a general j^{th} component of the vector ϕ is obtained as:

$$\phi_j = \frac{Q_j - \sum_{k=j+1}^n A_{jk}\phi_k}{A_{jj}} \quad (3.85)$$

This procedure of obtaining the solution starting from the last row is called back substitution.

It can be demonstrated that if the number of equations n is large, the computational cost by mean of a number of operations is proportional to the value $n^3/3$. For this reason, and also because this method is hard to implement in parallel codes, Gaussian elimination is rarely used in CFD codes. A number of methods derived from the Gaussian elimination have been therefore proposed in order to decrease the number of operations and take advantage of any sparse structure of a matrix, and also to avoid the numerical errors that are accumulated in the diagonalisation of the matrix. Among these, the most used one is the *LU* decomposition, which is basically the matrix form of Gaussian elimination. Other effective methods worth mentioning are the multigrid method and some of its derivatives such as the Krylov subspace methods, which most of the time are associated with orthogonalisation schemes.

3.9.2 Iterative methods

Iterative methods are mostly used in non-linear systems, where the direct methods cannot be adopted, but they are also used in linear systems because direct

methods are computationally too demanding for large grids and the error is such that their usage is not advantageous if compared to iterative methods.

The basic concept is to guess an initial solution and calculate the next one by using the previous one and the equations to improve it. Each solution is, therefore, more accurate than the previous one, and if the iteration process is cheap and the number of iterations is relatively small, then iterative methods are way faster than direct methods. The iterative process leads to an n^{th} guess of the solution which differs from the exact one by an error ϵ^n defined as:

$$\epsilon^n = \phi - \phi^n \quad (3.86)$$

where ϕ is the exact solution and ϕ^n the solution obtained by the iterative process. The system of equations applied to the guessed solution differs therefore from the exact one by a residual $\rho^n = \mathbf{A}\epsilon^n$:

$$\mathbf{A}\phi^n = \mathbf{Q} - \rho^n \quad (3.87)$$

The aim of the method is to drive the residual to zero, and this has to be obtained in the simplest and fastest way possible, in order to speed up the simulation calculation. This is achieved by what is called fast convergence, and the choice of the iterative method is fundamental to have an optimal value of convergence.

The calculation of the exact solution is never achieved in an iterative method, this because the residual will go to zero for an infinite number of iterative procedures, and this is obviously unachievable in reality. Therefore in CFD codes usually the final solution is traditionally calculated by setting a maximum number of iteration and/or a minimum value of the residual to be obtained.

Another method widely used in modern CFD codes is a variant of the Gauss-Seidel method, and it is called successive over-relaxation (SOR), used for solving a linear system of equations. For an algebraic system defined by $\mathbf{A}\mathbf{x} = \mathbf{b}$, the SOR method can be written in matrix terms as:

$$\mathbf{x}^n = (\mathbf{D} - \omega\mathbf{L})^{-1}[\omega\mathbf{U} + (1 - \omega)\mathbf{D}]\mathbf{x}^{n-1} + \omega(\mathbf{D} - \omega\mathbf{L})^{-1}\mathbf{b} \quad (3.88)$$

with \mathbf{D} , $-\mathbf{L}$, $-\mathbf{U}$ being the diagonal, strictly lower-triangular and strictly upper-triangular parts of \mathbf{A} , respectively and ω being the relaxation factor. Usually the choice of such factor is not easy and highly depends on the type of matrix of the problem analysed, but usually to achieve fast convergence a value

of $1 < \omega < 2$ is used.

3.9.3 Under-Relaxation

Stability is one of the core issues in the solution method. While the condition of having a Courant number smaller than 1 is enough in most problems, another technique is also used to control stability, especially in steady-state problems where the lack of a temporal term, which has a stabilising effect, can lead to instability problems. The concept of under-relaxation was developed by Patankar [79] and basically limits the change of a variable during an iteration. For a general variable ϕ this can be expressed as:

$$\phi^{n+1} = \phi^n + \alpha(\phi^{n+1} - \phi^n) \quad (3.89)$$

Therefore the new value of a variable is replaced using its own value, the value at the previous iteration and a coefficient α which is called the under-relaxation factor. This value has to be in the range $[0 : 1]$, where a value of 1 corresponds to no relaxation and a value of 0 to complete relaxation. An optimal value for this coefficient is problem dependent but as a general rule, we can assume a small value for α in the early iterations when a large change of the variables has to be controlled while changing to a value closer to unity once the solution gets close to convergence.

3.10 Pressure-Velocity coupling

The methods introduced in the previous section take into consideration for the general solution of a system of equations. In the momentum equation, there is a term that contains the gradient of pressure, in all the three components. This is an additional term that has to be known or calculated from another equation. In compressible flows, the continuity equation contains the variable ρ and its value changes within the computational grid. In these flows, the continuity equation is used to calculate the density and the pressure is then obtained by using the equation of state. This type of approach is called density-based approach. On the other hand, in incompressible flows, where the continuity equation is more a constraint on the other equations rather than something that adds information to the solution, the density cannot be calculated and is usually considered constant. Therefore another equation has to be obtained for the pressure so that there is an

equal number of variables and equations. This approach is called pressure-based and is largely used in incompressible flows even though it finds applications in compressible flows as well.

3.10.1 The pressure equation

In order to obtain an equation that can be solved to obtain the pressure, one can think of using the continuity equation and somehow use it along with the momentum equation. Calculating the divergence of the momentum equation, some terms cancel out (because $\nabla \cdot \mathbf{u} = 0$), leading to the Poisson equation for pressure:

$$\nabla \cdot \nabla p = -\nabla \cdot \left[\nabla \cdot (\rho \mathbf{u} \mathbf{u} - \mathbf{S}) - \rho \mathbf{g} + \frac{\partial \rho \mathbf{u}}{\partial t} \right] \quad (3.90)$$

In the case of incompressible flows, with constant density, and also considering that the viscosity is constant, the equation simplifies as:

$$\nabla^2 p = -\nabla \cdot (\nabla \cdot (\rho \mathbf{u} \mathbf{u})) \quad (3.91)$$

This equation is therefore solved along with the momentum equation. The discretisation process is the same used for the conservation equations described already. The difficulty of solving such equation along with the momentum equation is that the pressure and the velocity are coupled, therefore a segregated approach (where one equation is solved first and then the other one) cannot be used.

3.10.2 The SIMPLE algorithm

For steady state problem, Patankar and Spalding have developed an algorithm [103] which takes the name of SIMPLE (Semi Implicit Method for Pressure Linked Equations) [104]. This consists of several steps:

1. An initial guess for the pressure and velocity fields is considered, which can be either the value of such quantities at the previous time step or a general field believed to give faster convergence of the solution (usually only in the first step of the solution)
2. The momentum equation is then solved to obtain the new value of the velocity field. Because the pressure used in this equation is not the exact

one at the new time step, it will not satisfy the continuity equation

3. The values of the velocity field are used to calculate the mass fluxes on the cell faces
4. With the new mass fluxes calculated from the previous step, new values for the pressure are obtained from the solution of the pressure equation
5. The pressure and velocity fields are updated with new values using the continuity equation
6. The process starts again from step 2 until convergence is obtained

3.10.3 The PISO algorithm

Issa [105] developed an algorithm as an extension of the SIMPLE algorithm for unsteady flows, which is called PISO (Pressure Implicit with Splitting of Operator) [104]. The algorithm is computed using the following steps:

1. The solver sets the boundary conditions for the problem considered
2. The momentum equation is solved to obtain an intermediate velocity field
3. The values of the velocity field are used to calculate the mass fluxes on the cell faces
4. With the new mass fluxes calculated from the previous step, new values for the pressure are obtained from the solution of the pressure equation
5. The mass fluxes on the cell faces are updated again using the new values of the pressure field
6. The velocity is corrected using the new values of the pressure field
7. The boundary conditions are updated with the new fields values
8. The solver starts again from step 3 for a number of times specified by the user
9. The solution time is increased with the time step value and the process starts again from step 1

The PISO algorithm can give more stable results and usually takes less computational resources and can also be used for steady state problems.

3.10.4 The PIMPLE algorithm

The solution of coupled pressure momentum equations can be solved by the SIMPLE or PISO algorithm as shown in the previous section. In OpenFOAM, this can also be achieved by using a method which is a combined version of the two together, called PIMPLE [106].

The PIMPLE algorithm takes, therefore, advantage of both methods, and better stability can be achieved over the PISO method, allowing for larger time steps and therefore bigger courant numbers. The number of outer correctors is usually defined by the user, and the solver will iterate over the solution until convergence is reached. This is advantageous because if the solution is stable a low number of iteration will take place, but if there is high instability the solver will try to converge using a higher number of iterations.

The relaxation factor is fundamental in such method, and can be used as an advantage when unstable solutions are present, giving room for higher time steps, in change of a high number of iterations.

3.11 Chapter summary

In this chapter, the principal methodology used in the current work was explained, starting from the basic concepts of fluid dynamics, especially the solution of multiphase flows, up to the computational fluid dynamic approach. The main turbulence models were introduced, which will be mentioned later on. In the next chapter the development of the *cascadeFoam* will be presented and validated against experimental data, showing the limits of the currently available models and areas of improvement.

Chapter 4

Cascade Solver Development

In this section, the development of the `cascadeFoam` solver is explained and validated against numerical experiments. The solver was developed starting from the standard one available in OpenFOAM (*sprayFoam*) and then modified to accurately reproduce the physics of liquid spills from storage tanks. OpenFOAM has been previously used for a number of applications, including the dispersion of heavy gas into the atmosphere [107].

The *sprayFoam* solver is available in the standard version of OpenFOAM and was developed primarily for diesel internal combustion engines [108] (in fact it was previously called *dieselFoam*). It uses a Lagrangian approach to solve dispersed sprays of liquid droplets. The standard continuity and momentum equations along with the energy equation are solved for the continuum phase. For all the three equations source terms are added to take into account for the lagrangian phase. An additional transport equation is solved for all the species present in the flow (the continuum phase is composed of a mixture of gases) and source terms are present here as well relating the amount of liquid that evaporates for the selected component. The solver is capable of solving combustion using a list of models available in OpenFOAM. The lagrangian phase is solved using the equations described in the previous chapter and two way coupling can be activated between continuum and discrete phase.

4.1 Interaction of parcels with solid surfaces

Following the investigation carried out by HSL on Buncefield accident, the need for an appropriate tool to model the interaction between droplets and ground

turned out to be one of the most important key points of the solver development [109]. The standard *sprayFoam* solver does not allow any splashing of droplets onto solid surfaces, confining the user to use standard wall interaction models such as rebound, stick or simply disappearing. In reality, the regimes experienced in a droplet-wall interaction are vast and a good overview is represented in Figure 4.1.

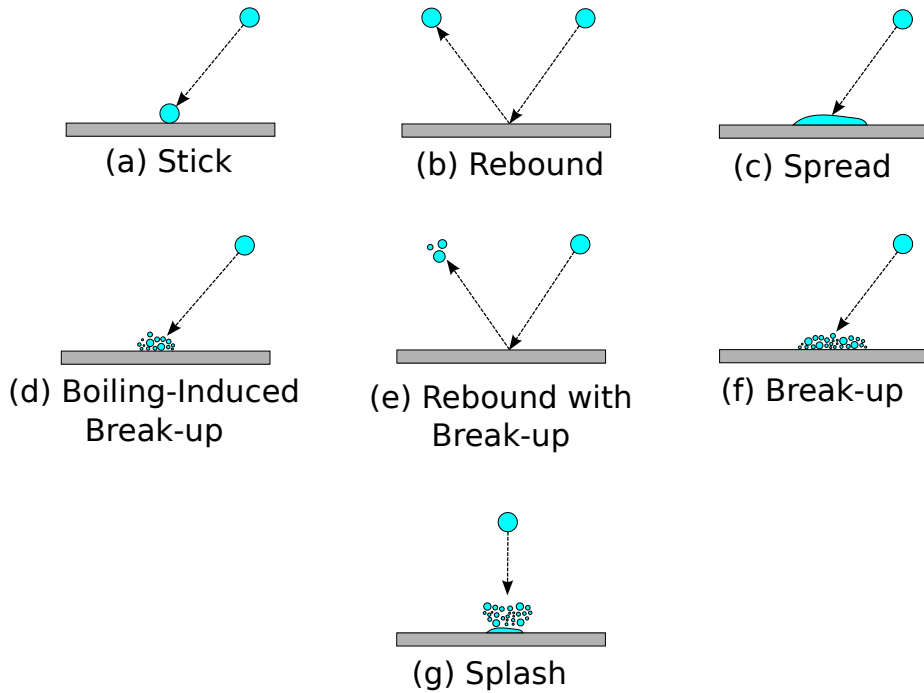


Figure 4.1: Schematic of the different impact regimes

The outcome of such interaction depends highly on a number of input parameters such as droplet velocity, diameter, physical properties, and also on the solid surface roughness, temperature and any existing liquid film present on the wall.

Although in the literature a large number of models applicable to lagrangian solvers are available [110, 111], the lack of appropriate wall-interaction modelling for the current application has to be addressed and a splashing model has to be introduced, in order to correctly model the interaction between droplets and walls, which can be either wet or dry.

4.2 Buoyancy effects

A second problem that had to be faced within the solver was the effect of buoyancy. The standard *sprayFoam* solver cannot model movements of air due to

density differences accurately, mainly because it was developed within a framework where this effect had a minor impact on the quality of the results.

The effects of gravity on the atmosphere are understandable if we think about the change in pressure, density and temperature with altitude. In applications where multispecies are present (in fact the Eulerian phase is solved as a mixture of components), or where the height of the domain is such that density varies within the vertical coordinate, the latter can vary in different regions of the domain and therefore air can move in the absence of external forces. This has to be taken into account in the solver with appropriate terms in the momentum equation. In the case of hexane, a liquid that will be used to validate the solver developed, its density is higher than the one of standard atmosphere, leading to a vapour cloud that tends to stay close to the ground in the absence of other obstacles. On the other hand, if we consider Liquefied Natural Gas, the vapour formed has different densities depending on the temperature at which it is stored. When it comes in contact with the atmosphere, the gas has a temperature equivalent to the one at which the liquid is stored, and the gas has a density higher than the atmosphere. While the temperature of Natural Gas gradually increases, getting close to normal atmospheric temperature, its density starts to lower and gets to a lower value respect to the atmospheric one (the dependency of density with temperature is shown in Figure 4.2), leading to a lighter gas that tends to rise.

This is easily observed in the dispersion of natural gas in very big domains, where the gas tends to stay close to the ground while it is cold, and with heat exchange with the surrounding air warming it up, becomes lighter than air and therefore tends to rise in the atmosphere.

The modelling of density-driven flows (also known as buoyancy-driven flows) can be done in several ways, depending on the accuracy and needs of the solution. The effect of buoyancy is also highly important in the solution of turbulence, and a number of models are available in the literature [112].

For many applications such as natural ventilation or gas dispersion, the differences in density are only present because of temperature gradients. For such flows, the mathematician Joseph Valentin Boussinesq developed an approximation named after him. Density variations are only considered in the terms multiplied by the gravity while inertia related effects are negligible. The conservation of mass is expressed by:

$$\frac{\partial \rho}{\partial t} + \nabla \cdot (\rho \mathbf{u}) = 0 \quad (4.1)$$

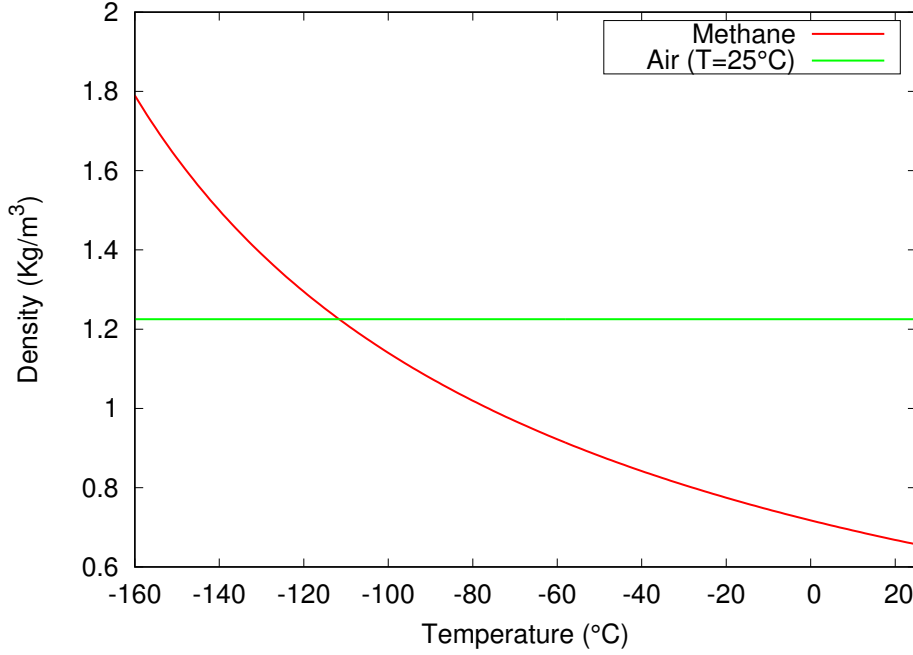


Figure 4.2: Methane (main component of LNG) density at atmospheric pressure compared to the air one

If variation of density is ignored, this simply leads to:

$$\nabla \cdot \mathbf{u} = 0 \quad (4.2)$$

The general momentum conservation equations is:

$$\frac{\partial \mathbf{u}}{\partial t} + \mathbf{u} \cdot \nabla \mathbf{u} = -\frac{1}{\rho} \nabla p + \nu \nabla^2 \mathbf{u} + \frac{1}{\rho} \mathbf{F}_g \quad (4.3)$$

where F_g represents the body force due to gravity. Density in the Boussinesq approximation is expressed as a sum of a fixed part and a term that depends on temperature. The gravity force can be therefore calculated as:

$$\mathbf{F}_g = \rho \mathbf{g} = (\rho_0 - \beta \rho_0 \Delta T) \mathbf{g} \quad (4.4)$$

where β is the thermal expansion coefficient and $\Delta T = T - T_0$ is the temperature difference. In the current application, this approximation is not used, and buoyancy is adequately treated in the momentum equation, leading to a more accurate solution.

4.3 Development of the cascadeFoam solver

Within the framework of OpenFOAM, the presence of a class able to solve liquid films and consequently the splashing process was implemented in the *cascadeFoam* solver. Along the development of a splashing model, the possibility to use enhanced buoyancy in the momentum equation was implemented too.

4.3.1 Liquid Film Region

In order to implement and allow the solver to model the splashing, a new region has to be introduced in the domain of solution, so that the droplet interacts with a liquid region representing the film formed by the splashed particles [113]. This is a 2.5D (two and a half dimensional) region where the conservation equations are solved for the thin liquid film. The assumption of thin-film is that [114]:

- The wall-normal velocity is equal to zero
- The wall-tangential diffusion (momentum, energy) is negligible compared to the wall-normal diffusion

With these assumptions the conservation equations for the film region can be written as:

$$\frac{\partial \rho \delta}{\partial t} + \nabla \cdot (\rho \delta \mathbf{u}) = S_{\rho \delta} \quad (4.5)$$

$$\frac{\partial \rho \delta \mathbf{u}}{\partial t} + \nabla \cdot (\rho \delta \mathbf{u} \mathbf{u}) = -\delta \nabla p + S_{\rho \delta u} \quad (4.6)$$

$$\frac{\partial \rho \delta h}{\partial t} + \nabla \cdot (\rho \delta \mathbf{u} h) = S_{\rho \delta h} \quad (4.7)$$

where δ is the thin film thickness, and S represents the source term for mass momentum and energy arising from the other phases or the solid surface where the film is located. These terms include the interaction with the splashed droplets, evaporation and condensation, heat transfer with the gas phase and with the solid substrate. Other secondary effects such as the capillary effect can be taken into account, but their impact is limited in the current application, while it cannot be avoided in another type of problems [115]. In order to 'couple' the two regions, the gas and liquid one, the solutions variables have to be mapped to/from the

gas phase mesh. A picture showing droplets splashing onto the liquid film region and the film thickness is shown in Figure 4.3.

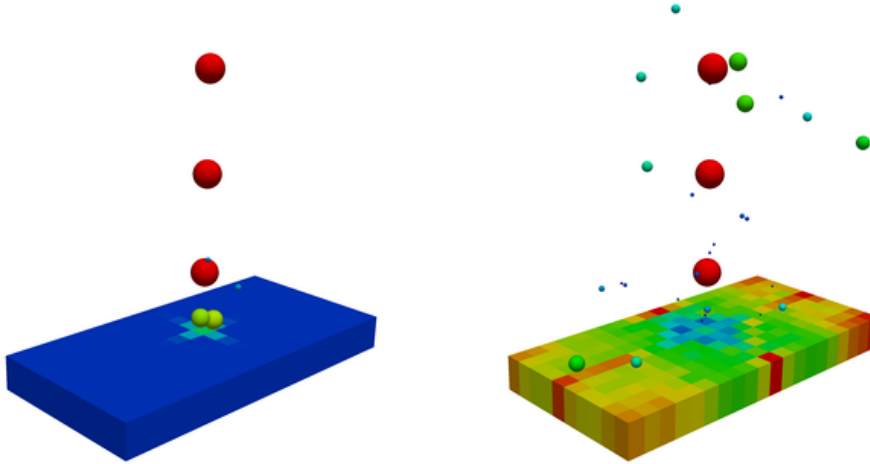


Figure 4.3: Splashing of droplets onto the liquid region [116]

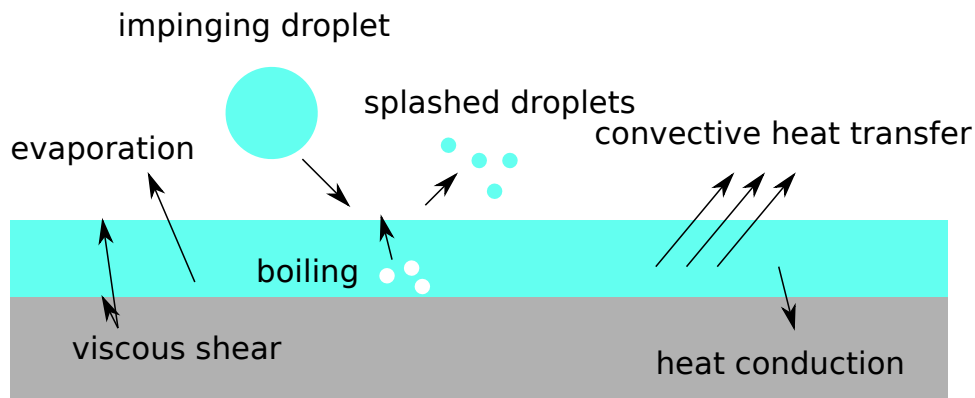


Figure 4.4: Liquid Region

The mechanism of the splashing model is such that any droplet whose path in the computational time step crosses the film region is considered to interact with the liquid. At the start of the simulation, where no liquid is present, particles will interact with the solid surface and a splashing model for dry surface will be applied. All the particles that do not splash will start to form the liquid pool. The model will then calculate some quantities and evaluate as to whether the droplet will be absorbed, rebounded, spread or splash.

The film region is solved at each time step alongside the gas region, and the

timestep depends on which of the two areas requires a smaller timestep with the set Courant number.

The mesh of the liquid phase is obtained by extruding the gas phase mesh on the patch where the film liquid is present. This is because in order to map the two solutions together the cells have to be superimposed one on the other.

The importance of the implementation of the liquid region is primarily because of the splashing model, while a second effect is the evaporation that takes place in this region [117], affecting the vapour production within the domain. For a very cold liquid such as LNG, the heat transfer that takes place when this liquid comes in contact with a solid surface at a normal temperature (20°C) makes the boiling/evaporation process really fast, and the presence of the liquid can have a considerable impact on the vapour formation and consequently the risk analysis of an accidental spill. On the other hand, when considering liquids that have a boiling point well above normal temperature, the evaporation that takes place is very slow and can be negligible. The role of the film is in this case merely for splashing purposes. Also, in the case of a boiling liquid, as it will be demonstrated in Chapter 6, the likelihood of any droplet to get to the ground is very low or equal to zero. Consequently, the film and splashing modelling are not necessary. For this reason and the other mentioned above, the equations describing the film were not modified, and the standard one available in OpenFOAM were used.

4.3.2 Enhanced Buoyancy

As mentioned earlier, buoyancy plays an important role in the current application, therefore gravity had to be accounted fully in the *cascadeFoam* solver. The original version of *sprayFoam* did not consider the gravity term in the momentum equation, for this reason the latter had to be modified along with the pressure equation. If we define a modified pressure p_{rgh} as:

$$p_{rgh} = p - \rho gh \tag{4.8}$$

where h is the value of the coordinate of the axis where gravity is acting (usually the y or z axis). The modified pressure is often more conveniently used to solve the pressure equation in place of the standard pressure, with some terms to be modified respect to the standard equation. When we calculate the gradient of the modified pressure (p_{rgh}) in the momentum equation, an additional term arises which has to be removed in order to compute the correct momentum equation.

The gradient is obtained as:

$$\nabla(p - \rho gh) = \nabla(p) + \rho g + gh\nabla(\rho) \quad (4.9)$$

The last term does not appear in the momentum equation, therefore it has to be removed for consistency.

These changes were introduced in the momentum and pressure equation, which allowed the solver to accurately reproduce buoyancy effects due to density variation within the domain.

4.3.3 Comparison of the two solvers

The implementation of the buoyancy terms and splashing modelling in the *sprayFoam* were discussed in the previous sections, and in order to understand the main differences between the new solver implemented and the standard one available Table 4.1 shows the main differences and capabilities of the new solver.

Table 4.1: Differences between standard solver and *cascadeFoam*

Feature	<i>sprayFoam</i>	<i>cascadeFoam</i>
Droplets Modelling	✓	✓
Turbulence Modelling	✓	✓
Buoyancy Effects	X	✓
Standard Wall Interaction	✓	✓
Splashing Interaction	X	✓

4.4 Solver Validation

The validation of the *cascadeFoam* solver was carried out comparing the results obtained from the Health and Safety Laboratory (HSL) [33], part of Health and Safety Executive (HSE), the UK body responsible for the regulation and enforcement of workplace health, safety and welfare. They investigated both experimentally and numerically the spill of liquid fuel from a storage tank as part of the Buncefield investigation.

4.4.1 Experimental Setup

Due to safety restriction, the experimental analysis carried out by HSL could not represent fully what happened in Buncefield, but the experiments can be used to validate the computational model and then the CFD model can be applied to different scenarios to evaluate the safety of a spill and the likelihood of a fire. The experimental setup is shown in Figure 4.5.

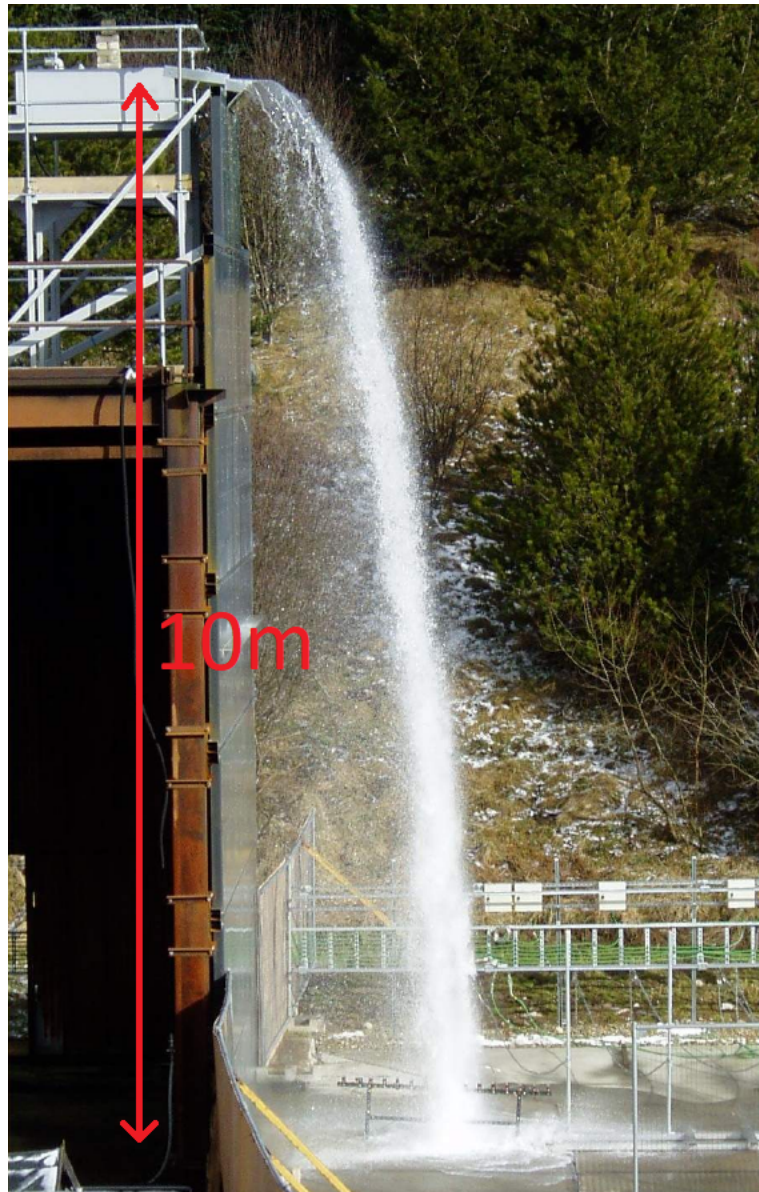


Figure 4.5: Experimental setup for the solver validation [33]

A liquid (Hexane) is injected through an aperture from a height of $10m$, and a solid surface representing the tank walls goes from the injection point until

the ground where the liquid splashes and the vapour produced is dispersed in the nearby region. Temperature measurements were taken at the base of the cascade using an array of collecting pots each equipped with a thermocouple at their base. In addition to the cascade measurements, an array of thermocouples was also positioned downstream of the cascade to record the temperature of the vapour current.

4.4.2 Computational Model used by HSL

A general-purpose CFD software, CFX 12.1, was used by HSL to model the experiment described in the previous section. A Lagrangian approach was used to model the dispersed phase (droplets formed by the liquid spill at the top of the tank), while a Eulerian representation was used for the gas phase. They have also carried out some sensitivity studies where the response to numerical inputs like mesh size, time step, inlet speed, iterations and number of particles was measured in terms of output parameters such as vapour volume, liquid and vapour temperature. The results showed that the parameter that influenced the results the most was the mesh size, which accounted for about 20% variation of the output parameters (the effect of each input variable was calculated from the difference between the high and low values for each input parameter, as a percentage of the mean overall eight simulations). The other parameters showed little impact on the solution. As a consequence of that, the mesh size needs to be chosen carefully, as in every Lagrangian simulation.

4.4.3 Computational Model

The simulation setup was chosen to be the closest possible to the one used by HSL to avoid any discrepancy arising from the setup rather than the physical modelling. The geometry was obtained from the pictures available in their report and the dimensions that were not specified were calculated manually trying to achieve the highest accuracy possible (the geometry given in their report is shown in Figure 4.6).

The size of the domain was chosen to be quite large ($30m \times 30m \times 20m$) to account for the large dispersion of the vapour cloud and to affect the least the solution by the boundary conditions. A structured hexahedral mesh was used throughout the whole domain to avoid the use of non-orthogonal correctors which damage the solution, and this led to a higher number of cells if compared to

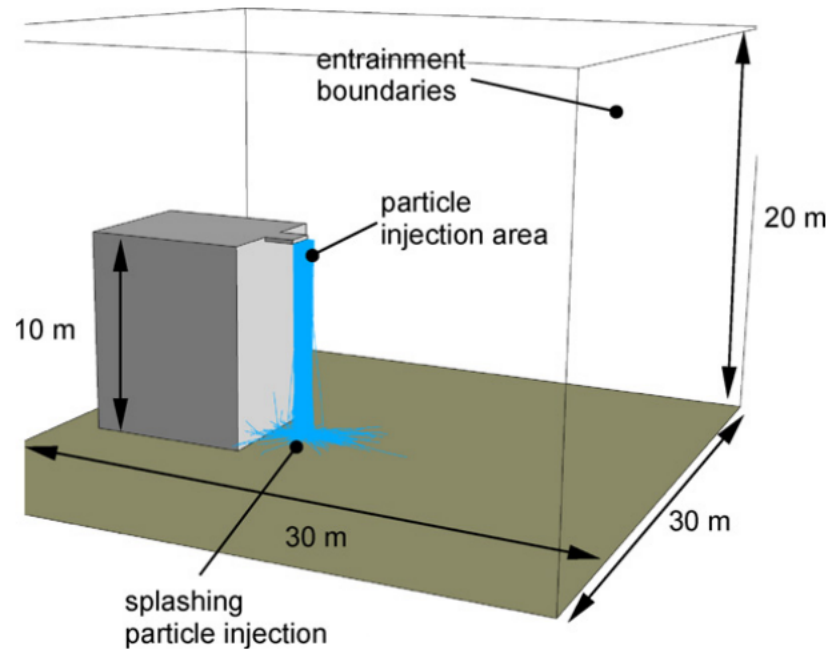


Figure 4.6: Geometry given in the HSL report

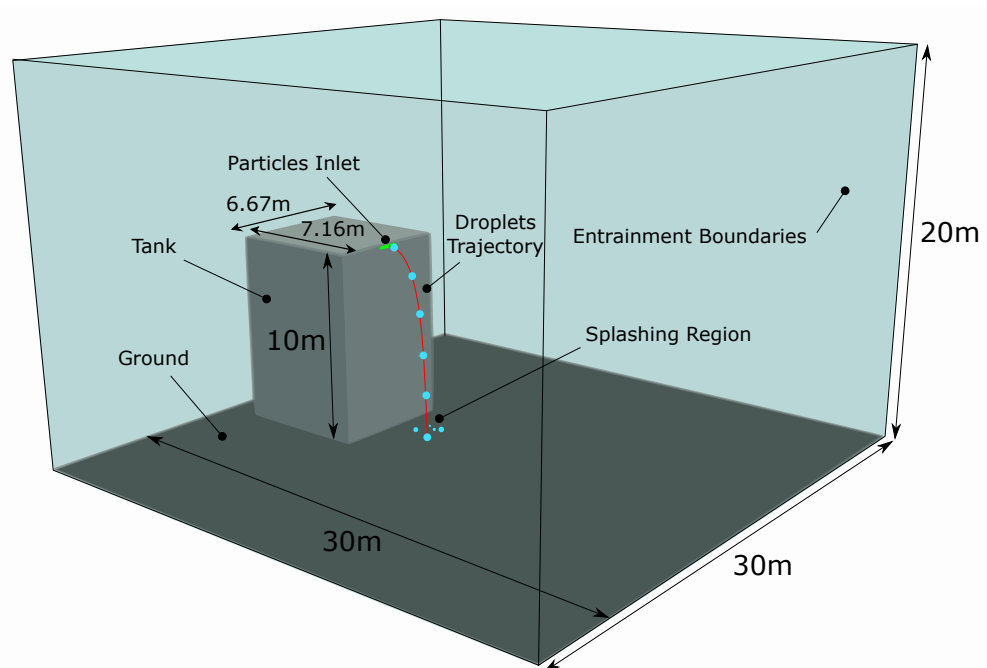


Figure 4.7: OpenFOAM Geometry

an unstructured mesh, but the increase in the simulation time was justified by a higher accuracy. A second mesh was also obtained using the *snappyHexMesh* tool available in OpenFOAM to reduce drastically the number of cells while keeping

a fine mesh in the cascade region and close to the ground where the vapour cloud would spread.

The boundaries surrounding the tank were all set as open boundaries where the air could move freely in both direction, and at constant total pressure so that the pressure and density vary with height. No wind was modelled in the simulation, because even though it affects the movement of the flammable cloud, it diffuses its concentration thus reducing the risk for a fire or explosion.

Turbulence interaction with droplets is fundamental for the correct prediction of the spray behaviour [118], and in the current work it was first modelled with a RANS approach using the standard SST model widely adopted in industrial applications [93, 119], also to compare the results obtained by HSL, while later a Large Eddy Simulation approach was used to show and compare the differences. The air surrounding the tank was considered to be quiescent (velocity equal to zero) and initial turbulence of 5% (based on a reference velocity of 0.01 m/s) with a turbulent to fluid viscosity equal to 10.

Earlier we introduced the splashing phenomenon, and the modifications made on the solver to take into account for the splashing process. HSL did not use any splashing model because the ones available are mostly used for internal combustion applications and not suitable for a fluid cascade where the scale of the domain and droplet sizes are orders of magnitude larger. Therefore, instead of using a splashing model, they have simulated the liquid impact on the ground introducing a second injection area at the bottom of the cascade as clearly visible in Figure 4.6. In this area, the droplets size, mass flow, temperature and velocity were prescribed in such a way as to match the pattern observed in the experiment. Unlike HSL, a splashing model was adopted in the current simulation, which can be assumed to be correct in terms of modelling, and in the following chapter the improvement in the splashing model will be introduced to obtain better results. The use of a secondary droplet inlet can lead to better results for a single simulation, but this is feasible only with the experimental results available, therefore not universally applicable, and resources consuming.

Simulations were run with and without the splashing model to show the capabilities and improvement of the use of it. In the simulation without the splashing model the droplets simply disappear when their trajectory crosses any boundary.

The liquid used in all the simulation was Hexane (Table 4.2 shows its main properties), which is a major constituent of gasoline. The use of multi-component mixture such as petrol can lead to different results because the evaporation tem-

perature of each component is different and therefore the evolution of the droplet diameter changes.

Table 4.2: Properties of Hexane

Property	Value
Chemical Formula	C_6H_{14}
Molar Mass	$86.18 \text{ g} \cdot \text{mol}^{-1}$
Density	$654.8 \text{ Kg} \cdot \text{m}^{-3}$
Boiling Point	68.5 to 69.1 °C
Dynamic Viscosity	$0.3 \text{ mPa} \cdot \text{s}$
Surface Tension	$0.0184 \text{ N} \cdot \text{m}^{-1}$

4.4.4 Droplet Setup

An important step in the simulation process was the setup of the Lagrangian cloud. In the theoretical description of the Lagrangian formulation, the central submodels were introduced, such as the evaporation, breakup, force, dispersion, heat transfer, atomization, stochastic collision and radiation model. Although in a correct approach of a spray simulation all the previous parameters have to be addressed correctly, in the following application some of them can be neglected by the nature of the flow or just by physical assumptions. The model was chosen to be as close as possible to the simulations carried out by HSL, but the *cascadeFoam* solver requires additional submodels, which were selected as to have the most accurate results compared with the experiments.

The forces acting on the droplets are gravity and aerodynamic drag, the heat transfer between droplets and surrounding air which affects the evaporation rate depends on the Nusselt number, calculated with the Ranz-Marshall correlation for spheres [89] following HSL, and last the breakup model used, which is widely recognised as one of the most reliable, was the Reitz-Diwakar model [120].

Radiation is important and cannot be neglected in case of a fire where the high temperature of the gas can irradiate the liquid droplets (and this is what water mists are trying to achieve in active protection systems for fires, in order to protect walls and solid surfaces from high radiation). In the following application, since no fire is modelled, no radiation model needs to be introduced for the Lagrangian phase, but the solver has the capability of modelling it.

Turbulence is produced by the droplets which transfer momentum to the carrier phase, and turbulence itself affects the droplets, and this is taken into account

by the dispersion models available in the solver. Usually, these models consider for a stochastic dispersion, randomly assumed by the turbulence intensity in the cell where the droplet is located. In the current application, this was neglected because low influence on the results was recorded.

The droplet size distribution is among the most important parameters in the set up of the Lagrangian cloud [121]. The function chosen to represent the distribution is the Rosin-Rammler distribution (which has been applied to a large number of different applications [122, 123]), which is an application of the Weibull distribution to particles.

The probability density function (PDF) of the Rosin-Rammler distribution used in OpenFOAM can be expressed as:

$$f(d, \bar{d}, n) = \frac{1 - e^{-[(x-d_{min})/\bar{d}]^n}}{1 - e^{-[(d_{max}-d_{min})/\bar{d}]^n}} \quad (4.10)$$

where d is the droplet diameter, \bar{d} , d_{min} , d_{max} are respectively the mean, minimum and maximum droplet diameter, and n is the spreading factor. The cumulative distribution function (CDF) is obtained by integrating the probability density function:

$$F(d, \bar{d}, n) = \int_0^d f(t, \bar{d}, n) dt \quad (4.11)$$

In the simulation setup the parameters used for the droplets distribution are the following:

$$\bar{d} = 2 \text{ mm}; \quad d_{min} = 0.1 \text{ mm}; \quad d_{max} = 2 \text{ mm}; \quad n = 3;$$

and the PDF for these parameters is shown along with the CDF in Figure 4.8.

4.4.5 Meshing

It was mentioned earlier that two types of meshes were investigated, one developed by *blockMesh*, a simple utility available in the OpenFOAM package that allows developing parametric meshes with grading and curved edges. The central concept behind this utility is to divide the domain into one or more three dimensional, hexahedral blocks [116]. It is a useful utility to create structured orthogonal meshes but only works with simple geometries. If a more complex geometry has to be meshed, it is not possible to create a mesh using *blockMesh*. In

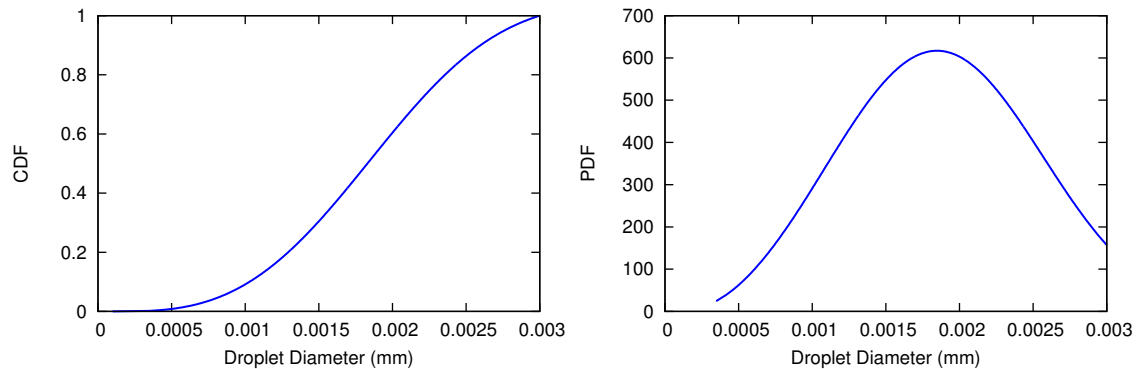


Figure 4.8: Cumulative Distribution and Probability Density Functions of the setup

the latter case, OpenFOAM has a utility called *snappyHexMesh*, able to generate 3-dimensional meshes containing hexahedra (hex) and split-hexahedra (split-hex) automatically from surface geometries. Obviously if considering split-hex meshes, the accuracy is lower if compared to a fully hexahedral mesh, but the numbers of cells are lower, leading to fastest times of simulation.

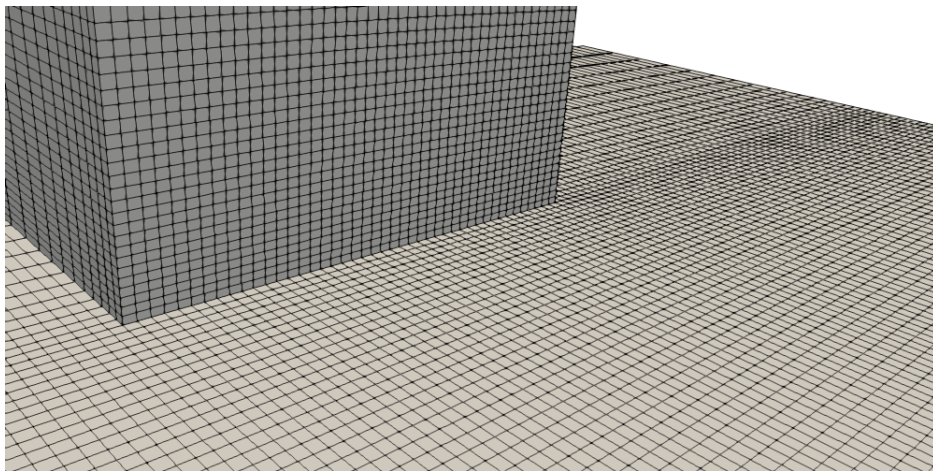


Figure 4.9: Mesh zoom obtained with the *blockMesh* utility

Independently from the tool used to obtain the mesh, the mesh presented a refined region in the zone occupied by the droplets, as well as in the region close to the ground where the vapour cloud initially dispersed. In order to use the $k - \omega$ SST turbulence model, the mesh size close to the ground had to be refined until a value of y^+ around 2 was obtained. Cell size in the regions far from the regions of interest was kept in the order of half a meter only to consider for large movements of air in the cascade, but the quantity gradients were small

in such region therefore no refinement was needed. A mesh sensitivity analysis was carried out and the most efficient mesh size was found to be the same one used by HSL in their calculations.

4.4.6 Simulation without splashing

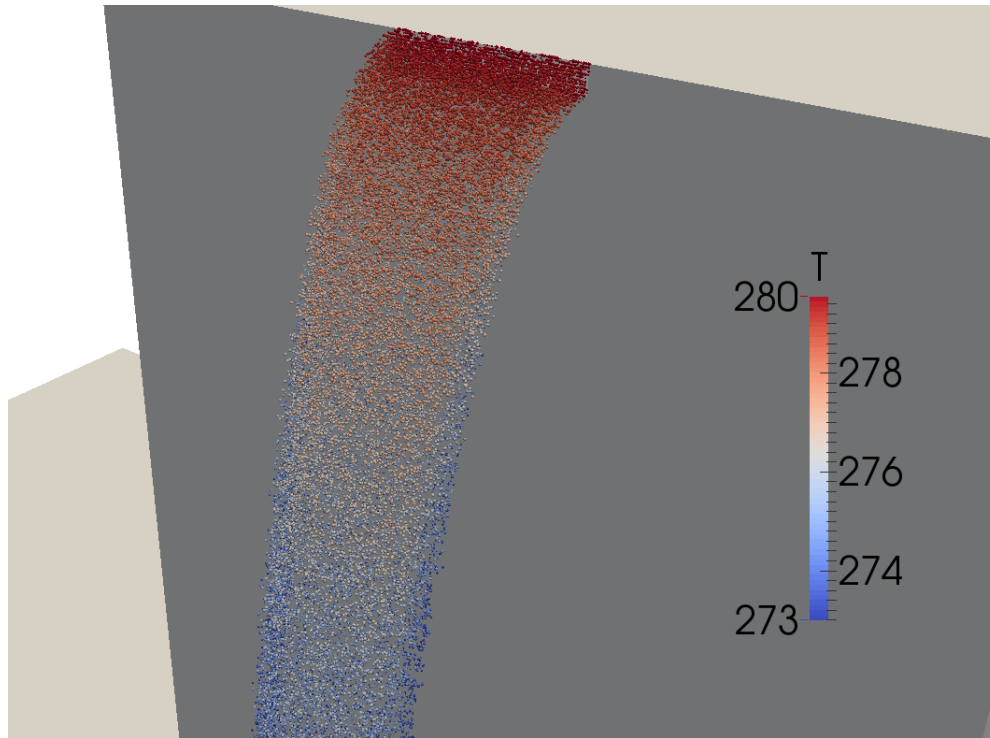


Figure 4.10: Parcels of Hexane droplets injected in the domain coloured by temperature

A first simulation without the use of a splashing model was carried out, in order to verify and better understand the effect of splashing in the vapour production and the flow field. Particles were injected through the rectangular region shown in Figure 4.7 with an initial temperature of 6.4°C while the temperature in the whole domain was set at 6°C . Some factors were not explicitly specified in Atkinson and Coldrick [29] such as the maximum and minimum sizes of the droplets, which are requested by the solver in the case set up. The trial and error practice was adapted to select the values which would lead to a good agreement with the experimental and previous CFD results in Atkinson and Coldrick [33]. The huge cloud of droplets produced in the cascade is represented by a finite number of parcels in the CFD simulation, each parcel containing a limited figure of droplets of the same size.

A picture showing the droplet being injected into the domain is shown in Figure 4.10. The droplets are obviously scaled with respect to their real size (with a factor of 20), and just a finite number of them are represented because of limitations in the postprocessing software. The droplets are coloured with their temperature and it can be seen how the temperature decreases during the cascade process, this is due to the latent heat released during the evaporation process.

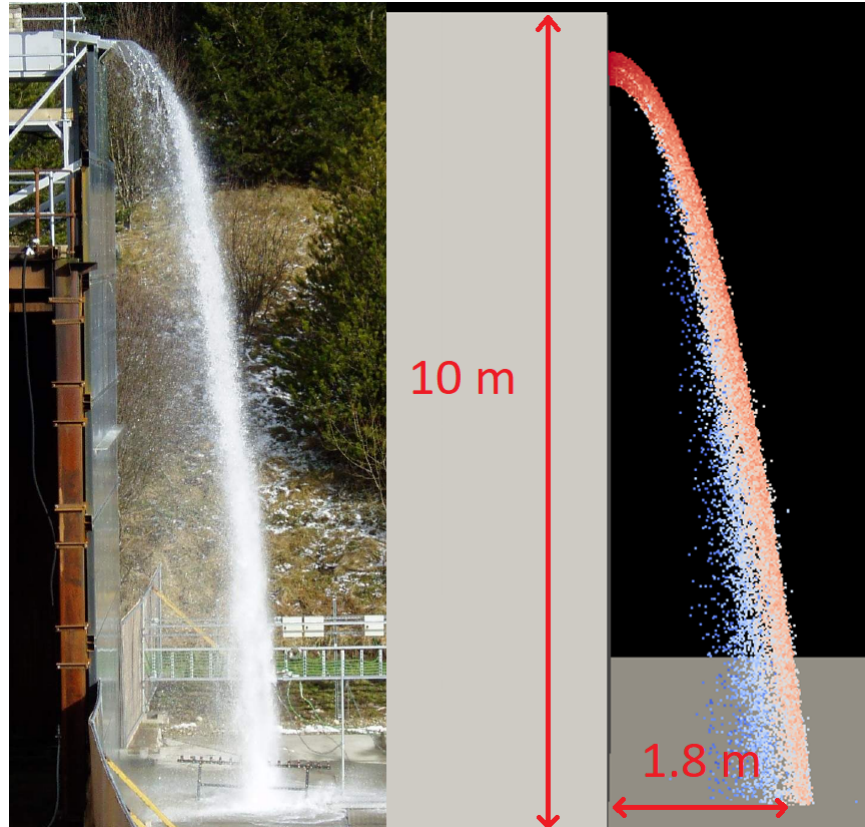


Figure 4.11: Comparison of the cascade shape between Experiments and CFD (droplets are coloured according to their temperature)

Figure 4.11 shows a comparison of the cascade shape in the Experiments and the CFD analysis carried out by *cascadeFoam*. Good agreement in terms of cascade shape and impact point was achieved, with the main difference evident in the impact region because of the absence of a splashing modelling.

A clearer picture of the spray pattern can be observed in Figure 4.12 and 4.13. The axes are not scaled therefore the dimensions of the spray do not represent the real aspect ratio.

The acceleration of the droplets and greater heat exchange on the sides of the spray gives it a bottleneck effect visible on the $y - z$ plane. On the $x - y$

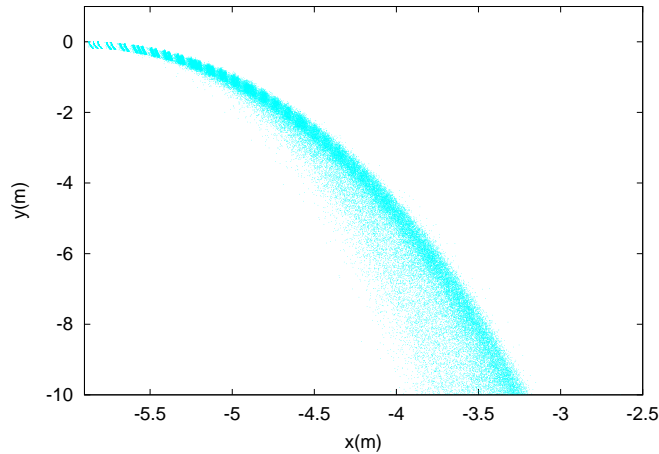


Figure 4.12: Side view for the spray pattern

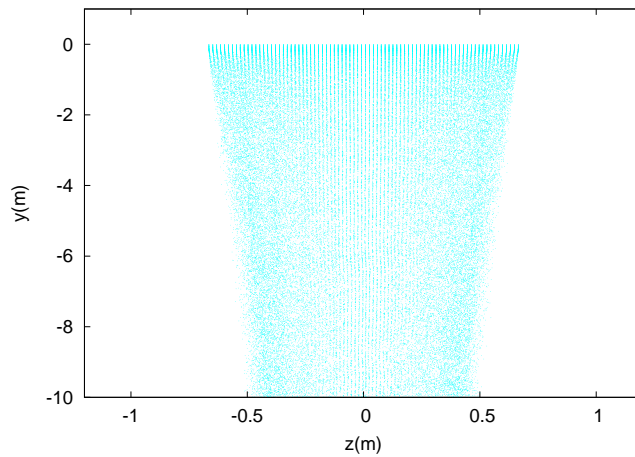


Figure 4.13: Front view for the spray pattern

plane the higher deceleration and faster evaporation of the smaller droplets can be observed, where the spray spreads on its path to the ground and the inner part of it (closer to the wall) has a much less density of droplets, due to reasons mentioned above.

Figure 4.14 and 4.15 show the maximum droplet diameter with respect to the height and the average velocity (calculated simply by averaging the velocity of each parcel within a fixed range of heights without weighting the values by the droplet diameter) of the droplets. It is clear how the maximum droplet diameter changes by less than 0.05mm during the fall, and this means that the greater part of the vapour cloud comes from the smaller droplets which evaporate much faster than the larger ones, especially at the sides of the cascade. The velocity shows a parabolic growth to a maximum value of around 9.5 m/s .

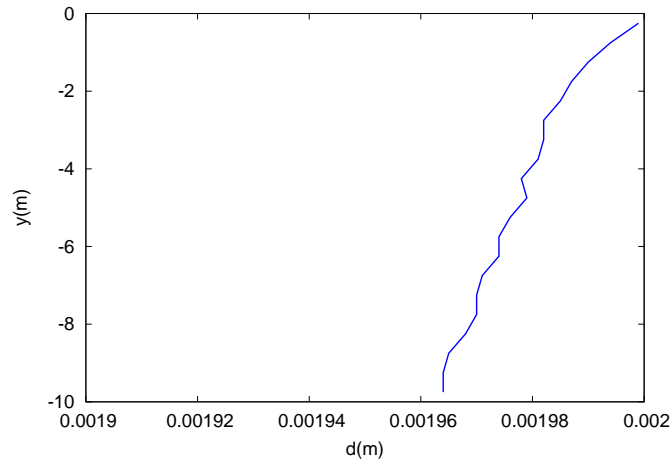


Figure 4.14: Maximum diameter of the droplets with height

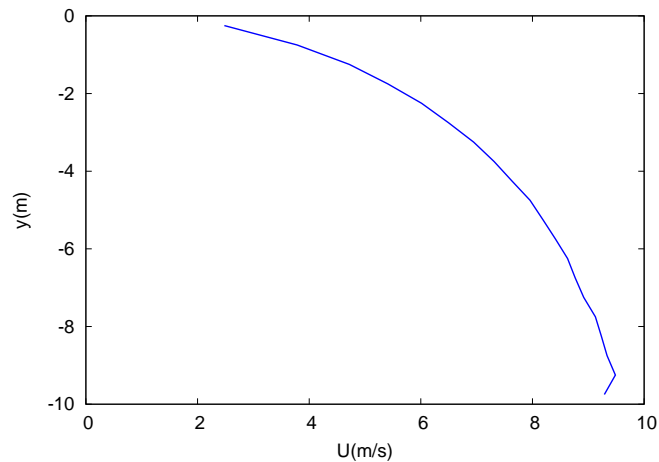


Figure 4.15: Average velocity of the droplets with height

4.4.7 Simulation with splashing

As evidenced by the results obtained without any splashing modelling, the need for improved results in the impact region is fundamental. The simulation with splashing is equivalent to the one without any droplet impact modelling, apart from two main differences, the droplets splash when impact any solid surface, and there is an additional region in the domain to be solved, which is the film formed on the ground. Clearly, the computational time of the simulation with splashing is bigger than the one without splashing, mainly due to the solver that has to calculate which droplets are going to splash and the splashed quantities, and also due to the film that has to be modelled. As it was mentioned already, and confirmed by Atkinson and Coldrick [29], the film modelling only had small

contributions to the vapour production, and in this case, approximately less than 2 g/s to the total vapour production.

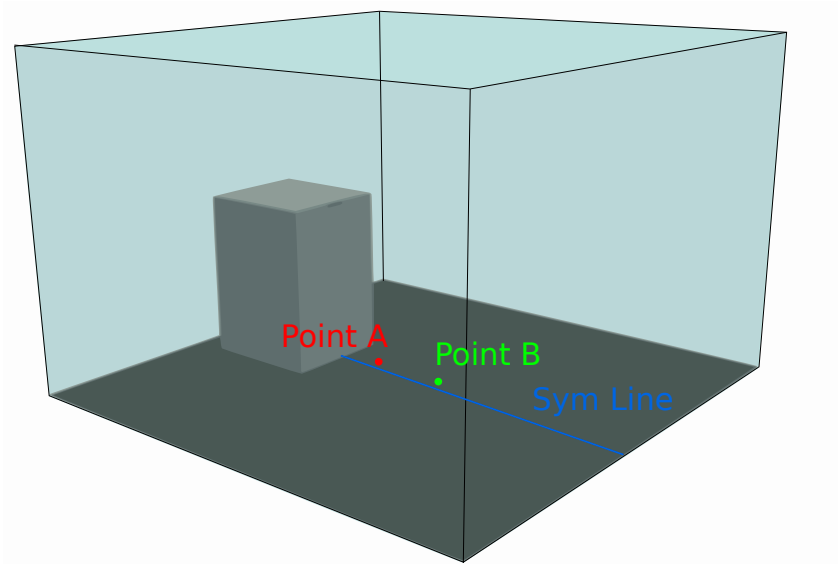


Figure 4.16: Domain showing the zones where the comparison was made

Figure 4.16 shows the points and the line where data was taken in the predictions in order to compare the results obtained from Coldrick et al. The location of the points and the line is as follows:

- Point A: Located in the symmetry plane at the centre of the cascade and 0.5 m from the ground
- Point B: Located in the symmetry plane 5 m from the tank wall and 0.5 m from the ground
- Sym Line: Located in the symmetry plane at 0.15 m from the ground

The predictions obtained from the simulation with splashing are shown in Figures 4.17,4.18,4.19,4.21,4.22 altogether with the results from the one without splashing. These are compared with the experimental results obtained by Coldrick et al. when available, and the CFD results from their CFX simulation. The main effect noticed from the results obtained from the simulation with splashing modelling was to decrease the temperature in the region close to the ground and increase the vapour production. From Figure 4.17 it is clear that splashing does not affect the temperature in the impact region, probably because

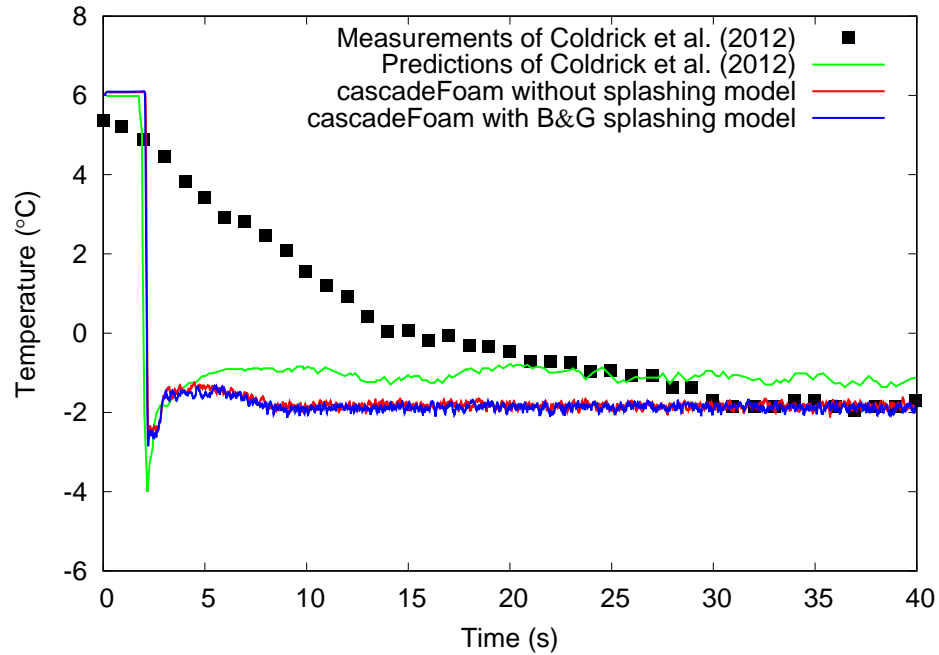


Figure 4.17: Temperature predictions in the bulk of the cascade (Point A)

a saturation condition is reached in both the simulation with and without splashing, while in the region far from the impact zone (Point B is shown in Figure 4.18) there is an evident decrease in temperature. The difference for the temperature steady state values between experiments and *cascadeFoam* is less than 1% for Point A and around 10% for Point B.

In terms of the flow field, this was not significantly affected by the splashing, mainly driven by the bulk flow in the cascade, as evidenced in Figure 4.19. While some initial simulations were run reproducing the droplet inlet used by Coldrick et al., in order to calibrate the simulation parameters, the main simulation was run trying to reproduce the closest set up from the experiments, with the droplets forming a parabolic trajectory rather than a straight line as from Coldrick et al. [33] experiments. A closer look on the impact region from both the CFD results obtained from *cascadeFoam* and the experiments is shown in Figure 4.20. Clearly, the splashing particles did not eject as far from the splashing region in the predictions as in the experiments, where they spread out further after hitting the ground, thus affecting the vapour temperature in the far region from the wall.

Another set of simulations was run with the same geometric conditions but different initial values of air and fuel temperature. The temperature of the air at the beginning of the simulation was set at 10°C while the hexane was injected at

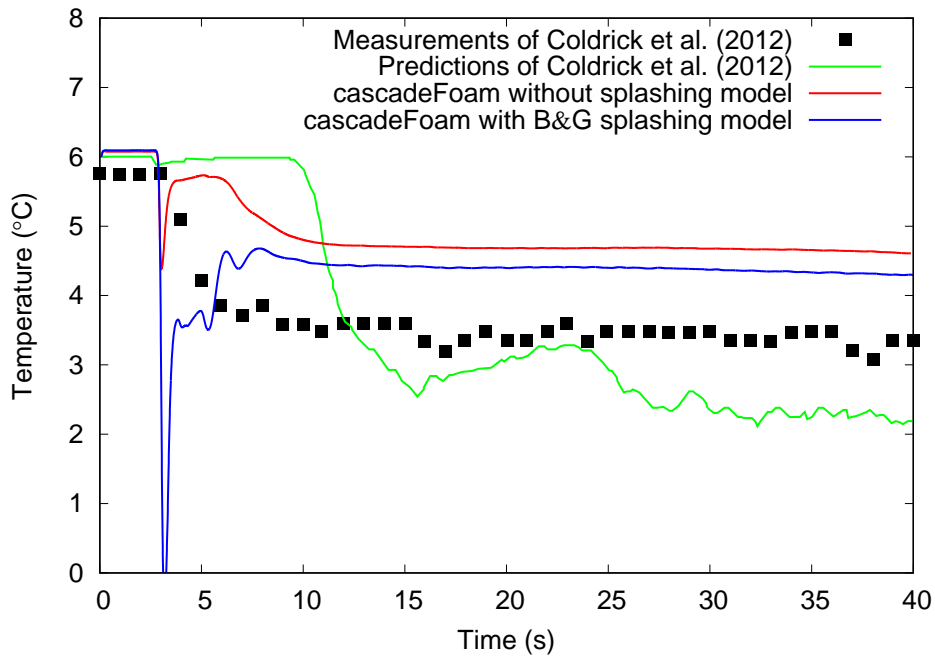


Figure 4.18: Temperature predictions far from the cascade (Point B)

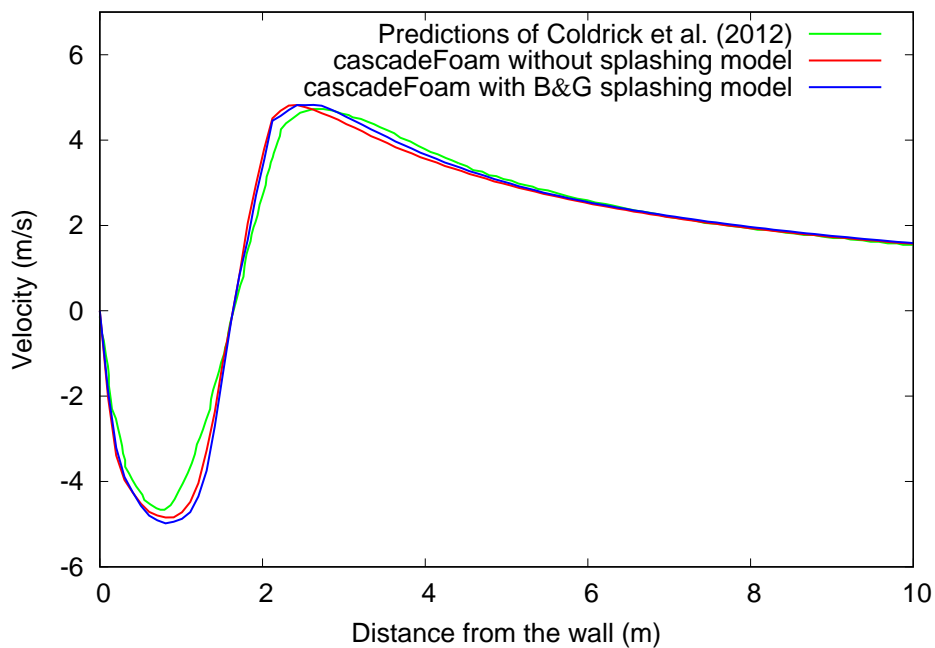


Figure 4.19: Velocity predictions on the line 0.15m from ground

12.6°C with a mass flow rate of 15 kg/s. The results obtained (shown in Figures 4.21 and 4.22) without any splashing modelling are in good agreement with the predictions of Coldrick et al., for both temperature and concentration predictions.



Figure 4.20: Comparison of the predicted droplet splashing with the experimental observation

On the other hand, the predictions obtained with the Bai and Gosman splashing model differ from their predictions. However, in Figure 4.18, the predictions for Point B are somehow in between the current and their predictions, and from this one could deduce that if experimental results were available for the second set of conditions, these would fall between the results obtained with *cascadeFoam* and CFX.

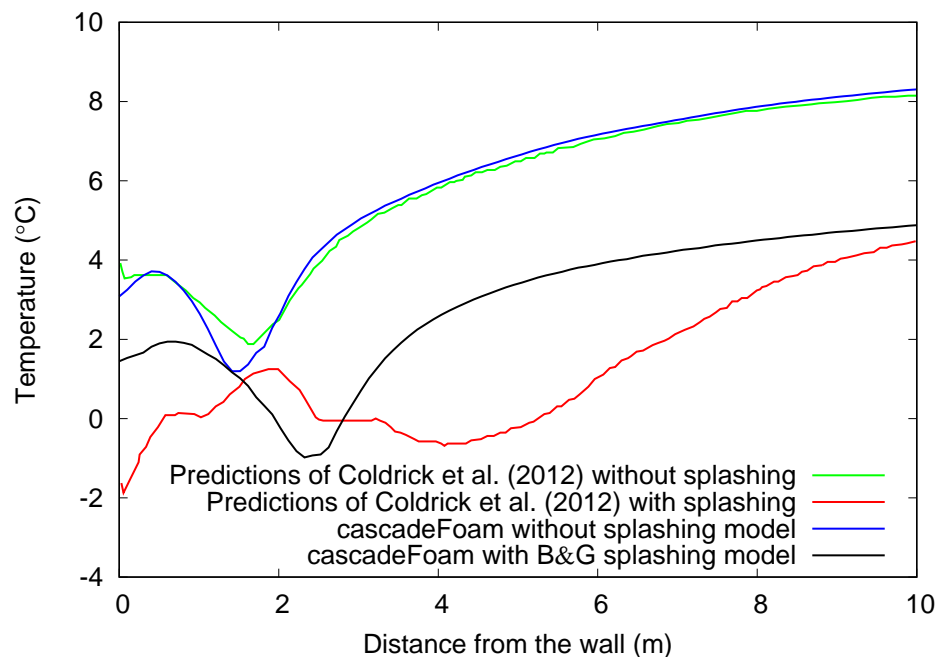


Figure 4.21: Temperature predictions on the line 0.15m from ground

In order to understand the cascade dynamics, a slice cutting the domain into half showing the temperature and turbulent kinetic energy is shown in Figures 4.24 and 4.25. The plots show that in the splashing region the lowest temperature

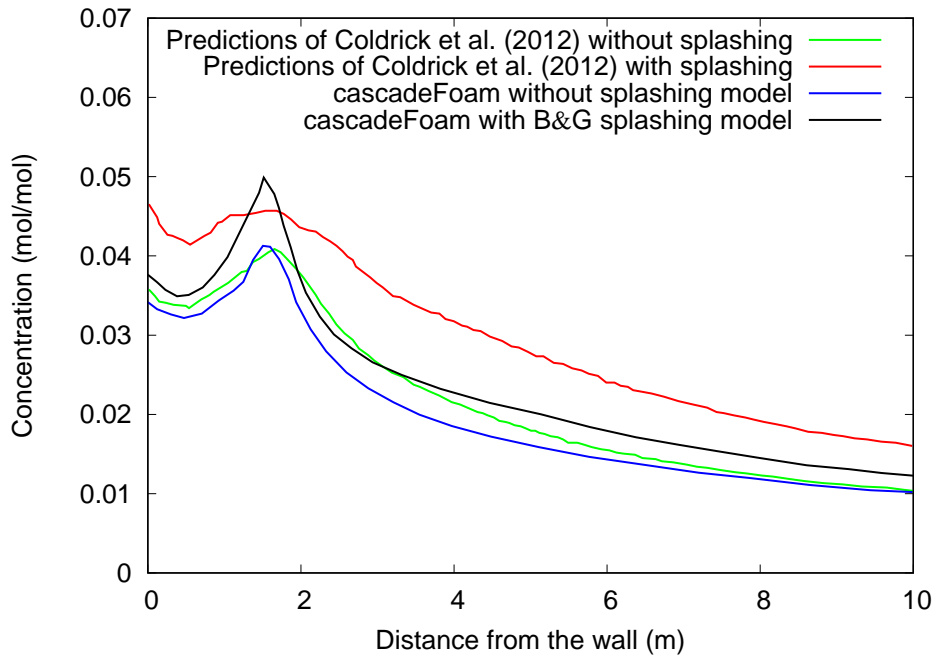


Figure 4.22: Hexane mass fraction predictions on the line 0.15m from ground

is achieved, while the turbulent kinetic energy has a maximum. It is also clear the cloud formed by the evaporated hexane in the far region from the tank. In between the tank and the cascade, a recirculation zone is formed shown in details in Figure 4.24. Because the impact zone has the highest turbulence intensity, the predictions would benefit from local mesh refinement in that region.

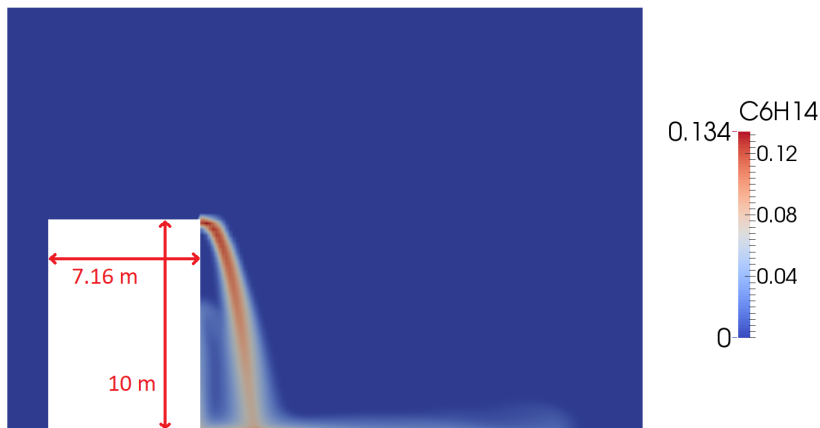


Figure 4.23: Contour plot of Hexane mass fraction in a slice

A clearer picture of the flammable cloud formed is evidenced in Figure 4.26. The cloud stays close to the ground because of the higher density of hexane in

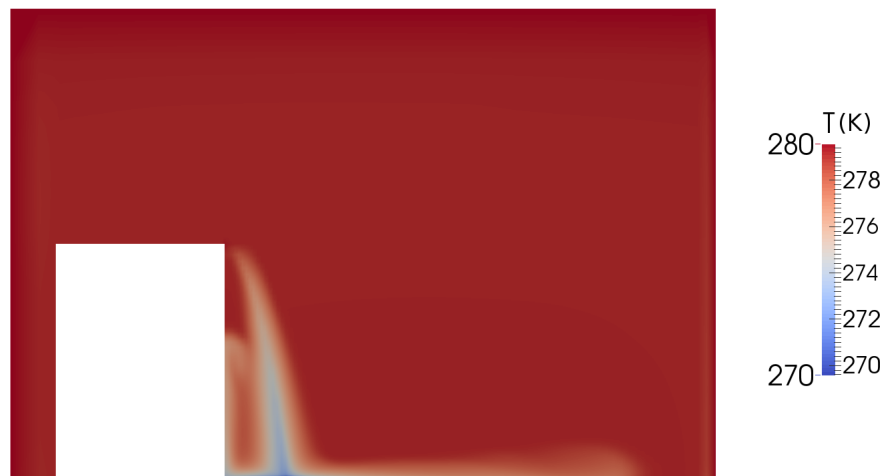


Figure 4.24: Contour plot of Temperature in a slice

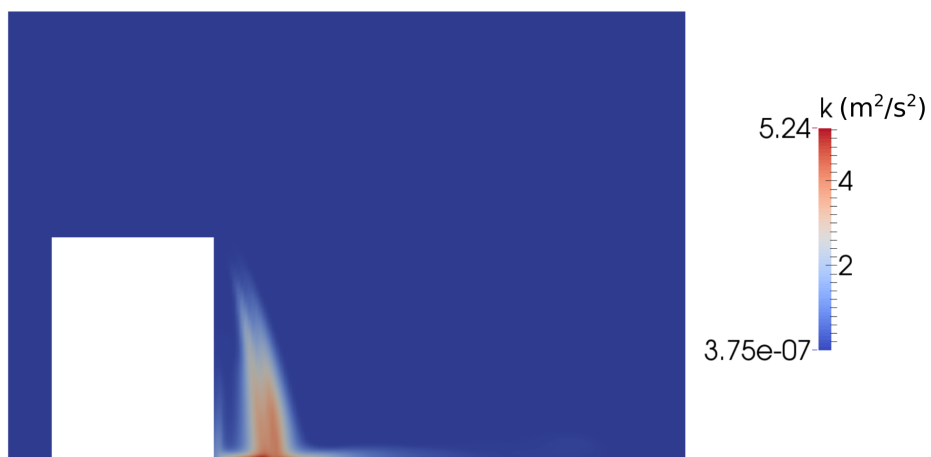


Figure 4.25: Contour plot of Turbulent Kinetic Energy in a slice

comparison with the surrounding air. The recirculation zone mentioned before between the tank walls and the cascade is also evident.

4.4.8 Large Eddy simulation setup

The predictions obtained in the last sections were made using a RANS turbulence modelling approach. This proved to give acceptable results especially in terms of mean quantities measured in determined points. In order to show any unsteady local behaviour of the flow an LES approach was used and compared with the results previously obtained. Obviously, the use of such turbulence model requires

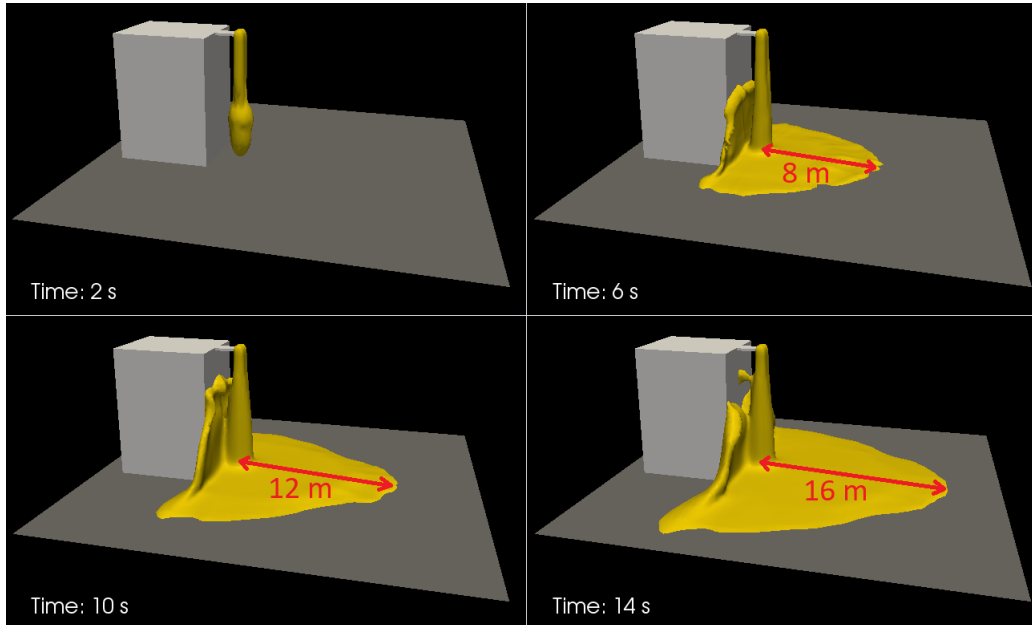


Figure 4.26: Contour plot of the predicted fuel concentration at 0.5 LFL

much more significant computational resources and time. To achieve a value of y^+ close to the unity, the mesh in the droplets impact region had to be refined.

4.4.9 Mesh size

In problems where turbulence is present, a quantity named Turbulent Length Scale (TLS) can be defined as:

$$l_m = C_\mu^{3/4} \frac{k^{3/2}}{\varepsilon} \quad (4.12)$$

where C_μ is a model constant that in most turbulence models is equal to 0.09, k is the turbulent kinetic energy and ε is the turbulent dissipation. This quantity identifies the size of the large energy-containing eddies in a turbulent flow. In an LES simulation, the model aims to capture and calculate these eddies while leaving a subgrid model for anything that lies in the universal length scale. Following the criteria discussed by Addad et al. [124], the grid used in an LES simulation needs to have cells with a width of 2 or 5 times smaller than the turbulence length scale l_m . Following the predictions obtained from the RANS simulations, the turbulence length scale was calculated at different points of the domain, defined as the following:

- Point A: at ground level in the bulk of the cascade

- Point B: 5 m from the ground in the bulk of the cascade
- Point C: 9 m from ground in the bulk of the cascade
- Point D: at ground level 10 m from the tank walls

The results obtained are summarized in Table 4.3 with the values of ε calculated as $\varepsilon = \omega\kappa C_\mu$.

Table 4.3: Turbulence quantities calculated for different locations

Point	ω (1/s)	κ (J/kg)	l_m (m)
A	153	4.65	0.026
B	42	3.5	0.08
C	25.5	1.1	0.068
D	21	0.125	0.03

The mesh was then derived using these values reduced by a factor of 2 or more. Structural hexahedral cells were used with a total number of cells of 6 million.

4.4.10 Results

Results obtained using the LES turbulence model were compared to the ones available for the RANS modelling. The extent of the vapour cloud was found to be very similar in both formulations, with the LES showing local variation due to the nature of the method. The temperatures in the monitor points were slightly different with LES showing better agreement locally, but with the steady state values getting close to each other.

A contour plot showing the concentration of hexane on a symmetry plane is shown in Figure 4.27. It is clear how eddies are formed straight after the liquid comes out of the tank, due to the coupling of the Lagrangian phase with the surrounding gas. Due to the gasoline vapour being heavier than air, this liquid moves close to the ground, due also to the momentum given to the air by the droplets, and then spreads away from the impact region, forming eddies that disperse in a semi-circular pattern. The recirculation region between the liquid and the tank wall is also clear, where the vapour rises along the tank because it is constrained to.

Results obtained by the LES formulation show therefore an improvement with respect to a RANS approach, but the increment in computational time (a typical run time for the RANS simulation was in the order of 1-2 days, while the LES simulation took around 3 weeks) due to the large mesh to be used and the consequent low time step are very large and it was not found to be justified in the current application, mainly because the quantities of interest are the extent of the vapour cloud and the temperatures across it, these being very close in both formulation.



Figure 4.27: Concentration of hexane on a symmetry plane through the domain

4.5 Chapter summary

The development of the *cascadeFoam* solver was explained in the current chapter. The solver was obtained using a Lagrangian-Eulerian approach starting from the existing *sprayFoam* solver, capable of solving multi-species flows with evaporating or boiling liquid particles. The solver was modified to solve buoyant flammable cloud changing the momentum and pressure equations, as well as allowing a splashing model to be used in conjunction with a liquid film region. Results were in good agreement with the experimental data, and the use of a splashing model improved the accuracy of the flammable cloud formed. RANS turbulence modelling proved to be reliable in order to calculate the mean quantities, and although the LES modelling showed an improvement in the unsteady quantities

estimated, the increase in computational time did not justify the improvements, especially considering that the values of interest were captured with the RANS model too. As mentioned before, the splashing model improved the results, but this showed limits, mainly because the Bai & Gosman model was built for a different type of application (the main limit of their model is the limited applicability to the range of Weber number, droplet size and other physical parameters which are significantly different in the current application than the characteristic values where their model was obtained). For this reason, the improvement of a splashing model is of primary importance and it will be addressed in the next chapter, using the Volume of Fluid approach.

Chapter 5

Splashing Model Development

In this chapter, a new splashing model is developed starting from the correlations available in the literature and on the model available in OpenFOAM [125], the Bai and Gosman splashing model [50, 51]. This is because the standard Bai and Gosman model has proven not to be reliable in a scenario such as the spill of a fuel tank [126]. The model was developed mainly for internal combustion engine applications where the droplet sizes are much smaller ($100\ \mu m$ at most) than the ones in fuel spills application where droplets can be as big as $2mm$ [127], and also the film thickness and droplet impact velocity are far from being comparable. The splashing process is highly complicated [128] and a large number of authors have investigated the process from an experimental point of view [129]. Nevertheless, currently there is no global correlation available in the literature that can take into account for all the values of the droplet size, film thickness, impact velocity and type of fluid (the properties of the fluid such as dynamic viscosity, surface tension and density can change completely the outcome of splashing [130] as well as the geometrical configuration of the impacting surface [131]). All these reasons have led different researchers to create their custom splashing model that works in a specific range of applications.

5.1 Numerical analysis of the process

With the increase of computational resources, many researchers started to investigate the process using CFD [132]. The main approaches used in the literature will be now discussed more into details.

5.1.1 Volume of Fluid method

In the VOF approach, a function called phase fraction is introduced, which assumes a value between 0 or 1. This function assumes a value of 1 in the liquid region and a value of 0 in the gas region. The points where this function is between 0 and 1 are considered to be the interface. This concept is better illustrated in Figure 5.1.

0	0	0	0	0
0	0.2	0.55	0.7	0.35
0.08	0.8	1	1	0.96
0.27	1	1	1	1
0.24	1	1	1	1

Figure 5.1: Definition of the phase fraction

Theoretically, this concept can be extended to a formulation with n fluids, and for each fluid, a phase fraction is defined. The main advantage related to such model is that conservation of mass is enforced by the formulation, while the main drawback is the fact that the interface is not sharply resolved, but is distributed over a finite number of cells. The main consequence of that is that in order to track the interface with a certain level of accuracy a high number of cells have to be used, or as an alternative adaptive mesh refinement can be adopted in the interface region (defined with values of α between 0 and 1). The second approach is usually more efficient in terms of the number of total cells used but more complicated from a formulation point of view. Figure 5.2 shows a refined local region in the interface with two levels of refinement (each level of refinement splits the cell into 8).

One of the most delicate parts in the formulation of a VOF solver is how the surface tension is implemented in the momentum equation. The main difference

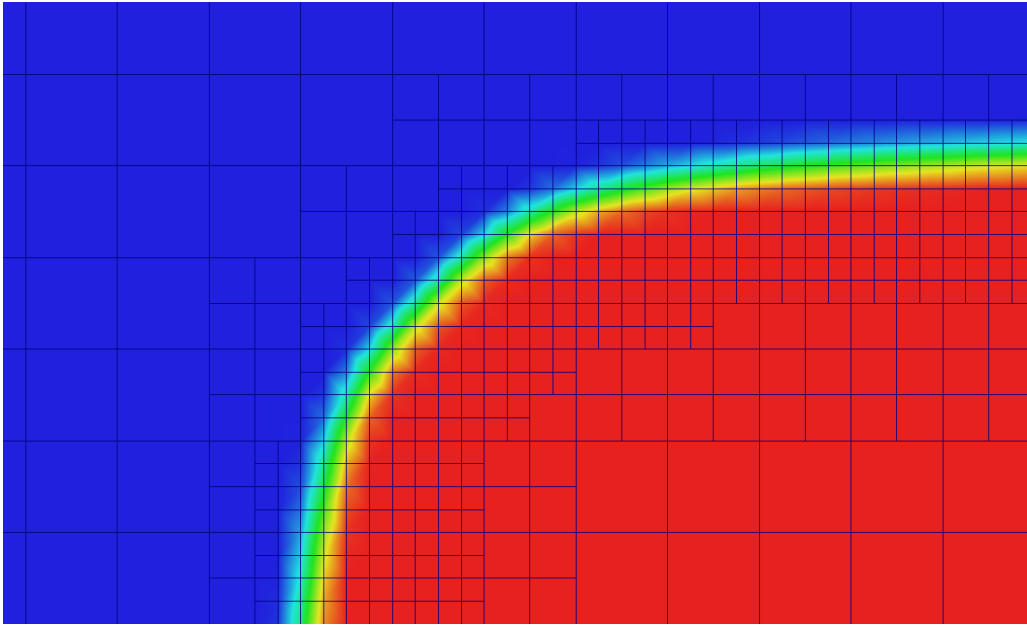


Figure 5.2: Local refinement used in OpenFOAM

between the momentum equation of a single phase solver and a two-phase one is the term that has to be implemented in the momentum equation due to the surface tension on the interface. Although this term is null in the rest of the domain, its value on the interface has to be implemented correctly. A number of different formulations exist for such purpose and the one used in the current application will be discussed in details later.

The main purpose of a multiphase solution is to track the interface. The VOF method uses an interface capturing approach, meaning that the interface is not directly solved by the use of a moving mesh, but it is 'captured' by solving the phase equation and then a method to compute the interface. A number of methods exist for this purpose and the most used ones are the donor-acceptor scheme which was the first one developed historically and the geometric reconstruction scheme, which usually achieve a better reconstruction of the interface. In the current work, as in most of the literature found on VOF methods, the interface is assumed to be located where the phase fraction assumes a value of 0.5. For this reason, all the results presented in the following sections will show a phase fraction obtained by an iso surface of phase fraction at value of 0.5.

5.1.2 Level Set method

The other principal approach to the simulation of multiphase flows where interface tracking is important is the Level Set method. This method was developed to overcome the problems arising from other formulations such as the VOF regarding oscillation problems at the interface using higher order schemes and the sharpness of the interface [133]. It is part of the interphase capturing methods.

The method starts from the definition of the level set function (ϕ), which is a smooth function that can define the interface quickly without the need to reconstruct the interface. This function assumes a value of zero on the interface, and positive or negative values if the point is located inside or outside the liquid phase. The evolution of the interface is therefore calculated using the following equation:

$$\frac{\partial \phi}{\partial t} + \mathbf{u} \cdot \nabla \phi = 0 \quad (5.1)$$

This equation is relatively simple to solve as the level set function is smooth.

As compared to the VOF method, the level set method has a better resolution of the interface, which makes it especially suitable for splashing simulations where the high number of droplets produced makes it necessary to solve the interface with a certain level of accuracy. However, this method presents its own drawback as well, the main one being the low mass conservativeness, which limits its application for a number of problems.

5.1.3 Coupled LS-VOF methods

A number of researchers have tried to use the advantages of both the Level Set and Volume of Fluid methods in one single formulation [84, 83, 134, 68, 135], namely the Coupled Level Set Volume of Fluid method. In the current application such method was implemented within OpenFOAM [136] and improvements were clear in the interphase computation but strong instabilities were experienced in the simulation of a splashing droplet. Both the phase fraction from the VOF (α) and the Level Set function (ϕ) are solved in the formulation, which can be summarized in the following for a single time step:

1. α is reconstructed from ϕ
2. α advection is solved

3. Properties such as density and viscosity are update with the α field
4. ϕ is reconstructed from α
5. the momentum equation is solved using the level set function for the calculation of the surface tension source term

The fact that α is advected makes sure that mass conservation is ensured and the use of the level set function in the momentum equation makes sure that the interphase is sharply resolved. Results of a single bubble rising in a column domain are shown in Figure 5.3. It is clear how the coupled solver calculates the interphase more sharply while the standard VOF method presents smearing of the interphase, especially in the ligaments detaching from the bottom of the bubble.

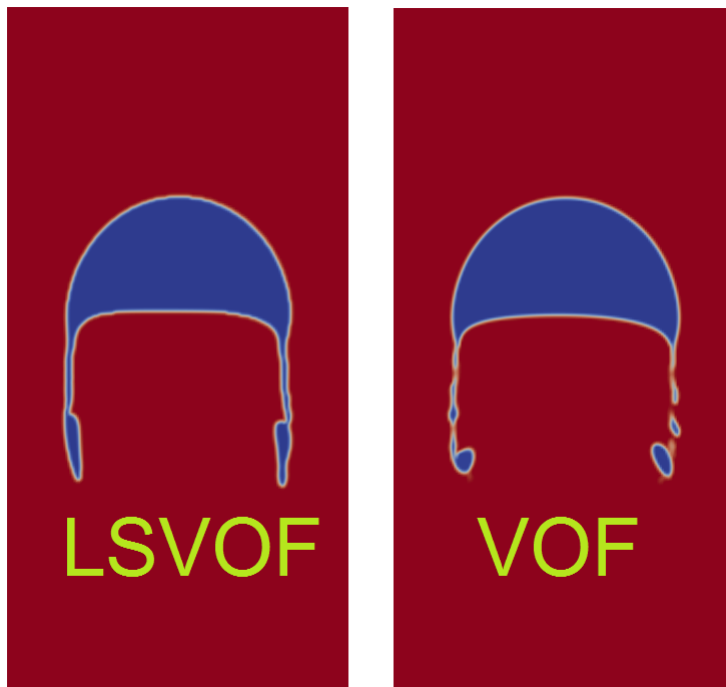


Figure 5.3: Results obtained with the coupled solver

5.2 Contact angle

The term wetting is usually used to describe the ability of a liquid to maintain contact with a solid surface, and the process deals with the three phases present

in the problem: solid, liquid and gaseous. When a liquid is in contact with a solid surface, the contact angle can be defined as the angle formed by the liquid-gas interface and the solid (Figure 5.4).

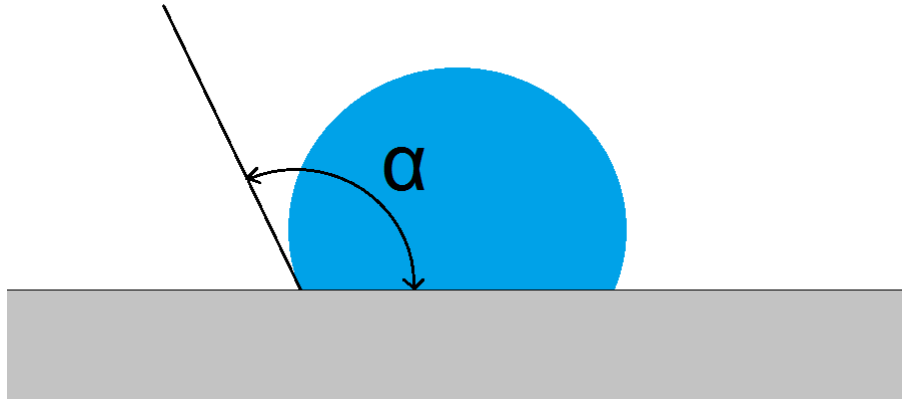


Figure 5.4: Definition of contact angle

The value of this quantity is usually calculated by the use of the Young-Laplace equation. When this angle has a low value, it means that the liquid spreads widely on the surface and therefore the wettability is high, while if this value is large, the wettability is low and the surface is said to be hydrophobic.

The contact angle is highly important in droplet impact applications, because its value determines the shape of the droplet in contact with a solid surface, affecting its dynamic [137, 138]. The contact angle is also found to be dependant on the droplet size [139]. One of the biggest challenges in the modelling techniques is the implementation of boundary condition for the phase fraction that accurately reproduces the behaviour of the contact angle. The main issue is that the latter depends on many parameters, the main one being the liquid properties and the solid surface material, which affects this value from both a macroscopic and a microscopic point of view. Another challenge is the fact that such value assumes a constant value for a static droplet, but for an unsteady calculation the angle varies, and this takes the name of dynamic contact angle.

In experimental analysis, a number of techniques are available to measure the value of the contact angle [140], the most widely used being the sessile drop method [141], the Wilhelmy plate method [142] and the capillary rise method [143]. In terms of numerical techniques, a widely used approach is to use a constant contact angle even for unsteady problems, but this obviously can lead to uncertainty in the calculations, and for this reason a number of models to

calculate the dynamic contact angle based on the droplet conditions are used [144, 145]. Although the formulations can use different methods, the base concept that all of them share is to use the value of the velocity of the contact line to calculate the contact angle value. Obviously, the value for a static contact line has always to give the static contact angle.

5.3 Physics of the process and model formulation

As we mentioned earlier, the splashing process is extremely complex, and no universal correlations are currently available to model all the types of splashing. As it is done in many other CFD applications, it is standard procedure to introduce some non-dimensional quantities that will help us in defining splashing regimes. In order to determine the outcome of a droplet splash, the following variables and fluid properties are needed: the initial diameter of the impinging droplet (D_0), the droplet impact velocity (V_0), the viscosity of the liquid (μ), the density (ρ), the surface tension (σ) and the film thickness (h). By applying the Buckingham theorem we can define four non-dimensional numbers:

$$\text{The Weber number} \quad We = \frac{\rho U_0^2 D_0}{\sigma} \quad (5.2)$$

which defines the ratio between inertia and surface tension forces;

$$\text{The Ohnesorge number} \quad Oh = \frac{\mu}{\sqrt{D_0 \rho \sigma}} \quad (5.3)$$

which defines the ration between the viscous forces and the inertial and surface tension forces;

$$\text{The dimensionless film thickness} \quad h^* = \frac{h}{D_0} \quad (5.4)$$

which defines how thick is our liquid film compared to the droplet size;

$$\text{The Bond number} \quad Bo = \frac{\Delta \rho g d^2}{\sigma} \quad (5.5)$$

which defines the ratio between body forces (gravity) and surface tension.

Splashing is defined as the formation of secondary droplets from the impact of one single droplet into a solid surface that can be dry or wet. The interaction

between a droplet and a wall can also feature other outcomes such as rebounding, adhesion or simple spreading. The transition regions between all these regimes are very hard to define, but some empirical correlations are available in the literature. Also, for these correlations to be used in any CFD applications, they have to be determined for certain specific values.

It has to be mentioned that most of the existing splashing models have been obtained from observation of single droplet impact onto a solid dry or wetted wall and that in reality spray impacts onto surfaces have a different dynamic because impinging droplets are affected by neighbours, and the outcome can be much different. Nonetheless, simulating this kind of process is complicated with the current experimental tools and correlations are much simpler to obtain in the observation of single droplet impact. Also, in the case of CFD applications, the simulation of multi-drop impact is too demanding and practically impossible.

The main steps in the formulation of any splashing model are explained below.

5.3.1 Transition Criteria

First of all, the model has to evaluate if the droplet is going to splash or if other regimes are going to be observed. The threshold between the two regimes is called transition criteria and is usually defined by an expression that includes the Weber number and one between the Ohnesorge and the Laplace number (the Laplace number is related to the Ohnesorge number with the following relationship $La = Oh^{-2}$). Usually a factor K is considered to be the reference point for the transition and is defined the following way:

$$K = We \cdot Oh^\alpha \quad (5.6)$$

Where the value alpha varies between different models but most of the ones available agree with a value of α of around 0.2. In the Bai and Gosman model, which is the one implemented in OpenFOAM, the transition criteria is defined slightly differently respect to the other model and relates the critical Weber number with the Laplace number in the following way:

$$We_{cr} = A \cdot La^{-0.183} \quad (5.7)$$

where A is a coefficient that varies with the surface roughness of the wall. They state that a wetted surface acts like a very rough surface and therefore

the value of alpha is the same as a very rough surface ($A = 1320$). One of the limitations of their model is that it does not take into account the film thickness which plays a fundamental role in the transition criteria and also in the outcome of splashing. In Kalantari model [57], the film thickness is taken into account and the transition criteria is varied accordingly. Four film thicknesses regimes are defined and reported in the table along with the value of K which correspond to the splashing threshold.

Film Thickness	Film Thickness Regime	Splashing Threshold (K)
$h^* \leq 0.1$	Wetted	$K = 1770 \div 1840$
$0.1 < h^* \leq 1$	Thin Liquid Film	$K = 5032h^* + 1304$
$1 < h^* \leq 2$	Shallow Liquid Film	$K = 6100(h^*)^{-0.54}$
$h^* > 2$	Deep Liquid Layer	$K = 4050$

5.3.2 Post-impingement characteristics

Once the model has evaluated whether the droplet will splash or not, if splashing occurs, it needs to calculate the quantities of the splashed dropped. It is therefore convenient to identify the main quantities that define the status of a droplet.

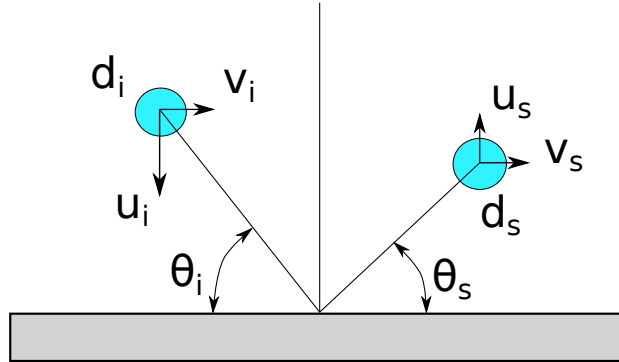


Figure 5.5: Impinging and Ejecting droplet main parameters

As it can be seen in Figure 5.5, both the impinging and the splashing droplets are characterised by their diameter (d_i and d_s), velocity (which can be decomposed in normal velocity u and tangential velocity v) and impact angle (θ_i and θ_s). In order to simplify the calculations, in numerical codes, the solver considers for parcels (which represent a group of droplets) rather than droplets, because it is usually too demanding to reproduce all the droplets in a computational domain.

For this reason, we have to introduce another parameter, the number of droplets in each parcel n , for both the impinging and splashing droplet.

Starting from the impinging characteristics, the splashing model has to evaluate post-impingement quantities such as splashing-to-incident mass ratio, droplet size, velocity, number of secondary droplets and ejection angle.

Considering the splashing-to-incident mass ratio (which is as the name suggests the ratio between the total mass of all the splashed droplets and the incident droplet mass), the Bai and Gosman model assumes the following value as observed from experiments:

$$r_m = \frac{m_s}{m_I} = \begin{cases} [0.2 : 0.8], & \text{for a dry impact} \\ [0.2 : 1.1], & \text{for a wet impact} \end{cases} \quad (5.8)$$

Other authors use a different approach for the mass ratio, being a function of the Weber number or the K variable. The main problem for applying these models to applications such as the spill of a fuel tank [126] is that the Weber number range investigated in their applications is much smaller than the ones that characterize fuel cascades, where the droplet diameters and velocities are much higher. Therefore a new correlation has to be developed to be applied in higher Weber numbers.

Another parameter that has to be given as an input is the droplet ejection angle. One of the main advantages of having a normal impact is that we do not need to consider the impact angle, therefore, the splashed droplet are symmetric. Most of the models available in the literature agree that the ejection angle depends strongly on the time of the ejection, meaning that early ejected droplet tend to have a bigger angle and higher velocities, while droplets ejected later are more likely to be slower and with a smaller angle. The experimental results analysed by Bai and Gosman report that droplets ejection angles are likely to lie in the range $[5^\circ; 50^\circ]$, and outside this range, the probability is very low. Other models use a different range and also use the impingement angle in their calculations. It is worth mentioning that the azimuthal angle (being the circumferential direction within the plane tangential to the wall) is chosen to be randomly between 0 and 2π , which is supposed to conserve tangential momentum statistically.

Velocity and size of the ejected droplets are also fundamental parameters to evaluate. Their calculation from the experiments is challenging, and statistical models can be used. Since each splash event produces hundreds or even thou-

sands of secondary droplets, focusing the attention on all of them is prohibitive with the current tools. In Bai and Gosman formulation, each splashing droplet is considered to produce p secondary droplets where p is a value greater than one. All of this secondary droplets contain the same amount of mass m_s/p where m_s is total the mass of the incoming splashing droplets. The value of p is usually chosen to be accurate and not too computationally costly. Experiment observations typically show that the secondary droplets follow characteristic distributions, similar to the general Rosin-Rammler distribution commonly used in spray simulations. First, the mean diameter is calculated from other parameters in the following way:

$$\bar{d} = \frac{d_v}{6^{1/3}} = \frac{1}{6^{1/3}} \left(\frac{r_m}{N_s} \right)^{1/3} d_I \quad (5.9)$$

where d_I is the incident droplet diameter, N_s is the total number of secondary droplets per splash and r_m is the splashing-to-incident mass ratio as mentioned before. Starting from the splashed mean diameter the distribution function of the splashed droplets diameter is calculated as:

$$f(d) = \frac{1}{\bar{d}} e^{-d/\bar{d}} \quad (5.10)$$

Along with the droplets sizes, we have to calculate their velocities. It was already mentioned before how to calculate the azimuthal angle and the ejection angle of the droplets, therefore the last quantity that has to be evaluated is the velocity magnitude which is done by energy considerations. The splash kinetic energy is calculated as:

$$E_{KS} = E_{KI} + E_{I\sigma} - E_D - E_{S\sigma} \quad (5.11)$$

where E_{KI} is the incident kinetic energy, $E_{I\sigma}$ the incident droplet surface energy, $E_{S\sigma}$ the surface energy of all the splashing droplets and E_D the dissipative energy loss. Even though this equation is physically right, the evaluation of the dissipated energy is complex and some of the formulations available seem to underestimate its value. The calculation of the splash kinetic energy is straightforward only if one parcel is considered ($p = 1$), but for more parcels we need to provide an additional equation:

$$\left(\frac{V_{SN,1}}{V_{SN,i}} \right) \approx \ln \left(\frac{d_1}{d_I} \right) / \ln \left(\frac{d_i}{d_I} \right) \quad (i = 2, \dots, p) \quad (5.12)$$

At last, this equation can be coupled with the one above to calculate the droplet velocity and therefore all the right quantities for the splashing model are available to implement the splashed droplet in the Lagrangian calculation.

5.4 Description of interFoam solver

The calculation of the physical solution is achieved by the use of a Volume of Fluid (VOF) solver part of the toolbox OpenFOAM. The solver uses a modified Volume of Fluid approach with an additional term in the momentum equation to account for the smearing of the interface.

If we consider a physical domain where both a gas and a liquid phase are present, we can define a function that indicates which phase the cell belongs to:

$$\alpha = \begin{cases} 1, & \text{if cell belongs to the liquid phase} \\ 0, & \text{if cell belongs to the gas phase} \end{cases} \quad (5.13)$$

Also, the function can assume values between 1 and 0, and those points are representative of the interface between gas and liquid. The conservation of mass can now be defined:

$$\frac{\partial \rho}{\partial t} + \nabla \cdot (\mathbf{u}\rho) = 0 \quad (5.14)$$

In this equation density is calculated using the function α :

$$\rho(\mathbf{x}, t) = \rho_l \alpha(\mathbf{x}, t) + \rho_g (1 - \alpha(\mathbf{x}, t)) \quad (5.15)$$

where ρ_l and ρ_g are the density of the liquid and the gas phase, respectively. Introducing this definition in the continuity equation, we obtain:

$$(\rho_l - \rho_g) \frac{\partial \alpha(\mathbf{x}, t)}{\partial t} + \nabla \cdot ((\rho_l - \rho_g) \alpha(\mathbf{x}, t) \mathbf{u}(\mathbf{x}, t)) + \rho_g \nabla \cdot \mathbf{U}(\mathbf{x}, t) = 0 \quad (5.16)$$

Now if we consider incompressible flow, the equation can be simplified into the following:

$$\frac{\partial \alpha}{\partial t} + \nabla \cdot (\mathbf{u}\alpha) = 0 \quad (5.17)$$

As already mentioned before, numerical diffusion is one of the major problems

encountered in VOF formulations, therefore in interFoam an additional term is introduced in the phase fraction equation, to compress the interface and avoid high diffusion. The equation becomes:

$$\frac{\partial \alpha}{\partial t} + \nabla \cdot (\mathbf{u}\alpha) + \nabla \cdot [\mathbf{U}_c \alpha (1 - \alpha)] = 0 \quad (5.18)$$

where \mathbf{U}_c is a the velocity compression term calculated in an appropriate way. The momentum equation is defined in the following way:

$$\frac{\partial(\rho\mathbf{u})}{\partial t} + \nabla(\rho\mathbf{u}\mathbf{u}) = -\nabla p + \nabla \cdot \mathbf{T} + \mathbf{F}_\sigma \quad (5.19)$$

where \mathbf{T} is the stress tensor and \mathbf{F}_σ is the source term arising from the surface tension. The calculation of this term is one of the most important steps in the formulation of a VOF solver and in interFoam is achieved in the following way (using the continuum surface model (CSF) of Brackbill et al [146]):

$$\mathbf{F}_\sigma = \sigma k \nabla \alpha, \quad k = -\nabla \cdot \mathbf{n}, \quad n = \frac{\nabla \alpha}{|\nabla \alpha|} \quad (5.20)$$

5.5 Validation of the solver for inertia-dominated flows

The solver interFoam has been validated for a wide range of applications [70], and in the following section it will be validated for inertia dominated flows (flows in which the inertia effects dominate the surface tension ones), such as droplet impact onto a solid surface. The main limitations of the solver, which represents the VOF limitations in general, are the smearing of the interface, which is partially corrected by the above-mentioned compression term, and the calculation of the normal and curvature of the interface. On the other hand, the main advantages are an easy implementation and the high mass conservativeness which cannot be achieved in any other formulation such as the Level Set method.

5.5.1 Water droplet impact on flat surface

The first testcase reproduced is the impact of a water droplet on a flat surface at low speed, so that no splashing occurs and the droplet sticks to the surface oscillating up and down.

A distilled water droplet of 2.28mm diameter impacts the ground at 1m/s . The experiments were reproduced by [145] along with numerical results using their Level Set solver with dynamic contact angle implementation. The contact angle is defined as the angle formed when a liquid-vapour interface meets a solid surface. In the formulation of a Eulerian solver, the contact angle implementation is one of the most delicate and uncertain, this because the evolution of it during time is difficult to predict and is driven by several parameters, the main one being the surface roughness. The contact angle assumes a constant value when the contact line is not moving and the so-called advancing and receding contact angles when the contact line is moving. As stated by many authors and also by Yokoi, these two values assume a maximum and a minimum, and the values assumed between these two depend on the interface velocity, leading to a value equal to the equilibrium one when the velocity approaches zero.

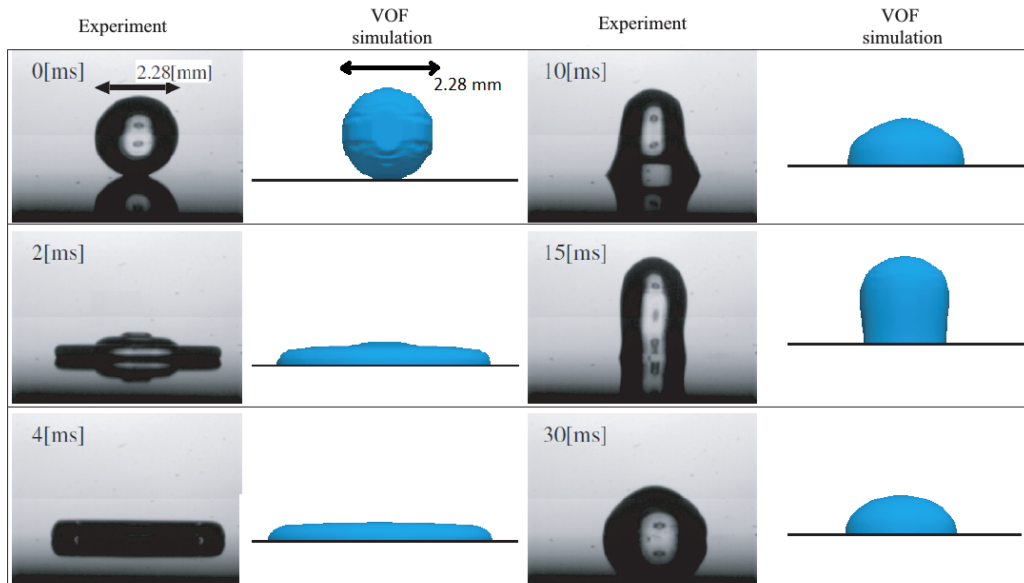


Figure 5.6: Qualitative comparison between CFD and experiment

Yokoi proposed a model for the dynamic contact angle which is supposed to represent the real values assumed more realistically. The contact angle θ is calculated from its equilibrium value θ_e , the maximum dynamic advancing angle θ_{mda} , the minimum dynamic receding angle θ_{mdr} , the velocity of the contact line U_{CL} and the capillary number $Ca = \mu U_{CL}/\sigma$. The equation used is the following:

$$\theta(U_{CL}) = \begin{cases} \min \left[\theta_e + \left(\frac{Ca}{k_a} \right)^{1/3}, \theta_{mda} \right] & \text{if } U_{CL} \geq 0 \\ \max \left[\theta_e + \left(\frac{Ca}{k_r} \right)^{1/3}, \theta_{mdr} \right] & \text{if } U_{CL} < 0 \end{cases} \quad (5.21)$$

the constants k_a and k_r are material related to advancing and receding, respectively. These are chosen to fit the curve from experimental data. Quantitative and qualitative results obtained from CFD calculations are compared with the experimental data and shown in pictures.

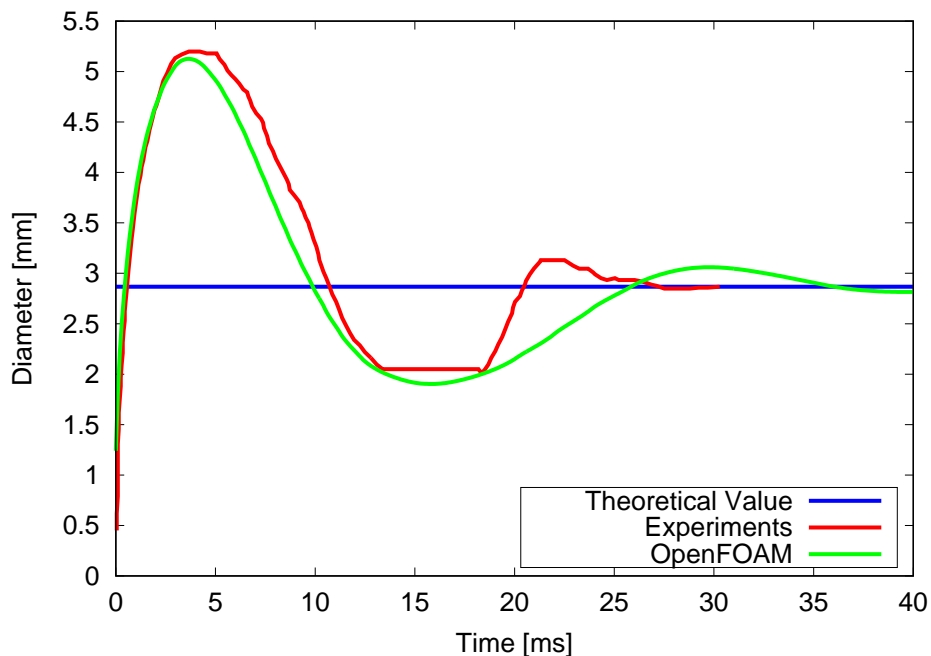


Figure 5.7: Droplet diameter evolution with time

Results show overall a good agreement with the experiments and the droplet diameter reaches its theoretical value at the end of the simulation, following the Experiment evolution with only some discrepancies after 20ms from the start of the simulation.

5.5.2 Crown Evolution of Droplet Impact

Single droplet impact on a thin film was investigated by Cossali et al. [64]. The liquid crown propagation of a droplet impacting a thin liquid film is investigated.

A single droplet of diameter $D = 3.82\text{mm}$ with speed $U = 3.56\text{m/s}$ impacts a pre-existing film of thickness $T = 2.3\text{mm}$. The Weber number is 670. Liquid crown diameter obtained from the CFD simulation is compared with the experimental results. A very good agreement (the error on the calculation was kept below 10%) was found.

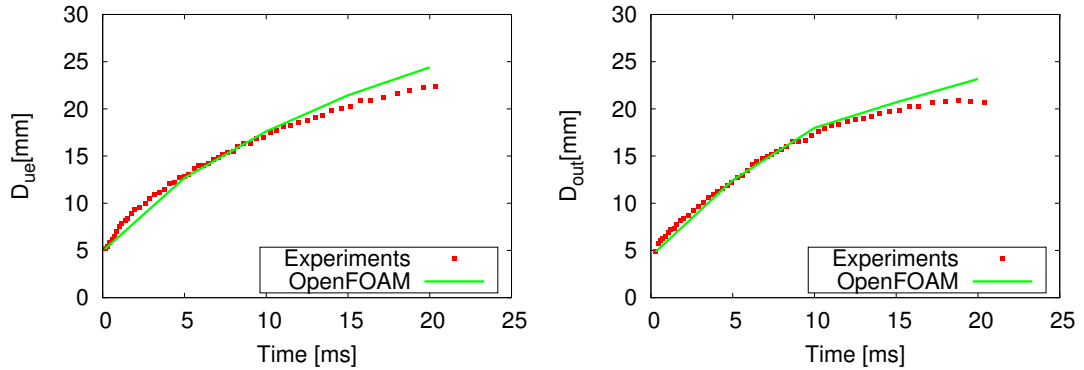


Figure 5.8: Crown evolution with time

5.5.3 Conservation of mass

One of the advantages of the VOF formulation is the conservation of mass. This is fundamental in the simulation of splashing of droplets because a decay or increase in the droplet mass would lead to an error in the evaluation of the splashed mass of the droplet as well as the number of secondary droplets and other parameters.

A simulation with a droplet splashing onto a solid surface was run in order to demonstrate that the *interFoam* solver is mass conservative. Figure 5.9 shows the integral value of the droplet volume computed in the whole domain and normalised to its initial value. It is clear that the droplet mass is conserved and the error is well below 0.1%.

5.5.4 Effect of liquid properties on splashing

It was mentioned earlier that the outcome of splashing depends on many parameters, among which the properties of the liquid considered. For this reason the effect of surface tension, kinematic viscosity and density were analysed by simulating two splashing droplets using water and hexane. Table 5.1 shows the difference in properties for the two liquids (values for LNG are also shown to illustrate the similarity with hexane).

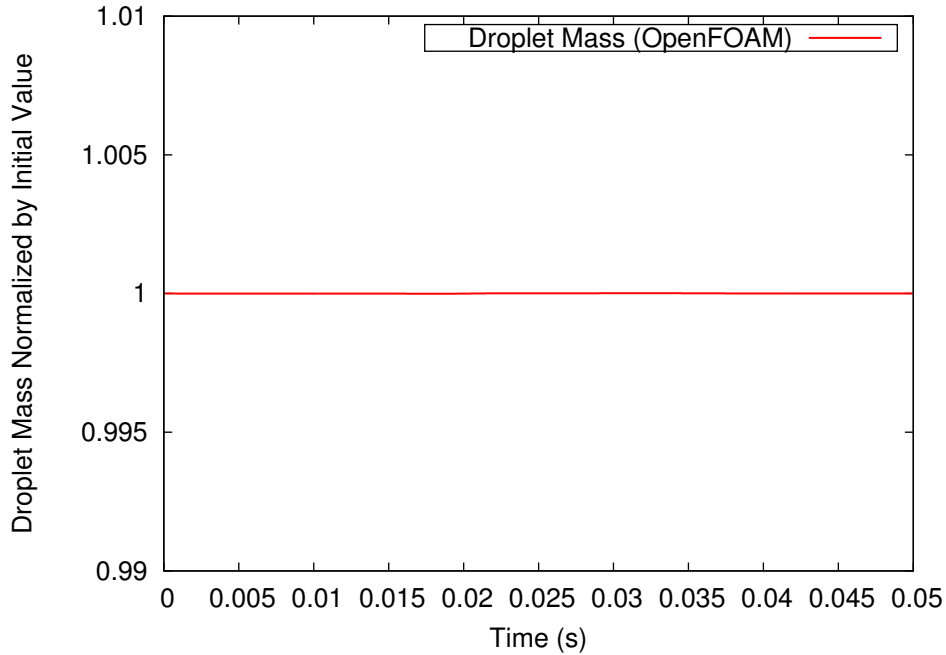


Figure 5.9: Droplet mass evolution with time

Table 5.1: Properties for the different liquids analysed

Property	Water	Hexane	LNG
$\nu(m^2/s)$	$1 \cdot 10^{-6}$	$5.7 \cdot 10^{-7}$	$3.12 \cdot 10^{-7}$
$\rho(kg/m^3)$	1000	654.8	468.1
$\sigma(N/m)$	0.07	0.01843	0.014

The results for water and hexane look quite different. Results with water show an earlier formation of droplets and the droplets are bigger than in the case of hexane. The physical demonstration behind this behaviour is that the higher surface tension and viscosity of water limit the extension of the ligaments which therefore break earlier. This is a further confirmation of the findings of HSE which showed how droplets formed from hydrocarbons are smaller and more homogeneous. The effect of density should not play an important role as there is no direct effect on the splashing phenomenon.

5.6 Splashing of Droplets

To develop the splashing model, the solver was first validated against experimental analysis and the Bai and Gosman correlation within their range of validity.

Vander Wal [147] investigated droplet impact on variable film depths and for different liquids.

The paper presents numerous results obtained varying the film thickness, impact velocity and properties of the liquid used. The most interesting ones from the current work point of view were the simulations of Heptane (C_7H_{16}), a hydrocarbon which possesses similar properties to hexane. Numerical simulations were therefore carried out using four different impact velocities and film depths, comparing them with the experiments. The results are shown in Figure 5.10 and 5.11 and the experiment settings described in the figure caption.

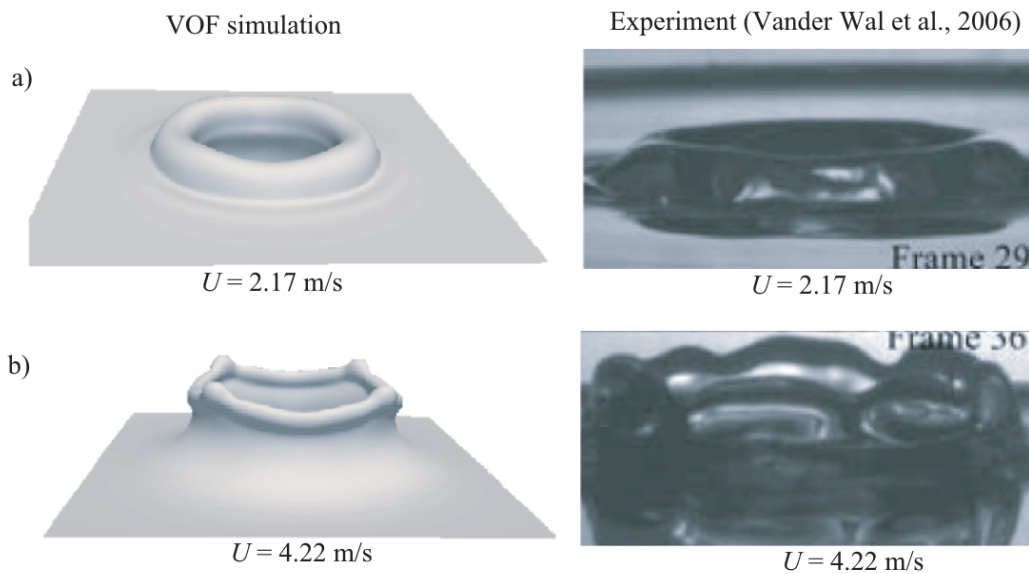


Figure 5.10: Comparison between simulations (left) and experiments (right) for velocities of 2.17 m/s (a) and 4.22 m/s (b) and non-dimensional film thicknesses of 1. Diameter of droplet is always 2mm.

Regarding the Bai and Gosman model, the range of applicability of their model is not applicable in the current work, but in order to validate the solver for splashing simulations VOF calculations were carried out for different Weber and Laplace number ranges and compared with the correlations of the Bai and Gosman model. The range of parameters used is reported in Table 5.2, as well as the results obtained in the simulations in terms of mass splash ratio and splashing angle.

Figure 5.12 and 5.13 show a 3 dimensional view of the mass splash ratio and splash angle as a function of the Weber and Laplace number (the points coloured in green are the ones for which the results are in agreement with the Bai and

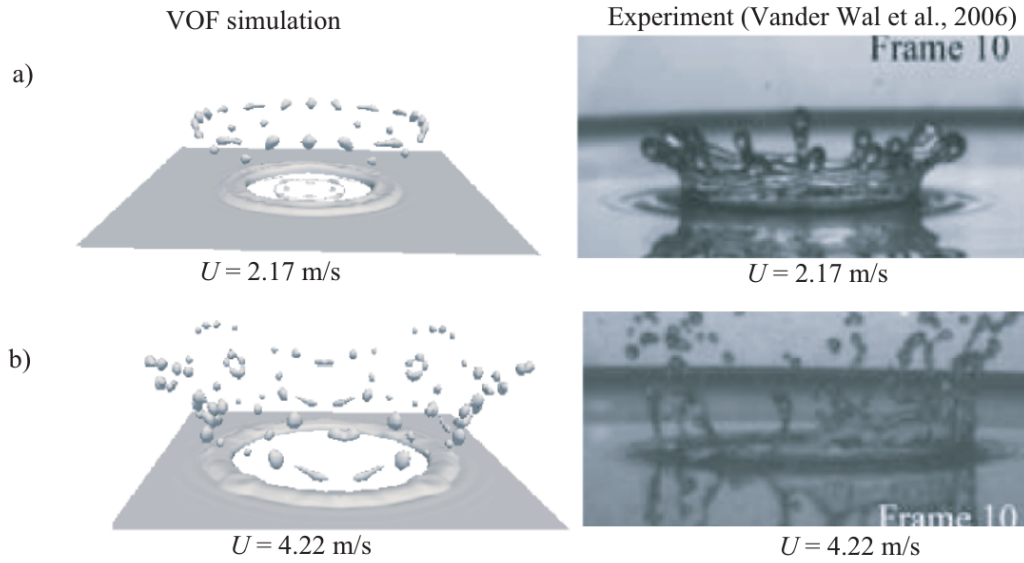


Figure 5.11: Comparison between simulations (left) and experiments (right) for velocities of 2.17 m/s (a) and 4.22 m/s (b) and non-dimensional film thicknesses of 0.1. Diameter of droplet is always 2mm.

Gosman model, on the other hand, the red points show a non-conformity of the results with the model), which give a much clearer view of how the increase of such parameters affects the validity of the model.

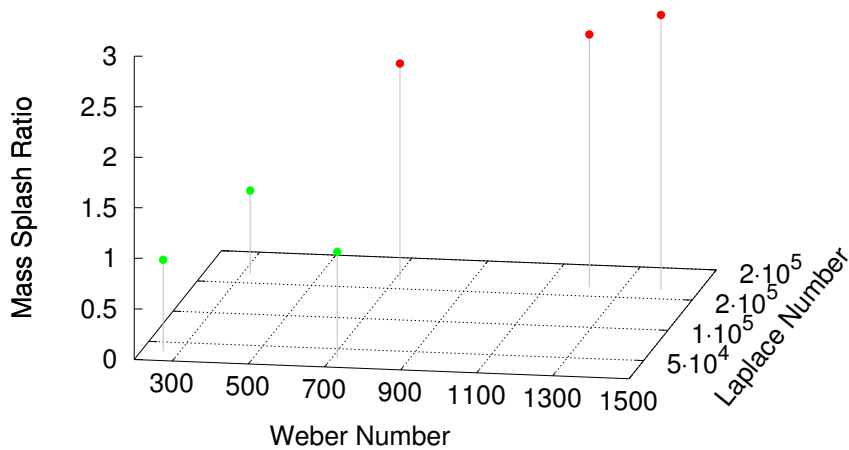


Figure 5.12: Mass splash ratio for the validation testcases

#	La	We	r_m	$\theta(^{\circ})$
1	35000	257	0.905	38
2	35000	714	1.05	45
3	164374	320	0.825	25
4	164374	1212	2.5	30
5	164374	714	2.14	30
6	164374	1400	2.72	65

Table 5.2: Results for Bai and Gosman validation

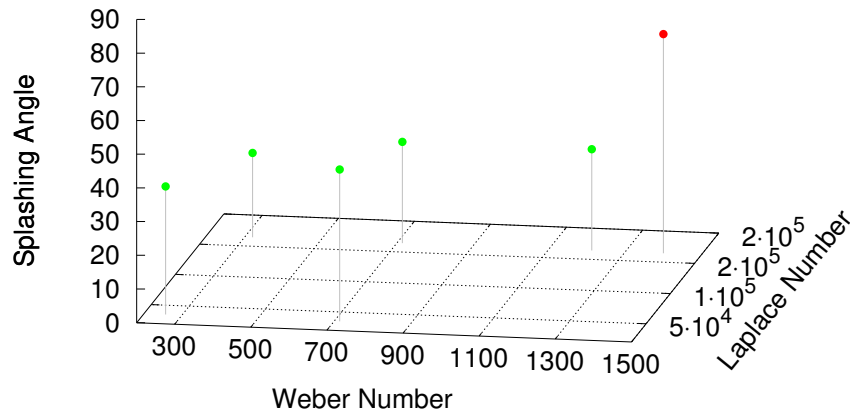


Figure 5.13: Splash angle for the validation testcases

The results for the mass splash ratio (r_m) point out that for small Weber numbers ($We < 700$) the CFD predictions are in agreement with the model, while increasing its value leads to ratios well above the limit imposed by the model ($r_m < 1.1$) which confirms the fact that the model gives wrong results for such range. The effect of the Laplace number is very similar, where an increase of its value leads to a much higher number for the mass splash ratio, outside the limit of applicability of the model.

For the splashing angle things are slightly more stable, meaning that for significant variation of the Weber and Laplace number the values obtained for θ fall

in the range of applicability of the model, with the only exception of case #6, where the values obtained are however pretty close to the one given in the model.

This is a further confirmation that in the simulation of large spills from a tank, the Bai and Gosman model is entirely out of range in terms of Weber and Laplace number, and it would give wrong values for the splashed quantities which would affect the solution for the Lagrangian phase as this is heavily influenced by the output values of the splashing model.

5.6.1 Model Development

In order to improve the current model available in OpenFOAM a set of simulations were carried out with different input parameters such as the droplet diameter (d), impact velocity (U_0) and initial film thickness (H). Although the splashing phenomenon is influenced by other parameters as well, such as the liquid properties, these parameters were assumed to be constant, for two main reasons; the first one is that the number of simulations to run in order to obtain the model would increase dramatically, unachievable from a realistic point of view, and the second reason is that the properties of most hydrocarbons are very similar (especially in terms of surface tension), therefore the outcome of splashing would not lead to observable differences (this means that although the correlations will be developed starting from simulations of hexane, they can be extended to a large number of hydrocarbons with similar properties). It has to be mentioned that one quantity that could lead to remarkable variations is the boiling temperature of the liquid. The contact angle of the droplet is highly dependant on the temperature of the solid surface, and the threshold is the boiling temperature of the liquid, above which the contact angle shows critical differences. This could be of particular interest in terms of LNG droplet impact, but it will be shown later that a cascade of LNG will most likely evaporate well above the ground level, therefore splashing would not be experienced at all. For this reason, it was assumed that the three parameters mentioned above are a good representation of all the conditions that can be obtained in a hydrocarbon spray impact.

These three parameters can be represented by non-dimensional quantities, more convenient and historically correct. These are the Weber number, Laplace number and non-dimensional film thickness. In order to cover the range of parameters that are observed in the type of application we are trying to develop the model for, a wide range of quantities was adopted, summarised in the table

below:

$d(mm)$	$U_0(m/s)$	$H(mm)$	La	We	H^*
0.2-3	1-11	0.5-2	$(0.17 - 2.6) \cdot 10^5$	7.1-130000	0.2 - 2

Table 5.3: Setup quantities range for the simulations

The same mesh was adopted in all the simulations, a structured hexahedral mesh made of 4 million cells, scaled according to the different droplet sizes. This was assumed to be a good compromise between accuracy of the simulation and computational time. Although an increase in the number of cells results in a higher number of splashed particles that can be captured, especially for the smaller droplets. Nonetheless, the quantities of interest in the splashing model development are the splashing threshold, splashing angle and mass splash ratio. These three quantities are not much influenced by the mesh size as long as a certain number of cells is used to represent the droplet. A zoom on the mesh is shown in Figure 5.14 for the droplet and the film below.

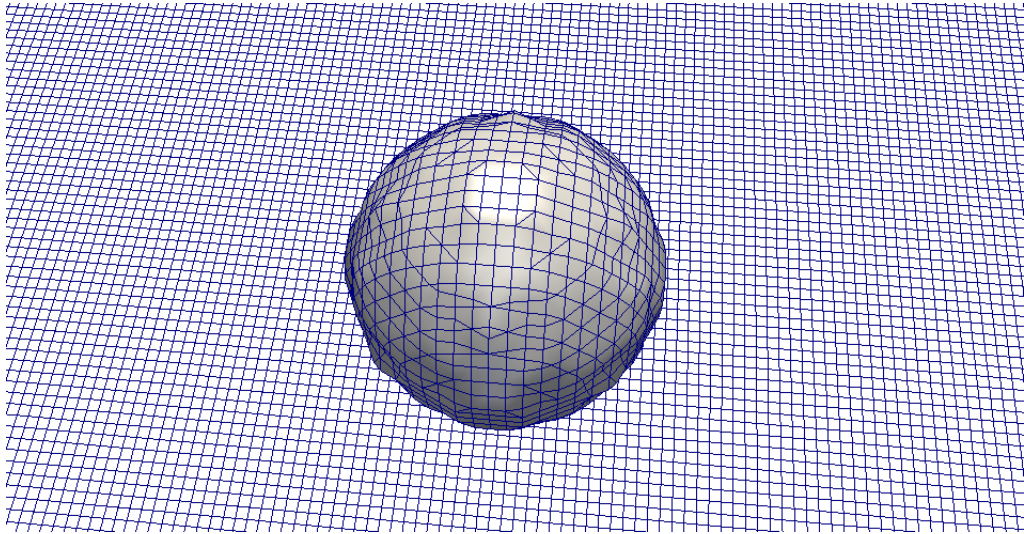


Figure 5.14: Mesh detail on the droplet and underlying film

The initial condition for the different simulations is shown in Figure 5.15.

The three quantities (splashing threshold, splashing angle and mass splashing ratio) were extrapolated in the following way:

- The droplet was considered to splash if any ligament or secondary droplet was formed on the splashed surface

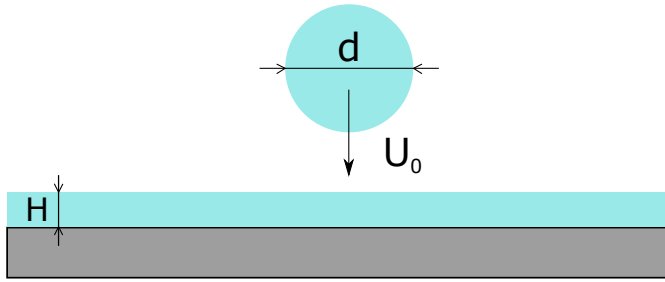


Figure 5.15: Initial Condition for the simulation

- The angle varies from the beginning until the end of the simulation, and the maximum and minimum values were recorded using isosurfaces at $\alpha = 0.5$ which represents the surface of the liquid
- The mass splash ratio was obtained integrating the droplet volume fraction at the beginning of the simulation and the volume fraction of all the secondary droplets

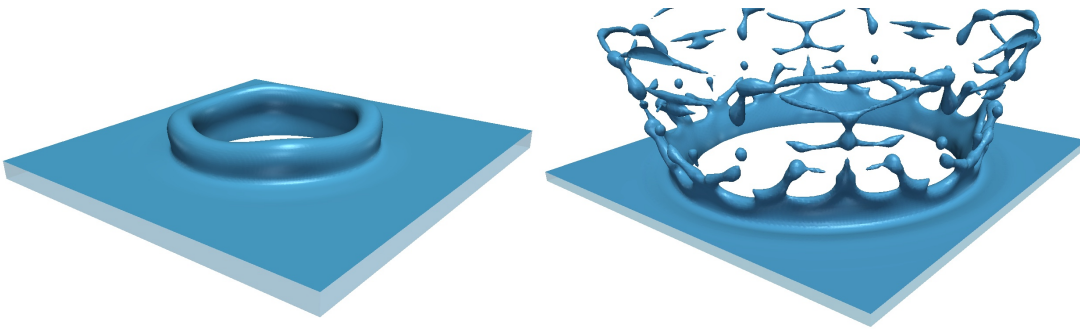


Figure 5.16: Droplet absorbed in the film (left, test 33) and droplet splashed (right, test 49)

Figure 5.16 shows two different testcases (test 33 and 49), where in the first a clear absorption in the liquid film was observed, while splashing can be seen in the second, where a large number of droplets was formed due to the high-velocity impact.

5.6.2 Development of the Correlations

All the simulations were postprocessed and analysed to obtain the desired quantities. For the testcases where the droplet did not splash, the equivalent simulation where only the film thickness was increased was assumed not to splash and therefore not run. This is in agreement with the fact that an increase in the film

thickness increases the splashing threshold and consequently a droplet with fixed diameter and velocity will not splash if the film is increased. Table 5.4 summarises the results obtained in terms of splash regime, splashing angle and mass splash ratio. For some of the testcases an accurate calculation of the mass splash ratio could not be done because of the high number of droplets exiting the domain, for which only the splashing angle was calculated.

Table 5.4: Simulation Setup

Sim. Num.	h (mm)	U (m/s)	d (mm)	Splash	$\theta(^{\circ})$	m_s
#1	0.5	1	0.2	×	-	-
#2	0.5	1	0.5	×	-	-
#3	0.5	1	1	×	-	-
#4	0.5	1	2	×	-	-
#5	0.5	1	3	×	-	-
#6	0.5	3	0.2	×	-	-
#7	0.5	3	0.5	×	-	-
#8	0.5	3	1	×	-	-
#9	0.5	3	2	✓	25	2.8
#10	0.5	3	3	✓	30	3.47
#11	0.5	6	0.2	×	-	-
#12	0.5	6	0.5	×	-	-
#13	0.5	6	1	✓	45	6.42
#14	0.5	6	2	✓	40-60	5.63
#15	0.5	6	3	✓	10-50	5.03
#16	0.5	9	0.2	×	-	-
#17	0.5	9	0.5	×	-	-
#18	0.5	9	1	✓	20-60	-
#19	0.5	9	2	✓	20-45	9.3
#20	0.5	9	3	✓	25-35	7.9
#21	0.5	11	0.2	×	-	-
#22	0.5	11	0.5	✓	60	1.01
#23	0.5	11	1	✓	20-45	-
#24	0.5	11	2	✓	10-45	10.71
#25	0.5	11	3	✓	20-40	7.62
#26	1	1	0.2	×	-	-
#27	1	1	0.5	×	-	-

Table 5.4: Simulation Setup

Sim. Num.	h (mm)	U (m/s)	d (mm)	Splash	$\theta(^{\circ})$	m_s
#28	1	1	1	×	-	-
#29	1	1	2	×	-	-
#30	1	1	3	×	-	-
#31	1	3	0.2	×	-	-
#32	1	3	0.5	×	-	-
#33	1	3	1	×	-	-
#34	1	3	2	×	-	-
#35	1	3	3	✓	20-30	5.48
#36	1	6	0.2	×	-	-
#37	1	6	0.5	×	-	-
#38	1	6	1	×	-	-
#39	1	6	2	✓	30-50	13.54
#40	1	6	3	✓	20-55	20.35
#41	1	9	0.2	×	-	-
#42	1	9	0.5	×	-	-
#43	1	9	1	✓	50	0.66
#44	1	9	2	✓	20-55	19.7
#45	1	9	3	✓	20-50	23.64
#46	1	11	0.2	×	-	-
#47	1	11	0.5	✓	-	-
#48	1	11	1	✓	50	-
#49	1	11	2	✓	40-50	-
#50	1	11	3	✓	25-50	27.2
#51	2	1	0.2	×	-	-
#52	2	1	0.5	×	-	-
#53	2	1	1	×	-	-
#54	2	1	2	×	-	-
#55	2	1	3	×	-	-
#56	2	3	0.2	×	-	-
#57	2	3	0.5	×	-	-
#58	2	3	1	×	-	-
#59	2	3	2	×	-	-
#60	2	3	3	×	-	-

Table 5.4: Simulation Setup

Sim. Num.	h (mm)	U (m/s)	d (mm)	Splash	$\theta(^{\circ})$	m_s
#61	2	6	0.2	×	-	-
#62	2	6	0.5	×	-	-
#63	2	6	1	×	-	-
#64	2	6	2	✓	55	1.24
#65	2	6	3	✓	35-50	27.04
#66	2	9	0.2	×	-	-
#67	2	9	0.5	×	-	-
#68	2	9	1	✓	50	0.598
#69	2	9	2	✓	45-55	-
#70	2	9	3	✓	40-55	-
#71	2	11	0.2	×	-	-
#72	2	11	0.5	×	-	-
#73	2	11	1	✓	55	-
#74	2	11	2	✓	40-55	-
#75	2	11	3	✓	30-50	-

In order to implement the splashing model in the upper lagrangian solver starting from the results obtained from the VOF simulations, correlations had to be developed for the quantities mentioned above in function of the three non-dimensional numbers (La, We, H^*).

The correlations were obtained using the regression analysis. This approach is able to model the relationship between a scalar quantity (such as splashing angle θ or mass splash ratio r_m) and a series of one or more independent quantities. If the relationship between these quantities is linear we talk about linear regression, if a polynomial expression is used the regression is called non-linear, which can make use of squares, cubes etc. of the independent variables to obtain a correlation. The method is here explained for a simple linear regression for simplicity, but for a more complex case, the approach is similar and easily obtained.

Lets consider two quantities related to each other, the independent quantity x and the dependent quantity y . If we consider n paired data $\{(x_i, y_i), i = 1, \dots, n\}$, an equation that describes the relation between the two quantities can be derived with an additional term that describes the error as:

$$y_i = \alpha + \beta x_i + \varepsilon_i \quad (5.22)$$

where ε_i represents the error for the i -th set of data. The aim of a linear regression model is to obtain the values of α and β that best fit the data, where the best fitting is achieved by minimising the global error. For a wide range of applications, the minimisation of the error is obtained by using the line that minimises the sum of the squares of the errors (the so-called least-squares approach). The mathematical expression of the error can be obtained as:

$$E(a, b) = \sum_{i=1}^n \varepsilon_i = \sum_{i=1}^n (y_i - a - bx_i)^2 \quad (5.23)$$

the regression analysis tells us how to obtain the values of a, b that minimise such function. These are obtained by expanding the above equation, giving the optimal values as:

$$\alpha = \bar{y} - \beta \bar{x} \quad (5.24)$$

$$\beta = \frac{\sum_{i=1}^n (x_i - \bar{x})(y_i - \bar{y})}{\sum_{i=1}^n (x_i - \bar{x})^2} \quad (5.25)$$

where \bar{x} and \bar{y} are the mean values of the sampled variables.

Splashing Threshold

The splashing threshold for most of the splashing models was presented before, and can be expressed as:

$$A = We \cdot La^{-0.183} \quad (5.26)$$

The Bai & Gosman model uses a fixed value for the A parameter, and this does not take into account for the change in film thickness that can affect the splashing behaviour. The CFD predictions showed a clear trend of an increase of the splashing threshold when the film thickness (both dimensional and non-dimensional) was increased. In short terms this means that a droplet will need a higher velocity (and therefore higher Weber number) in order to splash if the film thickness increases. Cossali et al [64] have developed a correlation considering the dependency of A on H^* , expressed in the following equation:

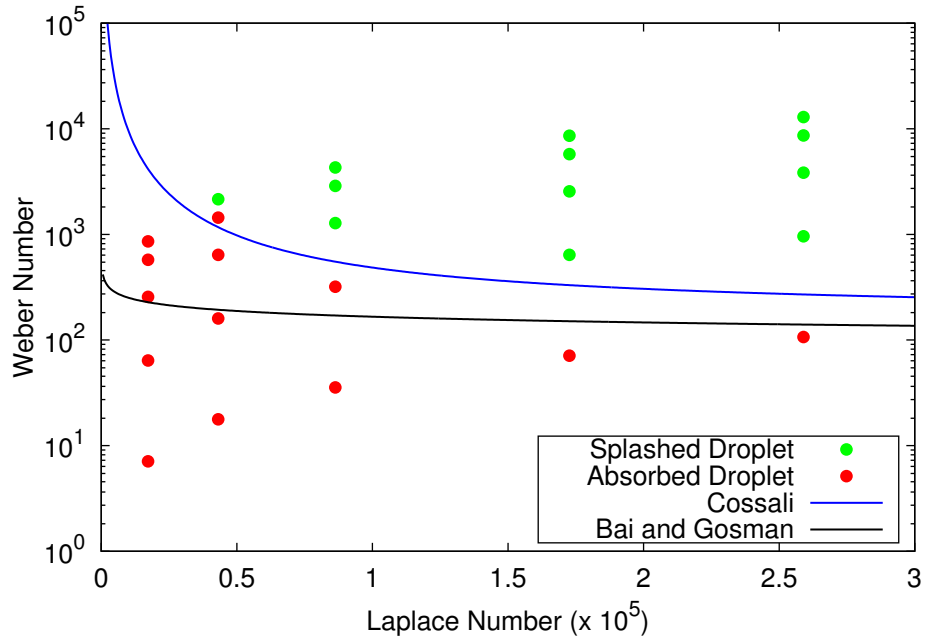


Figure 5.17: Splash Regimes for $H = 0.5\text{mm}$

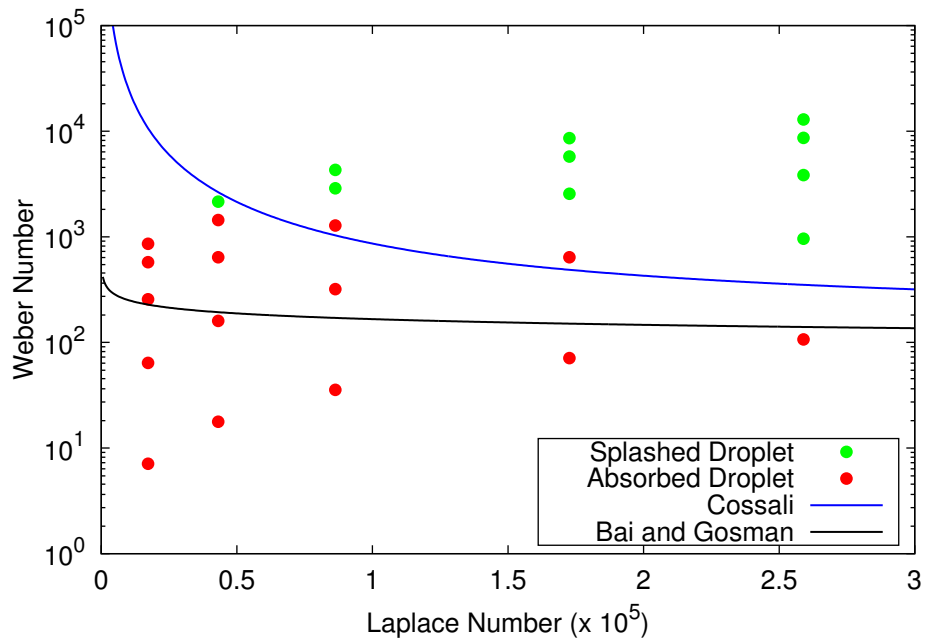
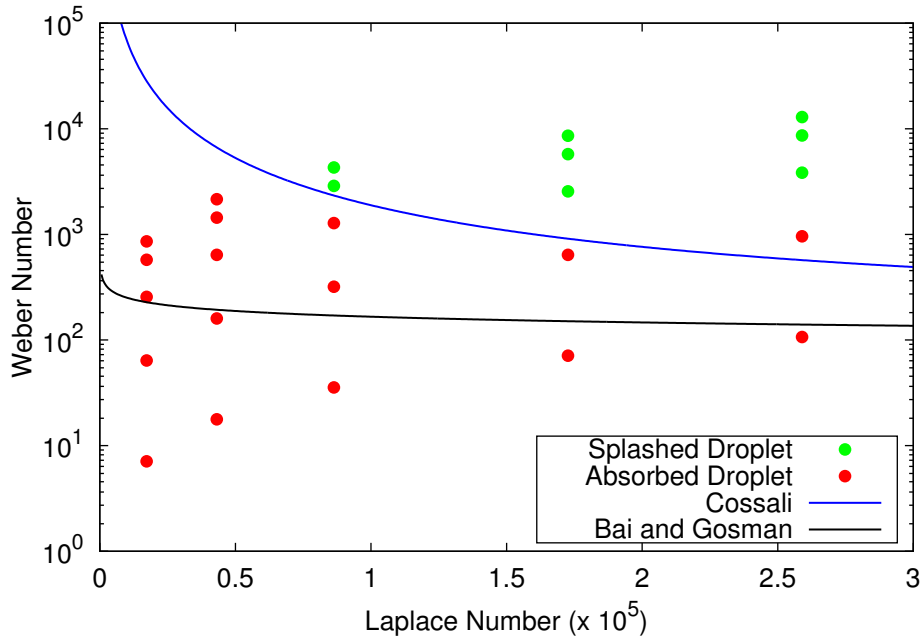


Figure 5.18: Splash Regimes for $H = 1\text{mm}$

$$A = La^{0.2}We = 2100 + 5880H^{*1.44} \quad (5.27)$$

The exponential value of the Laplace number is slightly different respect to the

Figure 5.19: Splash Regimes for $H = 2mm$

classical Bai and Gosman one, but in the literature, both values are used. Results for the splashing threshold obtained from the VOF simulations are compared with Cossali's correlation and for correctness Bai and Gosman correlation is shown as well.

As it can be seen, the threshold obtained from the Bai & Gosman correlation overestimates splashing for all the conditions, while the correlation proposed by Cossali show good agreement with the simulations.

Splashing Angle

The splashing angle is fundamental in the splashing process because it can change the spray pattern completely. In the literature, the angle is sampled between two values and chosen randomly. From the angles measured in the VOF calculations, these values change with the film thickness. These values are usually a function of many parameters such as Weber number, Laplace number, film thickness and also the impact angle of the droplet. In the type of application that we are developing the model for, the impact is usually perpendicular, meaning that we can neglect any effect coming from the tangential component of the droplet velocity.

Figure 5.20 shows the angles obtained from the VOF simulations and the correlations obtained with such data. The correlation takes into account for the

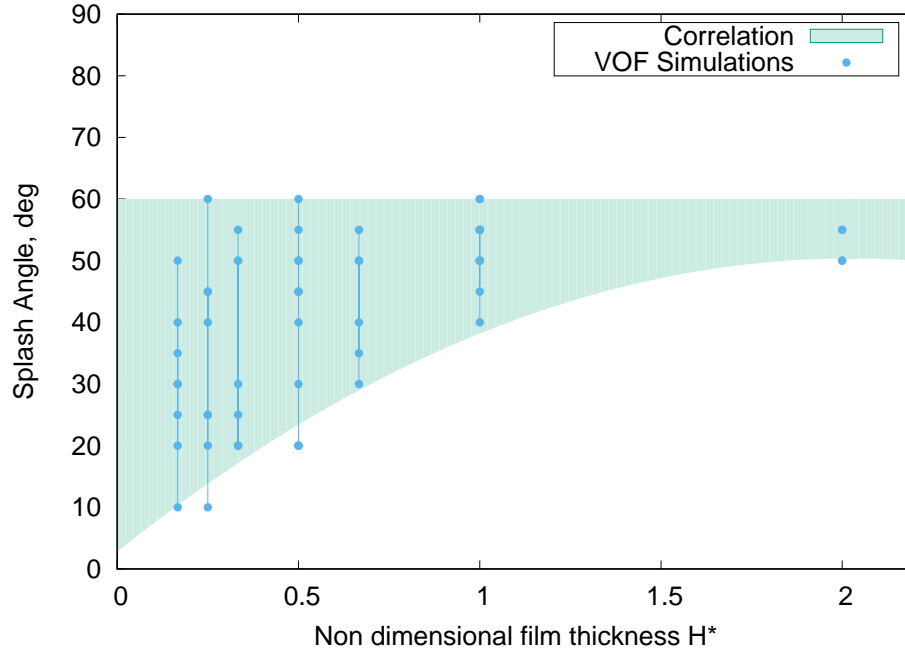


Figure 5.20: Correlation for the splashing angle

non-dimensional film thickness only because the splash angle did not show any dependency on the Laplace and Weber number for the range investigated.

While the maximum value of the splashing angle did not change much increasing H^* , the minimum value showed a strong dependency on the latter, and a quadratic correlation was obtained with the use of the regression analysis. The following equation describes it:

$$\theta_{min} = -11.6H^{*2} + 46.98H^* + 2.797 \quad (5.28)$$

Splash Mass Ratio

The splash mass ratio is probably the most complicated quantity to evaluate and in the literature this value is sampled in a wide range, depending on the type of splash (dry or wet). In a dry splash process, this value can assume a maximum value of 1, while in a wet condition, some mass can be introduced back from the film in the air by the splashing process. Therefore a value greater than 1 can be adopted. Extrapolating this value from our simulations, we obtained a wide range of values that sometimes exceeded 25. It was observed that this value depended on all the non-dimensional quantities (We , La , H^*) unlike the splashing angle, therefore a correlation that is a function of all the three quantities had to

be obtained.

Two different correlations were extrapolated from the data, linear and exponential, shown in the following expressions:

$$r_m = a_0 + a_1 La + a_2 We + a_3 H^* \quad (5.29)$$

$$r_m = b_0 La^{b_1} We^{b_2} H^{*b_3} \quad (5.30)$$

The values obtained from the correlations are shown in Figure 5.21 for both the linear and the exponential correlations.

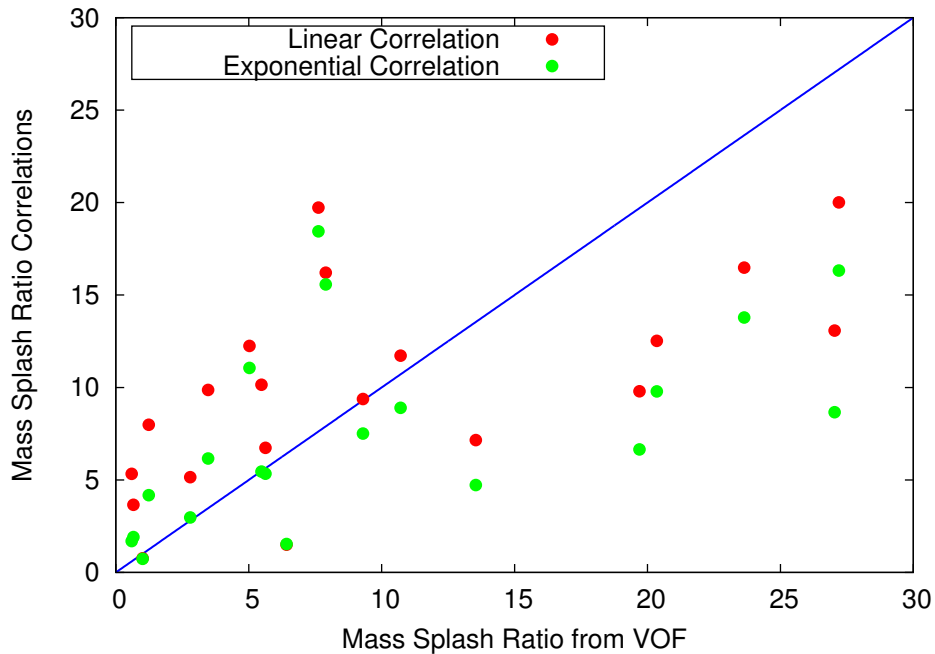


Figure 5.21: Correlation for the mass splash ratio

The two different correlations show similar results with the linear one being more accurate for higher values of r_m while the exponential seems to give better results in the region of low splashed mass.

5.7 Implementation of the new model in the lagrangian solver

The correlations obtained from the VOF simulations are here presented. For the splashing threshold the correlation obtained by Cossali [56] is used:

$$A = La^{0.2}We = 2100 + 5880H^{*1.44} \quad (5.31)$$

Values of A higher than the one calculated from this equation result in a splashing outcome, while smaller values result in absorption or spreading of the droplet onto the film.

The splashing angle was varied only in terms of its minimum value, while the maximum one was kept unchanged:

$$\theta_{min} = -11.6H^{*2} + 46.98H^* + 2.797 \quad (5.32)$$

This means that an increase in the non-dimensional film thickness results in an increase of the minimum splashing angle, for values of H^* less than 2. At last the mass splash ratio correlation is expressed using a linear correlation as:

$$r_m = a_0 + a_1La + a_2We + a_3H^* \quad (5.33)$$

or using an exponential correlation as:

$$r_m = b_0La^{b_1}We^{b_2}H^{*b_3} \quad (5.34)$$

where the values for the linear coefficient (which are the ones implemented in the solver for simplicity) terms are reported in Table 5.5.

Parameter	Value
a_0	-4.98
a_1	5.32e-05
a_2	8.26e-04
a_3	1.67

Table 5.5: Coefficients of the linear interpolation

In order to understand and show the effect of the new splashing model on a problem with splashing of particles a simple testcase has been set up using both the old Bai and Gosman model available in OpenFOAM and the new one implemented using the correlations mentioned above. A series of single droplets are splashed onto a solid surface which is initially dry, which eventually develops a thin liquid film due to the incoming droplets. Because the new model differs from the old one only in the wet regime, the two behave the same way in the

early stage of the simulation. As soon as the wet film is formed, the new model starts to show differences respect to the standard one, as it can be seen in Figure 5.22.



Figure 5.22: Droplets splashing at $t=0.053$ s using the Bai and Gosman model (left) and the new model (right)

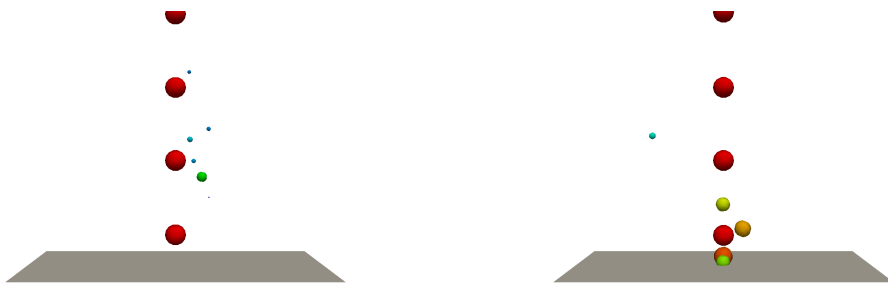


Figure 5.23: Droplets splashing at $t=0.067$ s using the Bai and Gosman model (left) and the new model (right)



Figure 5.24: Droplets splashing at $t=0.1$ s using the Bai and Gosman model (left) and the new model (right)

Comparison at later stages of the simulation shows the main differences between the two models in a more explicit way. The new model produces a smaller amount of droplets (because the splashing threshold increases with the film thickness, therefore a droplet is less likely to splash if the film is thicker), which are

however bigger in size, and also the angle of splashing is wider, leading to a wider shape of the splashing process. It has to be mentioned that the amount of parcels produced from a single impacting droplet has not changed in the new model, being fixed at two. This parameter can assume different values as reported by Bai [51], but two is the number that is more widely adopted.

5.8 Validation against experiments

The new model was tested and validated against the experimental results used in the validation of *cascadeFoam*, obtained by the HSL for a pure hexane cascade. The setup was the same used in the computational model used in chapter 3, the difference being only in the splashing model used. Results are shown for the experimental measurements, the ones obtained with the CFD model using the Bai and Gosman splashing model and the ones obtained with the new model implemented. Two points within the domain of interest are considered. The first one is within the core of the cascade in the impact point, while the second one is placed 5 meters from the tank walls at 0.5 m from ground level.

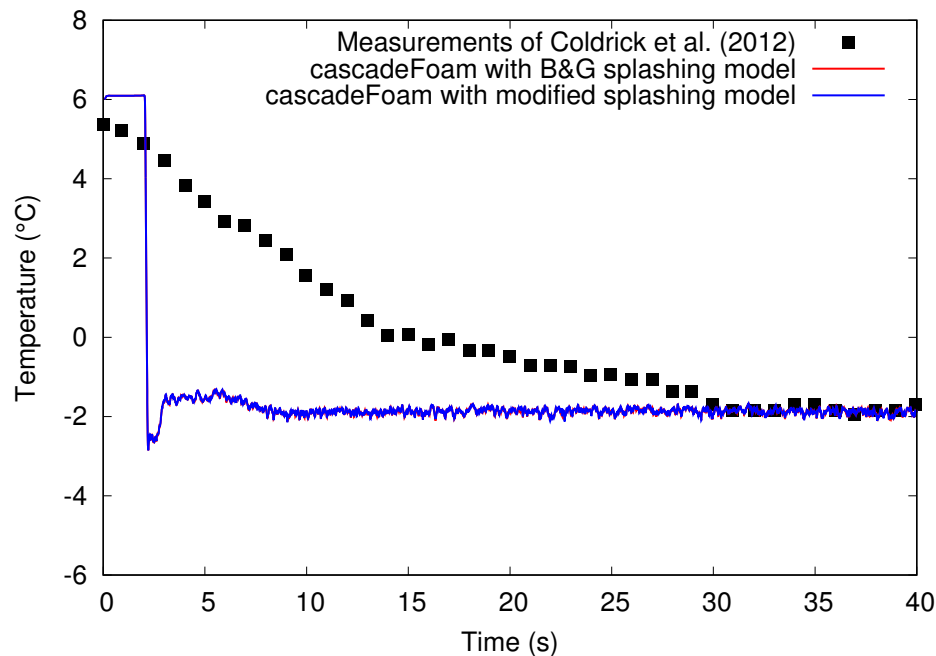


Figure 5.25: Temperature predictions in the bulk of the cascade (Point A)

Figure 5.25 and 5.26 present the results. The point placed in the impact region of the cascade show similar results for the two models used (for both the error is

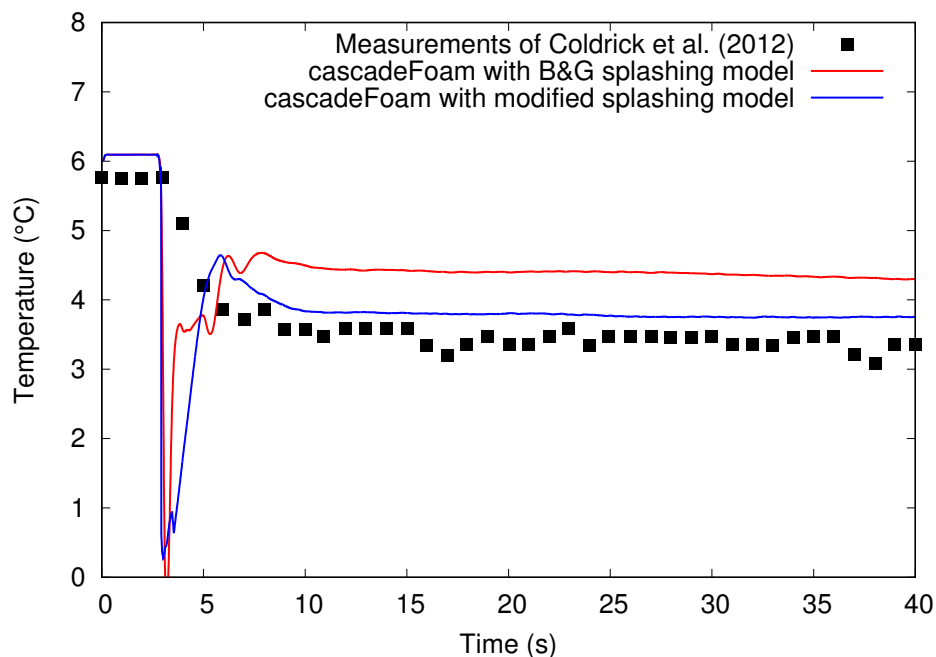


Figure 5.26: Temperature predictions far from the cascade (Point B)

kept below 1% between computational results and experiments), which confirms the findings discovered in chapter 3, where the splashing model was found to have a very little influence on the temperatures measured in the splashing zone, as well as for the concentration of hexane, mainly because the two are somehow correlated.

The point located far from the impact region shows, on the other hand, the differences between the two models. The new model predicts the temperature in such region with much higher accuracy (with an error of approximately 5%), leading to results which are close to the experimental measurements. The time at which the temperature drops is unchanged between the two models, due to the fact that this reflects the time at which the cloud reaches the point analysed. However, the temperature drops more in the new model, because the amount of mass splashed back into the gas phase is much higher and also the angle of splashing is much wider than in the previous model.

5.9 Chapter summary

The development of a modified splashing model was obtained using a large number of simulation by using the VOF method. The solver has been validated by

a large number of people and was compared to available experimental data and splashing models. The results obtained showed significant differences if compared to existing Bai & Gosman model, especially in terms of splashing threshold, angle and splash mass ratio. These values were interpolated in order to create a modified splashing model and implemented in the *cascadeFoam* solver, showing improved accuracy in the region far from the impact zone.

Chapter 6

Implementation of LNG

In this chapter, the development of Liquefied Natural Gas in the Lagrangian liquid library is described followed by a testcase where a liquid discharge from an LNG storage tank is simulated.

In the first Chapter the hazards that the handling of Natural Gas evidences were described, and in the previous chapters a tool capable of simulating a scenario in which a cascade of fuel creates a flammable cloud was developed. The liquids available in OpenFOAM in the Lagrangian library are many and include water, hexane, butane, nitrogen and other carbohydrates. Unfortunately, methane (the main component of LNG) is not present, mainly because very few researchers have simulated LNG with a Lagrangian approach. On the other hand, thermo-physical properties are available for methane in its gaseous state, allowing the simulation of LNG dispersion in the atmosphere.

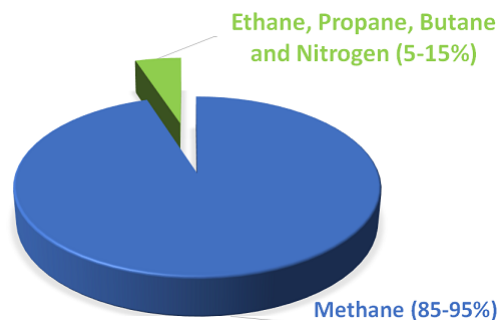


Figure 6.1: Composition of LNG

In the following, the assumption that LNG is equivalent to pure Methane will be made. This is because the composition of LNG is such that Methane accounts

for 85-95% plus of the total, meaning that the presence of other components (Ethane, Propane, Butane and Nitrogen) is much less important.

The class that implements the liquid properties of compounds in the Lagrangian formulation will be first described, then the development of methane will be introduced, and eventually, simulations of a possible scenario in an LNG plant will be carried out, showing the main differences with an oil plant.

6.1 Liquid Library for Lagrangian solvers

In some of the solvers available in OpenFOAM, the description of the thermo-physical properties of a liquid compound have to be introduced in the simulation folder, allowing to simulate any type of liquid if the quantities required by the solver are available. Unfortunately, for the nature of Lagrangian solvers, any liquid to be used needs to be present in a library, and any new liquid has to be introduced in that library using a determined set of function that will be described later.

The class is defined in such a way to have the quantities that do not depend on temperature or pressure on the top. These are the following:

- Molecular Weight
- Critical Temperature
- Critical Pressure
- Critical Volume
- Critical Compressibility Factor
- Triple Point Temperature
- Triple Point Pressure
- Normal Boiling Temperature
- Dipole Moment
- Pitzer's Accentric Factor
- Solubility Parameter

These quantities are defined by their numerical value and do not necessitate any function. Therefore the implementation of new liquid is straightforward if these values are known. Some of these parameters, however, are not going to affect the solution, such as the dipole moment, the accentric factor and the solubility parameter, and the lack of information regarding the liquid analysed can be neglected as these values are sometimes not present in the literature. After having defined the constant quantities for the liquid, the class requires the definition of quantities that depend on temperature and/or pressure, being the following:

- Density
- Vapour Pressure
- Heat of Vapourisation
- Heat Capacity
- Enthalpy
- Ideal Gas Heat Capacity
- Second Virial Coefficient
- Dynamic Viscosity
- Vapour Dynamic Viscosity
- Thermal Conductivity
- Vapour Thermal Conductivity
- Surface Tension
- Vapour Diffusivity

The dependency of these values on pressure is currently not implemented within the class, and therefore the functions are purely temperature dependant. The dependency on pressure is important when there are significant pressure changes in the domain, but considering our specific application, pressure is almost completely constant in the whole domain, therefore the assumption of considering the quantities at standard atmospheric pressure is acceptable.

In literature, we can find a wide range of functions describing the quantities listed above in function of temperature and pressure. OpenFOAM uses a set of functions called NSRDS developed by the National Institute of Standards and Technology (NIST) [148].

6.1.1 NSRDS Functions

In order to evaluate the value of the liquid properties at a certain temperature, OpenFOAM uses NSRDS functions. There are 9 functions called respectively: NSRDSfunc0, NSRDSfunc1, NSRDSfunc2, NSRDSfunc3, NSRDSfunc4, NSRDSfunc5, NSRDSfunc6, NSRDSfunc7, NSRDSfunc14. There is also an additional function called API that is used only for vapour mass diffusivity, developed by the American Petroleum Institute.

The NSRDS functions need a specific set of values in order to compute the thermophysical values. For example, the NSRDSfunc0 is computed as:

$$NSRDS0 = a + bT + cT^2 + dT^3 + eT^4 + fT^5 \quad (6.1)$$

where T is the temperature of the liquid and a, b, c, d, e, f are the 6 values required by the function.

The other functions are very similar and calculated as:

$$NSRDS1 = \exp(a + b/T + c \log(T) + d T^e) \quad (6.2)$$

$$NSRDS2 = a T^b / (1 + c/T + d/T^2) \quad (6.3)$$

$$NSRDS3 = a + b \exp(-c/T^d) \quad (6.4)$$

$$NSRDS4 = a + b/T + c/T^3 + d/T^8 + e/T^9 \quad (6.5)$$

$$NSRDS5 = a/b^{1+(1-T/c)^d} \quad (6.6)$$

$$NSRDS6 = a (1 - T_r)^{(e T_r + d)T_r + c)T_r + b} \quad (6.7)$$

$$NSRDS7 = a + b ((c/T)/\sinh(c/T))^2 + d ((e/T)/\cosh(e/T))^2 \quad (6.8)$$

for which a different number of parameters need to be specified. The function NSRDS14 has a longer formulation and was not reported here but it is based on the same concept and definition of constants.

6.2 Properties of Liquid Methane

As it was discussed already earlier, in order to implement and simulate spills of Liquefied Natural Gas, liquid methane properties have to be developed for the lagrangian library. LNG composition varies depending on its source and processing history but roughly 85 to 95 % of it is methane, the simplest of the hydrocarbons, with the rest of it being made mostly of ethane and some propane and butane, along with trace amounts of nitrogen.

The properties required by the liquid library in the lagrangian solvers are reported in Table 6.1.

Table 6.1: Properties of Methane (CH_4)

Property	Value
Molecular Weight (W)	16.04 $Kg/Kmol$
Critical Temperature (T_c)	190.85 K
Critical Pressure (p_c)	4640170 Pa
Critical Volume (V_c)	0.0062 $m^3/Kmol$
Critical Compressibility Factor (Z_c)	0.29
Triple Point Temperature (T_t)	90.66 K
Triple Point Pressure (p_t)	11679 Pa
Normal Boiling Temperature (T_b)	111.66 K
Dipole Moment ($dipm$)	0.0668 $\cdot 10^{-30} C \cdot m$
Accentric Factor (ω)	0.012 $(J/m^3)^{0.5}$
Solubility Parameter (δ)	-

The solubility parameter could not be found, but since its value will not affect the solution the value used for Ethane (C_2H_6) will be assumed.

These properties are easily implemented for methane in the lagrangian library. Moving now onto the thermophysical properties that depend on the temperature, these are a bit more complicated to implement, because of the NSRDS functions. In order to simplify the implementation, we will assume that all the liquid properties are constant with respect to temperature, so that the coefficients for the functions do not need to be calculated using a curve fitting procedure. This assumption comes from the fact that in the simulations that will be run for LNG the temperature at which the liquid is stored is exactly at the boiling point, therefore the liquid will not have temperatures lower than that. This means that we can assume constant properties (such as density) with respect to temperature. These properties are listed in Table 6.2.

Table 6.2: Properties of Methane to be considered constant with temperature

Property	Value
Density (ρ)	422.59 Kg/m^3
Heat of Vapourisation (h_l)	510000 J/Kg
Specific Heat Capacity (c_p)	3479.9 $J/Kg \cdot K$
Specific Enthalpy (h)	-557.34 J/Kg
Second Virial Coefficient (B)	-
Dynamic Viscosity (μ)	$1.172 \cdot 10^{-4} Pa \cdot s$
Thermal Conductivity (K)	0.18409 $W/m \cdot K$
Surface Tension (σ)	0.014 N/m

The second virial coefficient could not be found but again its dependency is negligible therefore the value assumed for Ethane is used. In order to implement a constant value for these properties, all of them are calculated using the *NSRDS0* function, which formula was shown before, therefore if we assume a value of 0 for the coefficients $b - f$ then the coefficient a can be assumed to be the exact value of the property, leading to a null dependency on temperature.

The only values that are left to define in order to implement methane in the lagrangian library are the gas properties such as vapour pressure, ideal gas heat capacity, vapour dynamic viscosity and vapour thermal conductivity. In the lagrangian solver, there seems not to be any use of the gas properties other than the vapour pressure, and this means that the only parameter to be fit using a NSRDS function is the latter, while the rest of the properties can be taken from

any other liquid, better if this is an hydrocarbon, so that the values will not be too different.

6.2.1 Calculation of the coefficient for vapour pressure

In order to calculate the coefficient to be used for the NSRDS function for the vapour pressure, we need to calculate the dependency of it with temperature or take the values from a table. The vapour pressure can be expressed for example using Antoine's equation, expressed by the following equation:

$$p_v = 10^{A - \frac{B}{C+T}} \quad (6.9)$$

This equation is valid for temperature values expressed in Celsius and the pressure obtained is in *mmHg* (millimetres of mercury). The values of A, B, C for methane depend on the temperature range selected, meaning that we can define two regimes with different coefficients. The values obtained for the two regimes are:

$$(1) \quad A = 6.34159, B = 342.22, C = 260.221, \quad 181^\circ C \leq T \leq -163^\circ C$$

$$(2) \quad A = 6.7021, B = 394.48, C = 264.609, \quad 162^\circ C \leq T \leq -83^\circ C$$

In terms of the functions used in OpenFOAM, the vapour pressure is in most cases calculated with the use of the NSRDS1 function, which expression is:

$$NSRDS1 = \exp\left(a + \frac{b}{T} + c \log(T) + d \cdot T^e\right) \quad (6.10)$$

Fitting the coefficients present in this equation with the values obtained by Antoine's Equation we obtain the following:

$$a = b = 0, \quad c = 1.26, \quad d = 4.4655 \cdot 10^{-4}, \quad e = 2$$

6.3 Simulation of liquid spill in an LNG plant

After having implemented liquid methane in the lagrangian library, it is possible to simulate a likely scenario in an LNG plant, regarding liquid spill from a storage tank.

It was previously shown what are the consequences if a storage tank fails and liquid starts to come out from its top. The liquid vaporised and hits the ground, leading to a flammable cloud that if ignited can lead to an explosion.

Even if an LNG plant has some characteristics in common with a fuel plant, there are some significant differences such as tank size, tank distribution, piping and other facilities. In a typical fuel plant, tanks usually do not exceed 20m in height, meaning that the maximum distance before the liquid hits the ground is not more than that; on the other hand, LNG storage tanks are usually bigger, ranging from 30 to 50 meters in terms of height. Also, their structure is significantly different because the risk associated with it, therefore the tank walls are built to stand very high pressures.

In terms of droplets behaviour, the lack of experimental data for LNG spills makes the setup complicated, meaning that an assumption for the droplet diameter distribution has to be made. As noted by HSL [30], surface tension affects the droplet diameter and distribution. For example, considering water, whose surface tension is about $0.07 N \cdot m$, being one of the fluid with the highest surface tension due to the strong attraction between its molecules, in case of a cascade, the atomization process that leads to the formation of droplets creates a wide spectrum of diameter with a high mean diameter (around $5mm$) if compared to most hydrocarbons whose surface tension is much smaller. In the simulation of hexane spills, HSL reported that droplets usually have a more uniform spectrum and their mean diameter is $2mm$. Methane (LNG is very similar) has a surface tension of $0.014 N \cdot m$, similar to the one of hexane ($0.018 N \cdot m$), therefore the droplet size and distribution can be assumed to be analogous. As mentioned already, the decrease in surface tension usually leads to smaller droplets, therefore an LNG cascade could result in smaller droplet compared to a fuel one. Dynamic viscosity of the fluid has the same effect, meaning that a decrease in the value of it leads to a decrease of the droplet size.

6.3.1 Geometry setup

A very basic geometry comparable to the one obtained for the fuel tests was made. A typical size for the LNG storage tank was assumed, with a tank height of 50 m and a 70 m diameter. The size of the domain was chosen to be large enough to consider for air movements, although the mesh was coarse in the far region from the cloud formation. A picture showing the domain analysed is shown in Figure 6.2.

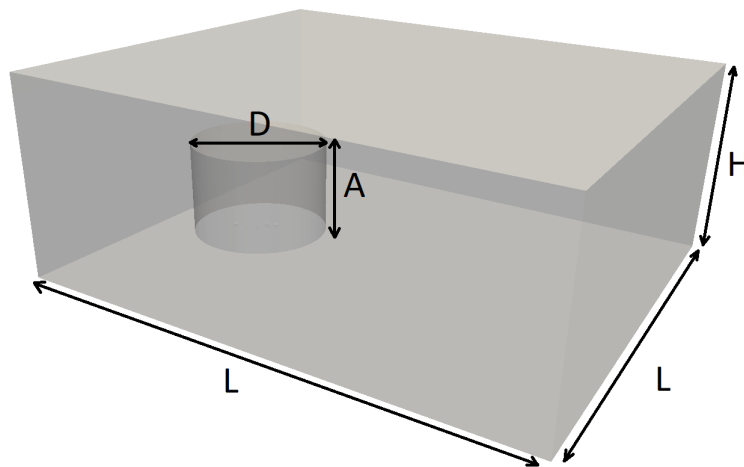


Figure 6.2: Domain used for the CFD calculations ($D=70\text{m}$, $A=50\text{m}$, $L=300\text{m}$, $H=100\text{m}$)

The droplets release point was chosen at the top of the tank, as it is the most likely scenario that can be obtained in an accidental spill.

6.3.2 Turbulence modelling

A RANS approach was used for the turbulence modelling with the $\kappa - \omega$ SST standard model. Due to the size of the domain and cloud formed an LES approach was somehow prohibitive and would not lead to an improvement of the results in terms of vapour production and cloud dispersion other than on local points.

6.3.3 Mesh sensitivity analysis

Mesh sensitivity tests were run in order to obtain a grid independent solution. Five levels of mesh refinement were analysed with a number of computational cells showed in Table 6.3.

Grid density	Number of cells
1	162651
2	349272
3	687619
4	1196559
5	2091647

Table 6.3: Grid level and number of computational cells used

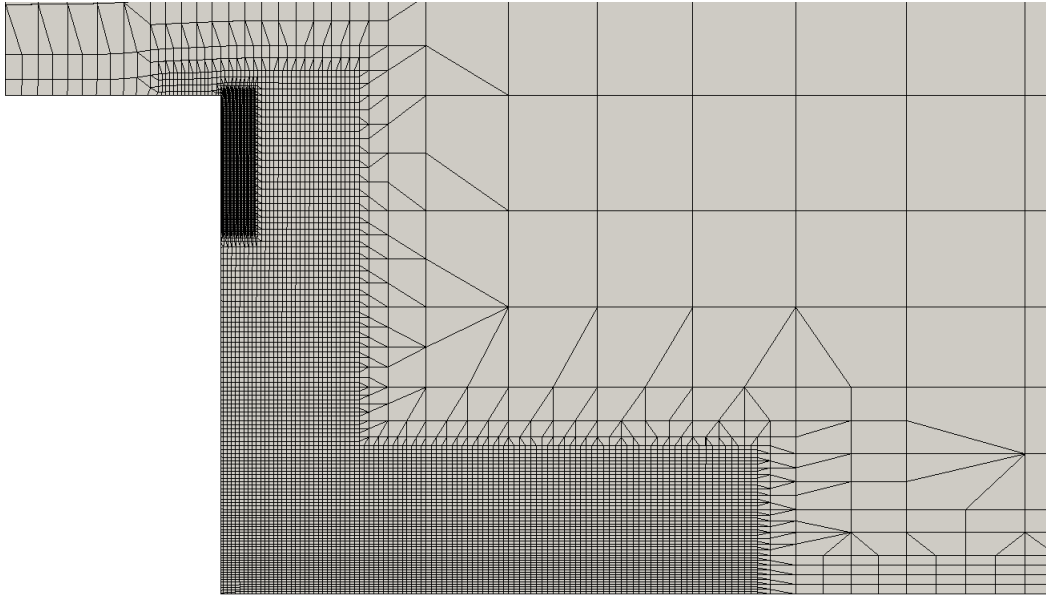


Figure 6.3: Mesh showed on the symmetry plane

The mesh was developed using the OpenFOAM utility *snappyHexMesh* which defined different zones where the initial grid was refined up to a certain level depending on the importance of the region. A symmetry cut of the domain in Figure 6.3 shows a close look on the mesh and part of the refinement regions.

The results obtained from the mesh sensitivity analysis are shown from Figure 6.4 to 6.7. These were obtained at 40 seconds after the beginning of the simulation on two sets of lines defined in Table 6.4.

Results clearly show that a grid independent solution was obtained with level 4 and 5, therefore a further refinement of the mesh would not lead to significant improvements for this type of analysis.

Line Number	Starting Point (m)	End Point (m)	Direction
1	(38,-49.5,0)	(60,-49.5,0)	x axis
2	(39,-49.5,0)	(39,10,0)	y axis

Table 6.4: Definition of line 1 and 2 for the mesh sensitivity results

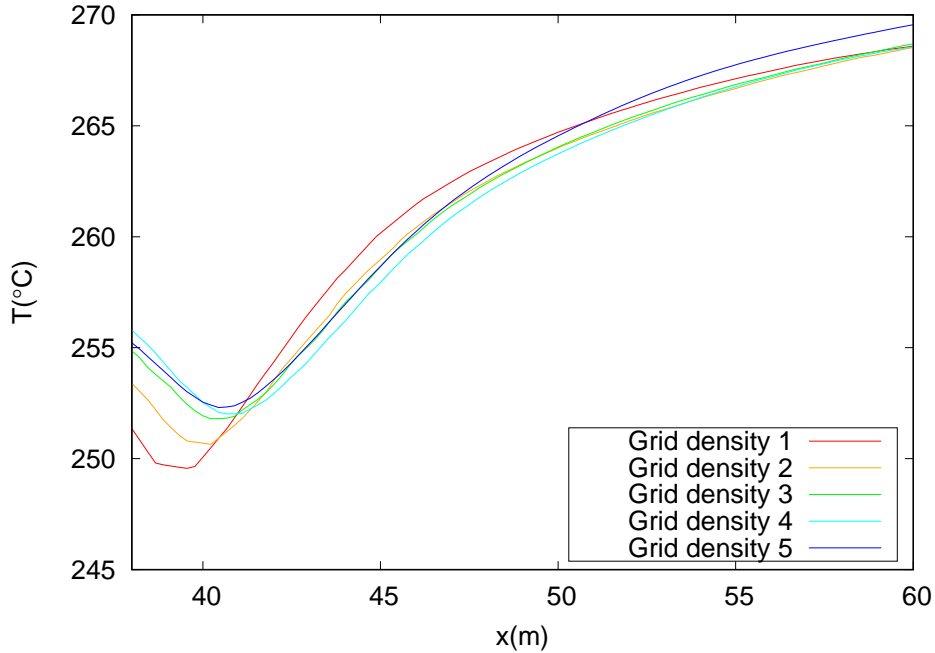


Figure 6.4: Temperature profile on line 1

6.3.4 Evaporation of droplets

Due to the temperature conditions, the methane droplets are all boiling, consequently they start to evaporate quickly, as shown in Figure 6.8 (the droplets diameter is scaled by a factor of 50 with the real value for more understandable results).

Figure 6.9 shows the evaporation mass flow rate of the liquid phase (blue line) within the first 8 seconds of the simulation. The green line represents the mass flow rate of the liquid (droplets phase) introduced in the domain. It is clear that an equilibrium is reached within 2 seconds since the start of the simulation, where the evaporation flow rate matches the introduced mass flow rate, meaning that after an initial transient condition the amount of mass that entrains the domain in liquid form matches the amount of vapour formed due to evaporation. This means that a huge amount of vapour is produced within the cascade, which

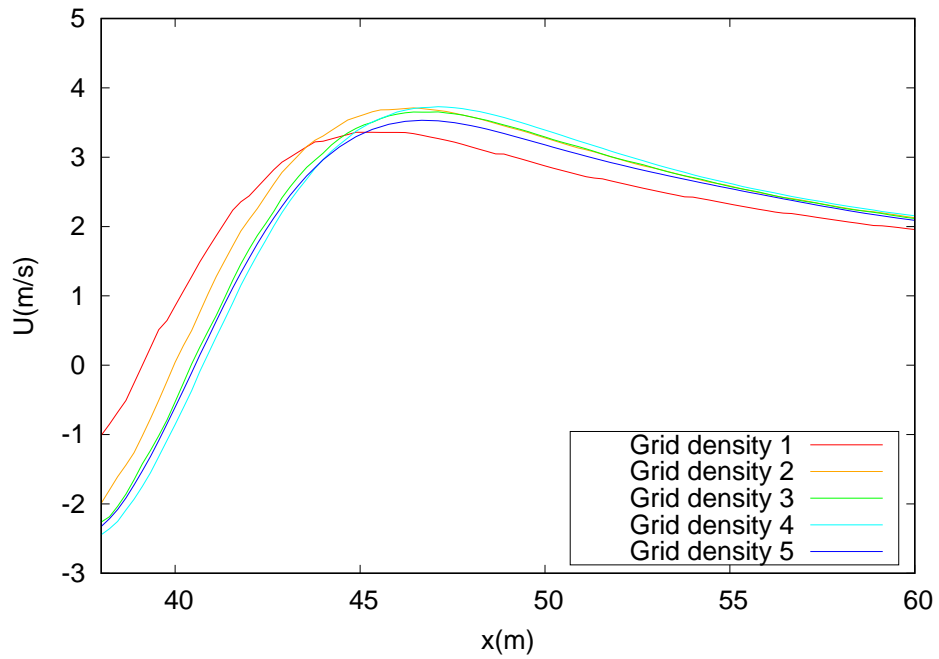


Figure 6.5: Velocity profile on line 1

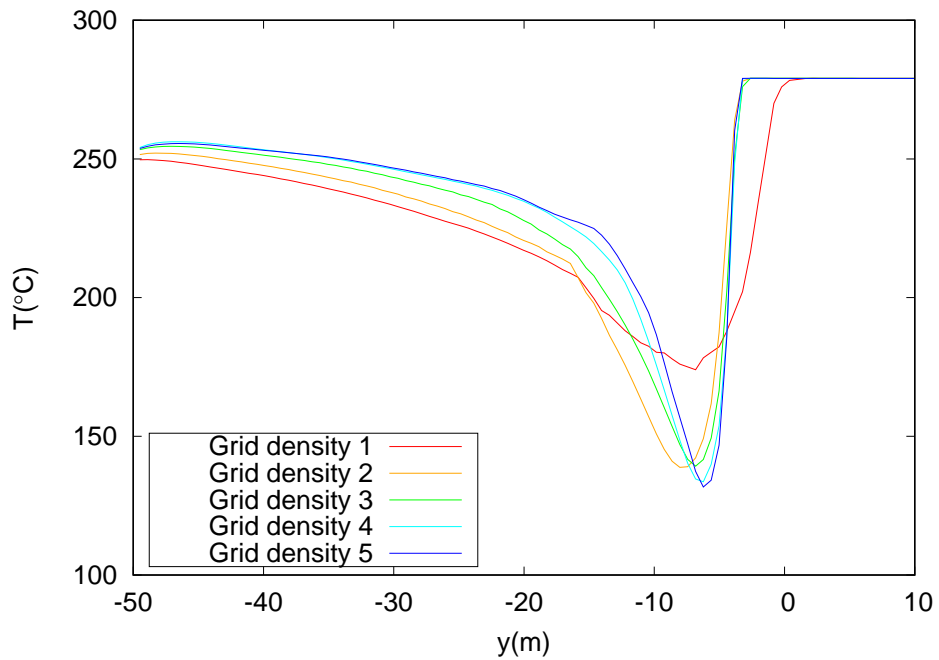


Figure 6.6: Temperature profile on line 2

eventually will spread on the ground due to buoyancy.

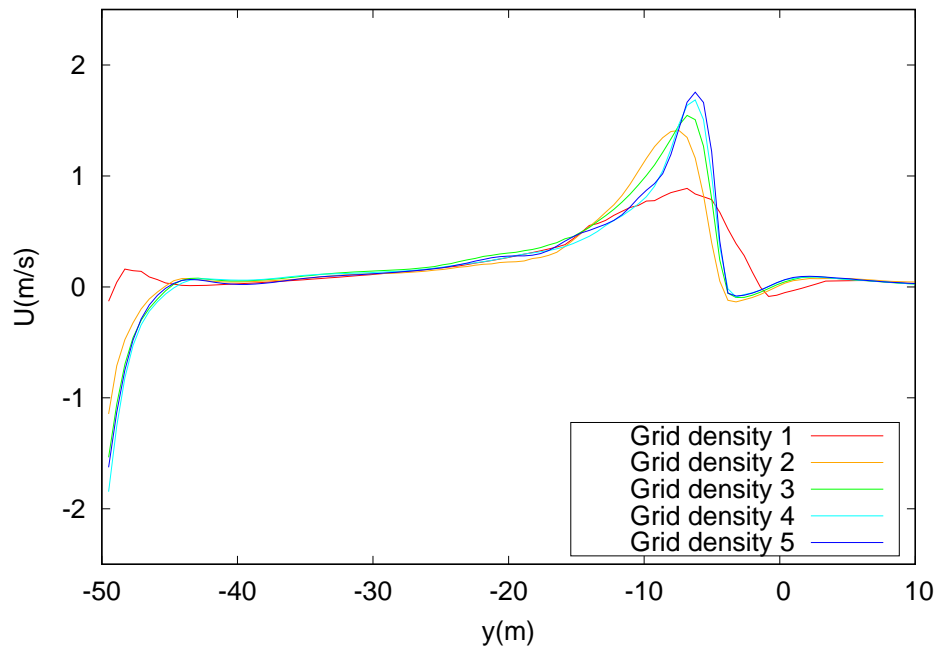


Figure 6.7: Velocity profile on line 2

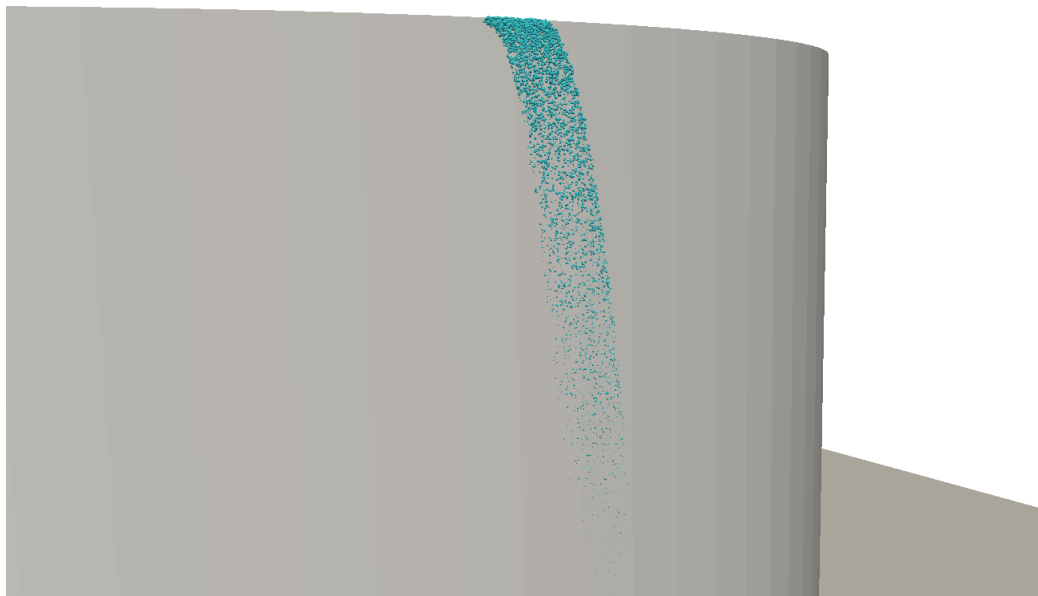


Figure 6.8: Cascade Evolution

6.3.5 LFL and cloud contour

One of the most important aspects when analysing the dispersion of flammable gas is the extent of the LFL profile. For methane, the LFL is 5% in volume. The contour of such value along with the vapour cloud extension are shown every 5

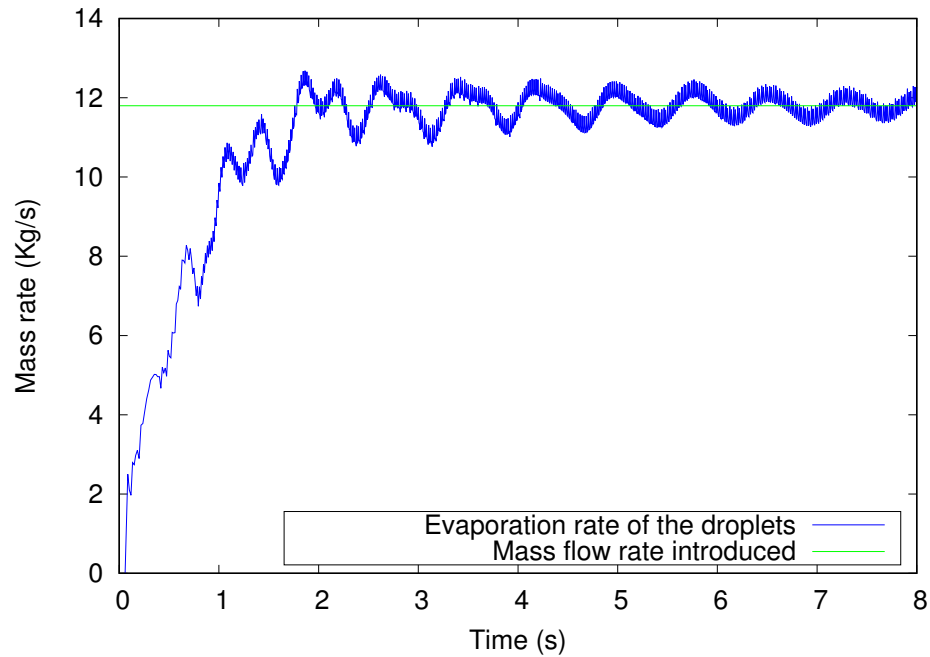


Figure 6.9: Droplets evaporation mass flow rate

seconds from Figure 6.10 to 6.17.

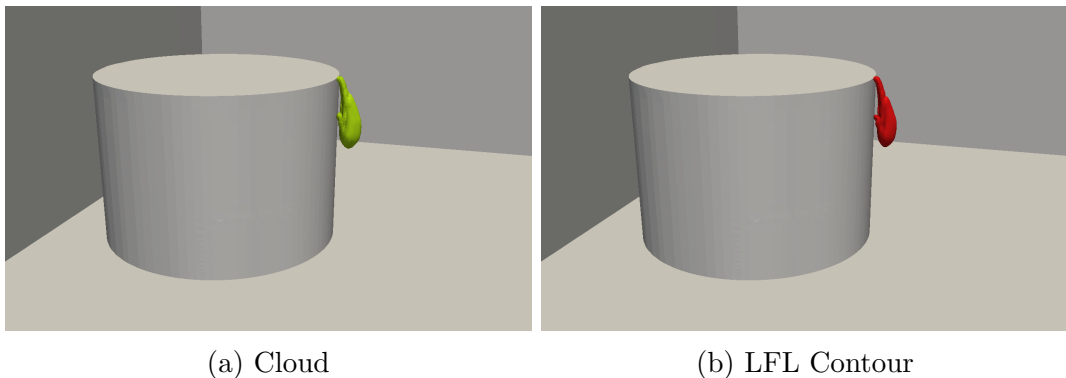
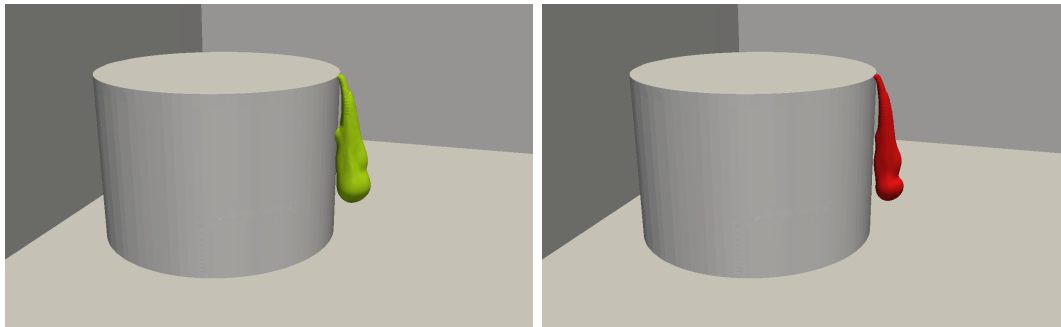


Figure 6.10: Contours showing the cloud and the LFL at 5s

It is clear that in the region close to the droplets where the vapour is produced and therefore high concentration of methane is present the LFL is very close to the cloud extension, while when the cloud moves close to the ground and starts spreading (15-20 seconds) the LFL contour is confined to a smaller radius compared to the cloud, because of mixing and dispersion in the air. This is a positive effect in terms of the safety of the plant because it limits the extent to which an ignition source in the proximity of the cloud can produce a fire.

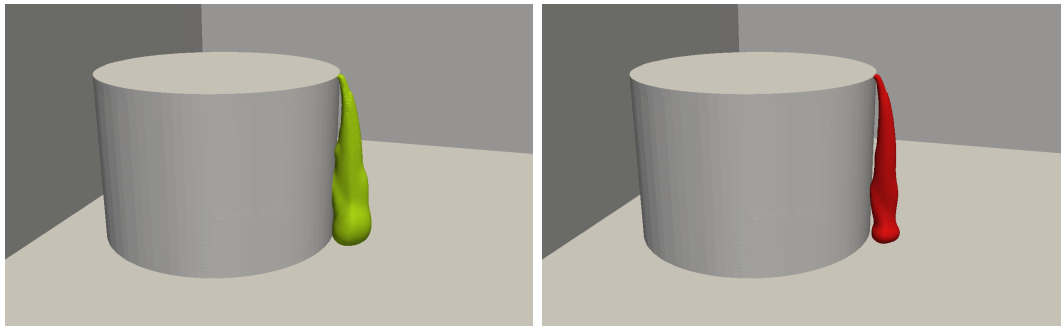
Another important aspect of the dispersion of LNG in the air is asphyxiation,



(a) Cloud

(b) LFL Contour

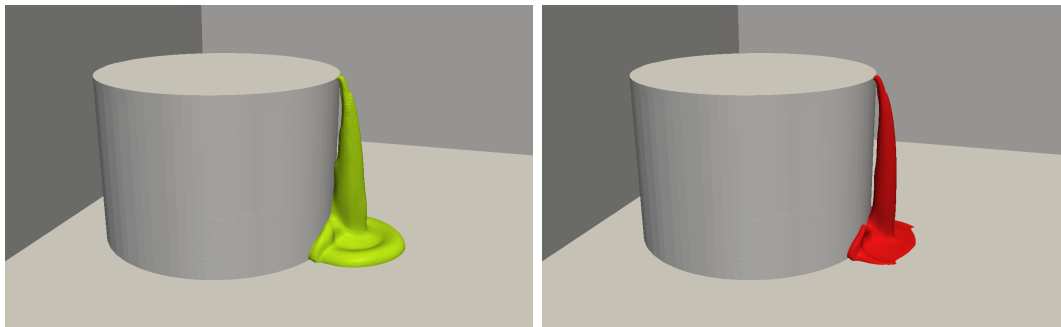
Figure 6.11: Contours showing the cloud and the LFL at 10s



(a) Cloud

(b) LFL Contour

Figure 6.12: Contours showing the cloud and the LFL at 15s

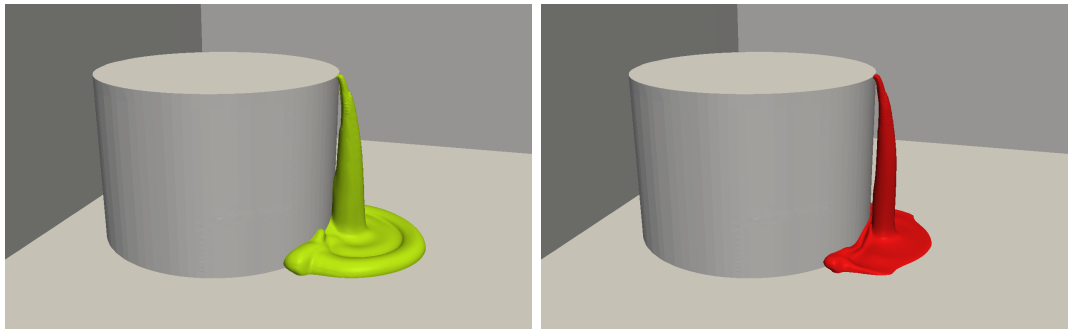


(a) Cloud

(b) LFL Contour

Figure 6.13: Contours showing the cloud and the LFL at 20s

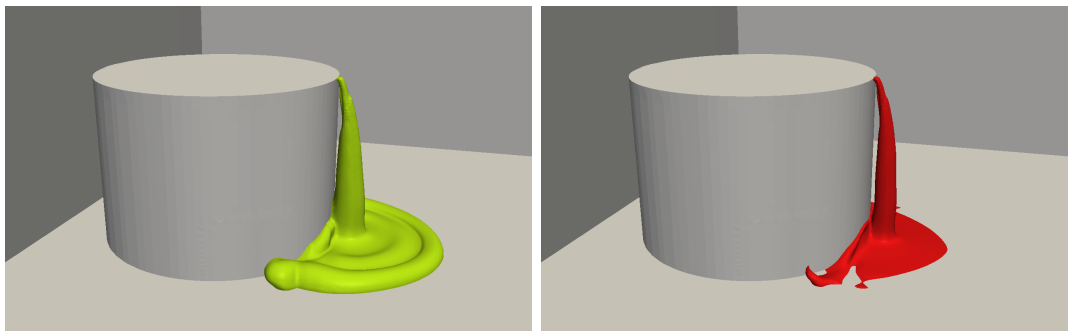
which occurs when the concentration of oxygen in the air drops below a certain value. This phenomenon is independent of any risk of fire because it is only related to the presence of LNG vapour in the air. Due to the large size of the domain used it can be somehow difficult to understand the height of the vapour cloud. Because the total amount of liquid is vaporised within seconds, a large vapour cloud is produced, and the height at which it spreads close to the ground



(a) Cloud

(b) LFL Contour

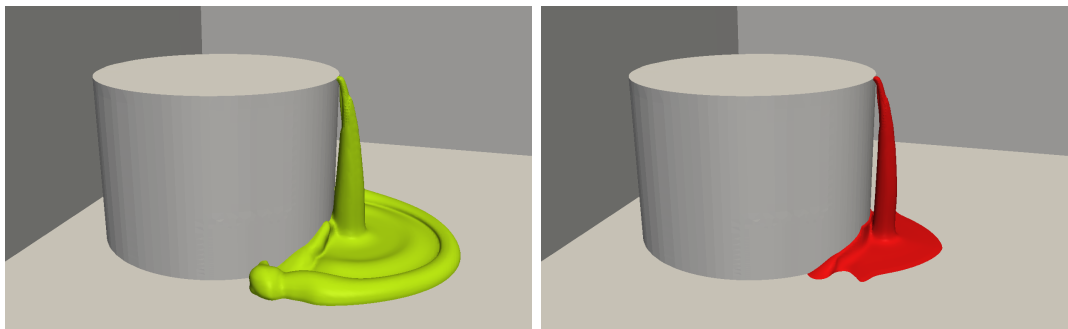
Figure 6.14: Contours showing the cloud and the LFL at 25s



(a) Cloud

(b) LFL Contour

Figure 6.15: Contours showing the cloud and the LFL at 30s



(a) Cloud

(b) LFL Contour

Figure 6.16: Contours showing the cloud and the LFL at 35s

can be appreciated in more details looking at Figure 6.18, where a sample of a human being is introduced in the domain, to shown that the cloud height is well higher, therefore breathing can be difficult.

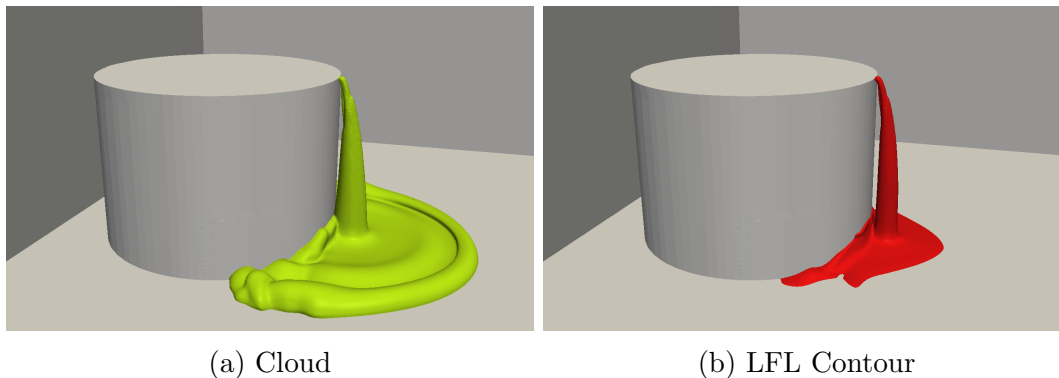


Figure 6.17: Contours showing the cloud and the LFL at 40s

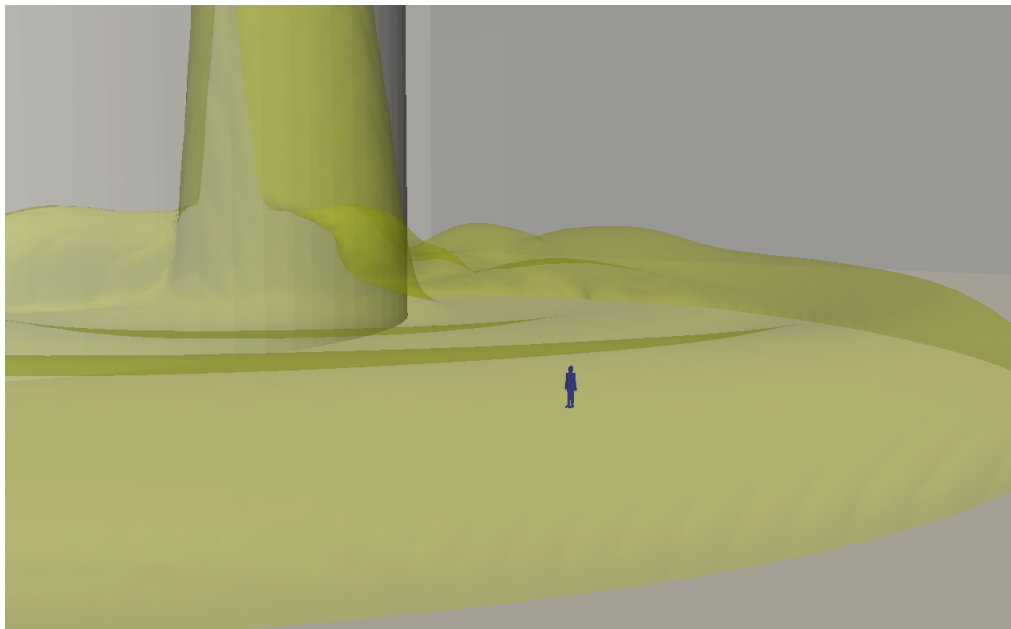


Figure 6.18: Human presence close to the tank

6.3.6 Spray Pattern

The dataset that OpenFOAM gives back to the user for post-processing of droplets is very complex and it can be easily read only on Paraview. For this reason a utility called *foamToMatlabLagrangian* was developed which takes all the information stored for the lagrangian phase and converts them in a more readable format which can be used in data processing software.

The spray pattern is examined in details in Figure 6.19 and 6.20. The front view shows that the spray becomes narrower while being driven down by gravity, this is because the droplets at the side of the spray are subject to higher heat exchange, therefore higher evaporation/boiling rate, also because the concentration

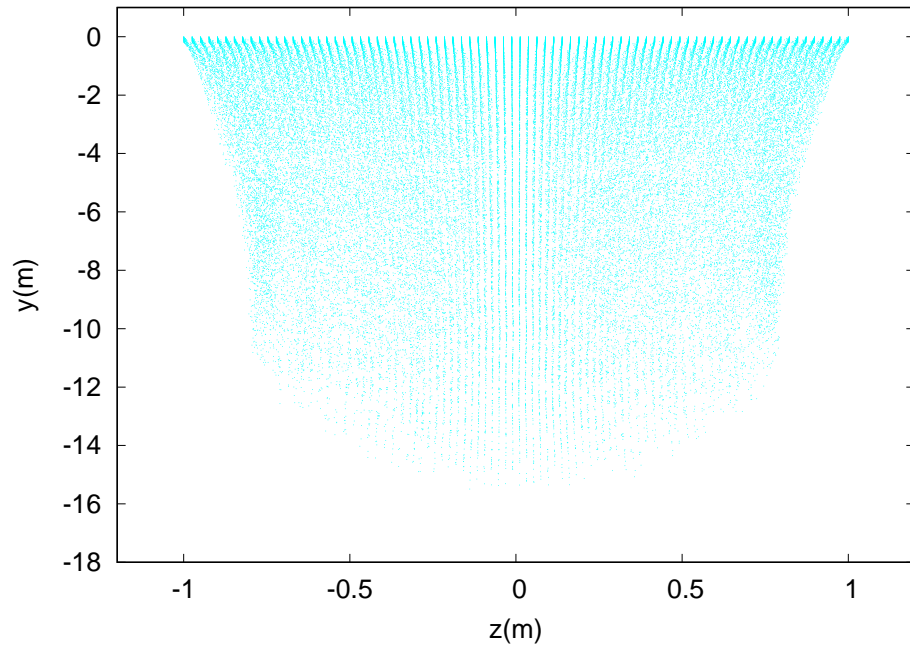


Figure 6.19: Front view of the spray

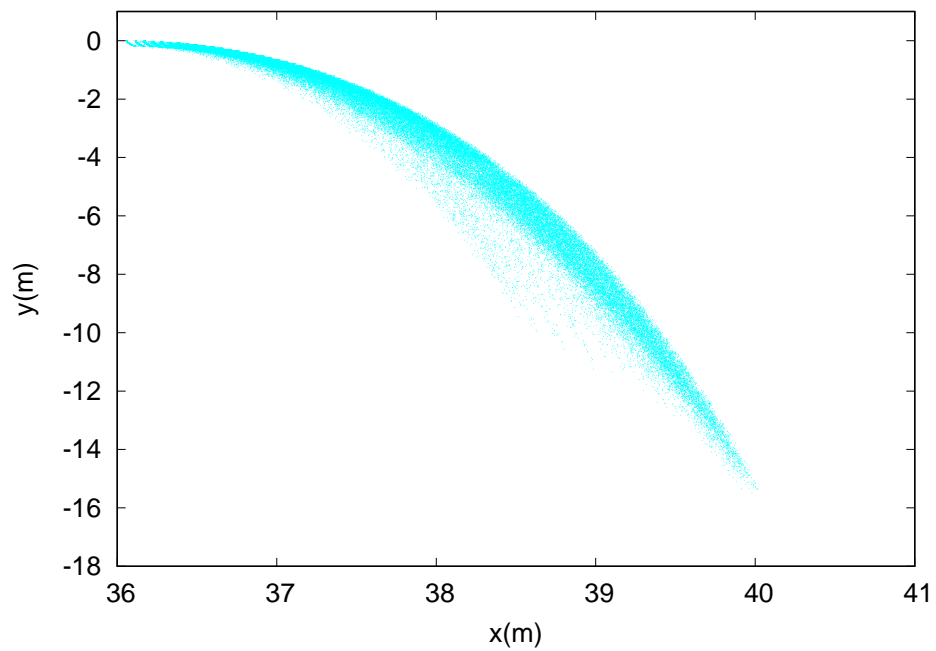


Figure 6.20: Side view of the spray

of CH_4 in the bulk of the cascade is higher, meaning less mass evaporated in the same time step.

The side view shows how the spray forms a parabola shape due to gravity

and aerodynamic drag acting on the droplets. The spray becomes wider, because the drag/weight ratio is higher for smaller droplets meaning that these will slow down more quickly than bigger droplets. At the same time, the smaller droplets evaporate completely much before the bigger ones, which is why the spray pattern present a thin shape at the very end of it.

The average diameter of the spray for different heights is shown in Figure 6.21. The evolution of such quantity is such that from an initial value of 1.4 mm, due to the evaporation of methane the mean diameter changes almost linearly reaching a value of 0.2 mm at the end of the spray.

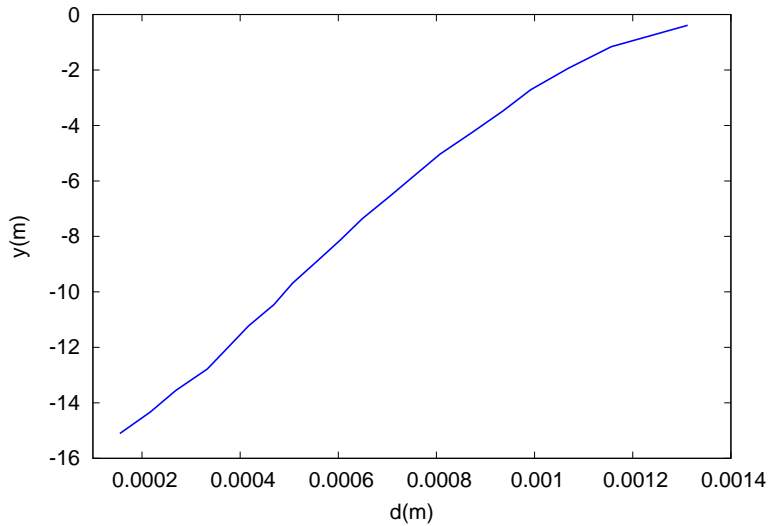


Figure 6.21: Average diameter of the droplets

A very similar shape can be observed in Figure 6.22 which shows the maximum diameter for different heights. From an initial value of 2 mm, the maximum diameter decreases down to a value of about 0.3 mm at the bottom of the cascade.

Figure 6.23 shows the average velocity of the droplets respect to their height. The initial condition for all the parcels was set at 2 m/s (to match the spill mass flow rate) on a direction parallel to the ground. While the horizontal component of the velocity starts decreasing due to aerodynamic drag, the vertical one starts increasing due to gravity, up to a certain value (the so-called asymptotic velocity), where the aerodynamic drag and gravity forces cancel out. Under such circumstances, the velocity should be kept constant, but due to evaporation of the droplet, its volume shrinks, and because the drag is a function of the square of the droplet radius while gravity is a function of the cube of the radius, the velocity starts decreasing again. This is well shown in the figure where the average

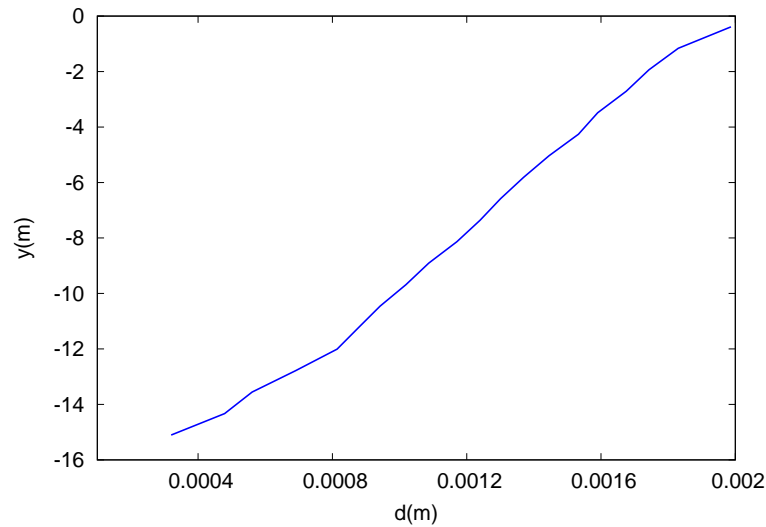


Figure 6.22: Maximum diameter of the droplets

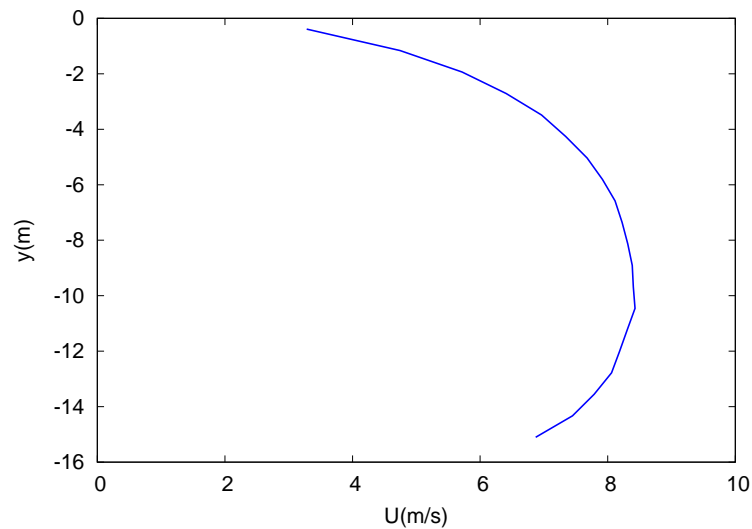


Figure 6.23: Average velocity magnitude of the droplets

velocity reaches a maximum value greater than 8 at -10 m, and decreases again down to a value of 7 m/s at the end of the cascade.

6.4 LNG dispersion in a plant and Explosion

Although the case examined in the previous section is interesting from a physical point of view, because it gives an insight of what the vapour cloud size is and the shape of the liquid spill, it does not show how the cloud will disperse in a real plant, where obstacles are present. In a real LNG plant, there is a wide range of

building and facilities which makes the risk of a spill from a tank more hazardous and with a higher probability of detonation. Although there is not a universal design, some of the characteristic facilities present in a plant are the same for different cases, such as storage tanks, high-pressure pumps, regaseifiers, metering stations, compressors and pipes.

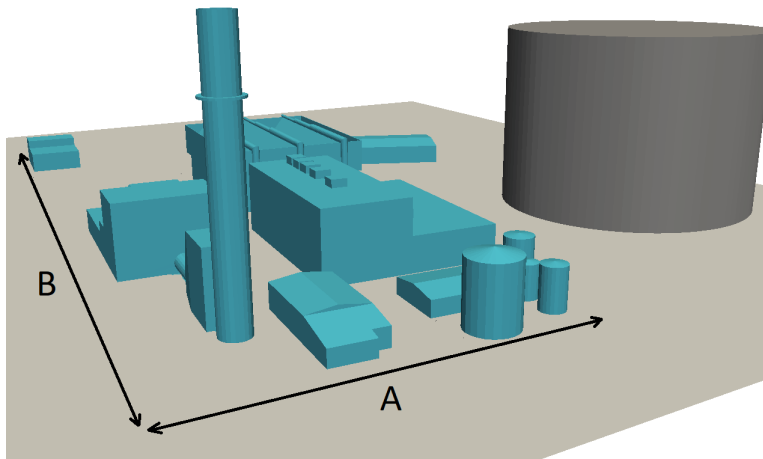


Figure 6.24: Geometry used for the CFD calculation (tank diameter is 70m, height is 50m, plant base area is $A=150\text{m}$, $B=80\text{m}$ and domain size is $450\times 450\times 100\text{m}$)

Figure 6.24 shows the geometry used for the testcase, where the same tank is used from the previous calculations while some of the components of a typical power plant are introduced in front of the release point. The size of the tank is 50 m is height with a radius of 35 m. The plant occupies an area of $200\text{m}\times 125\text{m}$, with a height varying from building to building, with a peak of 60 m for the tower. The minimum distance from the tank to the plant is about 25 m, in the direction where the spill is supposed to take place, to account for the worst-case scenario.

The mesh was obtained using the tool *snappyHexMesh*, with refinement boxes in the region of the liquid spill and close to the ground where the cloud will spread. The number of cells used was around 4 million. The $k-\omega$ SST model was used to model the effects of turbulence. Regarding wall treatment, due to the constraints on the geometry size, resolving the turbulence up to the wall would have been too demanding. Therefore a wall treatment approach was used. The values obtained for y^+ were satisfactory and between the range $30 < y^+ < 300$ throughout the whole simulation.

No mesh sensitivity analysis was studied, because the same mesh size used in the single tank analysis was assumed, and the same level of accuracy was assumed

in the current case.

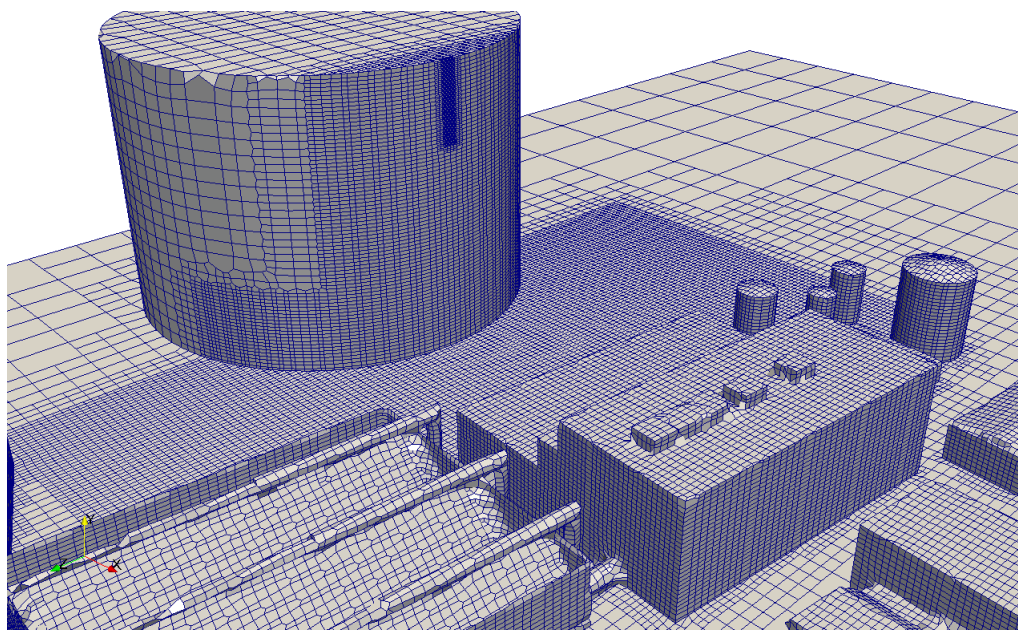


Figure 6.25: Mesh obtained by *snappyHexMesh*

Initial conditions considered for a quiescent domain, with a low turbulence intensity and a constant temperature of 6°C . Regarding boundary conditions, the tank, ground and power plant were considered as no-slip walls, with an adiabatic condition for the temperature.

In order to study the effect of different spills on the evolution of the LFL, two cases have been simulated using a different spray pattern and mass flow rate. The risk of an explosion is directly related to the presence of obstacles within the domain and how far the cloud spreads within these obstacles. The first case used the same set-up adopted for the case where only the tank was present, with a mass flow rate of methane around 12 Kg/s . The second testcase assumed a wider inlet for the Lagrangian phase and a mass flow rate of 36 Kg/s .

6.4.1 Results

Figure 6.26 shows a countour of the LFL for different times for the 12 Kg/s case. The mass flow rate is such that a steady condition in terms of the LFL is reached at around 150 s since the start of the simulation. In terms of cloud dispersion, the simulation was run for 10 minutes and the vapour cloud keeps expanding within the domain, but as mentioned earlier the properties of methane are such that this

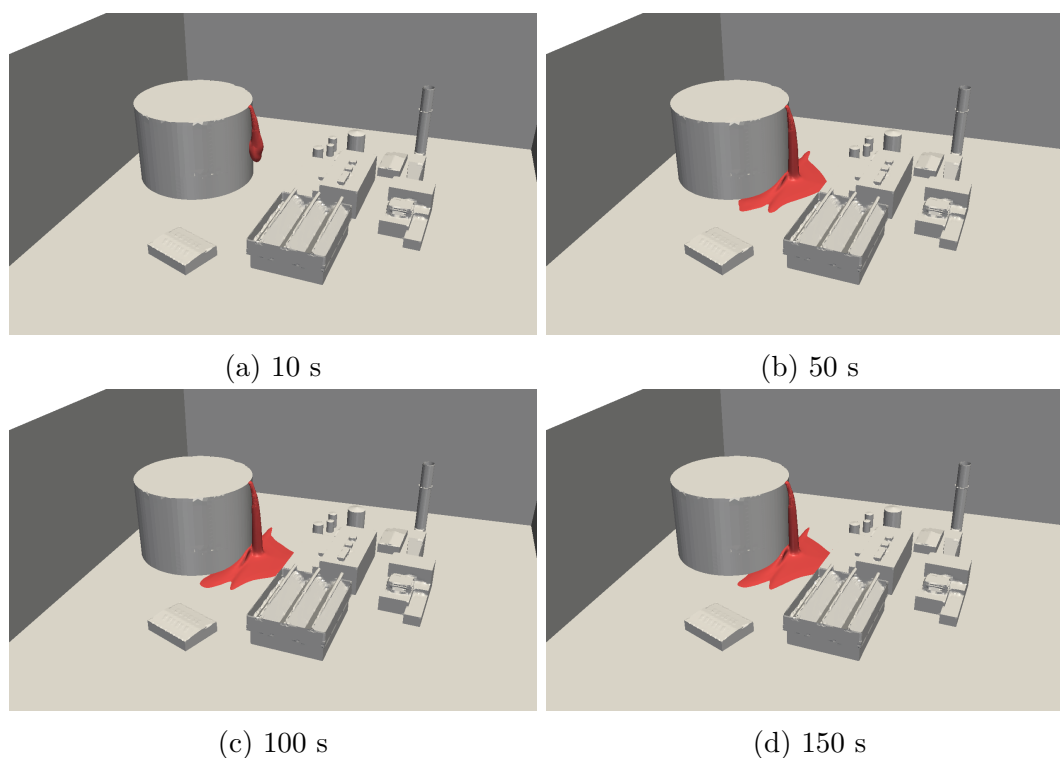


Figure 6.26: Contours showing the LFL for the 12 kg/s case

cannot be ignited, due to the LFL being confined in a region close to the tank walls.

Figure 6.27 shows the contour of the LFL for the 36 Kg/s case. Different times are chosen because of the larger mass flow rate. Here the flammable cloud develops on a much bigger area covering the plant facilities as well.

The results obtained for the 12 kg/s case show consequently that the flammable cloud formed is such that within the highly congested area the volume concentration is lower than the LFL, therefore it could not be ignited. This, however, does not mean that a fire is less likely to happen, but only that the damage and fire size could be confined in the area close to the tank, with a low probability of a detonation to occur, which would extend the damage on a larger area and intensity.

Increasing the spill size in terms of area and volume released (which could be a consequence of a larger failure in the tank structure or higher flow rate injected in the tank), leads to a larger area covered by the LFL contour. This is particularly obvious analysing the results of the 36 kg/s case, where the LFL depicted in red penetrates the plant facilities to a large extent. This means not only that the cloud is more likely to be ignited due to a large amount of electrical

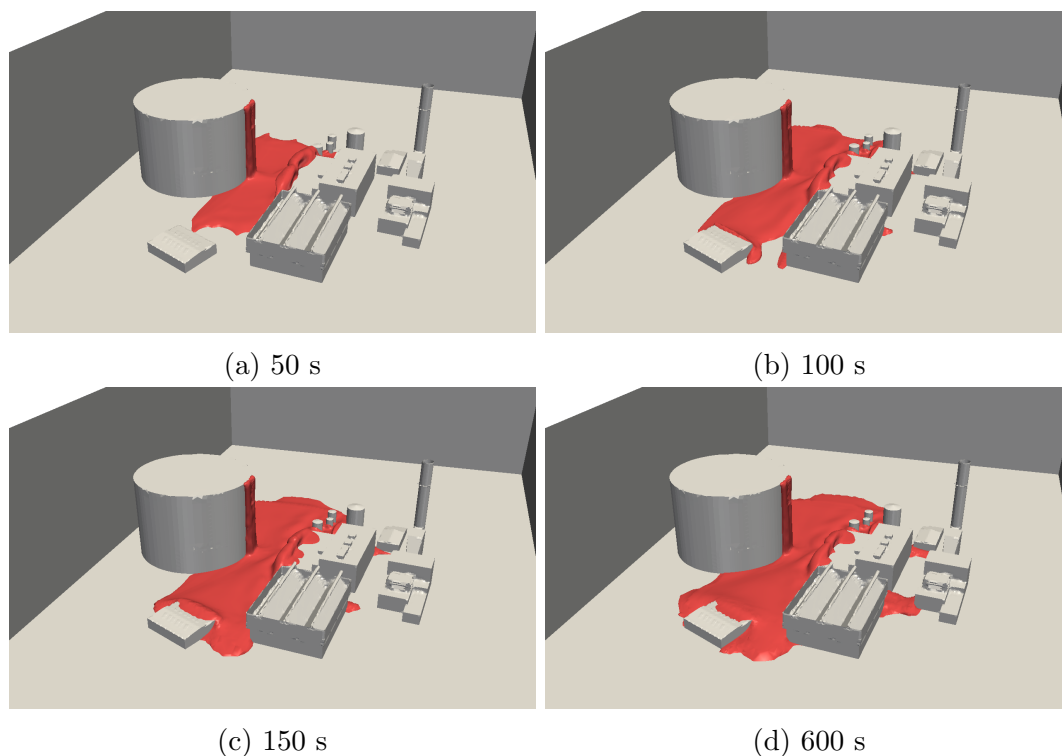


Figure 6.27: Contours showing the LFL for the 36 kg/s case

equipment present in the buildings and facilities, but also that if a fire occurs in such area, the large number of obstacles (various in size) could enhance the combustion process and lead to a Deflagration to Detonation transition (DDT), with catastrophic consequences.

Results obtained varying the spill size show therefore that the extent of the cloud formed increased with the mass flow rate, and that although the cloud keeps dispersing in the domain, the LFL contour is limited and reaches a maximum size, from which one could determine the risk of a potential fire. Also, the amount of liquid that evaporates matches the mass flow rate released after an initial transitory period, after which the whole liquid mass introduced in the domain is converted into vapour that initially moves close to the ground due to the movement of air consequent the liquid cascade and density differences with the surrounding air.

6.5 Chapter summary

Liquid Methane was implemented in the lagrangian library of OpenFOAM using data available at its boiling point. The approximation of LNG being made entirely of methane was made and has been used already in the literature. Due to the lack of data available, no validation could be done with the numerical data, leading to a purely numerical analysis of the simulation. A simple testcase with a circular tank was first assumed and the characteristics of the cascade analysed. The main findings were the liquid to be fully evaporated well above the vertical mid section of the tank, which is not surprising considering the fact that LNG is boiling when in contact with room temperature. The initial density of LNG vapour is such that the flammable cloud moves close to the ground, and heats up to a point where it starts behaving as a buoyant cloud. A second testcase was analysed, similar to the previous one but in the context of an LNG plant. An stl file containing standard facilities present in a plant were incorporated in the mesh and different spill sizes were analysed. The LFL contour of the vapour cloud was found to be highly affected by the spill size, where an increase of this value leads a higher penetration in the plant facilities of the flammable cloud. If compared to a gasoline cascade, the main difference was found in the amount of liquid evaporated (all the liquid that comes out vapourises within a fall of 20m), as well as in the pattern of the spray, with LNG at the sides of the cascade vapourising much quicker than the one in the core of the liquid region.

Chapter 7

Conclusions

The aim of the present work is the development of a computational tool capable of solving and predicting liquid spills of hydrocarbons, called *cascadeFoam*.

The first part of the work is based on the development of a solver that was able to deal with the physics involved in the liquid spill of a volatile substance. The main effects that needed to be considered were the multiphase nature of the flow, the buoyancy effects, the splashing of liquid droplets on solid surfaces and the turbulence formed by the interaction of the droplet with the gas phase. The solver was developed within the OpenFOAM toolbox, starting from the existing solver *sprayFoam* which however lacked important models for the current application.

The buoyancy effects were fundamental for all the type of spills analysed, starting from heavy hydrocarbons such as hexane or decane which will tend to stay close to the ground once a vapour cloud is formed from a spill, because their vapour density is higher than the one of standard air at room temperature. At the same time, if not more important, the buoyancy plays a fundamental role in the liquid spill of Liquefied Natural Gas, because the density of the gas phase of such material varies with temperature. LNG vapour is heavy once the liquid vapourises, at very low temperatures (at its boiling point), and the density starts decreasing while the temperature of the gas rises until it reaches a point where the two density equalises, and after that, the LNG becomes lighter than air. This has to be approached within the computational model, and that is why explicit buoyancy modelling was implemented in the momentum and pressure equation, in order to simulate the spreading of buoyant vapour clouds appropriately.

The second thing that was approached was the multiphase nature of the flow, and the method used to solve this was consistent with the literature, using a

Lagrangian-Eulerian approach. This is because the method is a good compromise of accuracy and speed of the results. The cascade was modelled as an array of droplets from their source at the top of the tank down to the ground. However, the cascade is not composed entirely of droplets from the beginning, but it is rather a uniform liquid spill that due to hydrodynamic instabilities starts breaking into smaller ligaments and eventually into small droplets. This process is very complicated to model and it requires the use of other approaches such as the Eulerian-Eulerian method, and was outside the scope of the current research. For this reason, the primary breakup of the liquid spill was neglected, and the droplets were considered to be formed right at the beginning of the spill, also using experimental findings from the HSL, which showed how liquid spills of hydrocarbons form almost immediately an array of droplets with a remarkably constant diameter distribution.

As pointed out in reports from the HSL, one of the fundamental effects to be modelled and investigated within the CFD model was the interaction between droplets and solid surfaces, such as the concrete ground at the bottom of the tank. The outcome of such process has been investigated by a large number of authors, and there is no universal model currently available that gives accurate results for any type of interaction. Among the different types of outcome, the most difficult to model and the most interesting is the so-called splashing. The process depends on a high number of parameters such as impact velocity, droplet diameter, properties of the liquid, which are usually described by non-dimensional quantities. Previous work done by HSL did not include any splashing modelling within the Lagrangian solver they used, which resulted in the use of predefined droplet inlet at the bottom of the cascade to mimic the effect of splashing. In the current work a splashing model available within OpenFOAM was used, the Bai and Gosman model, which proved to improve the comparison with experimental results. However, the model was developed for applications in which the droplet sizes and impact velocities were far from the ones experienced in cascades of hydrocarbons. It was therefore fundamental to improve the current splashing model to apply to the current application and give satisfactory results.

The development of a modified splashing model was approached using the Volume of Fluid method, using a large number of simulations of single droplet impact onto thin liquid films. Although in real applications a large number of droplets splashes almost simultaneously, single droplet simulations are easier to analyse and although they do not give the exact outcome, they are statistically

conservative. Three main parameters were varied within the large set of simulations, such as the droplet diameter, impact velocity and liquid film thickness. The results were analysed in terms of splashing mass ratio, splashing angle and splashing threshold. For the latter, a correlation developed by Cossali was used and proved to be reliable for the current application. For the splashing angle, the values were consistent with the previous model for small values of the Weber number, but as this increased, the lower limit of the angle increased to an asymptotic value. The splashing mass ratio showed a similar behaviour with values increasing with the Laplace and Weber number, as well as the non-dimensional film thickness. All the values that were extrapolated from the simulations were used to produce a number of correlations that were then implemented in a new splashing model.

The new splashing model was then used to improve the results of the Lagrangian solver against experimental data, which showed an improvement of the temperature measurements in the far region of the cascade, as well as increasing the vapour formation from the liquid cascade.

The last part of this work was about LNG cascades using the Lagrangian solver developed previously. First liquid methane had to be implemented because it is not available in the standard version of OpenFOAM. Liquid properties of methane were considered at its boiling point and interpolated using functions available within the liquid library. First simulations were carried out on a single tank to understand the differences with other types of hydrocarbons. The size of LNG tanks is usually larger than gasoline tanks, and usually, reach 50 m in height. Such height demonstrated to be enough for a liquid spill to vaporise completely before hitting the ground, showing that the liquid droplets cease to exist before 20 m from the spill at the top of the tank. The vapourisation rate is such that after a transitory period of few seconds the whole amount of liquid spilled is transformed into a heavy vapour that is driven down to the ground by gravity and spreads low, leading to the risk of explosion if any source ignition is present. This is obviously a much greater risk than any other hydrocarbon spill where much of the fluid is spread on the ground as a liquid film as the fluid is usually at a lower temperature than its boiling point.

At a second stage, the tank was put into a more realistic context, being surrounded by a number of facilities which are usually present in a power plant, which would confine the flammable cloud and form obstacles that could lead to a deflagration to detonation transition, the effect of which are catastrophic, as

it happened in Buncefield. Two different spill flow rates were analysed, to understand the effect on the flammable cloud and whether the Lower Flammability Limit would spread at the same rate. The first spill analysed showed that although the vapour cloud spreads largely into the power plant and beyond its limits, the LFL contour, which is the one we are ultimately interested in, remains confined within the tank region, and does not spread into the plant facilities. The second larger spill, showed differences with the first one when it comes to the LFL contour. Although the cloud dispersion shows significant similarities between the two cases, in the second one the LFL moves into the plant, and keeps growing, which has obviously a much higher risk if the cloud is ignited.

Proposed future work

The work developed dealt with the spill of flammable liquids and showed that among the fundamental things to capture within the computational model the splashing model and spreading of the buoyancy-driven cloud are essential.

The physics of the topic is highly complicated and a series of assumptions had to be made in order to build a solid tool within the timescale of the project. Such assumptions include the atomization region of the liquid spill and the multiple interactions of the splashed droplets. The atomization region is of interest for a large number of applications, but the large size of spills presented in this work has little if no previous work in the literature. Future work could be done on this topic, analysing how different spills and liquids develop into droplets, and if the assumptions and conclusion led by the HSL are applicable or not.

Research could also be oriented towards understanding the effect of multiple droplets splashing on a liquid film, following the assumption made to develop the splashing model adopted in the current work. Several droplets impacting on a pre-existing liquid film behave differently from single droplet impacting, mainly because of the craters formed by previous impacts. It would also be interesting to analyse the effect on averaged properties such as mass splash ratio or splashing angle, and understanding if these effects are somehow similar between single and multiple splashing.

Work is currently being done on the other topics of the SafeLNG project, and the effect on igniting the cloud analysed in the current work. This will give a better understanding of the whole process and provide more detailed results on whether the flammable cloud could lead to catastrophic consequences for an LNG

spill as it happened with gasoline in Buncefield.

References

- [1] A. L. Brown, G. J. Wagner, and K. E. Metzinger, “Impact, fire, and fluid spread code coupling for complex transportation accident environment simulation,” *Journal of Thermal Science and Engineering Applications*, 2012.
- [2] M. Mannan, “A technical analysis of the buncefield explosion and fire,” *Institution of Chemical Engineers Symposium Series*, pp. 662–673, 2009.
- [3] S. Gant and G. Atkinson, “Dispersion of the vapour cloud in the buncefield incident,” *Process Safety and Environmental Protection*, vol. 89, no. 6, pp. 391 – 403, 2011.
- [4] BBC News, “Evacuation from Puerto Rico Fire.” <http://news.bbc.co.uk/1/hi/world/americas/8323569.stm>, 2009.
- [5] T. E. Toolbox, “Gas - Concentration Limits.” <https://www.engineeringtoolbox.com/explosive-concentration-limits-d423.html>, 2018.
- [6] S. Mokhatab, J. Y. Mak, J. V. Valappil, and D. A. Wood, “Chapter 9 - lng safety and security aspects,” in *Handbook of Liquefied Natural Gas*, pp. 359 – 435, Boston: Gulf Professional Publishing, 2014.
- [7] Royal Dutch Shell plc, “<http://www.shell.com/energy-and-innovation/natural-gas/liquefied-natural-gas-lng.html>,” 2017.
- [8] International Gas Union, “2017 World LNG Report,” 2017.
- [9] Shell, “Prelude FLNG.” <https://www.shell.com/about-us/major-projects/prelude-flng.html>, 2018.
- [10] Y. Li, Z. Li, and W. Wang, “Simulating on rollover phenomenon in lng storage tanks and determination of the rollover threshold,” *Journal of Loss Prevention in the Process Industries*, vol. 37, pp. 132 – 142, 2015.

-
- [11] C. Habchi, D. Verhoeven, C. H. Huu, L. Lambert, J. L. Vanhemelryck, and T. Baritaud, “Modeling atomization and break up in high-pressure diesel sprays,” in *SAE Technical Paper*, SAE International, 02 1997.
- [12] D. Schmidt, S. Gopalakrishnan, and H. Jasak, “Multi-dimensional simulation of thermal non-equilibrium channel flow,” *International Journal of Multiphase Flow*, vol. 36, no. 4, pp. 284 – 292, 2010.
- [13] H. W. M. Witlox and P. J. Bowen, “Flashing liquid jets and two-phase dispersion. Contract Research Report 403,” 2002.
- [14] C. J. Wang, J. X. Wen, and Z. B. Chen, “Simulation of large-scale lng pool fires using firefoam,” *Combustion Science and Technology*, vol. 186, no. 10-11, pp. 1632–1649, 2014.
- [15] P. D. Patel and T. G. Theofanous, “Hydrodynamic fragmentation of drops,” *Journal of Fluid Mechanics*, vol. 103, pp. 207–223, 2 1981.
- [16] C. Habchi, D. Verhoeven, H. C Huu, L. Lambert, J. L. Vanhemelryck, and T. Baritaud, “Modeling atomization and break up in high-pressure diesel sprays,” vol. 106, 02 1997.
- [17] M. Boivin, O. Simonin, and K. D. Squires, “On the prediction of gas–solid flows with two-way coupling using large eddy simulation,” *Physics of Fluids*, vol. 12, no. 8, pp. 2080–2090, 2000.
- [18] L. Y. M. Gicquel, P. Givi, F. A. Jaber, and S. B. Pope, “Velocity filtered density function for large eddy simulation of turbulent flows,” *Physics of Fluids*, vol. 14, no. 3, pp. 1196–1213, 2002.
- [19] X. Jiang, G. Siamas, K. Jagus, and T. Karayiannis, “Physical modelling and advanced simulations of gas–liquid two-phase jet flows in atomization and sprays,” *Progress in Energy and Combustion Science*, vol. 36, no. 2, pp. 131 – 167, 2010.
- [20] S. Yoon, J. Hewson, P. DesJardin, D. Glaze, A. Black, and R. Skaggs, “Numerical modeling and experimental measurements of a high speed solid-cone water spray for use in fire suppression applications,” *International Journal of Multiphase Flow*, vol. 30, no. 11, pp. 1369 – 1388, 2004.
-

- [21] G. E. Cossali and S. Tonini, "Oscillating droplet evaporation modelling for spray combustion simulation," in *DIPSI Workshop 2012 on Droplet Impact Phenomena & Spray Investigation*, 2012.
- [22] R. Schmehl, G. Maier, and S. Wittig, "CFD analysis of fuel atomization, secondary droplet breakup and spray dispersion in the premix duct of a LPP combustor," *Eight International Conference on Liquid Atomization and Spray Systems*, 2000.
- [23] M. M. Foss, "LNG safety and security," CEE, 2003.
- [24] W. Huang, J. Bai, S. Zhao, and A. Lv, "Investigation of oil vapor emission and its evaluation methods," *Journal of Loss Prevention in the Process Industries*, vol. 24, no. 2, pp. 178 – 186, 2011.
- [25] G. Atkinson, S. Coldrick, S. Gant, and L. Cusco, "Flammable vapor cloud generation from overfilling tanks: Learning the lessons from buncefield," *Journal of Loss Prevention in the Process Industries*, vol. 35, no. Supplement C, pp. 329 – 338, 2015.
- [26] D. Johnson, "Vapor cloud explosion at the ioc terminal in jaipur," *Hazards XXIII*, pp. 556 – 564, 2012.
- [27] CBS News, "<https://www.cbsnews.com/news/fire-explosion-puerto-rico-power-substation-today-2018-02-11/>," 2018.
- [28] Reuters, "<https://uk.reuters.com/article/uk-venezuela-refinery-startup/venezuela-struggles-with-refinery-blaze-after-deadly-blast-idukbre87p0bo20120826>," 2012.
- [29] G. Atkinson and S. Coldrick, "Vapour cloud formation: Experiments and modelling. Health and Safety Laboratory RR908," 2012.
- [30] G. Atkinson and S. E. Gant, "Buncefield investigation: Liquid flow and vapour production. Health and Safety Laboratory RR936," 2012.
- [31] G. Atkinson and S. E. Gant, "Flammable vapour cloud risks from tank overfilling incidents. Health and Safety Laboratory RR937," 2012.
- [32] R. S. Brodkey, *The Phenomena of Fluid Motions*. Dover Publications, 1995.

- [33] S. Coldrick, S. Gant, G. Atkinson, and R. Dakin, “Factors affecting vapour production in large scale evaporating liquid cascades,” *Process Safety and Environmental Protection*, vol. 89, no. 6, pp. 371 – 381, 2011.
- [34] S. Chandra and C. T. Avedisian, “On the collision of a droplet with a solid surface,” *Proceedings of the Royal Society of London A: Mathematical, Physical and Engineering Sciences*, vol. 432, no. 1884, pp. 13–41, 1991.
- [35] C. Mundo, M. Sommerfeld, and C. Tropea, “Droplet-wall collisions: Experimental studies of the deformation and breakup process,” *International Journal of Multiphase Flow*, vol. 21, no. 2, pp. 151 – 173, 1995.
- [36] E.-S. R. Negeed, S. Hidaka, M. Kohno, and Y. Takata, “High speed camera investigation of the impingement of single water droplets on oxidized high temperature surfaces,” *International Journal of Thermal Sciences*, vol. 63, pp. 1 – 14, 2013.
- [37] J. Shen, C. Graber, J. Liburdy, D. Pence, and V. Narayanan, “Simultaneous droplet impingement dynamics and heat transfer on nano-structured surfaces,” *Experimental Thermal and Fluid Science*, vol. 34, no. 4, pp. 496 – 503, 2010.
- [38] Š. Šikalo, C. Tropea, and E. Ganić, “Impact of droplets onto inclined surfaces,” *Journal of Colloid and Interface Science*, vol. 286, no. 2, pp. 661 – 669, 2005.
- [39] A. Šlančiauskas and R. Kalpokaitė, “Behaviour of a heavy fuel oil droplet on a hot surface,” *International Journal of Heat and Mass Transfer*, vol. 49, no. 5–6, pp. 1050 – 1057, 2006.
- [40] S. S.a, M. F. Trujillo, X. Wu, and G. Chahine, “Computational and experimental characterization of a liquid jet plunging into a quiescent pool at shallow inclination,” *International Journal of Heat and Fluid Flow*, vol. 34, pp. 1 – 14, 2012.
- [41] E. Berberovic, *Investigation of Free-surface Flow Associated with Drop Impact: Numerical Simulations and Theoretical Modeling*. PhD thesis, Technische Universität, Darmstadt, November 2010.

-
- [42] A. V. Mahulkar, G. B. Marin, and G. J. Heynderickx, “Droplet–wall interaction upon impingement of heavy hydrocarbon droplets on a heated wall,” *Chemical Engineering Science*, vol. 130, pp. 275 – 289, 2015.
- [43] K. Yokoi, “A numerical method for free-surface flows and its application to droplet impact on a thin liquid layer,” *Journal of Scientific Computing*, vol. 35, no. 2, pp. 372–396, 2008.
- [44] A. M. Worthington, “On the forms assumed by drops of liquids falling vertically on a horizontal plate,” *Proceedings of the Royal Society of London*, vol. 25, pp. 261–272, 1876.
- [45] O. G. Engel, “Waterdrop collisions with solid surfaces,” *Journal of Research of the National Bureau of Standards*, vol. 54, no. 5, pp. 281 – 298, 1955.
- [46] P. Savic and G. T. Boulton, *The fluid flow associated with the impact of liquid drops with solid surfaces*, pp. 43–84. Heat Transfer and Fluid Mechanics Institute, Stanford University Press, Stanford, CA, US, 1957.
- [47] Z. Levin and P. V. Hobbs, “Splashing of water drops on solid and wetted surfaces: Hydrodynamics and charge separation,” vol. 269a, pp. 555–585, 1971.
- [48] C. D. Stow and R. D. Stainer, “The physical products of a splashing water drop,” *Meteorological Society of Japan Journal*, vol. 55, pp. 518–532, 1977.
- [49] C. D. Stow and M. G. Hadfield, “An experimental investigation of fluid flow resulting from the impact of a water drop with an unyielding dry surface,” *Proceedings of the Royal Society of London A: Mathematical, Physical and Engineering Sciences*, vol. 373, no. 1755, pp. 419–441, 1981.
- [50] C. Bai and A. D. Gosman, “Development of methodology for spray impingement simulation,” in *SAE Technical Paper*, SAE International, 1995.
- [51] C. X. Bai, H. Rusche, and A. D. Gosman, “Modeling of gasoline spray impingement,” *Atomization and Sprays*, vol. 12, no. 1-3, pp. 1–27, 2002.
- [52] D. Kalantari and C. Tropea, “Phase doppler measurements of spray impact onto rigid walls,” *Experiments in Fluids*, vol. 43, no. 2, pp. 285–296, 2007.
-

- [53] D. W. Stanton and C. J. Rutland, “Multi-dimensional modeling of thin liquid films and spray-wall interactions resulting from impinging sprays,” *International Journal of Heat and Mass Transfer*, vol. 41, no. 20, pp. 3037 – 3054, 1998.
- [54] D. Kalantari, “Evaluation of some of the existing models for droplet and spray/wall interactions,” *Fluid Dyn. Mater. Process.*, vol. 92, pp. 169–182, 2013.
- [55] R. L. V. Wal, G. M. Berger, and S. D. Mozes, “The splash/non-splash boundary upon a dry surface and thin fluid film,” *Experiments in Fluids*, vol. 40, no. 1, pp. 53–59, 2006.
- [56] G. Cossali, A. Coghe, and M. Marengo, “The impact of a single drop on a wetted solid surface,” *Experiments in Fluids*, vol. 22, no. 6, pp. 463–472, 1997.
- [57] D. Kalantari and C. Tropea, “Spray impact onto flat and rigid walls: Empirical characterization and modelling,” *International Journal of Multiphase Flow*, vol. 33, no. 5, pp. 525 – 544, 2007.
- [58] D. Kalantari and C. Tropea, “Spray impact onto rigid walls: Formation of the liquid film,” *10th International Conference on Liquid Atomization and Spray Systems*, 2006.
- [59] D. Kalantari and C. Tropea, “Liquid spray impact onto flat and rigid walls: Formation and spreading of accumulated wall film,” *Fluid Dynamics and Material Processing*, vol. 10, pp. 37–61, 2014.
- [60] D. Kalantari, *Characterization of liquid spray impact onto walls and films*. PhD thesis, Technische Universität, Darmstadt, February 2007.
- [61] R. Schmehl, H. Roskamp, M. Willmann, and S. Wittig, “Cfd analysis of spray propagation and evaporation including wall film formation and spray/film interactions,” *International Journal of Heat and Fluid Flow*, vol. 20, no. 5, pp. 520–529, 1999.
- [62] A.-B. Wang and C.-C. Chen, “Splashing impact of a single drop onto very thin liquid films,” *Physics of Fluids*, vol. 12, pp. 2155–2158, 09 2000.

- [63] H. Zhao, A. Brunsvold, and S. T. Munkejord, “Transition between coalescence and bouncing of droplets on a deep liquid pool,” *International Journal of Multiphase Flow*, vol. 37, no. 9, pp. 1109 – 1119, 2011.
- [64] G. E. Cossali, M. Marengo, A. Coghe, and S. Zhdanov, “The role of time in single drop splash on thin film,” *Experiments in Fluids*, vol. 36, no. 6, pp. 888–900, 2004.
- [65] L. Wachters and N. Westerling, “The heat transfer from a hot wall to impinging water drops in the spheroidal state,” *Chemical Engineering Science*, vol. 21, no. 11, pp. 1047–1056, 1966.
- [66] M. F. Trujillo, J. Alvarado, E. Gehring, and G. Soriano, “Numerical simulations and experimental characterization of heat transfer from a periodic impingement of droplets,” *Journal of Heat Transfer*, vol. 133, p. 122201, 12 2011.
- [67] H. Fujimoto, Y. Oku, T. Ogihara, and H. Takuda, “Hydrodynamics and boiling phenomena of water droplets impinging on hot solid,” *International Journal of Multiphase Flow*, vol. 36, no. 8, pp. 620 – 642, 2010.
- [68] K. Yokoi, “A practical numerical framework for free surface flows based on CLSVOF method, multi-moment methods and density-scaled CSF model: Numerical simulations of droplet splashing,” *Journal of Computational Physics*, vol. 232, no. 1, pp. 252 – 271, 2013.
- [69] S. Hysing, S. Turek, D. Kuzmin, N. Parolini, E. Burman, S. Ganesan, and L. Tobiska, “Quantitative benchmark computations of two-dimensional bubble dynamics,” *International Journal for Numerical Methods in Fluids*, vol. 60, no. 11, pp. 1259–1288, 2008.
- [70] S. Deshpande, L. Anumolu, and M. F. Trujillo, “Evaluating the performance of the two-phase flow solver interFoam,” *Computational Science & Discovery*, vol. 5, 2012.
- [71] J. Roenby, H. Bredmose, and H. Jasak, “A computational method for sharp interface advection,” *Royal Society Open Science*, vol. 3, no. 11, pp. 693–711, 2016.

- [72] R. P. Koopman and D. L. Ermak, “Lessons learned from LNG safety research,” *Journal of Hazardous Materials*, vol. 140, no. 3, pp. 412 – 428, 2007. LNG Special Issue - Dedicated to Risk Assessment and Consequence Analysis for Liquefied Natural Gas Spills.
- [73] J. Wells, “Public safety consequences of a liquefied natural gas spill need clarification,” *Maritime Security*, 2007.
- [74] F. Gavelli, S. Davis, R. Olav, O. Hansen, and M. Ichard, “CFD Simulation of Vapor Dispersion From LNG Jetting and Flashing Releases,” *10AIChE - 2010 AIChE Spring Meeting and 6th Global Congress on Process Safety*, 2010.
- [75] K. Koyama, “CFD Simulation on LNG Storage Tank to Improve Safety and Reduce Cost,” in *Systems Modeling and Simulation* (K. Koyamada, S. Tamura, and O. Ono, eds.), (Tokyo), pp. 39–43, Springer Japan, 2007.
- [76] J. D. Anderson, *Computational Fluid Dynamics*. McGraw-Hill Series in Mechanical Engineering, 1995.
- [77] H. Jasak, *Error Analysis and Estimation for the Finite Volume Method with Applications to Fluid Flows*. PhD thesis, University of London, 1996.
- [78] J. H. Ferziger and M. Peric, *Computational Methods for Fluid Dynamics*. Springer, 2002.
- [79] S. V. Patankar, *Numerical Heat Transfer and Fluid Flow*. McGraw-Hill, 1980.
- [80] S. Subramaniam, “Lagrangian–eulerian methods for multiphase flows,” *Progress in Energy and Combustion Science*, vol. 39, no. 2, pp. 215–245, 2013.
- [81] G. Gouesbet and A. Berlemont, “Eulerian and lagrangian approaches for predicting the behaviour of discrete particles in turbulent flows,” *Progress in Energy and Combustion Science*, vol. 25, no. 2, pp. 133 – 159, 1999.
- [82] C. Hirt and B. Nichols, “Volume of fluid (VOF) method for the dynamics of free boundaries,” *Journal of Computational Physics*, vol. 39, no. 1, pp. 201 – 225, 1981.

-
- [83] M. Jadidi, M. Tembely, S. Moghtadernejad, and A. Dolatabadi, “A coupled level set and volume of fluid method with application to compressible two-phase flow,” in *Proceedings of the 22nd Annual Conference of the CFD Society of Canada, Toronto, ON, Canada*, pp. 1–4, 2014.
- [84] A. Albadawi, D. Donoghue, A. Robinson, D. Murray, and Y. Delauré, “Influence of surface tension implementation in volume of fluid and coupled volume of fluid with level set methods for bubble growth and detachment,” *International Journal of Multiphase Flow*, vol. 53, pp. 11 – 28, 2013.
- [85] C. T. Crowe, *Multiphase flow handbook*, vol. 59. CRC press, 2005.
- [86] S. Hoyas, A. Gil, X. Margot, D. Khuong-Anh, and F. Ravet, “Evaluation of the eulerian–lagrangian spray atomization (elsa) model in spray simulations: 2d cases,” *Mathematical and Computer Modelling*, vol. 57, no. 7, pp. 1686 – 1693, 2013.
- [87] A. Desportes, M. Zellat, G. Desoutter, D. Abouri, Y. Liang, and F. Ravet, “Validation and application of the eulerian-lagrangian spray atomization (elsa) model for the diesel injection simulation,” *SAE Technical Paper*, 2010.
- [88] L. Schiller and A. Naumann, “A drag coefficient correlation,” *Z. Ver. Deutsch. Ing.*, vol. 77, pp. 318–320, 1935.
- [89] W. E. Ranz and W. R. Marshall, “Evaporation from drops: Part 2,” *Chemical Engineering Progress*, 1952.
- [90] L.-P. Hsiang and G. Faeth, “Near-limit drop deformation and secondary breakup,” *International Journal of Multiphase Flow*, vol. 18, no. 5, pp. 635 – 652, 1992.
- [91] M. Jain, R. S. Prakash, G. Tomar, and R. V. Ravikrishna, “Secondary breakup of a drop at moderate weber numbers,” *Proceedings of the Royal Society of London A: Mathematical, Physical and Engineering Sciences*, vol. 471, no. 2177, 2015.
- [92] S. B. Pope, *Turbulent Flows*. Cambridge University Press, 2000.
- [93] F. Menter, M. Kuntz, and R. Langtry, “Ten years of industrial experience with the sst turbulence model,” *Turbulence, heat and mass transfer*, vol. 4, no. 1, pp. 625–632, 2003.
-

- [94] S. Apte, K. Mahesh, F. Ham, G. Constantinescu, and P. Moin, “Large-eddy simulation of multiphase flows in complex combustors,” *Advances in Fluid Mechanics*, vol. 37, pp. 53–62, 2004.
- [95] S. Navarro-Martinez, “Large eddy simulation of spray atomization with a probability density function method,” *International Journal of Multiphase Flow*, vol. 63, pp. 11 – 22, 2014.
- [96] L. Lignarolo, C. Gorlé, A. Parente, and C. Benocci, “Large eddy simulation of the atmospheric boundary layer using openfoam,” in *13th International Conference on Wind Engineering–Amsterdam, The Netherlands*, 2011.
- [97] L. Berselli, T. Iliescu, and W. J. Layton, *Mathematics of large eddy simulation of turbulent flows*. Springer Science & Business Media, 2005.
- [98] A. Leonard, “Energy cascade in large-eddy simulations of turbulent fluid flows,” in *Turbulent Diffusion in Environmental Pollution*, pp. 237 – 248, Elsevier, 1975.
- [99] M. Germano, “Turbulence: the filtering approach,” *Journal of Fluid Mechanics*, vol. 238, pp. 325–336, 1992.
- [100] J. Smagorinsky, “General circulation experiments with the primitive equations,” *Monthly Weather Review*, vol. 91, no. 3, pp. 99–164, 1963.
- [101] F. Moukalled, L. Mangani, and M. Darwish, *The Finite Volume Method in Computational Fluid Dynamics*. Springer, 2016.
- [102] G. Allaire and S. M. Kaber, *Direct Methods for Linear Systems*, pp. 97–124. New York, NY: Springer New York, 2008.
- [103] S. Patankar and D. Spalding, “A calculation procedure for heat, mass and momentum transfer in three-dimensional parabolic flows,” *International Journal of Heat and Mass Transfer*, vol. 15, no. 10, pp. 1787 – 1806, 1972.
- [104] H. K. Versteeg and W. Malalasekera, *An introduction to Computational Fluid Dynamics*. Longman Scientific & Technical, 1995.
- [105] R. Issa, “Solution of the implicitly discretised fluid flow equations by operator-splitting,” *Journal of Computational Physics*, vol. 62, pp. 40–65, jan 1986.

- [106] T. Maric, J. Höpken, and K. Mooney, *The OpenFOAM Technology Primer*. 2015.
- [107] A. Mack and M. Spruijt, “Validation of OpenFOAM for heavy gas dispersion applications,” *Journal of Hazardous Materials*, vol. 262, pp. 504 – 516, 2013.
- [108] C. Kralj, *Numerical simulation of Diesel spray processes*. PhD thesis, University of London, 1996.
- [109] S. Gant, A. Heather, and A. Kelsey, “CFD modelling of evaporatin hydrocarbon sprays. Health and Safety Laboratory CM/07/04,” 2007.
- [110] A. L. Brown and R. A. Jepsen, “An improved drop impact model for lagrangian/eulerian coupled codes,” in *ASME International Mechanical Engineering Congress and Exposition*, SAE International, 2009.
- [111] Y. Zhang, M. Jia, H. Liu, and M. Xie, “Development of an improved liquid film model for spray/wall interaction under engine-relevant conditions,” *International Journal of Multiphase Flow*, vol. 79, pp. 74 – 87, 2016.
- [112] R. Kumar and A. Dewan, “Assessment of buoyancy-corrected turbulence models for thermal plumes,” *Engineering Applications of Computational Fluid Mechanics*, vol. 7, no. 2, pp. 239–249, 2013.
- [113] S. O’Brien and L. Schwartz, “Theory and modeling of thin film flows,” *Encyclopedia of surface and colloid science*, vol. 5283, 2002.
- [114] K. Meredith, “Thin liquid film modeling in openfoam,” in *5th OpenFOAM Workshop, Chalmers, Gothenburg, Sweden*, 2010.
- [115] M. Stange, M. E. Dreyer, and H. J. Rath, “Capillary driven flow in circular cylindrical tubes,” *Physics of Fluids*, vol. 15, no. 9, pp. 2587–2601, 2003.
- [116] OpenFOAM Foundation, “OpenFOAM,” 2018.
- [117] E. Sjölander, “Spray and wall film modeling with conjugate heat transfer in openfoam,” Master’s thesis, Linköping University, Applied Thermodynamics and Fluid Mechanics, 2012.

-
- [118] F. Mashayek and R. Pandya, “Analytical description of particle/droplet-laden turbulent flows,” *Progress in Energy and Combustion Science*, vol. 29, no. 4, pp. 329 – 378, 2003.
- [119] C. Argyropoulos and N. Markatos, “Recent advances on the numerical modelling of turbulent flows,” *Applied Mathematical Modelling*, vol. 39, no. 2, pp. 693 – 732, 2015.
- [120] R. Reitz and R. Diwakar, “Structure of high-pressure fuel sprays,” 1987.
- [121] R. A. Mugele and H. D. Evans, “Droplet size distribution in sprays,” *Industrial & Engineering Chemistry*, vol. 43, no. 6, pp. 1317–1324, 1951.
- [122] A. Macías-García, E. M. Cuerda-Correa, and M. Díaz-Díez, “Application of the rosin–rammler and gates–gaudin–schuhmann models to the particle size distribution analysis of agglomerated cork,” *Materials Characterization*, vol. 52, no. 2, pp. 159 – 164, 2004.
- [123] P. González-Tello, F. Camacho, J. Vicaria, and P. González, “A modified nukiyama–tanasawa distribution function and a rosin–rammler model for the particle-size-distribution analysis,” *Powder Technology*, vol. 186, no. 3, pp. 278 – 281, 2008.
- [124] Y. Addad, D. Laurence, C. Talotte, and M. Jacob, “Large eddy simulation of a forward–backward facing step for acoustic source identification,” *International Journal of Heat and Fluid Flow*, vol. 24, pp. 562–571, 08 2003.
- [125] H. G. Weller, G. Tabor, H. Jasak, and C. Fureby, “A tensorial approach to computational continuum mechanics using object-oriented techniques,” *Computers in Physics*, vol. 12, no. 6, pp. 620 – 631, 1998.
- [126] M. Macchi, J. X. Wen, K. Volkov, A. Heidari, and Y. M. Chung, “Modeling liquid fuel cascades with openfoam,” *Process Safety Progress*, vol. 35, no. 2, pp. 179 – 184, 2016.
- [127] S. Coldrick, G. Atkinson, and S. Gant, “Large scale evaporating liquid cascades—an experimental and computational study,” in *Proc. IChemE Hazards XXII Symposium, Liverpool, UK. IChemE, Rugby, ISBN*, vol. 1212422483, 2011.
-

-
- [128] R. D. Deegan, P. Brunet, and J. Eggers, “Complexities of splashing,” *Non-linearity*, vol. 21, no. 1, pp. C1–C11, 2008.
- [129] M. Angioletti, R. D. Tommaso, E. Nino, and G. Ruocco, “Simultaneous visualization of flow field and evaluation of local heat transfer by transitional impinging jets,” *International Journal of Heat and Mass Transfer*, vol. 46, no. 10, pp. 1703 – 1713, 2003.
- [130] K.-L. Pan and C.-Y. Hung, “Droplet impact upon a wet surface with varied fluid and surface properties,” *Journal of Colloid and Interface Science*, vol. 352, no. 1, pp. 186 – 193, 2010.
- [131] Y.-S. Shim, G.-M. Choi, and D.-J. Kim, “Numerical and experimental study on effect of wall geometry on wall impingement process of hollow-cone fuel spray under various ambient conditions,” *International Journal of Multiphase Flow*, vol. 35, no. 10, pp. 885 – 895, 2009.
- [132] K. Yokoi, “A density-scaled continuum surface force model within a balanced force formulation,” *Journal of Computational Physics*, vol. 278, pp. 221 – 228, 2014.
- [133] M. Sussman, P. Smereka, and S. Osher, “A level set approach for computing solutions to incompressible two-phase flow,” *Journal of Computational Physics*, vol. 114, no. 1, pp. 146 – 159, 1994.
- [134] C. Kunkelmann and P. Stephan, “Modification and extension of a standard volume-of-fluid solver for simulating boiling heat transfer,” in *Proceedings ECCOMAS CFD 2010 – Fifth European Conference on Computational Fluid Dynamics*, 2010.
- [135] M. Dianat, M. Skarysz, and A. Garmory, “A coupled level set and volume of fluid method for automotive exterior water management applications,” *International Journal of Multiphase Flow*, vol. 91, pp. 19 – 38, 2017.
- [136] T. Yamamoto, “Setting and usage of openfoam multiphase solver (s-clsvof),” in *30th OpenCAE study meeting, Kansai, Japan*, 2014.
- [137] M. Griebel and M. Klitz, *Simulation of Droplet Impact with Dynamic Contact Angle Boundary Conditions*, pp. 297–325. Springer International Publishing, 2014.
-

- [138] Š. Šikalo, H.-D. Wilhelm, I. V. Roisman, S. Jakirlić, and C. Tropea, “Dynamic contact angle of spreading droplets: Experiments and simulations,” *Physics of Fluids*, vol. 17, no. 6, 2005.
- [139] R. J. Good and M. Koo, “The effect of drop size on contact angle,” *Journal of Colloid and Interface Science*, vol. 71, no. 2, pp. 283 – 292, 1979.
- [140] Y. Yuan and T. R. Lee, *Contact Angle and Wetting Properties*, pp. 3–34. Berlin, Heidelberg: Springer Berlin Heidelberg, 2013.
- [141] W. D. Kingery and M. Humenik, “Surface tension at elevated temperatures. i. furnace and method for use of the sessile drop method; surface tension of silicon, iron and nickel,” *The Journal of Physical Chemistry*, vol. 57, no. 3, pp. 359–363, 1953.
- [142] E. Ramé, “The interpretation of dynamic contact angles measured by the wilhelmy plate method,” *Journal of Colloid and Interface Science*, vol. 185, no. 1, pp. 245 – 251, 1997.
- [143] G. Jones and L. D. Frizzell, “A theoretical and experimental analysis of the capillary rise method for measuring the surface tension of solutions of electrolytes,” vol. 8, pp. 986–997, 01 1940.
- [144] A. Criscione, R. Röhrig, S. Jakirlić, I. Roisman, and C. Tropea, “Impacting droplets: Dynamic contact angle modeling in openfoam,” in *7th Open-FOAM Workshop, Darmstadt (Germany)*, 2012.
- [145] K. Yokoi, D. Vadillo, J. Hinch, and I. Hutchings, “Numerical studies of the influence of the dynamic contact angle on a droplet impacting on a dry surface,” *Physics of Fluids*, vol. 21, no. 7, 2009.
- [146] J. Brackbill, D. Kothe, and C. Zemach, “A continuum method for modeling surface tension,” *Journal of Computational Physics*, vol. 100, no. 2, pp. 335 – 354, 1992.
- [147] R. L. Vander Wal, G. M. Berger, and S. D. Mozes, “Droplets splashing upon films of the same fluid of various depths,” *Experiments in Fluids*, vol. 40, no. 1, pp. 33–52, 2006.

- [148] NIST, “National Standard Reference Data Series (NSRDS).”
<https://www.nist.gov/srd/srd-publications/national-standard-reference-data-series-nsrds>, 2018.